Efficient Transmission Design for Machine Type Communications in Future Wireless Communication Systems

Shendi WANG

A thesis submitted for the degree of Doctor of Philosophy.
The University of Edinburgh.
September 2016

Abstract

With a wide range of potential applications, the machine type communication (MTC) is gaining a tremendous interest among mobile network operators, system designers, MTC specialist companies, and research institutes. The idea of having electronic devices and systems automatically connected to each other without human intervention is one of the most significant objectives for future wireless communications. Low data rate transmission and the requirement for low energy consumption are two typical characteristics for MTC applications. In terms of supporting low cots MTC devices, industrial standards will be more efficient if designers can re-use many features of existing radio access technologies. This will yield a cost effective solution to support MTC in future communication systems. This thesis investigates efficient MTC waveform and receiver designs for superior signal transmission quality with low operational costs.

In terms of the downlink receiver design, this thesis proposes a novel virtual carrier (VC) receiver system for MTC receivers, which aims to reduce the maximum bandwidth to improve the data processing efficiency and cost-efficiency by using analogue filters to extract only sub-carriers of interest. For the VC receiver systems, we thus reduce the sampling rate in order to reduce the number of subsequent processing operations, which significantly reduces the analogue-to-digital converter (ADC) cost and power consumption while providing high signal to interference noise ratio (SINR) and low bit to error rate (BER) to support low data rate MTC devices. Our theoretical equations account for the interference effect of aliasing on the sub-carrier location, and this helps the system designer to evaluate what kind of filters and receiver sampling rate can be used to balance the energy cost and detection performance.

In terms of the uplink waveform design, considering the enhanced number of MTC devices in the future communication systems, i.e. the fifth generation (5G) communications, the same tight synchronisation as used in today appears not to be cost-effective or even possible. Synchronisation signals, which aim to provide a perfect time or frequency synchronisation in the current fourth generation (4G) communication systems (known as the long-term evolution, LTE), is much more costly for low data rate MTC transmissions. The system bandwidth will be significantly reduced if a base station tries to synchronise all received signals among hundreds or thousands MTC devices in one transmission time period. In terms of relaxing the synchronisation requirements, this thesis compares and analyses the side-lobe reduction performance for several candidate multi-carrier waveforms to avoid these problems. We also propose the infinite impulse response universal filtered multi-carrier (UFMC) system and the overlap and add UFMC system, which significantly reduce the processing complexity compared with the state of the art UFMC techniques. This thesis derives closed-form expressions for the interference caused by time offsets between adjacent unsynchronised MTC users. Our analytical equations can be used in both simple and complex time-offset transmission scenarios, and enable the system designer to evaluate the SINR, the theoretical Shannon capacity and the BER performance.

Declaration of originality

I hereby declare that the research recorded in this thesis and the thesis itself was composed and originated entirely by myself in the Institute for Digital Communications (IDCOM), School of Engineering, The University of Edinburgh.

Shendi WANG

September, 2016

Acknowledgements

First of all, there is no any single word can represent my thanks to my supervisor Prof. John S. Thompson, who not only guide me on the knowledges, technique issues, researches, etc. The most important thing is how to research successfully, how to find the key point or *blue sky*, and then how to dramatically develop and critically evaluate it. I will never forget his unlimited encouragement. John always provides a positive atmosphere to me, especially when I tough issues/problems on my research. Without his constructive suggestions and continuous supports, this thesis would not be done or even possible.

I am heartily thankful to Prof. Peter M. Grant, who carefully proofread this thesis and our papers. He uses his immense knowledges provide lots of constructive advices and suggestions for me. His rigorous research attitude influences me on the way to be a distinctive researcher and it will encourage me in my whole life.

I am here grateful to thank Prof. Jean Armstrong, who provides lots of useful suggestions on our works and encourages me on my study. I would also like to sincerely thank my associate supervisor Dr. David I. Laurenson, who gives me lots of advices in the early stage of this study and also protect a good working space for our study.

I truly thank to my PhD. classmates, Cheng Chen, Yibo He, Yichen Li, Wenjun Fu, and Zhe Chen, as friends, we are living together, studying together and moving forward together. I also say thank you to all my colleagues in the IDCOM. Their support and companionship gave me wonderful experiences during this four years.

A very special thank my parents, Li Wang and Lanzhen Song for their constant words of encouragement that gave me the strength to keep going and funded on my study. I wish to thank my wife Youyun Yuan for her continuous love and always stay with me no matter where we are. I thank her family for care my study and my life.

Contents

List of figures

List of tables

Acronyms and abbreviations

1G	First generation of wireless telephone technology
3GPP	Third-generation partnership project
4G	Fourth generation of wireless mobile telecommunications technology
5G	5th generation mobile networks
ADC	Analogue-to-digital converter
AWGN	Additive white Gaussian noise
BER	Bit error rate
BS	Base station
CA	Carrier aggregation
CCDF	Complementary cumulative distribution function
CFO	Carrier frequency offset
CP	Cyclic prefix
DFT	Discrete Fourier transform
DL	Downlink
ETSI	European telecommunications standards institute
FBMC	Filter bank multi-carrier
FDD	Frequency division duplex
FFT	Fast Fourier transform
FIR	Finite impulse response
GPRS	General packet radio service
GSM	Global system for mobile
H2H	Human to Human
HTC	Human type communication
ICI	Intercarrier interference
IEEE	Institute of electrical and electronics engineers
IFFT	Inverse fast Fourier transform
IIR	Infinite impulse response
IoT	Internet of Things
ISI	Intersymbol interference

LPF	Low pass filter
LTE	Long-term evolution
M2M	Machine to machine
MIMO	Multiple-input multiple-output
MTC	Machine type communication
OA	Overlap and Add
OFDM	Orthogonal frequency-division multiplexing
OFDMA	Orthogonal frequency-division multiple access
PAPR	Peak-to-average power ratio
PCC	Polynomial cancellation coded
PDCCH	Physical downlink control channel
PON	Passive optical network
PSCH	Primary synchronisation channel
PSD	Power spectral density
PSS	Primary synchronisation signal
PUCCH	Physical uplink control channel
RACH	Random access channel
SC	Separate carrier
SCC	Symmetric cancellation coding
SC-FDMA	Single carrier frequency division multiple access
SINR	Signal-to-interference-noise ratio
SNR	Signal-to-noise ratio
SSCH	Secondary synchronisation channel
SSS	Secondary synchronisation signal
STBC	Space time block codes
UE	User equipment
UFMC	Universal filtered multi-carrier
UL	Uplink
VC	Virtual carrier
VCCS	Virtual carrier control signal
WOLA	Weighted overlap and add
ZF	Zero forcing
ZP	Zero-padding

Nomenclature

$A(n)$ PCC-OFDM modulated signal in the frequency domain

$a(t)$ PCC-OFDM modulated signal in the time domain

A_{PB} Passband ripple in dB

A_{S} Stopband attenuation in dB

A_{SL} OFDM side-lobe attenuation

$B(n)$ Filter frequency response

$B_{\mathrm{d}}(e^{j\omega})$ Ideal filter frequency response

$b(t)$ Filter impulse response in the time domain

$b_{\mathrm{d}}(t)$ Ideal filter impulse response in the time domain

B_{PB} Bandwidth of transmission (passband)

B_{W} Bandwidth of baseband

C Capacity

C_u Capacity for the uth user

d_{o} Minimum distance between two symbols

d_u Distance between the $u^t h$ MTC terminal device and the base station

E_{b} Energy per bit

E_{b}/N_0 Bit to noise ratio

E_{n} Noise energy in one symbol period

E_{s} Energy per symbol

f_{cf} Normalised cut-off frequency

f_{ds} Down sampled sampling frequency

f_{s} Sampling frequency

f_{vc} Sampling frequency of VC receiver

$G(n)$ FFT of AWGN noise sequence g in the frequency domain

$g(t)$ AWGN noise sequence in time domain

$H(n)$ Channel frequency response

$h(t)$ Channel impulse response in time domain

H_{ent}	Entropy (i.e. the number of bits per symbol)
I_{A}	Aliasing term in the frequency domain
i_{Err}	Interference term for timing sample error
$i_A(t)$	Aliasing noise
i_u^{OFDM}	Interference terms caused by time offsets for u^{th} OFDM user in the time domain
I_u^{OFDM}	Interference terms caused by time offsets for u^{th} OFDM user in the frequency domain
i_u^{UFMC}	Interference terms caused by time offsets for u^{th} UFMC user in the time domain
I_u^{UFMC}	Interference terms caused by time offsets for u^{th} UFMC user in the frequency domain
K	Number of sub-carriers for sub-user
k	Index number, k = [0, K-1]
k_{B}	Boltzmann's constant
L	Length in samples of transmitted signal
L_{com}	Length of the combined channel and filter impulse response in samples
L_{CP}	Length of CP in samples
L_{F}	Length of filter impulse response in samples
l_{H}	Channel taps index
L_{H}	Length of multipath channel taps (or Length of channel impulse response in samples)
L_{OL}	Length of the overlapped samples
L_{T}	Length of tail of UFMC filter impulse response
N	Number of FFT or The total number of sub-carriers
n	Index number, n = [0, N-1]
N_0	Noise power spectral density
N_{b}	Number of bits per symbol
$N_{\mathrm{I}}(k)^2$	Interference power for aliasing
N_{sym}	Number of symbols per OFDM modulation scheme
$P_{4\mathrm{PSK}u}^{\mathrm{OFDM}}$	Probability of bit error with OFDM, 4PSK, and u^{th} user
$P_{4\mathrm{PSK}u}^{\mathrm{UFMC}}$	Probability of bit error with UFMC, 4PSK, and u^{th} user
P_{ADC}	Power dissipation of an ADC
P_{b}	Probability of bit error
P_{noise}	Power of noise
P_{signal}	Power of transmitted signal

$P_{\text{ISI}}(k)$	PSD of ISI
$P_{\text{ISI}u}^{\text{OFDM}}(k)$	PSD of ISI for the CP-OFDM uth user
$P_{\text{ISI}u}^{\text{UFMC}}(k)$	PSD of ISI for the UFMC uth user
$PAPR_{\text{dB}}$	PAPR in dB
q	quantisation step size
$q_{\text{qua}}(t)$	Quantisation noise
$R^{\text{PCC}}(n)$	Received signal for PCC-OFDM in the frequency domain
$r^{\text{PCC}}(t)$	Received signal for PCC-OFDM in the time domain
$R_{\text{A}}(k)$	Received signal for VC receiver over the AWGN channel in the frequency domain
r_{am}	Envelope amplitude of the received signal
$R_{\text{Lo}}(k)$	Received signal for VC receiver when $L_{\text{CP}} > L_{\text{com}}$ in the frequency domain
$r_{\text{LPF}}(t)$	Received signal after an IIR filter
R_{sym}	Symbol rate
$R_{\text{F}}(k)$	Received signal over the VC receiver in the frequency domain
$S(k)^2$	Received signal power of VC receiver
$s_u(t)$	Transmitted UFMC signal for the uth user in the time domain
$S_u^{\text{E}}(m)$	Efficient FFT windowed baseband signal in the frequency domain
$s_u^{\text{IIR}}(t)$	Truncated IIR-UFMC signal with L samples in the time domain
SNR	Signal to noise ratio
T_{s}	Sample period
T_{Temp}	Temperature
U	Maximum number of transmitted sub-users in the uplink
u	User index in the uplink
$U_c(k)$	FFT of the tail of the combined impulse response
$w(t)$	Window function
$W_{\text{cn}}(n)$	Frequency response of combined channel and filter
$w_{\text{cn}}(t)$	Combined channel and filter impulse response in the time domain
$X(n)$	Baseband signal on the n th sub-carrier in the frequency domain
$x(t)$	Transmitted signal in the time domain
$x_{u,i}(t)$	Transmitted signal of the ith OFDM symbol of the uth user in the time domain
X^{E}	Frequency domain extra sequence samples for the efficient FFT
X^{Total}	Baseband signal for the input of the efficient FFT

$X_u(n)$	Transmitted baseband signal for the uth user in the frequency domain
$x_u(t)$	Transmitted baseband signal for the uth user in the time domain
$Y^{\text{PCC}}(n)$	Weighting and then summing the received PCC-OFDM signal in the frequency domain
$y_{\text{F}}(t)$	Filter outputs in the time domain
$y_{\text{Lo}}(m)$	Filter outputs of received signal when $L_{\text{CP}} > L_{\text{com}}$
$Z_u^{\text{OFDM}}(k)$	Residual ISI of the OFDM uth user on the kth sub-carrier in the frequency domain
α_{ol}	Overlap factor between overlapped samples and N
β	Scaling mismatch factor between IFFT and FFT
δ	Dirac delta
δ_{PB}	Passband ripple
δ_{SB}	Stopband ripple
Δf	Sub-carrier spacing
η	Spectral efficiency
γ	Sampling reduction ratio
γ_{ro}	Ratio between the number of sub-carriers per user and total number of available sub-carriers
ρ	SINR
$\rho_u(k)$	SINR for the uth user
σ	Gaussian standard deviation
σ_{r}	Rayleigh fading deviation
τ	Time offset in samples between two adjacent users
τ_{Err}	Timing error in samples
$\tilde{A}$	Average number of the nearest neighbour symbols in the OFDM constellation
$\tilde{S}_u(m)$	Transmitted OA-UFMC signal for the uth user in the frequency domain
$\tilde{s}_u(t)$	Transmitted OA-UFMC signal for the uth user in the time domain
Γ	Computational complexity in operations
$\varrho(r_{\text{am}})$	Probability density function (pdf) of the Rayleigh distribution
$\text{erfc}(.)$	complementary error function
$\mathbb{E}[\cdot]$	Expectation operation
$\otimes$	Convolution operation

Chapter 1
Introduction

This thesis addresses the machine type communication (MTC) systems considering cost-efficiency in both downlink and uplink channels. Our main aim is to achieve a good signal quality for MTC applications and at the same time reduce the operation costs to enable low cost MTC devices. In this introductory chapter, Section 1.1 introduces the motivation of the thesis. Section 1.2 summarises the main objectives and key contributions of the research. Section 1.3 provides the outline of the remaining chapters of the thesis.

1.1   Motivation

Wireless communication technologies have been improved rapidly, especially in the last decade. Systems have evolved from the first generation (1G) communication networks based on the analogue telecommunications radio system developed in 1980s, to current fourth generation (4G) networks, known as the long-term evolution (LTE). LTE has the advantage of high spectrum efficiency, which allows it to provide high data rate transmission. It implements the orthogonal frequency-division multiple access (OFDMA) scheme in the downlink, which is a physical channel link used for transmitting signals from a base station (BS) to a user equipment (UE). LTE uses the single carrier frequency division multiple access (SC-FDMA) scheme in the uplink, which is used for transmitting signals from the UEs to the BS. Given the worldwide growth in the number of the UEs and in high data rate services, they increase the contribution of information technology to the overall energy consumption of the world [1]. Among, spectral efficiency and energy efficiency could be the main performance metrics for designing green radio networks [2]. The study of the "green" and low cost communication systems has become a significant issue for researchers. Moreover, with the previous focus to achieve high data rate transmission techniques, low cost and low data rate machine type communication (MTC) or machine to machine (M2M) communication systems have became a new frontier for wireless research [3].

In terms of the population, there are 7 billion people and 80% of them have been linked through
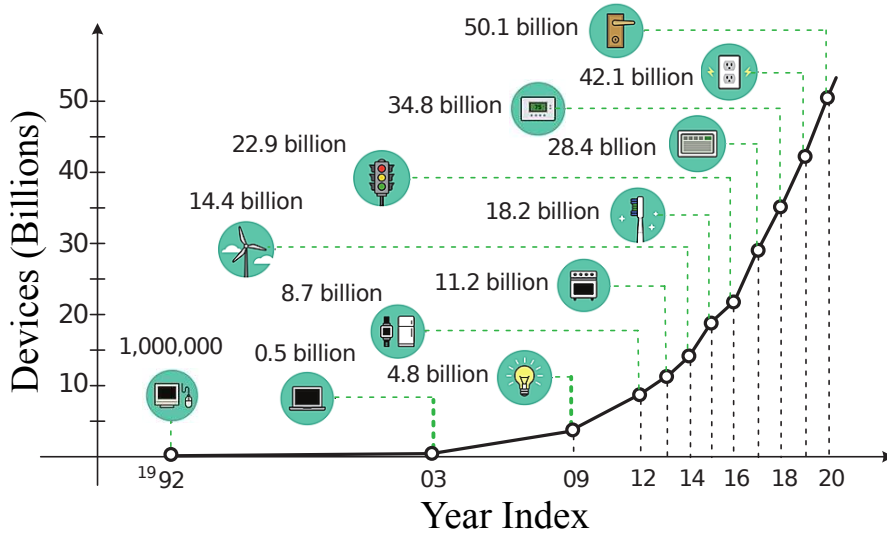
Figure 1.1: *Expected Number of Connected MTC Devices to the Internet [6].*

the mobile network [4]. With the move towards the internet of things (IoT) [5], the idea of having machines communicate with machines automatically with minimal human intervention has been mentioned in terms of improving human life. The ultimate objective of MTC is to construct comprehensive connections among all the machines distributed over extensive coverage area. A recent study [6] shows that the number of machines or devices in the IoT increases significantly, i.e. there were only about 4.8 billion machines connected to internet in 2009, but the expected growth in the projected number of MTC devices will reach a total of approximately 50 billion by the year 2020, as shown in Figure 1.1. Wireless communications in the near future is thus shifting from the existing human type communication (HTC) mode to the MTC mode.

In order to satisfy HTC high data rate requirements, i.e. using the mobile networks for web surfing, playing on-line games and even watching high definition videos, high spectrum efficiency systems based on the orthogonal frequency-division multiplexing (OFDM) techniques are been widely using in the current LTE systems. Unlike current HTC, MTC normally requires small data packets for automated data transmissions and interacting between MTC devices and IoT application centres [7]. MTC devices are designed to measure and collect data, i.e. body temperature, vehicular traffic information, and transmit them to the networks using the smart sensors. Moreover, many sensors have a small form factor, which directly limits the available battery space. In order to maximise the battery life, MTC should be cost-efficient and energy-efficient.

Due to the different features, modifying the existing radio access technologies (i.e. LTE) to enable support for both high data rate HTC and cost-efficient low data rate MTC becomes one of the key issues for researches. This requirement has been highlighted in the third-generation partnership project (3GPP) specification [8].

First, in terms of the MTC downlink channel, in LTE Release 12 [9], several concepts that may provide significant cost savings for supporting the low data rate MTC devices were presented, such as reducing the LTE maximum bandwidth, the peak rate, the transmit power, and the reduction of supported downlink transmission modes [8]. LTE normally can provide a maximum bandwidth of 20 MHz to the UEs, which can yield data rates up to 100.8 Mbps if using a single antenna. MTC usually only requires a narrow bandwidth carrier to transmit occasional data packets. If an MTC device receives at a low data rate (which can be operated within 1 MHz) on a LTE 20 MHz bandwidth carrier, a large number of sub-carriers do not need to be processed. Moreover, Reference [8] reported that the reduction of the maximum bandwidth from 20 MHz to 1.4 MHz can save about 37.2% of the overall operation costs, such as the costs of analogue-to-digital converter (ADC) and fast Fourier transform (FFT). Thus, it will be more efficient to reduce the maximum bandwidth to a narrower bandwidth, i.e. 1.4 MHz, 3 MHz or 5 MHz, for MTC device and also support the HTC modes with the high data rate transmissions, i.e. 15 MHz.

Second, in terms of the MTC uplink channel, the thesis is motived to relax the signal synchronisation requirements. In detail, OFDM, as the core technique, is widely used in today 4G LTE networks. In OFDM systems, every orthogonal sub-carrier shape is a rectangular window in the time domain and hence a sinc-shaped sub-carrier in the frequency domain. If the orthogonality is destroyed by time or frequency offsets, the overall OFDM system performance will be reduced significantly [10]. In order to protect its orthogonality, LTE provides several control channels in a cellular system with the function of conveying physical layer messages, such as the physical uplink control channel (PUCCH) [11]. With increasing the number of MTC devices, one of the key purposes for the 5th generation wireless systems (5G) [12] is that devices will be able to connect to multiple access points. The same synchronisation techniques used in LTE may not suitable for "massive" MTC for two reasons: 1) The overhead of the synchronisation signals will not be cost-efficient for low data rate and low bandwidth MTC devices. 2) In the case of huge numbers of MTC devices, which might experience dynamic changes in distance and cause variable time-offsets, it will thus more complex if not impossible for a BS

to synchronise the received signals for all the users.

1.2   Objectives and Contributions

1.2.1   Objectives

The aim of this thesis is to modify OFDM systems in order to achieve cost-efficient MTC and at the same time provide a good signal detection performance in both downlink and uplink channels. More specifically, the thesis has the following two main objectives:

- In the MTC downlink channel, design analogue filters to reduce the maximum LTE bandwidth and extract only sub-carriers of interest, which are used for carrying low data rate MTC messages. This enables a reduction of the sampling rate at the MTC receiver in order to reduce the operation costs.

- In the MTC uplink channel, reduce the OFDM side-lobe levels in order to improve the robustness against intercarrier interference (ICI) caused by asynchronous wireless communications. This can relax the synchronisation requirements in order to provide more efficient MTC.

1.2.2   Key Contributions

The main contributions of this thesis are summarised as follows:

- Propose a reduced sampling rate virtual carrier (VC) receiver system for the MTC downlink channel. It significantly improves the bandwidth efficiency compared with the current LTE carrier aggregation (CA) technique. By reducing the sampling rate at the VC receiver, the ADC power consumption is lower and the computational complexity has been reduced significantly by reducing the number of operations in the FFT. Moreover, the VC system provides high signal-to-interference-noise ratio (SINR) and low bit error rate (BER) close to a full sample rate OFDM receiver for the sub-carriers of interest.

- Derive a closed-form expression for SINR which accounts for the effect of aliasing on the sub-carrier location for the reduced sampling rate VC system. Our SINR analysis includes the effect of the filter cut-off frequency, the receiver ADC sampling rate and

the sampling reduction ratio. The BER can also be evaluated in closed-form to show the trade-off between system parameter choices and detection performance. This helps the system designer to evaluate what kind of filters and receiver sampling rate can be used to balance the energy cost and detection performance. This thesis also derives a closed-form expression for the effect of intersymbol interference (ISI) caused by asynchronism in sampling for the VC receiver.

- Simulation evaluation the sidelobe reduction performance for 5 existing candidate multi-carrier waveforms designed for the 5G uplink channel, which are cyclic prefix (CP) OFDM, zero-padding (ZP-OFDM), weighted overlap and add (WOLA-OFDM), polynomial cancellation coded (PCC-OFDM) and universal filtered multi-carrier (UFMC). This thesis provides a detailed comparison including different filter designs, power spectral density (PSD), SINR, BER, overlap effects, computational complexity and peak-to-average power ratio (PAPR). We provide the first study of the time offset performance for UFMC with the analogue infinite impulse response (IIR) filters (IIR-UFMC) and propose the overlap and add UFMC (OA-UFMC) system in terms of reducing the computational complexity compared with UFMC.

- Derive closed-form expressions for the different types of interference caused by the integer time offset. Our closed-form expressions can be easily derived for the SINR, the Shannon capacity and the BER and can be used in both simple and complex time-offset transmission scenarios. This works will help in evaluating the performance of 5G uplink systems.

1.3 Thesis Outline

The remainder of the thesis is organised as follows:

Chapter 2

This chapter presents a basic background for this thesis, it provides an overview of MTC and highlights the key challenges. Then, the state of the art of OFDM systems is presented, including the a brief overview of OFDM, the transmission model and performance analysis. In terms of aliasing effects, this chapter provides a review of the Shannon sampling theorem. Basic filter designs and OFDM waveform behaviours are introduced at the end of this chapter.

Chapter 3

This chapter proposes the VC receiver systems using a mathematical model and analyses the LTE downlink efficiency and energy saving performance. A basic synchronisation processing methods is provided. Then, this chapter mathematically analyses the aliased interference and users it for SINR equations, which considers the additive white Gaussian noise (AWGN) channel, Rayleigh multipath channels and the intersymbol interference caused by the long channel impulse responses.

Chapter 4

This chapter concentrates on the practical simulations of time offset effects in the 5G uplink system and presents a detailed waveform side-lobe reduction performance comparison between CP/ZP-OFDM, WOLA-OFDM, PCC-OFDM, UFMC as well as proposing the IIR-UFMC method. This chapter compares the performance in terms of side-lobe behaviour, SINR vs BER results, computational complexity and also considers a large time-offset scenario with very dispersive multipath channels.

Chapter 5

This chapter describes the OA-UFMC systems and computes its computational complexity for comparison with UFMC systems. It then provides a closed-from expression for the ICI for both the OFDM, PCC-OFDM and UFMC systems and extends it to the SINR and BER theoretical equations. Finally, numerical results are provided with the conclusion of IIR-UFMC has a similar SINR, Shannon capacity and BER performance compared with UFMC, but it achieves a much lower complexity.

Chapter 6

This chapter concludes the whole thesis and introduces several future research directions.

<div align="right">

Chapter 2
Background

</div>

In this chapter, a basic background for this thesis is provided. We will start to introduce the machine type communications (MTC) with the basic developments, architectures and main challenges. In terms of supporting cost-efficient MTC, there are two aspects: In the MTC downlink channel, the maximum bandwidth should be reduced. In the uplink, reducing the OFDM side-lobe levels can relax the synchronisation requirements. Moreover, OFDM is a core technology for the LTE downlink and might be used for the 5th generation wireless system (5G) uplink. Then, this chapter will provide a detailed background for standard OFDM systems and also analyses the basic performance. An introduction to the Shannon sampling theorem will then be provided in terms of the aliasing effects during sampling reduction processing. In this thesis, we use filters to reduce the maximum bandwidth to achieve low cost transmission for the downlink, and we also use the narrow band filters to reduce the OFDM side-lobe levels to protect against the ICI caused by the time-offsets in the uplink. Filter designs are widely used in the thesis. Thus, a basic review of finite impulse response (FIR) filters and infinite impulse response (IIR) filters will be provided in the following sections. Finally, the OFDM side-lobe behaviour performance for the multi-user transmission will be provided at the end of this chapter.

2.1 Overview of the MTC Systems

In this section, a brief overview on the machine type communication (MTC) systems will be presented, including the MTC developments, architectures and challenges.

2.1.1 MTC Developments

Wireless communication technologies have been rapidly developing in the recent years, and mobile communications has become a basic tool for the modern society [13]. It has progressed from the first generation of cellular systems (1G), based on the analogue telecommunications

standards in the 1980s, through to the current fourth generation (4G) networks based on the long-term evolution (LTE) standards [14]. With the increasing demand for signal bandwidth to support data applications, orthogonal frequency-division multiplexing (OFDM) was unanimously adopted for 4G [15]. Today's wireless communication technologies focus on supporting high data transmission services, for instance, LTE aims to provide up to 100 Mbps (in the downlink) and 50 Mbps (in the uplink) speed for a 20MHz carrier bandwidth allocation [16].

Despite the focus to achieve high data transmission techniques, there is a new communication model with very different requirements, which is known as machine type communications. There will soon be 50 billion machines alongside the 7 billion people in the world, and about 80% of the population has been connected by using the mobile network worldwide [4] [17]. The idea of having devices connected to each other, operating in an autonomous manner, and without human intervention has become one of the most significant objectives in the future [18]. The third-generation partnership project (3GPP) mentioned that communication networks will shift from the existing human to human (H2H) communication mode to the machine to machine (M2M) communication mode. M2M will be experience exponential growth in the next generation of communication networks due to the demand for automated systems such as the smart grid and the smart home [17].

M2M communication, which is referred to as machine type communication (MTC) in the 3GPP terminology [18], supports automated data transmissions and enables interactions between devices and applications through the cellular networks or internet that is called Internet of Things (IoT) [7]. Interactions include data measurement, collection and transmission between mechanical or electronic devices with applications in three main aspects: 1) remotely controlled systems, i.e. utilities, building automation, security and manufacturing, 2) smart systems, i.e. smart meters, smart grids, smart cars and smart traffic control, 3) medical systems, i.e. smart medical sensors and e-health [10].

2.1.2 MTC Architecture

Currently, there is still not a global standard to ensure the success of MTC due to the various applications that may be used in the future [19]. With all the different MTC standards activities for in various scenarios, to establish an unique and global MTC standard seemingly might be difficult. Today, many organisations, such as the 3GPP, institute of electrical and electronics engineers (IEEE), and European telecommunications standards institute (ETSI) have activated
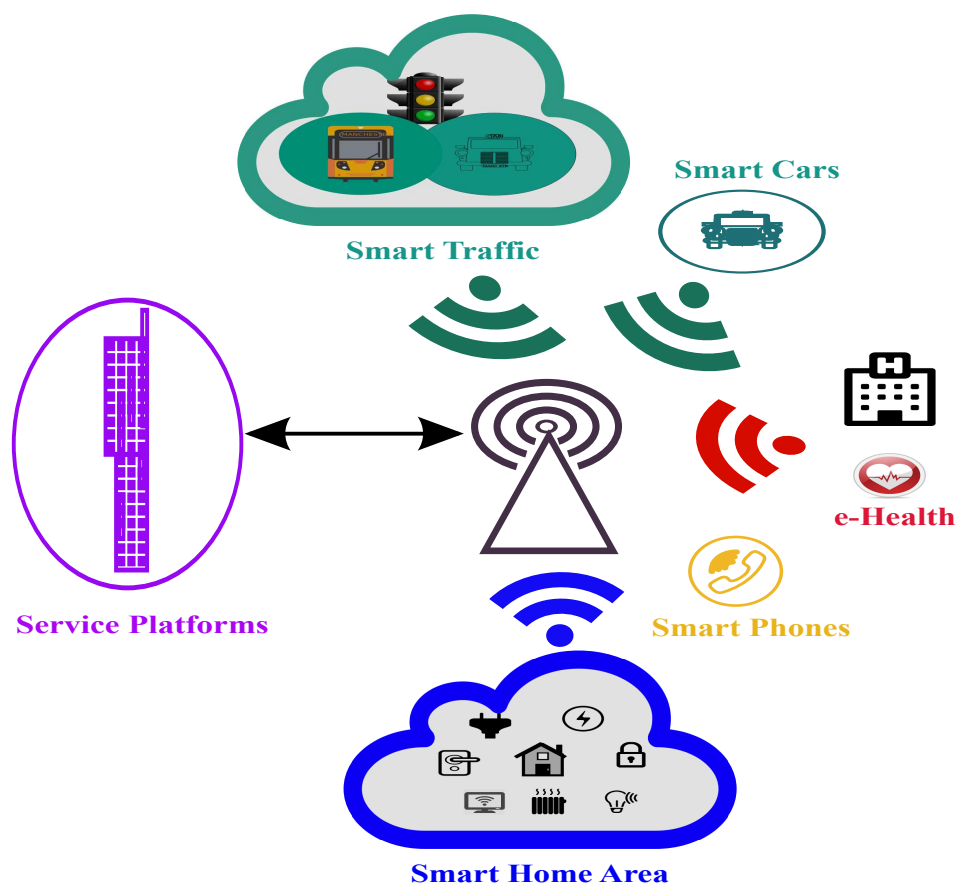
Figure 2.1: *An Example of an MTC Architecture.*

in the MTC standard development [19], [20], [21].

An example of a feasible MTC network architecture is shown in Figure 2.1, based on the standard proposed by ETSI [22]. MTC devices and application centres will be connected through the wireless networks. In this architecture, MTC devices may connect to the base station in two different ways: one alternative is to directly connect to the base station, e.g., a smart vehicular sensor is placed on a car in order to collect the traffic data such as speed or distances between vehicles then transmits it to a traffic centre through the base station. The second alternative is that MTC devices transmit data using short range links to an MTC gateway, then the gateway forwards all received messages from different MTC devices to the base station to save operation costs, i.e. the smart home scenario. Smart meters, heating, or other home applications transmits the data to a gateway using the short range technologies such as WiFi (Bluetooth or ZigBee). Then, the gateway forwards the messages to the base station, which transmits them to the service platforms.

2.1.3   Key Challenges of MTC

There are several previous papers present the major challenges in facilitating MTC over the existing and future cellular infrastructures [6], [8], [21], [23] and [24], we now summarise the major challenges as below:

First, the operation costs should be limited. Many sensors, such as the medical sensors, are limited by their resources including power, sensing, transmission and computation. The demand for small sensors leads to the small size of batteries, which have tight constraints on power conservation [25]. How to save the operation cost in terms of extending the battery life becomes one of the most significant challenges in MTC.

Second, modifying the existing radio access technologies. There are many companies now focusing on an efficient MTC system by developing a new access wireless technology for MTC. The 3GPP specification [8] highlights that it will be more efficient for designers to be able to use the existing radio access technology, such as OFDM, which is widely used in LTE. In LTE Release 12 [8], several concepts that may provide significant cost savings were presented, such as reduction of maximum bandwidth, reduction of peak rate, reduction of transmit power, and reduction of supported downlink transmission modes. In detail, normally the maximum bandwidth for the user equipments (UEs) is 20 MHz. In MTC, many MTC devices only require low data rates, which can be operated in low bandwidth channels. Therefore, one potential technique is to reduce the maximum bandwidth (e.g., to 1.4 MHz, 3 MHz or 5 MHz) and meanwhile, the system can also support H2H modes with higher bandwidth carriers, i.e. 15 MHz. Reference [8] showed that if the maximum bandwidth is reduced to 1.4 MHz, the overall relative cost savings is about 37.2%, such as the costs of the analogue-to-digital converter (ADC), the digital-to-analogue converter (DAC), the fast Fourier transform (FFT), the inverse fast Fourier transform (IFFT), the post-FFT data buffering, the receiver processing block, decoding and synchronisation blocks. In terms of the reduction of peak rate, several techniques can be used, such as the reduction of maximum transport block sizes and restricting the maximum modulation order.

Third, relax the synchronisation requirements. Currently, many researchers study the 5th generation wireless systems (5G). One of the main applications for 5G is to support massive numbers of MTC devices accessing to the network [24]. In LTE, control channels in a cellular system with the functions of conveying physical layer messages to support data transmissions, such

as the physical uplink control channel (PUCCH), require access to the UL shared channel. In OFDM systems, which are used in the current LTE system, each signal sub-carrier is shaped using a rectangular window in the time domain which is a sinc-shaped sub-carrier in the frequency domain [10]. In order to protect the orthogonality of the uplink, LTE uses the control signals for perfect time and frequency synchronisation. MTC may not use the control signals due to two reasons: Firstly, as mentioned above, MTC normally transmits only few bytes of information or requires a guarantee of low latency e.g., real time vehicular traffic informations. Thus, the overhead of multiple symbols for transmitting control signals will be not efficient. Secondly, one key aspect in 5G is designed to support the multi-user MTC devices. The dynamic changes in distance between the MTC devices might require a flexible synchronised processing. Therefore, the tight synchronisation techniques used in LTE might not be efficient and even possible in the future [26].

Fourth, there are some other type of challenges, such as the dynamic resource allocation protocol and MTC transmission physical layer security, introduced in [23], [27] and [28]. The behaviour of MTC devices might be coordinated according to state of the network. Especially, when the network is overloaded by the excessive access attempts caused by the large number of MTC devices access to the network may be blocked for a short time. Reference [29] addressed the energy efficiency optimisation problems consisting of a macro-cell and multiple pico-cells, which could be used for the massive low data rate MTC systems. Transmit beamforming design and power allocation policies to optimise the system's energy efficiency or cost efficiency. Reference [23] proposed that MTC data transmission should be guaranteed with both reliability and security, i.e. protect against physical layer attacks or configuration attacks (such as a malicious software update).

This thesis mainly focuses on addressing MTC data transmission issues as described above in the first three challenges. In the next sections, we will briefly introduce the basic OFDM transmission model and the filter designs used in this thesis.

2.2 OFDM Systems

The multi-carrier technology, orthogonal frequency-division multiplexing (OFDM) [30], has been widely studied and used, e.g., today's LTE designs based on OFDM. It has several advantages, such as high spectral efficiency (orthogonal multi-carrier access), robust against the

intersymbol interference (ISI) and fading caused by the multipath propagations (using the cyclic prefix), and the high data rate transmission (higher modulation schemes, e.g., 64QAM).

2.2.1 Brief Overview of the OFDM Systems

2.2.1.1 Orthogonal Sub-carriers

In OFDM systems, sub-carriers are orthogonal and mapped into different frequencies, e.g., the sub-carrier spacing in LTE is $\Delta f = 15$ kHz [8]. An example of the orthogonal sub-carriers in the frequency domain is shown in Figure 2.2. Each sub-carrier carries one modulated symbol
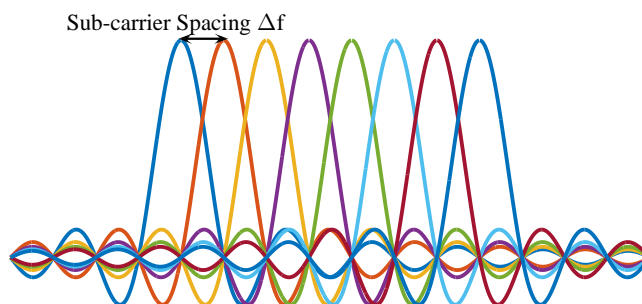
Figure 2.2: *An Example of OFDM Sub-carriers.*

through varying the phase or amplitude (such as in the 4QAM scheme, each symbol contains 2 bits message, e.g., the complex signal 1+j). With the advantages of FFT/IFFT, the very complex process of modulating (and demodulating) of a large number of sub-carriers can be easily carried out by using the IFFT and FFT algorithms, which computes the Fourier transformation very efficiently, and provides a simple way of ensuring the carrier signals produced are orthogonal. An N-point IFFT converts N complex data samples, which presents a baseband signal in the frequency domain, into the equivalent time domain signal with the same number of N in samples. At the OFDM receiver, using same N-point FFT converts the received time domain samples into the frequency domain.

2.2.1.2 Spectral Efficiency

In OFDM, several modulation schemes are used based on the spectral efficiency and data rate, such as 2PSK (or BPSK), 4PSK (or QPSK), 8PSK, 16QAM and 64QAM. High order modula-

tion schemes increase the spectral efficiency but also require high signal-to-noise ratio (SNR). The spectral efficiency is given by [31]:

$$\eta = \frac{R_{\text{sym}} H_{\text{ent}}}{B_{\text{PB}}}, \tag{2.1}$$

where R_{sym} is the symbol rate i.e. the number of symbols per second, H_{ent} is the entropy measured in the number of bits per symbol, and B_{PB} in Hz is the bandwidth of the passband signal. The value of η is expressed in bits/sec/Hz, which measures the bit rate that can be transmitted in 1 Hz bandwidth. In practice, the spectral efficiency can be simply defined as:

$$\eta = \log_2(N_{\text{sym}}), \tag{2.2}$$

where N_{sym} is the number of symbols per OFDM modulation scheme (or the order of the modulation scheme). For 16QAM as an example, the spectral efficiency can be computed as $\eta = \log_2(16) = 4$ bits/sec/Hz. The 16QAM modulation constellation is shown in Figure 2.3, each constellation point can represent 4 bits of data, with two bits on the I axis and two on the Q axis.
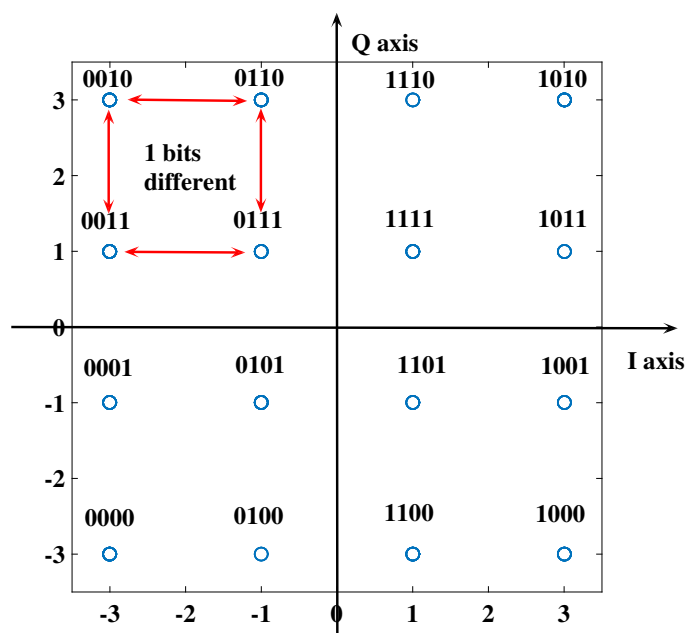
Figure 2.3: *16QAM Constellation.*

2.2.1.3 OFDM Peak-to-Average Power Ratio

One of the drawbacks for OFDM is the high peak-to-average power ratio (PAPR) [32]. As mentioned above, the IFFT processing results in the sum of all frequency domain signal samples. In this case, the time domain signals of OFDM starts looks like samples from a Gaussian distribution when increasing the number of sub-carriers, which directly causes high PAPR [33]. The PAPR is defined as:

$$PAPR_{\mathrm{dB}} = 10\mathrm{log}\big(\frac{\max[|x(t)|^2]}{\mathbb{E}[|x(t)|^2]}\big), \tag{2.3}$$

where $x(t)$ is the transmitted OFDM symbol in the time domain and $\mathbb{E}[\cdot]$ represents the expectation operation. High PAPR requires a power amplifier whose gain is linear over a wide dynamic range. The large amplitude variation increases in-band noise and increases the bit error rate (BER), especially for a non-linear power amplifier [34].

2.2.1.4 OFDMA in LTE

3GPP employs the orthogonal frequency division multiple access (OFDMA) technology, which utilises OFDM as its key modulation technique, for the LTE downlink radio transmission [35]. Due to the use of relatively narrowband sub-carriers in combination with a cyclic prefix (CP) as a guard interval, copying the final L_{CP} samples into the front of the symbol, OFDMA transmission is inherently robust to time dispersion in a multipath channel.

There are many reasons for OFDMA to be a successful waveform in the LTE downlink, such as the multipath handling capability, scalability of operation in different bandwidths, the ability to handle different data rates, and the ability to operate efficiently with multiple antenna techniques [35] and [36]. In OFDMA networks, multiple users share the total bandwidth to exploit multiuser diversity and improve the system capacity with dynamic resource allocation strategies [2]. In OFDMA systems, the available spectrum can be split into several smaller sub-channels, where each sub-channel is designed for various services as required. This flexibility for managing the sub-carriers helps LTE to use channel dependent scheduling in both the time and frequency domain, e.g., schedulers which decide which users are allowed to transit on what frequency resources, and what data rate to use [37].

2.2.2   OFDM Transmission Model

The OFDM system block diagram is shown in Figure 2.4. As mentioned in Section 2.2.1.2, in order to transmit binary data into the time domain efficiently, firstly, the mapping operator converts the binary data vector into a complex digital constellation, such as the PSK or QAM modulation schemes. Here we take the 16QAM with Gray coding [38] as an example, see in Figure 2.3, which is widely used to facilitate error correction in digital communications [39]. The Gray code provides the same Hamming distance for any two adjacent symbols in which two successive values differ in only one bit.

Transmitter

Binary Data → Modulator → Serial to Parallel → N - IFFT → Parallel to Serial → Cyclic Prefix Extension

White Gaussian Noise $g(t)$ → ⊕ → Multipath Channel h

Receiver

Binary Data ← Demodulator ← Parallel to Serial ← N - FFT & Equalisation ← Serial to Parallel ← Cyclic Prefix Remove
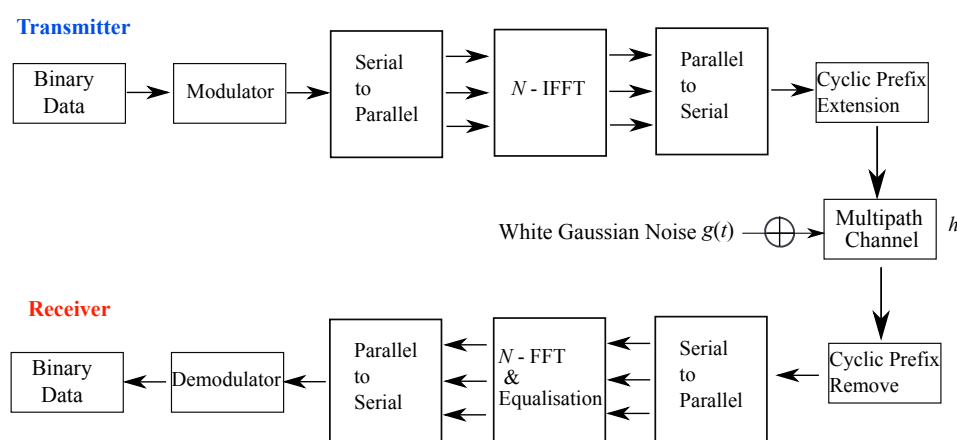
Figure 2.4: *OFDM System Block Diagram.*

Assume that the number of sub-carriers for data transmission is N, which refers to N complex modulated symbols. The baseband signal on the nth sub-carrier in the frequency domain is defined as $X(n)$, where $n \in [0, N-1]$. The baseband OFDM signal at the output of the N-point IFFT after adding the CP in the time domain can be expressed as:

$$x(t) = \frac{1}{\sqrt{N}} \sum_{n=0}^{N-1} X(n) \cdot e^{j2\pi nt/N}, \ t \in [0, L-1], L = N + L_{\text{CP}}, \qquad (2.4)$$

where X is the N-point FFT of x, and L_{CP} is the length of CP in samples. The CP as a guard interval protects against the ISI caused by the multipath propagation delays, and only works when $L_{\text{CP}} > L_{\text{H}}$, where L_{H} is the number of multipath channel taps. An example of a multipath channel is shown in Figure 2.5.

Multipath fading occurs to varying extents in many wireless communication systems, when the radio energy arrives at the receiver by more than one path [31]. Multipath propagation delays
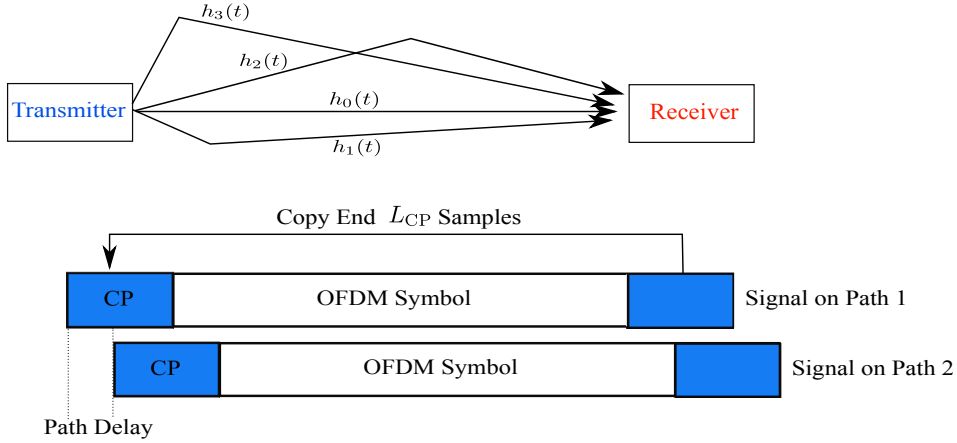
Figure 2.5: *Effect of the Multipath Delays on the OFDM Symbol with CP.*

may occur due to various reflections, e.g., from the ground, tropospheric layers or buildings. The multipath fading phenomena can be characterised into two types, as large-scale fading and small-scale fading [40]. The large-scale fading represents the signal power attenuation or path loss at the receiver after travelling over large areas, e.g., hills, buildings or other obstacles [40]. The small-scale fading, known as the Rayleigh fading, refers to the dramatic changes in signal amplitude and phase that can result due to small changes in distance. Rayleigh fading is widely used to simulate the wireless multipath fading channels when there is no direct ray component, which is often classified as the worst case fading type. The probability density function (pdf) of the Rayleigh distribution is given by [40]:

$$\varrho(r_{\mathrm{am}}) = \frac{r_{\mathrm{am}}}{\sigma_{\mathrm{r}}^2} e^{-\frac{r_{\mathrm{am}}^2}{2\sigma_{\mathrm{r}}^2}}, (r_{\mathrm{am}} > 0) \tag{2.5}$$

where r_{am} is the envelope amplitude of the received signal, and σ_{r}^2 is the pre-detection mean power of the multipath signal. Thus, we can compute the mean amplitude as:

$$\begin{aligned}
\mathbb{E}(R_{\mathrm{am}}) &= \int_{-\infty}^{+\infty} r_{\mathrm{am}}\varrho(r_{\mathrm{am}})dr_{\mathrm{am}} = \int_{0}^{+\infty} \frac{r_{\mathrm{am}}^2}{2} e^{-\frac{r_{\mathrm{am}}^2}{2\sigma_{\mathrm{r}}^2}} dr_{\mathrm{am}} \\
&= \int_{0}^{+\infty} -r_{\mathrm{am}} d((e^{-\frac{r_{\mathrm{am}}^2}{2\sigma_{\mathrm{r}}^2}})) = \underbrace{-r_{\mathrm{am}}(e^{-\frac{r_{\mathrm{am}}^2}{2\sigma_{\mathrm{r}}^2}})}_{=0} + \underbrace{\int_{0}^{+\infty} e^{-\frac{r_{\mathrm{am}}^2}{2\sigma_{\mathrm{r}}^2}} dr_{\mathrm{am}}}_{\text{Similar to Gaussian}} \\
&= \sqrt{2\pi}\sigma_{\mathrm{r}} \int_{0}^{+\infty} \frac{1}{\sqrt{2\pi}\sigma_{\mathrm{r}}} e^{-\frac{r_{\mathrm{am}}^2}{2\sigma_{\mathrm{r}}^2}} dr_{\mathrm{am}} = \sigma_{\mathrm{r}}\sqrt{\pi/2}.
\end{aligned} \tag{2.6}$$

16

The Rayleigh multipath channel can be expressed as:

$$h(t) = \sum_{l_{\mathrm{H}}=0}^{L_{\mathrm{H}}-1} h_{tl_{\mathrm{H}}} \delta(t - l_{\mathrm{H}} T_{\mathrm{s}}), \tag{2.7}$$

where each channel tap $h_{t,l_{\mathrm{H}}}$ follows the Rayleigh distribution, T_{s} is the sample period, and $\delta(t)$ is the Dirac delta function. For the additive white Gaussian noise (AWGN) channel without multipath, $L_{\mathrm{H}} = 1, h_{tl} = 1$. Then, we assume the transmitted signal over the Rayleigh multipath channel and the receiver AWGN noise can be defined as $y(t)$:

$$y(t) = x(t) \otimes h(t) + g(t), \tag{2.8}$$

where $\otimes$ denotes the convolution operation and $g(t)$ represents AWGN with power spectral density $N_0/2$. The received signal firstly passes a matched filter and is sampled as the same transmitted frequency f_{s}. After removing the CP and applying the FFT, the frequency domain signal can be expressed as:

$$Y(n) = X(n) \cdot H(n) + G(n), \tag{2.9}$$

where $H(n)$ is the FFT of the vector $[h_{0t}, h_{1t}, ..., h_{L_{\mathrm{H}}-1 t}]$ and G is the FFT of the noise sequence g in the frequency domain. In order to decode the received messages, several channel equalisation methods, e.g., zero forcing equalisation [41] can be used to estimate the transmitted data as:

$$\hat{X}(n) = \frac{Y(n)}{H(n)} = X(n) + \frac{G(n)}{H(n)}. \tag{2.10}$$

2.2.3 Analysis of the Performance of the OFDM System

2.2.3.1 BER

In the AWGN channel, with a white noise power spectral density N_0 at the receiver input, the total noise power is $P_{\mathrm{noise}} = N_0/2T_{\mathrm{s}}$, so that over one symbol interval T_{s} the noise energy can be expressed by [42]:

$$E_{\mathrm{n}} = \sigma^2 = P_{\mathrm{noise}} T_{\mathrm{s}} = N_0/2. \tag{2.11}$$

17

The energy per bit to noise power spectral density ratio E_b/N_0 can be expressed as:

$$E_b/N_0 = \frac{E_s}{N_0 \cdot N_b} = \frac{E_s}{2\sigma^2 \cdot N_b},$$ (2.12)

where E_b is the average energy per bit, E_s is the average energy per symbol and N_b is the number of bits per symbol.

Thus we can represent the σ^2 as:

$$\begin{aligned} \sigma^2 &= \frac{E_s}{2N_b E_b/N_0} \\ &= \frac{E_s}{2N_b}\left(\frac{E_b}{N_0}\right)^{-1}, \end{aligned}$$ (2.13)

The theoretical BER equation for any type of the modulations in the AWGN channel is given by [43]:

$$P_b = \frac{\tilde{A}}{2N_b}\text{erfc}\left(\sqrt{\frac{N_b d_o^2}{4E_s} \cdot \frac{E_b}{N_0}}\right),$$ (2.14)

where $\tilde{A}$ the average number of the nearest neighbour symbols in the constellation and d_o is the minimum distance between two symbols. Now, the theoretical BER equations for the comment modulations, (e.g., BPSK, 4PSK, 8PSK, 16QAM and 64QAM) can be expressed separately as described below.

BPSK and 4PSK

Each transmitted symbol in BPSK is located at $1 + 0j$ or $-1 + 0j$, as shown in Figure 2.6(a), thus

$$\tilde{A}_{\text{BPSK}} = \frac{1+1}{2} = 1,\; E_{s\text{BPSK}} = \frac{1^2 + 0^2 + (-1)^2 + 0^2}{2} = 1,\; d_{o\text{BPSK}} = 2^2 = 4,$$

then we can write the BER equation for BPSK as:

$$\begin{aligned} P_{\text{BPSK}} &= \frac{\tilde{A}}{2N_b}\text{erfc}\left(\sqrt{\frac{N_b d_o^2}{4E_s} \cdot \frac{E_b}{N_0}}\right) \\ &= \frac{1}{2}\text{erfc}\left(\sqrt{\frac{E_b}{N_0}}\right). \end{aligned}$$ (2.15)
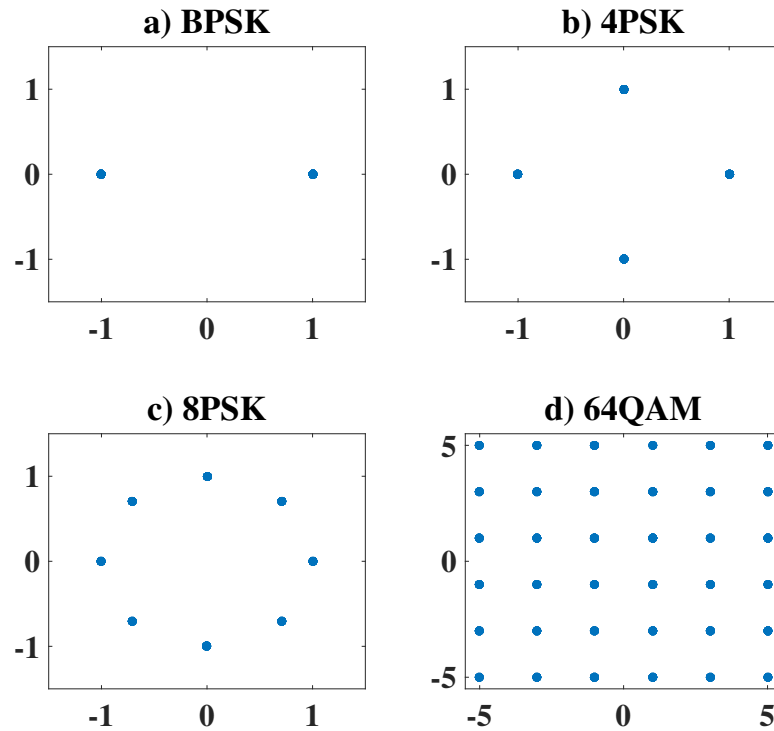
Figure 2.6: *OFDM Constellation Schemes, a) BPSK, b) 4PSK, c) 8PSK and d) 64QAM.*

Similar with BPSK, the average number of the nearest neighbour symbols for 4PSK, as shown in Figure 2.6(b), increases to $\tilde{A}_{4\text{PSK}} = 2$ and the number of bits per symbol also increases to $N_{\text{b4PSK}} = 2$, thus the BER equation for 4PSK is same as the BPSK:

$$P_{4\text{PSK}} = \frac{1}{2}\text{erfc}\left(\sqrt{\frac{E_\text{b}}{N_0}}\right). \tag{2.16}$$

8PSK

In terms of computing the d_o for 8PSK, as shown in Figure 2.6(c), we use the Cosine Rule, and the d^2_{o8PSK} can be computed as:

$$d^2_{\text{o8PSK}} = 1^2 + 1^2 - 2 \cdot 1 \cdot 1 \cos(\pi/4) \tag{2.17}$$
$$= 2 - \sqrt{2}.$$

The BER for 8PSK can be expressed as:

$$P_{8PSK} = \frac{2}{2 \cdot 3} \text{erfc}\left(\sqrt{\frac{3(2 - \sqrt{2})}{4} \cdot \frac{E_b}{N_0}} \right) \tag{2.18}$$

$$= \frac{1}{3} \text{erfc}\left(\sqrt{\frac{6 - 3\sqrt{2}}{4} \cdot \frac{E_b}{N_0}} \right).$$

Note that, the d_{o8PSK}^2 for the 8PSK also can compute as $d_{o8PSK}^2 = 4\sin^2(\pi/8)$.

16QAM and 64QAM

In 16QAM, each transmitted sub-carrier or constellation symbol reports 4 data bits, as shown in Figure 2.3. We count the average number of the nearest neighbour symbols for 16QAM as:

$$\tilde{A}_{16QAM} = 4(1 \cdot 2 + 1 \cdot 4 + 2 \cdot 3)/16 = 3, \tag{2.19}$$

symbols. And we computed the average energy per symbol is $E_{s16QAM} = 10$, and $d_o = 4$. For 64QAM, as shown in Figure 2.6(d), the $\tilde{A}_{64QAM}$ can be easily computed as:

$$\tilde{A}_{64QAM} = \frac{4(9 \cdot 4 + 6 \cdot 3 + 1 \cdot 2)}{64} = 3.5, \tag{2.20}$$

and the energy per symbol for the 64QAM is computed as $E_{s64QAM} = 42$. Thus we can present the BER equation for 16QAM and 64QAM as:

$$P_{16QAM} \approx \frac{3}{8} \text{erfc}\left(\frac{2}{5} \cdot \frac{E_b}{N_0} \right) \tag{2.21}$$

$$P_{64QAM} \approx \frac{7}{24} \text{erfc}\left(\frac{1}{7} \cdot \frac{E_b}{N_0} \right). \tag{2.22}$$

In terms of the Rayleigh fading channel, previous papers [44], [45] have provided the BER equations as:

$$P_{4PSK} = \frac{1}{2}\left(1 - \sqrt{\frac{E_b/N_0}{1 + E_b/N_0}} \right), \tag{2.23}$$

$$P_{16QAM} = \frac{1}{2}\left(1 - \frac{3}{4}\sqrt{\frac{4 \cdot E_b/N_0}{5/2 + 4 \cdot E_b/N_0}} - \frac{1}{2}\sqrt{\frac{4 \cdot E_b/N_0}{5/18 + 4 \cdot E_b/N_0}} + \frac{1}{4}\sqrt{\frac{4 \cdot E_b/N_0}{1/10 + 4 \cdot E_b/N_0}} \right). \tag{2.24}$$

BER Numerical Results
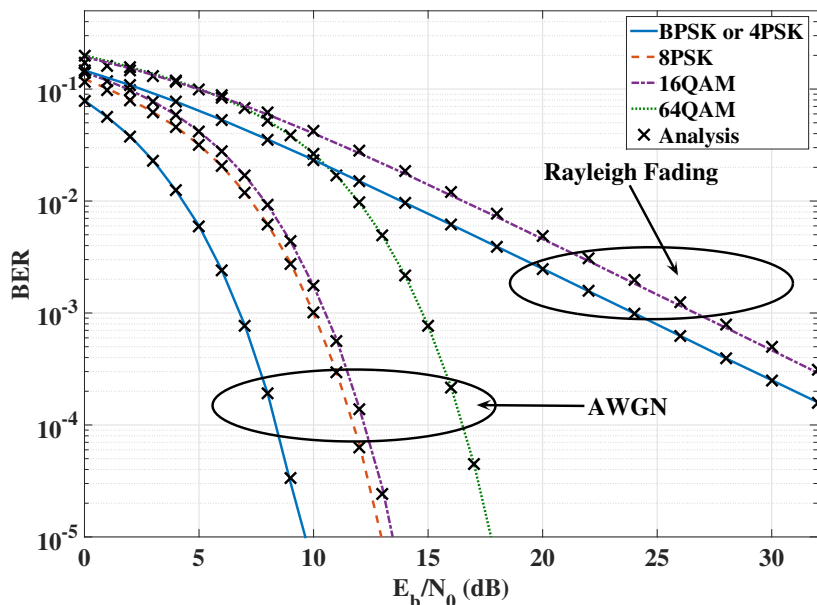
Figure 2.7: *BER Performance of the Basic OFDM System for the AWGN and Rayleigh Multi-path Fading Channels,* $N = 1024, L_{\mathrm{H}} = 20, L_{\mathrm{CP}} = 256.$

Assume that, the number of the transmitted sub-carriers is $N = 1024$, and the modulation schemes used for this transmission are including 4PSK, 8PSK, 16QAM and 64QAM. The corresponding spectral efficiency is $\eta = 2, 3, 4$ or 6 bits/sec/Hz. The BER performance of the standard OFDM system over the AWGN and Rayleigh multipath fading channels is shown in Figure 2.7. The analytical values are computed using the equations as we mentioned above, which are closely match with the simulations. According to the IEEE 802 wireless system's protocols [46], it is normally required that the minimum receiver input power measured at the antenna port at which the BER is calculated does not exceed the specific value of $\mathrm{BER} < 10^{-3}$. This means there is only one bit error over the received 1000 bit messages. In terms of the AWGN channel results as showing in Figure 2.7, with increasing the order of modulation schemes, the spectral efficiency increases with the cost of increasing E_{b}/N_0. To achieve a BER of 10^{-3}, 4PSK needs about $E_{\mathrm{b}}/N_0 = 6.7$ dB, 8PSK needs about 10 dB, 16QAM needs about 10.5 dB, and the 64QAM scheme costs about 14.8 dB. Compared with 16QAM, 8PSK only saves about 0.5 dB E_{b}/N_0 at the cost of losing 1 bits/sec/Hz spectral efficiency. Therefore, in the LTE systems, only 4PSK, 16QAM and 64QAM have been considered for the data transmissions.

Compared with the AWGN channel, there is a significant BER degradation for the Rayleigh multipath fading channel. We assume the channel information or the channel impulse response $(h(t))$ is known and that zero forcing equalisation as in equation (2.10) is used. 4PSK costs about $E_b/N_0 = 23.95$ dB for achieving the BER of 10^{-3}, which is about 17.25 dB higher than the AWGN channel. In terms of the 16QAM, which needs to cost about 16 dB higher than the AWGN channel.

2.2.3.2 FFT Computational Complexity

A FFT algorithm computes the discrete Fourier transform (DFT) of a sequence, or its inverse. In general, for the radix-2 FFT algorithm, the number of complex multiplications is $\frac{N}{2}\log_2(N)$ and the number of complex additions is $N\log_2(N)$ [47]. In a N-point FFT butterfly diagram [47], the total number of the FFT stages is $\log_2(N)$ and as well as $N/2$ complex multiplications and N complex additions for each stage. In the wireless communication systems, normally use the number of complex multiplications to present the computational complexity, which can be expressed as:

$$\Gamma^{\text{OFDM}} = \frac{N}{2} \cdot \log_2(N).\qquad(2.25)$$

The computational complexity performance with increasing the number of FFT N is shown in Figure 2.8. The complexity is almost a linear function of N. The computational complexity directly relates to power consumption and raises implementation issues in practice [48]. Thus, reducing the number of points in FFT can significantly reduce the computational cost and improve the battery life, which is the one of the main purposes for designing the low cost MTC communication devices.

2.3 Shannon Capacity and Sampling Theorem

2.3.1 Shannon Capacity

The Shannon-Hartley equation relates the maximum capacity (transmission bit rate) that can be achieved over a given channel with SNR and bandwidth. Reference [31] introduces the maximum capacity of the AWGN channel is:

$$C = B_W \log_2\left(1 + \frac{P_{\text{signal}}}{P_{\text{noise}}}\right) \text{ (bit/sec)},\qquad(2.26)$$
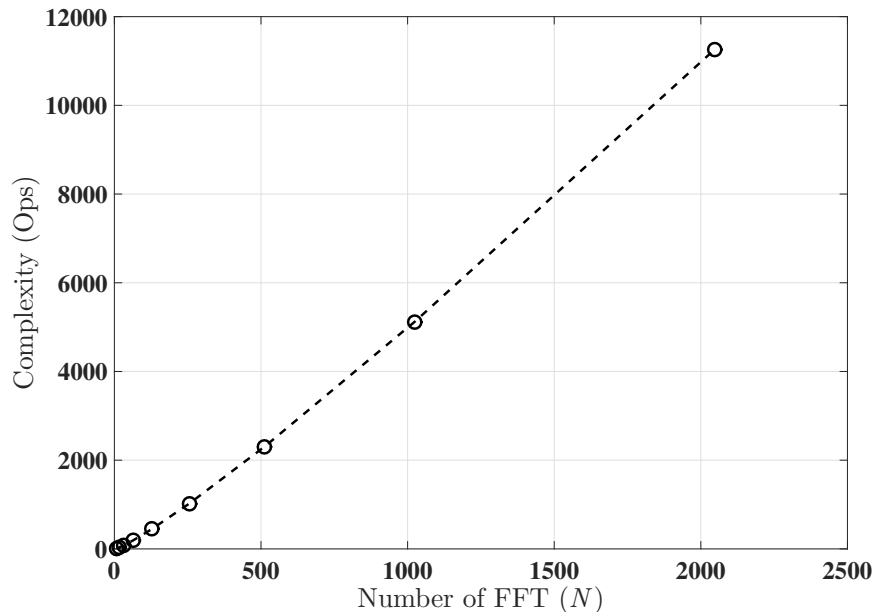
Figure 2.8: *Computational Complexity Performance with N.*

where C is the maximum capacity of a given channel bandwidth B_W (Hz) in bits/sec, and it is also called the Shannon's capacity limit for the given channel. The $\frac{P_{signal}}{P_{noise}}$ is also known as the signal to noise ratio (SNR), P_{signal} is the transmitted signal power in (W) and P_{noise} is the noise power in (W). Therefore, with increasing bandwidth B_W, the SNR can be decreased to compensate [31]. Now we assume the E_b presents the average signal energy per bit (J/bits), and N_0 presents the noise power spectral density. Then the signal power in one symbol P_{signal} can be represented as:

$$P_{signal} = E_b C \ (\text{J/bits} \cdot \text{bits/sec} = \text{J} \cdot \text{sec} = \text{W} \cdot \text{sec/sec} = \text{W}), \qquad (2.27)$$

and the noise power can be represented as:

$$P_{noise} = N_0 B_W \ (\text{W/Hz} \cdot \text{Hz} = \text{W}). \qquad (2.28)$$

Then the SNR can be rewritten as:

$$SNR = \frac{P_{signal}}{P_{noise}} = \frac{E_b}{N_0} \cdot \frac{C}{B_W}. \qquad (2.29)$$

23

According to Reference [42], let the spectral efficiency equals the ratio $\frac{C}{B_W}$, which is the bandwidth efficiency of the system $\eta = \frac{C}{B_W}$. Then, the Shannon capacity can be rewritten in the equivalent from as:

$$\frac{C}{B_W} = \log_2 \left(1 + \frac{E_b}{N_0} \cdot \frac{C}{B_W} \right) \tag{2.30}$$

$$\eta = \log_2 \left(1 + \frac{E_b}{N_0} \cdot \eta \right). \text{ (bit/sec/Hz)}.$$

The equivalent Equation (2.30) can be rewritten as:

$$\frac{E_b}{N_0} = \frac{2^\eta - 1}{\eta}. \tag{2.31}$$

The performance of the Shannon limit is shown in Figure 2.9. As the spectral efficiency $\eta \to 0$, we can compute the minimum value of the bit to noise ratio E_b/N_0 as:

$$\frac{E_b}{N_0}\bigg|_{B_W \to \infty} = \lim_{\eta \to 0} \frac{2^\eta - 1}{\eta} = \lim_{\eta \to 0} \frac{(2^\eta - 1)'}{\eta'} \tag{2.32}$$

$$= \lim_{\eta \to 0} \frac{2^\eta \ln(2) - 0}{1}$$

$$= \ln(2) = 0.6931 = -1.5917 \text{ (dB)}$$

This means that for any digital communication systems, the bit to noise ratio should higher than $E_b/N_0 > 0.6931$ or equivalently to -1.5917 dB.

2.3.2 Sampling Theorem

Reference [31] introduces the Shannon sampling theorem, which requires that the minimum sampling rate is specified as the twice of the bandwidth of the analogue signal $f_s > 2B_W$, which is also called the Nyquist sampling rate. In order to understand the sampling theorem, Reference [42] introduces the sampling processing which is to multiply the analogue time domain signal $x_{an}(t)$ and the switch signal $\delta_{Ts}(t)$, which is an impulse train of period T_s to cause the electronic switch to close and open instantaneously. Time domain multiplication can be expressed as:

$$x_s(t) = x_{an}(t)\delta_{Ts}(t) \tag{2.33}$$
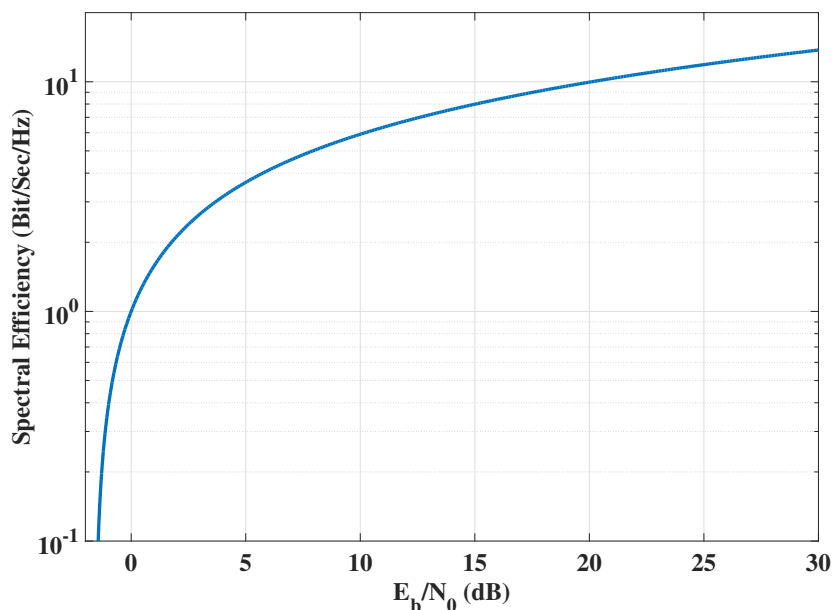
Figure 2.9: *Spectral Efficiency η Performance with Bit to Noise Ratio $E_{\rm b}/N_0$.*

Thus, the Fourier transform of the sampled signal can be computed as the convolution operation in the frequency domain. A example of the Fourier transform of the sampled signal in the frequency domain is shown in Figure 2.10(a). For this example, we assume the Fourier transform of the analogue signal is triangular in shape as shown in Figure 2.10(b). The Fourier transform of the analogue signal $X_{\rm an}$ is convolved with the impulse at the $1/T_{\rm s} = f_{\rm s}$, then with the impulses at the sampling frequency, i.e. at $2f_{\rm s}, 3f_{\rm s}$ to produce the complementary components [49], as shown in Figure 2.10 (c). The sampling processing is repeated for all impulses from the positive to negative frequencies to produce all the complementary components [49]. From Figure 2.10, as long as the sampling frequency is $f_{\rm s} > 2B_{\rm W}$, there is no overlap between the original component and the complementary components. The original component can be recovered without any distortion by designing a low-pass filter with a ideal cut-off frequency of $f_{\rm cf} = B_{\rm W}$, which preserves the baseband signal and blocks all other side-band components.
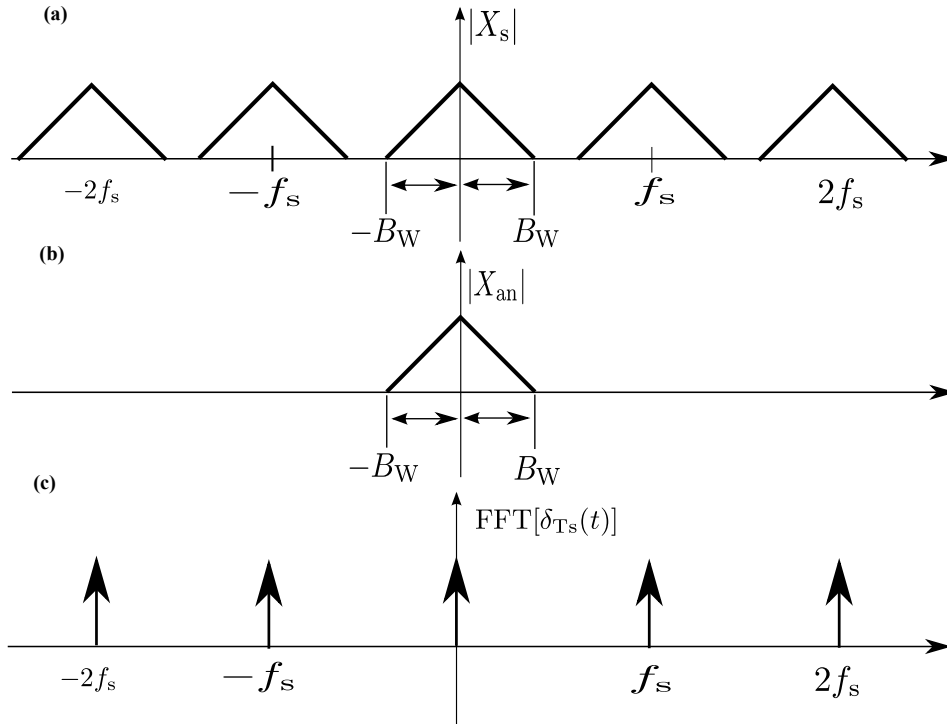
Figure 2.10: *Sampling of Analogue Signals: (a) Sampled Signal in the Frequency Domain, (b) Analogue Signal in the Frequency Domain, (c) Impulse Train in the Frequency Domain.*

2.3.3 Aliasing Effects in Down-sampling

We now study the aliasing effects when reducing the sampling rate (or down-sampling processing). Now, we define the sampling reduction ratio γ is:

$$\gamma = \frac{f_s}{f_{ds}}, \tag{2.34}$$

where f_s is the initial sampling rate and f_{ds} is the down-sampled frequency. As in [49], the aliasing effects of $\gamma = 2$ and $\gamma = 4$ are shown in Figure 2.11. The sampled signal is the same as we assumed as above with the triangular shape, which is shown in Figure 2.11(a). If we set the sampling reduction ratio $\gamma = 2$, then the reduced sampling rate can be expressed as $f_{ds} = 1/2 \, f_s$. The aliasing terms, which is presented as the dashed curves, are overlapped with the original signal. Reducing the sampling rate by two thus moves the aliased frequency domain side-bands to half the frequency of their previous position [49].

An example of down-sampled by 4 is shown in Figure 2.11 (c): there are 3 alias terms which

26
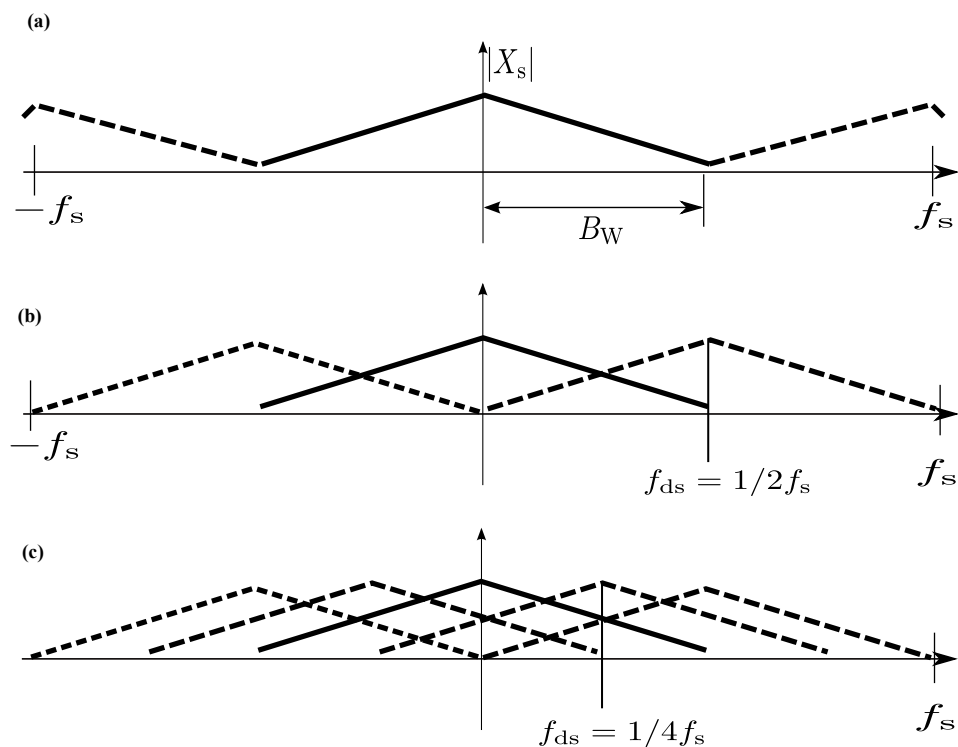
Figure 2.11: *Sampling of Analogue Signals: (a) Original Signal in the Frequency Domain, (b) Down-sampled by 2 in the Frequency Domain, (c) Down-sampled by 4 in the Frequency Domain.*

are located at the frequencies $1/4f_s, 2/4f_s, 3/4f_s$, and overlapped with the original signal. Therefore, in general, if we set the sampling reduction ratio as γ, there are γ copies of the original signal centred at frequencies $0, f_s/\gamma, 2f_s/\gamma, ..., (\gamma - 1)f_s/\gamma$.

Reference [49] mentioned there is a requirement to apply filtering to remove the unwanted signal components. Therefore, the same as the baseband signal, we can remove or reduce the aliasing effects through filter designs. Reducing the aliasing effects by applying filters is shown in Figure 2.12. For example, if we want reduce the sampling rate by $\gamma = 2$, then we can set the cut-off frequency is $f_{cf} = \frac{B_W}{2}$, which will reduce the bandwidth of the original signal. After sampling at the frequency $f_{ds} = 1/2f_s$, the aliased components then fill in the parts of the spectrum, which were previously suppressed by the filter.
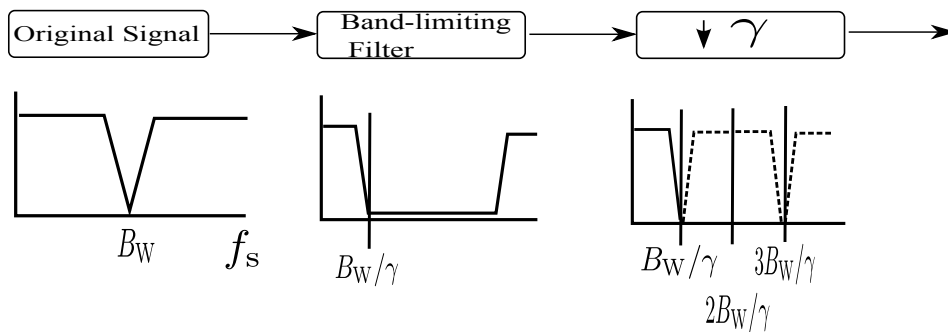
Figure 2.12: *Reducing Sampling Rate by Applying Band-limiting Filters.*

2.4 Filter Design

As mentioned above, filtering is usually formulated as a type of process that covers and selects certain components out of the maximum bandwidth. Moreover, in our VC receiver systems, we design filters to reduce the bandwidth then reduce the sampling rate to reduce the costs. In the 5G uplink massive MTC scenario, filters can also be used to reduce the OFDM side-lobe levels in terms of relaxing the synchronisation requirements. Thus, this section briefly introduces two types of filters, digital and analogue filters.

2.4.1 Finite Impulse Response

The finite impulse response (FIR) filters described here are non-recursive, making them unconditionally stable and achieving a linear phase characteristic. Compared with the infinite impulse response (IIR) filters, in terms of a similar passband magnitude specification, FIR filters will have longer impulse responses and therefore require a higher complexity to implement [49].

For a FIR filter, we define there are L_F non-zero values of the impulse response, so the filter output can be expressed as:

$$y_\mathrm{F}(t) = \sum_{l_\mathrm{F}=0}^{L_\mathrm{F}-1} b_{l_\mathrm{F}} \, x(t - l_\mathrm{F}), \tag{2.35}$$

where $x(t)$ is the input signal, and $y_\mathrm{F}(t)$ is the output. Now, we take the z-transform of equation

(2.35):

$$Y_{\mathrm{F}}(z) = \sum_{l_{\mathrm{F}}=0}^{L_{\mathrm{F}}-1} b_{l_{\mathrm{F}}} \, X(z) \, z^{-l_{\mathrm{F}}} \tag{2.36}$$

$$= X(z) \sum_{l_{\mathrm{F}}=0}^{L_{\mathrm{F}}-1} b_{l_{\mathrm{F}}} \, z^{-l_{\mathrm{F}}},$$

where the z-transform of the impulse response is:

$$B_{\mathrm{F}}(z) = \sum_{l_{\mathrm{F}}=0}^{L_{\mathrm{F}}-1} b_{l_{\mathrm{F}}} \, z^{-l_{\mathrm{F}}}. \tag{2.37}$$

The equivalent equation (2.36) can be written as:

$$H_{\mathrm{F}} = \frac{Y_{\mathrm{F}}(z)}{X(z)} = \sum_{l_{\mathrm{F}}=0}^{L_{\mathrm{F}}-1} b_{l_{\mathrm{F}}} \, z^{-l_{\mathrm{F}}}. \tag{2.38}$$

Therefore, the pole-zero configuration in the z-plane is then described as:

$$\begin{aligned} H_{\mathrm{F}} &= \frac{b_0 \, z^0 + b_1 \, z^{-1} + \cdots + b_{L_{\mathrm{F}}-1} \, z^{-(L_{\mathrm{F}}-1)}}{1} \\ &= \frac{b_0 \, z^{L_{\mathrm{F}}-1} + b_1 \, z^{L_{\mathrm{F}}-2} + \cdots + b_{L_{\mathrm{F}}-1} \, z^0}{z^{L_{\mathrm{F}}-1}}. \end{aligned} \tag{2.39}$$

Thus, for a general FIR filter with order L_{F}, there are $L_{\mathrm{F}} - 1$ zeros and $L_{\mathrm{F}} - 1$ poles, which are at the origin in the z-plane and are beyond the unit circle respectively. A physical structure of the FIR filter is shown in Figure 2.13. The value $x(t - l_{\mathrm{F}})$ in these terms are commonly referred to as the filter taps, this represent the convolution of the time domain input signal $x(t)$ with the filter impulse response $b(t)$.

In signal processing, to achieve an ideal filter, the impulse response should be as long as possible. In practice, we truncate an infinite time-domain impulse response to a finite set of values [49]. Truncating the impulse response introduces undesirable ripples and overshoots in the frequency response. This effect is known as the Gibbs phenomenon. Time domain truncation is achieved by multiplying a rectangular window function $w(t)$ [50]. In the frequency domain, conversely, this truncation is achieved by the convolution operation.
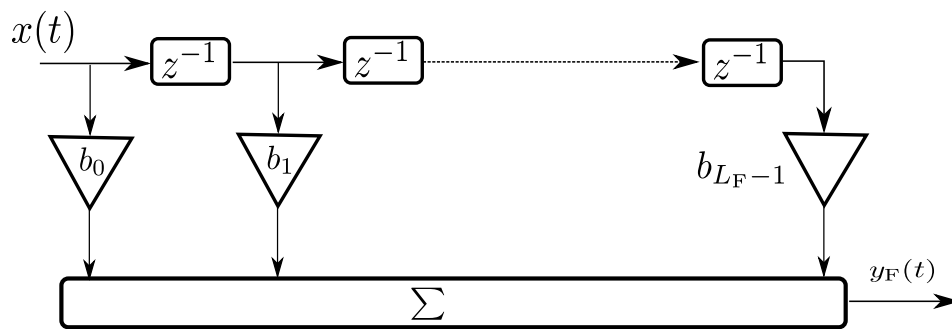
Figure 2.13: *Finite Impulse Response Filter Structure.*

2.4.2   Basic Methods of FIR Filter Design

This subsection introduces two basic methods of FIR filter design including the frequency-sampling method and the windowing method. According to [50], an ideal FIR filter frequency response and the infinite impulse response can be expressed using the Fourier Series as:

$$B_{\mathrm{d}}(e^{j\omega}) = \sum_{n=-\infty}^{\infty} b_{\mathrm{d}}(n)e^{-jn\omega}, \tag{2.40}$$

$$b_{\mathrm{d}}(n) = \frac{1}{2\pi} \int_{-\pi}^{\pi} B_{\mathrm{d}}(e^{j\omega})(e^{jn\omega})d\omega. \tag{2.41}$$

Thus, the coefficients of an ideal FIR filter can be found from the Fourier Series coefficients of the desired frequency response. However, it is not possible to implement the corresponding low-pass filter design from two reasons: first, the number of coefficients is infinite. Second, the impulse response is a non-causal system, i.e. $b_{\mathrm{d}}(n)$ exists between $n = -\pi$ and $n = 0$. In terms of the frequency-sampling method [50], the truncated impulse response $b(n)$ can be obtained directly from the DFT of the desired frequency response as:

$$B(k) = B_{\mathrm{d}}(e^{j\omega})|_{\omega=\frac{2\pi}{L_{\mathrm{F}}}k} = \sum_{n=0}^{L_{\mathrm{F}}-1} b(n)e^{-j\frac{2\pi}{L_{\mathrm{F}}}nk}, k \in [0, L_{\mathrm{F}}-1], \tag{2.42}$$

$$b(n) = \frac{1}{L_{\mathrm{F}}} \sum_{k=0}^{L_{\mathrm{F}}-1} B(k)e^{j\frac{2\pi}{L_{\mathrm{F}}}nk}, n \in [0, L_{\mathrm{F}}-1], \tag{2.43}$$

where the FIR filter order is equal to $(L_F - 1)$. Now, we assume the number of filter taps is 33 and the cut-off frequency is $(\pi/2)$, $B(e^{j\omega})$ is then specified over one period by the equation:

$$\left| B(e^{j\omega}) \right| = \begin{cases} 1, & |\omega| < \pi/2, \\ 0, & \text{otherwise.} \end{cases} \tag{2.44}$$

In this case, the ideal FIR filter impulse response (from the Fourier Series) can be computed as:

$$b_d(n) = \frac{1}{2\pi} \int_{-\pi/2}^{\pi/2} (e^{jn\omega}) d\omega = \frac{1}{2} \cdot \frac{\sin(n\pi/2)}{n\pi/2}, n \in (-\infty, +\infty), \tag{2.45}$$

the truncated filter impulse response (from the IDFT) can be computed as:

$$b(n) = \frac{1}{33} \sum_{k=0}^{32} B(k) e^{j\frac{2\pi}{L_F} nk}, \ n \in [0, 32]. \tag{2.46}$$

Now, we consider a more complex filter parameter setting, i.e. in the passband the magnitude of the frequency response must approximate unity within an error of $\pm\delta_{PB}$, where δ_{PB} is the passband ripple. Thus, the filter coefficients can be approximated as:

$$(1 - \delta_{PB}) \leq \left| B(e^{j\omega}) \right| \leq (1 + \delta_{PB}), \ |\omega| \leq \omega_{PB}, \tag{2.47}$$

where ω_{PB} is the cut-off frequency of the passband. In terms of the stopband, the magnitude response must approximate zero with an error less than δ_{SB}, i.e.

$$\left| B(e^{j\omega}) \right| \leq \delta_{SB}, \ \omega_{PB} \leq |\omega| \leq \omega_{SB}, \tag{2.48}$$

where ω_{SB} is the cut-off frequency of the stopband. Furthermore, the passband ripple in dB A_{PB} and the stopband attenuation in dB A_S can be computed as:

$$A_{PB} = 20 \log_{10}(1 + \delta_{PB}), \tag{2.49}$$

$$A_S = 20 \log_{10}(\delta_{SB}). \tag{2.50}$$

According to [50], because b_d will generally be infinite in length, it is necessary to generate an FIR approximate to $B_d(e^{j\omega})$. In terms of the window design method, the filter is designed by

Window Type	Weight Equation
Rectangular	$w(n) = 1$
Hamming	$w(n) = 0.54 - 0.46\cos(\frac{2\pi n}{L_{\mathrm{F}}-1})$
Hanning	$w(n) = 0.5 - 0.5\cos(\frac{2\pi n}{L_{\mathrm{F}}-1})$
Blackman	$w(n) = 0.42 - 0.5\cos(\frac{2\pi n}{L_{\mathrm{F}}-1}) + 0.08\cos(\frac{4\pi n}{L_{\mathrm{F}}-1})$

Table 2.1: *COMMON WINDOWS.*

windowing the unit sample response as:

$$b(n) = b_{\mathrm{d}}(n) \cdot w(n),\ 0 \le n \le L_{\mathrm{F}} - 1, \qquad (2.51)$$

where $w(n)$ is a finite-length window, which is equal to zero outside the interval $(0, L_{\mathrm{F}} - 1)$. Several common windows are listed in Table 2.1 [49] and [50].

2.4.3 Generate Filters Using Matlab Toolbox

In this thesis, we use the Matlab function "**sptool**", which is a signal processing toolbox using the graphical user interface to design filters with different windows or edit filters with the filter designer (includes a Pole/Zero editor). To open the toolbox, type the "**sptool**" in the Matlab command widow then press the "**New**" button under the Signals of "**mtlb[vector]**", Filters of "**FIRbp[design]**" and Spectra of "**mtlbse[auto]**" to create a new filter. A visualisation filter design toolbox is shown in Figure 2.14, which allows to design and edit filters of various lengths and types, with standard (i.e. low-pass, band-pass, high-pass or bandstop) configurations. Select different filter orders, frequency and magnitude specifications can specific the filter's length, cut-off frequency and magnitude in order to support different systems. We can view the characteristics a designed filter with its magnitude response, phase response, group delay, pole-zero plot, impulse response and step response. To activate the Filter Viewer, select the plot type from the Analysis menu or from the toolbar as shown in Figure 2.14. Finally, to export the coefficients of the designed filter, press the "**Export**" button under the File menu.

The frequency response performance of filters with the Hamming, Blackman, Rectangular and Gaussian windows are shown in Figure 2.15. The rectangular window presents the worst performance in both the passband ripple A_{PB} and the stop attenuation A_{S}, which is about -25 dB. The maximum sidelobe level of the Hamming window is about 53 dB, which is about 11 dB
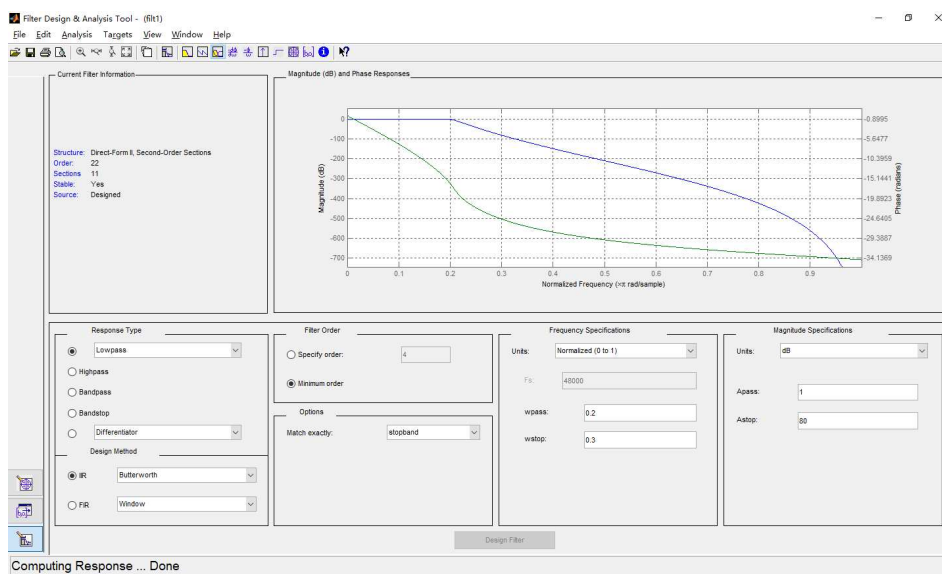
Figure 2.14: *"sptool"* *with Matlab for Filter Designs.*

lower than the Gaussian window and 22 dB lower than the Blackman window. In terms of the ripped frequency roll-off performance, the rectangular window and the Hamming window are better than the Gaussian and Blackman windows.

2.4.4   Infinite Impulse Response

Infinite impulse response (IIR) filters are known as feedback recursive systems, which can generate infinitely long impulse responses to a finite input [49]. In practice the impulse response of the IIR filter usually approaches to zero and can be neglected past a certain point. In analogue systems, IIR filters are generally designed and composed with resistors, capacitors, and inductors. In the digital signal processing systems, the discrete time delay filters based on a tapped delay line and without the feedback are the digital FIR filters.

To illustrate the various sources of error arising from the discretisation process in the implementation of a digital filter, consider for simplicity, a first-order digital filter is shown in Figure 2.16. The filter output can be expressed as:

$$y_F[n] = by_F[n-1] + x[n], \tag{2.52}$$

where $y_F[n]$ and $x[n]$ are the output and input variables. The corresponding transfer function is
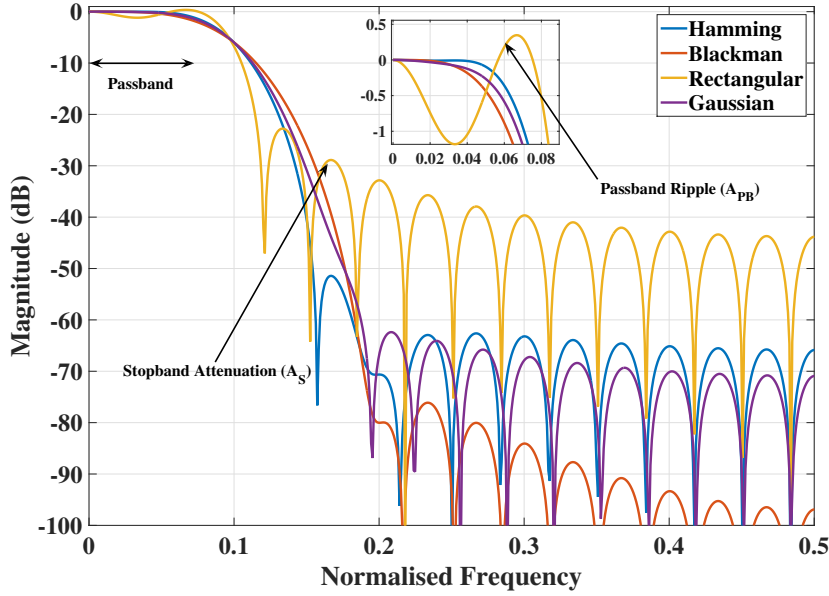
Figure 2.15: *FIR Filter Frequency Response,* $L_{\mathrm{F}} = 31$, $f_{\mathrm{cf}} = 0.18$.
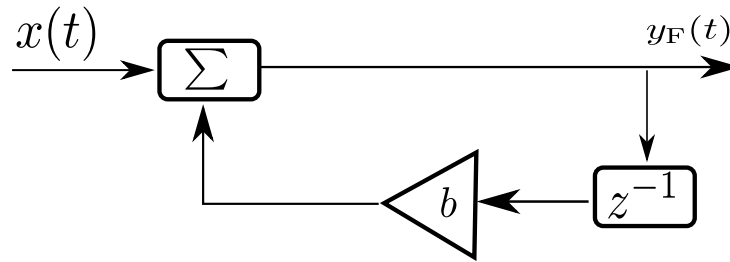
Figure 2.16: *A First-order Infinite Impulse Response Filter Structure.*

given by [49]:

$$H_{\mathrm{F}}(z) = \frac{1}{1 - bz^{-1}}. \tag{2.53}$$

In comparison with FIR filters, which provide a comparable quality of signal processing and design flexibility, IIR filters require lower filter orders in terms of the computational complexity [50]. In principle, a fundamental disadvantage of IIR filters is that they usually have non-linear phase responses. However, we can reduce the non-linear phase effects through a suitable selection of the passband. There are several common types of analogue filters, such as the Butterworth [49], which has a maximally flat passband in filters with the same order. Chebyshev filters have a ripped frequency roll-off performance and are equiripple (more ripples) in the
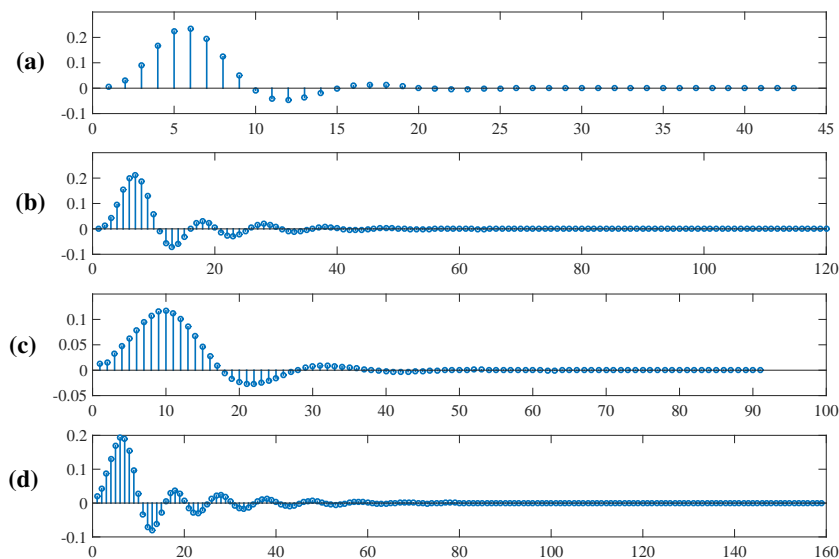
Figure 2.17: *IIR Time Domain Impulse Response, (a) Butterworth, (b) Chebyshev I (c) Chebyshev II (d) Elliptic.*

passband (for Chebyshev type I) or equiripple in the stop attenuation (for Chebyshev type II). Elliptic filters are equiripple in both the passband and the stop attenuation [50].

In terms of the analogue filter design, the usual technique is to specify a prototype low-pass filter, which can produce an equivalent high-pass, band-pass, or band-stop filter. The analogue IIR filter is then converted into the approximated digital filter using a relevant transformation method. In terms of the IIR filter designs, several basic methods can be found in Reference [51]. In terms of simplifying, we use the Matlab function "**sptool**" to design IIR filters in the thesis. The approximated impulse response for IIR filter is shown in Figure 2.17. Here we set the normalised cut-off frequency for all filters is $f_{\text{cf}} = 0.2$, the filter order is 4, the passband ripple for the Chebyshev I and Elliptic filters is $A_{PB} = 1$ dB. The stop attenuation for the Chebyshev II and Elliptic filters $= 40$ dB. It is clearly showing that the approximated impulse response approaches to zero. The Butterworth filter has the shortest impulse response length for the same filter order. The frequency response is shown in Figure 2.18. Compared with the Butterworth and Chebyshev I filters, both the Chebyshev II and Elliptic filters provide faster frequency roll-off but with a higher side-lobe attenuation 40 dB. The Butterworth filter provides a flat magnitude in the passband. Thus, understanding the different characteristics

35
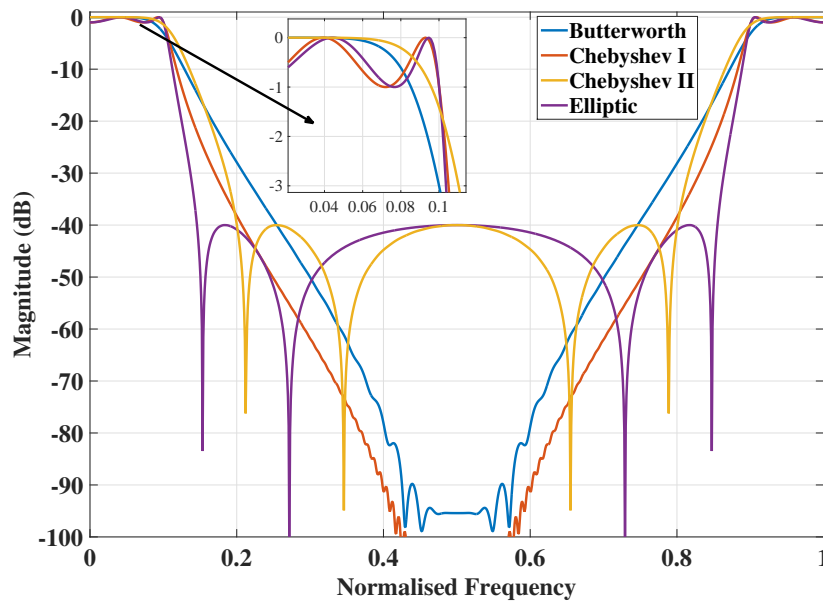
Figure 2.18: *IIR Filter Frequency Response.*

can help to design IIR filters with different system requirements on the passband ripple, stop attenuation and the frequency roll-off performance.

2.5 Side-lobe Behaviour for the Multi-user MTC Systems

As mentioned in Section 2.1.3, with significant growth in the number of MTC devices, one key challenge is how to relax the synchronisation requirements in terms of the massive low data rate devices in the future communication systems (i.e. 5G). As mentioned above, the orthogonal sinc-shaped sub-carriers technique provides high spectrum efficiency and also high side-lobe levels, which comprises sinc pulses as shown in Figure 2.19. If we transmit 13 sub-carriers, the highest side-lobe attenuation is about -10 dB, which causes significant interference to the adjacent sub-carriers if the received signal is not synchronised perfectly in time or frequency. Moreover, there is a "flat" frequency roll-off at the band-edge and it is about -20 dB attenuation to the adjacent users, i.e. the 1th user and the 3th user. The OFDM system is thus significantly sensitive to timing and frequency errors.

There are several methods to reduce the side-lobe levels in terms of relaxing the needs of time and frequency synchronisation. We can inset number of zero sub-carriers as a frequency guard
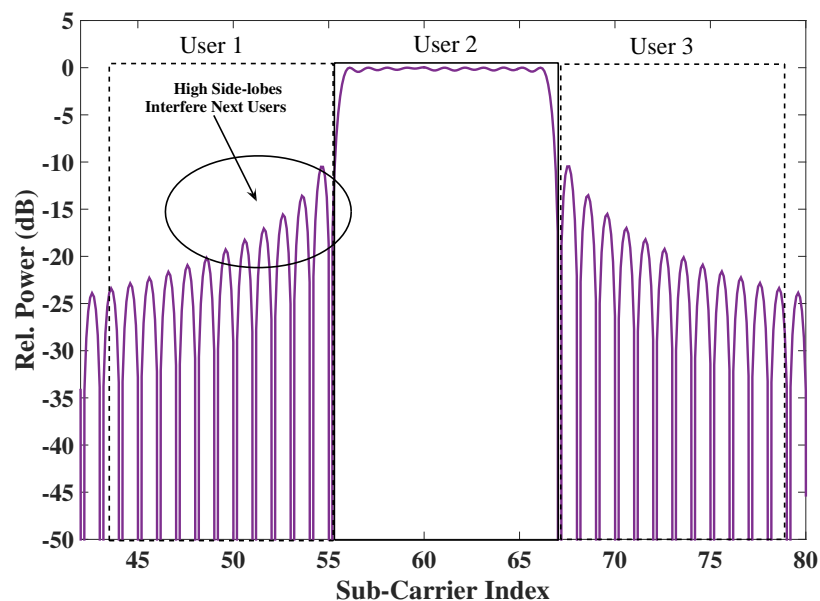
Figure 2.19: *Standard OFDM System Side-lobe levels, 13 sub-carriers.*

interval [52] technique between each adjacent users. However, increasing the number of zero sub-carriers will reduce the spectrum efficiency significantly. Moreover, we can also design filters, i.e. using the narrowband filter bank techniques [53] or use frequency coding techniques, i.e. frequency polynomial cancellation coding (PCC) [54] to reduce the out of band radiations. This thesis will provide a detailed comparison and analysis in Chapters 4 and 5.

2.6   Conclusion

First, this chapter introduced the basic background of the MTC, and highlighted the key issues: the operation costs should be limited in terms of the battery life, modifying the existing radio access technologies (e.g. the OFDM used in the LTE) in order to be more efficient. In terms of the MTC uplink scenario, the tight synchronisation techniques used in the current wireless communication systems, e.g. the LTE, would be removed for supporting the MTC devices with the dynamic changes in distance. Second, this chapter provided a brief overview of the standard OFDM systems, includes the orthogonal sub-carrier systems, spectral efficiency, PAPR problems and the OFDMA systems, which are used in the LTE downlink channel. The state of the art for basic OFDM system data transmissions has been provided in detail. This chapter also

analysed the basic BER and FFT computational complexity performance using mathematical equations. Third, in terms of reducing the maximum LTE downlink bandwidth and the receiver sampling rate for reducing the ADC costs, this chapter provided a basic view of the Shannon theorem and introduced the aliasing effects, which is caused by the sampling reduction operations. Fourth, a brief review of the filter designs was given. FIR filters with the advantages of the non-recursive, stable and the linear phase with the cost of high complexity are widely used in digital signal processing. In order to reduce the computational complexity in low cost receivers, this chapter provided a basic IIR filter designs, which will be mainly used in the thesis. Finally, a brief review of OFDM side-lobe behaviour was provided, which can cause significant interference to the adjacent sub-carriers when there is imperfect time or frequency synchronisation.

This thesis will provide a novel virtual carrier system, which is designed to reduce the LTE bandwidth for the MTC downlink channel, and mathematically analyse its performance in Chapter 3. In terms of the MTC uplink asynchronous scenario, the OFDM side-lobe levels should be limited. Several candidate waveforms, including the performance evaluations will be presented in Chapter 4. In Chapter 5, we will provide a closed-form expression for the interference caused by the time-offset scenario. Chapter 5 will also propose the OA-UFMC systems in terms of reducing the computational complexity for the FIR filters, which is used in the UFMC systems.

Chapter 3

Virtual Carrier System for the MTC Downlink Based on OFDMA

In this chapter, we propose a novel receiver system, the virtual carrier (VC) system, which aims to improve the orthogonal frequency-division multiple access (OFDMA) downlink bandwidth efficiency and cost-efficiency, using analogue filters to extract only sub-carriers of interest. MTC emerged as a cutting edge technology for next-generation communications, and are undergoing rapid development and inspiring numerous applications, such as smart city, smart sensor and smart house. Modifying existing OFDMA communication systems, such as the LTE system, to successfully support low data rate MTC devices has become an important issue. In LTE Release 12 and beyond, the reduction of maximum bandwidth, the reduction of transmission power and the reduction of downlink transmission model should be studied for supporting low data rate MTC. Our VC system will reduce the sampling rate at the MTC ADC leading to improvements in ADC power consumption and the computational complexity. The results indicate that the VC system can provide significant high SINR performance without significant BER degradation.

The rest of this chapter is organised as follows: Section 3.1 introduces the background and motivation of this chapter. Section 3.2 introduces the state of the art. We discuss the VC receiver system model and derive the performance analysis in Sections 3.3 and 3.4, respectively. The LTE bandwidth efficiency and analytical results comparing with different SINR and BER performance are shown in Section 3.5 and Section 3.6 concludes the chapter.

3.1 Introduction

As mentioned in Chapter 2, with the growth of automated systems such as e-health, the smart grid, smart homes and smart cites, MTC services will experience an exponential growth in the next generation of mobile communication systems [55]. MTC is one of the most promising solutions for revolutionising future intelligent wireless applications [17]. The major idea of MTC

39

system is allowing MTC terminal devices or components to be interconnected, networked, and controlled remotely [56], with the advantages of low-cost, scalable and reliable technologies. Projections for the growth in MTC devices range up to 50 billion in the next decades, and with the expectation of over 2 billion devices will be directly attached to the cellular network by this time [4].

Wireless communication technologies have been rapidly developing in recent years. The current 4G-LTE networks [14], provide high spectrum efficiency by combining advanced multi-antenna techniques and they implement the OFDMA scheme in the downlink (DL) from the base station to the mobile terminals. However, this scheme cannot meet the aim of making MTC devices lower cost and more energy and bandwidth efficient. For instance, in terms of supporting synchronisation, LTE uses a subset of carriers to transmit downlink control information in the physical downlink control channel (PDCCH) [57]. With increasing the number of PDCCH, the sub-carrier efficiency will decrease.

Unlike H2H communications, which normally involves voice/video calls, messages and web surfing, the objective of MTC is to improve the performance of system automation in which the terminal devices and systems can exchange and share data [58]. Therefore, low data rates, low cost, low energy consumption and minimal human intervention are key features for realising efficient MTC.

Currently, many MTC applications are implemented by using the general packet radio service (GPRS) infrastructure and specific services such as the low cost short message services [59]. However, GPRS also has several limitations which will not satisfy the future MTC requirements of network operators, particularly relating to energy efficiency and scalability. For instance, in order to achieve an advanced intelligent system, the number of access technologies in the network will be increased when using the legacy GPRS system, which will not meet the aim of future network efficiency. Assuming only GPRS traffic, the spectral efficiency of a GPRS cell is not more than 150 kb/s/cell/MHz [60], which is significantly lower than for 4G LTE systems (4.08 Mb/s/cell/MHz).

OFDMA, also referred to as multiuser-OFDM, is being implemented as the multiple access method for the high data rate transmissions in LTE. OFDMA is an extension of OFDM [61], allowing different users to transmit simultaneously on the different sub-carriers per OFDM symbol. In an OFDMA system, the available spectrum is divided into orthogonal sub-carriers,

which are grouped into sub-channels. OFDMA works as a multi-access technique by allocating users to different groups of orthogonal sub-channels. Due to the different users' demands, OFDMA can separate its bandwidth into distinct sub-channels [62].

How to reduce the cost of LTE in order to support many MTC low cost devices which maximising the battery life is a major issue for standardisation beyond Release 12 of LTE. The bandwidth reduction and the operation cost reduction are the two general aspects addressed by [8]. The LTE downlink channel can provide up to 20 MHz bandwidth. However, MTC usually only requires low data rate transmissions, for instance, an MTC terminal device may only be allocated only 1 MHz out of the 20 MHz LTE downlink channel. In this case, most of the sub-carriers are not relevant to the MTC device. We thus focus how reduced sampling rates in MTC receiver devices can improve their energy efficiency without compromising decoding performance.

There are several recent published references on supporting the MTC. Reference [63] quantified the limits of the random access channel (RACH) of LTE in terms of access delay and energy consumption in order to determine if the random access (RA) scheme used by the standard is suitable for the MTC traffic. Moreover, [64] proposed an overlay mechanism that allows MTC traffic to share the RACH resource with H2H traffic without the need for more complex separation schemes. In [65], a narrowband LTE-M system was proposed for the low cost MTC with modifying the existing 1.25 MHz LTE bandwidth into 180 kHz. A hybrid framework for the dynamic spectrum management of the MTC networks was proposed in [66], which trusted non-3GPP access points to perform sub-Nyquist sampling. Reference [67] proposed the use of opportunistic MTC encountering events among users to provide additional location indicators for localisation systems based on the particle filter fusion technique and presented a prototype system using off-the-shelf smart-phones bundled with ZigBee interfaces. Several other papers, which focus on the resource allocation schemes for MTC are [68], [69], [70] and [5].

To the best of our knowledge, there are no previous studies on reducing the LTE bandwidth in order to support low data rate MTC. Reference [71] only proposes a possible solution: insert a MTC low data rate message into the LTE downlink channel and design a VC to contain the message. This VC can be separately scheduled to support low bandwidth MTC devices and the remaining sub-carriers are designed to support high data rate services as normal. However, reference [71] did not describe a detailed system structure nor how to extract the low data rate virtual carrier messages at the receiver.

We now summarise the main contributions of this chapter: Firstly, we propose a novel reduced sample rate VC receiver system. Compared with the current LTE carrier aggregation technique, it significantly improves the bandwidth efficiency. Secondly, the VC system significantly reduces the ADC cost and computational complexity while providing high SINR and BER performance to support low data rate MTC devices. Thirdly, we derive a closed-form expression for SINR which includes the additional interference caused by aliasing effects. Our previous study [72] shows that aliasing effects caused by the filter and the lower sampling rate ADC can reduce the VC system performance. Our SINR analysis includes the effect of the filter cut-off frequency, the receiver ADC sampling rate and the sampling reduction ratio. The BER can also be evaluated in closed from to show the trade-off between system parameter choices and detection performance. Finally, we derive a closed-form expression for the effect of inter symbol interference (ISI) caused by asynchronism. We also consider several cases, including: very dispersive multipath channel effects on ISI and inter carrier interference (ICI) plus the additional interference caused by sample timing errors.

3.2 OFDM System: State of the Art

This section briefly introduces the standard OFDM transceiver model and provides three options to reduce the maximum bandwidth of OFDMA for the low cost MTC devices.

3.2.1 Standard OFDM Transceiver System

As a guard interval, CP eliminates the ISI from the previous symbol in cellular systems such as LTE and WiMAX [61]. We assume the length of CP in samples is defined as L_{CP} , and the message bits are to be transmitted using OFDM modulation with N sub-carriers. We assume $X(n)$ denotes modulation symbol to be transmitted on the nth sub-carrier. The baseband OFDM block at the output of the N-point IFFT can be expressed as:

$$x(t) = \frac{1}{\sqrt{N}} \sum_{n=0}^{N-1} X(n) \cdot e^{j2\pi nt/N}, \ n \in [0, N-1] \tag{3.1}$$

where $X(n)$ is the FFT of x. The signal $x(t)$ is up-converted to radio frequency, transmitted and propagates through the Rayleigh multipath channel as:

$$h(t) = \sum_{l=0}^{L_{\mathrm{H}}-1} h_{tl}\delta(t - lT_{\mathrm{s}}), \tag{3.2}$$

each channel tap h_{tl} follows the Rayleigh distribution, T_{s} is the sample period, and $\delta(t)$ is the Dirac delta function. (For the AWGN channel without multipath, $L_{\mathrm{H}} = 1, h_{tl} = 1$). The received signal over the Rayleigh multipath channel and AWGN channel can be defined as $y(t)$:

$$y(t) = x(t) \otimes h(t) + g(t), \tag{3.3}$$

where $\otimes$ denotes the convolution operation and $g(t)$ represents AWGN with power spectral density $N_0/2$ is assumed. For a standard OFDM receiver, the received signal is match filtered and sampled at frequency f_{s}. After removing the CP and applying the FFT, the frequency domain signal can be expressed as:

$$Y(n) = X(n) \cdot H(n) + G(n), \tag{3.4}$$

where $H(n)$ is the FFT of the vector $[h_{0t}, h_{1t},..., h_{L_{\mathrm{H}}-1}t]$ and G is the FFT of the noise sequence g in the frequency domain. Finally, to decode the transmitted messages, zero forcing (ZF) equalisation [41] can be used to estimate the transmitted data.

3.2.2   Options to Reduce OFDMA Bandwidth

Reference [71] generally lists three possible options to reduce the maximum bandwidth of OFDMA systems such as LTE, including separate carrier (SC), carrier aggregation (CA), and virtual carrier (VC).

First, SC separates a high bandwidth carrier into several narrower band carriers to support low bandwidth MTC devices. For instance, a 20 MHz bandwidth carrier can be split into several 1.4 MHz and 3 MHz carriers. Low bandwidth MTC devices then transmit and receive messages on each separate carrier and all narrow bandwidth MTC devices then share the same OFDMA channel. However, the SC option will no longer support full bandwidth 20 MHz data transmissions and data capacity will be limited by the maximum bandwidth carrier.

Second, the carrier aggregation technique [73] is one of the key features for LTE-Advanced. It allows a user equipment (UE) to receive data on multiple carriers simultaneously. One 20 MHz band can be formed by component carriers of bandwidth 1.4 MHz, 3 MHz, and 15 MHz. The low bandwidths support MTC, and the high bandwidth carriers, such as 15 MHz, can support high data rate transmissions. However, CA does not improve the bandwidth efficiency, as each sub-band still needs several carriers to support synchronisation of the downlink channel.

Third, the transmitter insets a virtual carrier to carry the MTC messages into a 20 MHz downlink OFDMA channel to support low cost devices. High data rate devices can still use the remaining carriers.

Section 3.5 will show that compared with SC and CA, by using a virtual carrier mapped into a 20 MHz band the transmitter obtains the highest bandwidth efficiency at the meanwhile the receiver ADC power cost reduces linearly with reduced sampling rate. In the following sections, this chapter will study the VC receiver system in detail.

3.3   The Virtual Carrier System

This section introduces the proposed VC receiver system then analyses the LTE downlink efficiency and the ADC energy cost performance. We assume that the filter information has been transmitted through the PDCCH channel to each terminal devices.

3.3.1   Sub-sampling Receiver for VC Option

The VC receiver system model is shown in Figure 3.1. We assume that a standard OFDMA receiver received a set of messages over a 20 MHz channel bandwidth, the signal will pass through a 20 MHz analogue circuit filter and then be passed to an ADC with sampling rate of 30.72 MHz as in LTE. Unlike the traditional OFDMA receiver, the major feature of the VC receiver system is integrating both low data rate MTC messages and high data rate wideband messages in one downlink channel. MTC receivers reduce the ADC processing cost by reducing the maximum bandwidth to capture only the MTC sub-carriers of interest and filter out other sub-carriers. Therefore, a VC receiver implements one or more narrow band IIR filters to extract the transmitted MTC signals from the received OFDMA signal. It operates the ADC at a much lower sample rate to reduce the power consumption and the number of subsequent digital
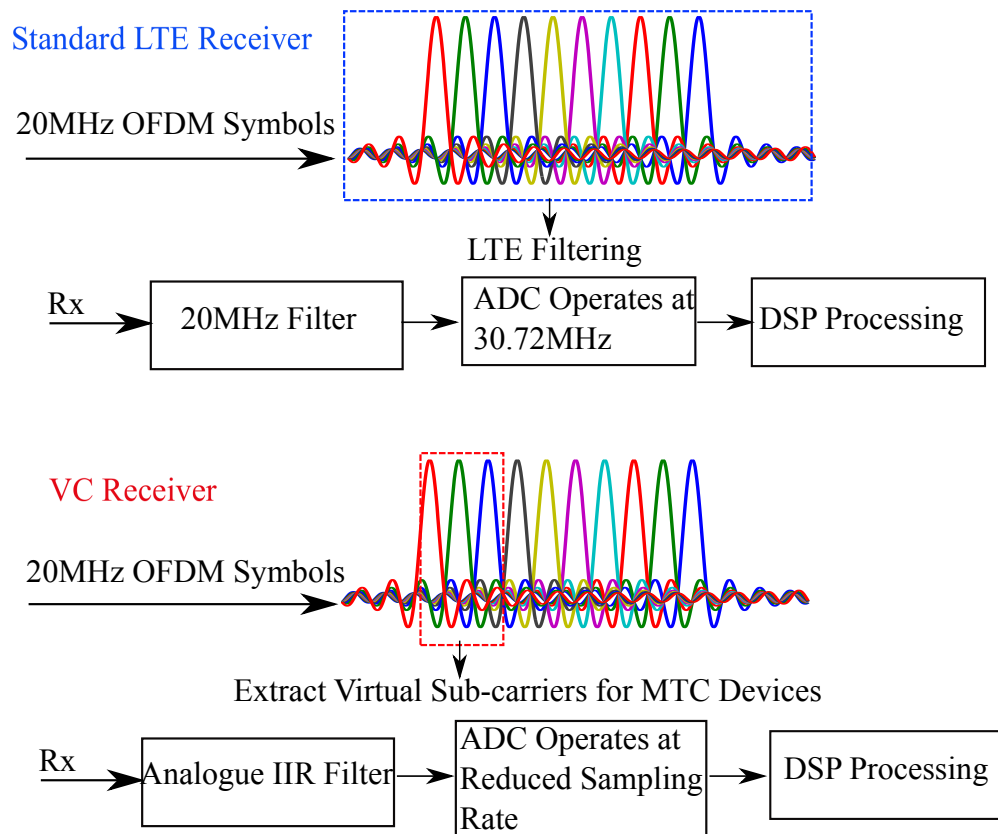
Figure 3.1: *System Model of the Standard LTE Receiver and VC Receiver.*

signal processing computations to decode the signal. The scenario where an MTC receiver has received a 20 MHz bandwidth LTE signal but only a few sub-carriers (e.g. 70 carriers) are used for this terminal device as in Figure 3.1(b). A standard 20 MHz LTE bandwidth maps to a FFT size of 2048 with a sampling rate of 30.72 MHz. Therefore, the useful sub-carrier ratio for the MTC device can be calculated as the number of VC sub-carriers (70) divided by the total number of sub-carriers (2048), which is approximately $1/32$ in this case. Thus, a 0.625 MHz low pass filter (LPF) can be designed to extract the relevant sub-carriers from the 20 MHz bandwidth signal. A correspondingly lower sampling rate ADC is used at the LPF output; in this case, we can choose a 0.96 MHz sampling frequency ADC instead of 30.72 MHz.

3.3.2 Mathematical Model of the VC Receiver

The VC receiver block diagram is shown in Figure 3.2. The major function of the VC receiver system is to demodulate only the sub-carriers of interest. Therefore, the major difference of the VC receiver compared to a standard OFDM receiver is that the received signals are passed

Transmitter

Frequency Domain Input Data
$X(n)$

Time Domain

White Gaussian Noise $g(t)$

| MTC Data | Remaining Data | → | Modulation | → | N - Point IFFT | → | Cyclic Prefix Extension | → ⊕ → ⊗ h |

MTC VC Receiver

| MTC Data | ← | ZF Equalisation and Demodulation | ← | N/γ - Point FFT | ← | Remove Cyclic Prefix | ← | ADC | ← r_{LPF} | IIR LPF | ← |

Sample frequency at f_{s}/γ

Multipath Channel

b
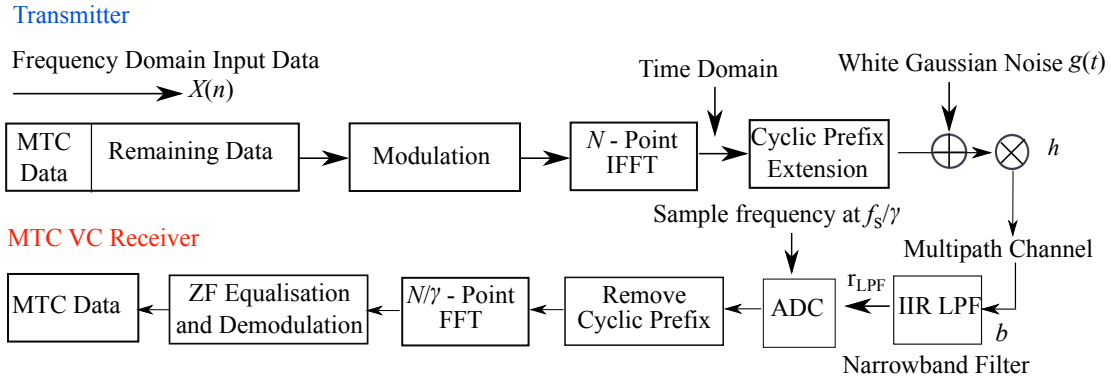
Narrowband Filter

Figure 3.2: *Block Diagram of the VC Receiver System.*

to a narrowband IIR filter which separates the virtual carriers from the rest of the OFDM sub-carriers, then samples those carriers using a much lower sample frequency ADC. In order to determine the SINR performance, the narrowband IIR filter can be approximately expressed as an finite impulse response (FIR) filter with the impulse response written as $b(t)$ with length of L_{F}. Denote the composite effect of the multipath channel and the IIR filter by $w_{\text{cn}}(t)$:

$$w_{\text{cn}}(t) \approx h(t) \otimes b(t) = \sum_{z=0}^{L_{\text{com}}-1} w_{\text{cn}}(z)\delta(t - zT_{\text{s}}), \tag{3.5}$$

where, L_{com} is the length of the combined channel and filter impulse response. In the rest of paper, every combined filter is approximated as being FIR. The received signal after an IIR filter can be designed as r_{LPF}:

$$r_{\text{LPF}}(t) = \big(x(t) \otimes h(t) + g(t)\big) \otimes b(t) = x(t) \otimes w_{\text{cn}}(t) + g'(t) + i_{\text{A}}(t) + q_{\text{qua}}(t). \tag{3.6}$$

The scalar $i_A(t)$ is the aliasing noise (due to the effect of the narrow band filter and the reduced sample rate processing) and $q_{\text{qua}}(t)$ is the quantisation noise. For a realistic system, the effect of uniform quantisation can often be modelled by an additive noise term due to quantisation noise, which is uncorrelated with the input signal and has zero mean and a variance of $q^2/12$, where q is the quantisation step size [74]. In order to simplify the analysis results, this chapter will assume that the aliasing effect dominates over the quantisation noise. Transforming w_{cn} into the frequency domain yields the following expression for the frequency response of sub-carrier n:

$$W_{\text{cn}}(n) = \sum_{t=o}^{L_{\text{com}}-1} w_{\text{cn}}(t) \cdot e^{-j2\pi nt/N}. \tag{3.7}$$

46

In terms of reducing the ADC cost and the number of subsequent digital signal processing computations, the VC receiver system employs a much lower sampling rate f_{vc} rather than the standard sampling rate f_{s}, thus the sampling reduction ratio γ can be defined as:

$$\gamma = \frac{f_{\mathrm{s}}}{f_{\mathrm{vc}}}. \tag{3.8}$$

With the effect of the analogue IIR filter and reduced sampling rate ADC, the number of operating sub-carriers has been reduced to $K = N/\gamma$, which means the VC receiver FFT size is reduced to N/γ. Assuming that L_{CP} is longer than L_{com}, and the signal is sampled with the correct timing, the received MTC signal in the frequency domain after removing CP can be denoted as:

$$R(k) = \beta \cdot X(k) \cdot W_{\mathrm{cn}}(k) + \beta \cdot G(k) + I_{\mathrm{A}}(k) \quad (k = 0, 1, ..., N/\gamma - 1). \tag{3.9}$$

Where I_{A} is the aliasing term and the term β is the scaling mismatch factor between the transmitter and the receiver and reflects the different sample rates and FFT sizes at these two devices. Given that this scaling mismatch factor affects both the signal and the noise equally, then we can neglect it and assume $\beta = 1$ without loss of generality. After zero forcing equalisation, we can decode the MTC signal in the frequency domain $\hat{X}(k)$ as:

$$\hat{X}(k) = \frac{R(k)}{W_{\mathrm{cn}}(k)}. \tag{3.10}$$

3.3.3 LTE Downlink Efficiency

The LTE downlink bandwidth directly relates to the overall transmission efficiency of the system as this determines the proportion of data sub-carriers in a radio frame. In the LTE downlink channel, in terms of providing good signal synchronisation performance, it uses several synchronisation channels such as the primary synchronisation channel (PSCH), the secondary synchronisation channel (SSCH) and the PDCCH channel. However, those synchronisation channels will share lots of sub-carriers. In order to estimate the LTE downlink channel bandwidth efficiency, the percentage capacity of the LTE FDD (frequency division duplex) downlink channel is computed as:

$$C_{\mathrm{BW}} = \frac{N_{\mathrm{A}}}{N_{\mathrm{T}}} \cdot 100\%, \tag{3.11}$$

where we assume that a 10 ms radio frame is divided into 20 equal size slots of 0.5 ms [16]. A subframe consists 2 consecutive slots, therefore one 10 ms radio frame contains 10 subframes. C_{BW} is the capacity of one 10 ms LTE FDD radio frame, N_{A} is the number of available sub-carriers and N_{T} is the number of total occupied sub-carriers in one frame, which can be computed from reference [75]. The standard LTE downlink channel bandwidth is 1.4 MHz, 3 MHz, 5 MHz, 10 MHz, 15 MHz or 20 MHz.

3.3.4 Synchronisation for the VC System
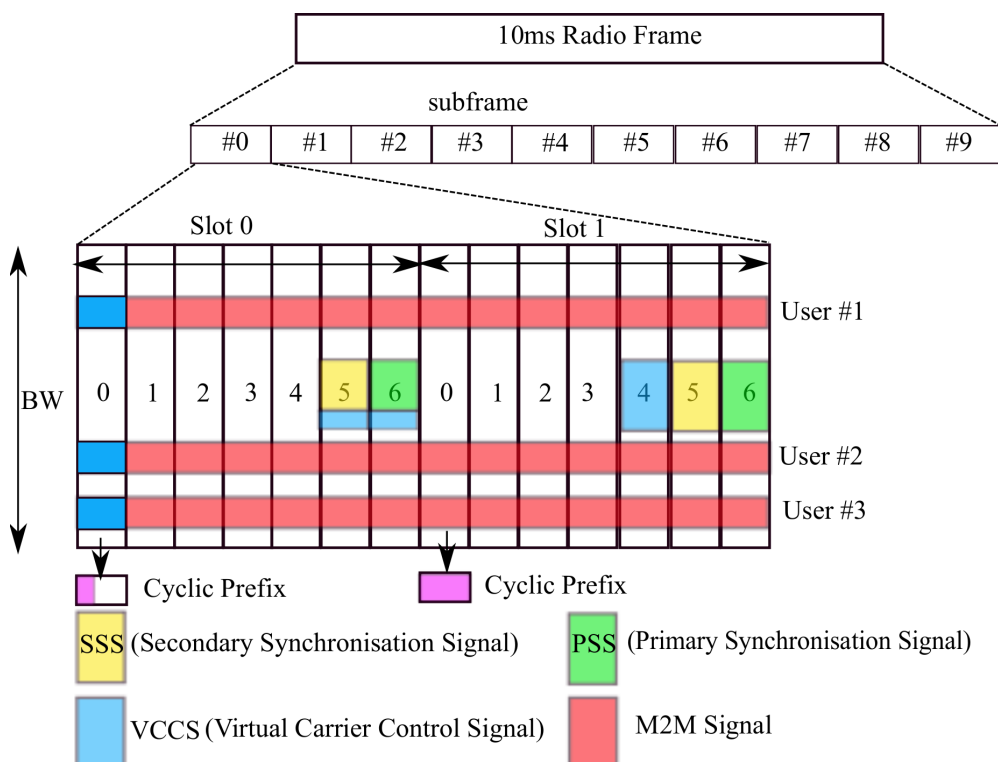
Figure 3.3: *Virtual Carrier Synchronisation Signals.*

As mentioned above, cell synchronisation is the very first step when an MTC device wishes to connect to a cell. A cyclic prefix is appended as guard time for each OFDM symbol to enable against time delay spread. One downlink slot consists of 6 or 7 OFDM symbols as shown in Figure 3.3, depending on whether extended or normal cyclic prefix is configured, respectively. The extended cyclic prefix is able to cover larger cell sizes with higher delay spread of the radio channel, but reduces the number of available symbols [16]. The first step of cell search in LTE is based on specific synchronisation signals. LTE uses a hierarchical cell-search scheme, which includes the primary and the secondary synchronisation signals. They are designed to carry

the physical layer identity and the physical layer cell identity. The synchronisation signals are transmitted twice per 10 ms on predefined slots, which locate in the last OFDM symbol of first time slot of the first subframe as shown in Figure 3.3. This enables users to be synchronised at the subframe level. In the next step, the terminal finds the secondary synchronisation signal (SSS) which determines the physical layer cell identity group number. In order to decode the VC message, a VC control signal (VCCS) should be included in the VC carrier as shown in Figure 3.3. The VCCS includes the VC carrier locations, filter parameters and sampling reduction ratio. When the VCCS has been decoded, the MTC terminal devices can easily decode the received signals intended for it. The VCCS can be also mapped into the VC carrier to assist the MTC receiver in maintaining accurate symbol timing. The VC system decoding processing is shown in Table 3.1.

Virtual Carrier Receiver System Synchronisation
Step 1: Search for the PSS and the SSS
Step 2: Decode the VCCS to identify VC carrier location
Step 3: Compute the number of operating sub-carriers K and sampling reduction ratio γ
Step 4: Set filter parameters and receiver sampling rate f_{vc}
Step 5: Decode received MTC messages from the specified VC location

Table 3.1: *VC Synchronisation Processing Steps.*

3.3.5   Energy Saving For The VC Receiver

The basic motivation for VC is that the ADC power dissipation is a linear function of the sampling rate. A previous study [76] derived the power dissipation of an ADC as P_{ADC},

$$P_{\text{ADC}} = 48 k_{\text{B}} T_{\text{Temp}} \cdot 2^{2V} \cdot f_{\text{s}}, \tag{3.12}$$

where k_{B} is Boltzmanns constant, T_{Temp} is temperature, f_{s} is the sampling frequency and V is the SNR-bits, which is given by [76]:

$$V = \frac{\text{SNR[dB]} - 1.76}{6.02}. \tag{3.13}$$

The ADC power dissipation presents a linear reduction by reducing the sampling frequency.

In terms of the FFT computational complexity, compared with the standard OFDM system, the VC receiver also reduces the number of subsequent digital signal processing computations. The

computational complexity [77] for the standard OFDM receiver can be defined as Γ^{OFDM}:

$$\Gamma^{\mathrm{OFDM}} = \frac{N}{2} \cdot \log_2(N).$$

(3.14)

In terms of the VC receiver system, the FFT size decreases to N/γ. Therefore, the computational complexity for the VC receiver system can be defined as:

$$\Gamma^{\mathrm{VC}} = \frac{N/\gamma}{2} \cdot \log_2(N/\gamma).$$

(3.15)

3.4 Performance Analysis

In this chapter, we focus on three distinct channel scenarios to evaluate system performance and will not consider the effect of time or frequency offset, thus, we make the assumption of a perfect sampling timing. In this chapter, $\mathbb{E}[\cdot]$ represents the expectation operation, $\otimes$ represents the convolution operation and $(\cdot)^*$ represents the complex conjugate operation.

3.4.1 Aliasing Analysis

First, we analyse the effect of filter aliasing in $i_{\mathrm{A}}(t)$ in a simple scenario. We assume that the received MTC message $y_{\mathrm{F}}(t)$ is not corrupted by background noise or multipath channel effects. The received signal can be expressed as:

$$y_{\mathrm{F}}(t) = x(t) \otimes b(t).$$

(3.16)

With the assumptions of perfect sampling timing, a sampling reduction rate of γ and $L_{\mathrm{CP}} > L_{\mathrm{F}}$, we can write down an expression for the FFT output of $y_{\mathrm{F}}(t)$, after the CP is removed. The m-th frequency bin can be denoted as [49]:

$$
\begin{aligned}
y_{\mathrm{F}}(m) &= \sum_{n=0}^{N-1} X(n) \cdot B(n) \cdot e^{-j2\pi nm/K} \\
&= \sum_{k=0}^{K-1} \left(\sum_{a=0}^{\gamma-1} X(aK+k) \cdot B(aK+k) \right) \cdot e^{-j2\pi km/K},
\end{aligned}
$$

(3.17)

where $B(n)$ is the N-point FFT of $b(t)$. Therefore, the received k-th sub-carrier signal after

reducing the sampling rate in the frequency domain can be written as:

$$R_{\mathrm{F}}(k) = \sum_{a=0}^{\gamma-1} X(aK + k) \cdot B(aK + k), \ k \in [0, K - 1] \tag{3.18}$$

where $K = \frac{N}{\gamma}$. After reducing the sampling rate at the receiver, there are γ copies of the original OFDM signal centred at frequencies $0, f_{\mathrm{s}}/\gamma, 2f_{\mathrm{s}}/\gamma, ..., (\gamma - 1)f_{\mathrm{s}}/\gamma$. The 0 frequency term is the desired spectrum of the transmitted signal $x(t)$ while the remaining frequencies represent undesired aliased components. Thus, equation (3.18) can be re-written as:

$$R_{\mathrm{F}}(k) = X(k) \cdot B(k) + \sum_{a=1}^{\gamma-1} X(aK + k) \cdot B(aK + k), \tag{3.19}$$

the aliasing term can be expressed as:

$$I_{\mathrm{A}}(k) = \sum_{a=1}^{\gamma-1} X(aK + k) \cdot B(aK + k), \tag{3.20}$$

and it represents all the aliased interference present in the received signal. The SINR equation for the received signal is computed as ρ:

$$\rho(k) = \frac{\mathbb{E}[S(k)^2]}{\mathbb{E}[N_{\mathrm{I}}(k)^2]}, \tag{3.21}$$

where $\mathbb{E}[\cdot]$ denotes statistical expectation, $S(k)^2$ is the received signal power over at the output of the IIR filter, and $N_{\mathrm{I}}(k)^2$ is the interference power arising from the $(\gamma - 1)$ aliased terms. Thus, the interference power for no channel effect case N_{IF} can be written as:

$$\mathbb{E}[N_{\mathrm{IF}}(k)^2] = \mathbb{E}\left[|R_{\mathrm{F}}(k) - X(k) \cdot B(k)|^2\right] = \sum_{a=1}^{\gamma-1} \mathbb{E}\left[X(aK + k)^2\right] \cdot |B(aK + k)|^2. \tag{3.22}$$

Thus, the theoretical SINR value at the output of the VC receiver without channel effects can be derived as:

$$\rho_{\mathrm{F}}(k) = \frac{\mathbb{E}\left[X(k)^2\right] \cdot |B(k)|^2}{\sum_{a=1}^{\gamma-1} \mathbb{E}\left[X(aK + k)^2\right] \cdot |B(aK + k)|^2}. \tag{3.23}$$

3.4.2 AWGN Channel Effect SINR Analysis

Assume now the transmitted MTC signals go through an AWGN channel where the noise has mean zero and a noise standard deviation of $\sigma = \sqrt{f_s N_0/2}$. Similar to equations (3.19), the received MTC messages from the AWGN channel in the frequency domain can be expressed as:

$$R_A(k) = X(k) \cdot B(k) + \sum_{a=1}^{\gamma-1} X(aK + k) \cdot B(aK + k) + G(k). \tag{3.24}$$

Thus, the closed-form expression for SINR of VC receiver at k sub-carrier at the AWGN channel can be derived as:

$$\rho_A(k) = \frac{\mathbb{E}\left[X(k)^2\right] \cdot |B(k)|^2}{\sigma^2 + \sum_{a=1}^{\gamma-1} \mathbb{E}\left[X(aK + k)^2\right] \cdot |B(aK + k)|^2}. \tag{3.25}$$

3.4.3 Multipath Channel SINR Analysis

This section is devoted to address the effect of multipath channels by analysing the combined impulse response w_{cn} of both the multipath Rayleigh channel and the analogue filter in equation (3.5). We consider two cases when the length of combined response (L_{com}) is both longer and shorter than the CP length (L_{CP}) in samples.

3.4.3.1 CP Longer Than Combined Response

Assume that a MTC receiver has received the signals over a Rayleigh multipath channel and an IIR filter has been applied at the receiver. We assume L_{CP} is longer than L_{com} and the received signal is sampled with the correct timing. The received signal can be expressed as:

$$
\begin{aligned}
y_{Lo}(m) &= \sum_{n=0}^{N-1} X(n) \cdot W_{cn}(n) \cdot e^{-j2\pi nm/K} + g(m) \\
&= \sum_{k=0}^{K-1} \left(\sum_{a=0}^{\gamma-1} X(aK + k) \cdot W_{cn}(aK + k) \right) \cdot e^{-j2\pi km/K} + g(m).
\end{aligned}
\tag{3.26}
$$

The k-th received sub-carrier in the frequency domain can be derived as:

$$R_{Lo}(k) = X(k) \cdot W_{cn}(k) + \sum_{a=1}^{\gamma-1} X(aK + k) \cdot W_{cn}(aK + k) + G(k). \tag{3.27}$$

Thus, the average SINR value of the VC receiver over the Rayleigh fading multipath channel can be expressed as:

$$\rho_{\mathrm{Lo}}(k) = \frac{\mathbb{E}\left[X(k)^2\right] \cdot \mathbb{E}[|W_{\mathrm{cn}}(k)|^2]}{\sigma^2 + \sum_{a=1}^{\gamma-1} \mathbb{E}\left[X(aK+k)^2\right] \cdot \mathbb{E}[|W_{\mathrm{cn}}(aK+k)|^2]}. \tag{3.28}$$

3.4.3.2 CP Much Shorter Than Combined Response

The major function of the cyclic prefix is that it removes the intersymbol ISI and ICI. In order to address the impact of the case when CP is shorter than the channel response in the VC receiver system, we need to compute both the ISI and ICI noise terms. According to a previous study [78], the ISI and ICI cause interference at the tail of the impulse response. Based on [78], the ISI noise for the VC receiver, in the case that the L_{CP} is shorter than the length (L_{com}) of combined channel and filter impulse response, can be expressed as:

$$P_{\mathrm{ISI}}(k) = \sigma^2 \sum_{c=L_{\mathrm{CP}}+1}^{L_{\mathrm{com}}-1} |U_c(k)|^2, \tag{3.29}$$

where $U_c(k)$ is defined as:

$$U_c(k) = \sum_{c=L_{\mathrm{CP}}+1}^{L_{\mathrm{com}}-1} w_{\mathrm{cn}}(c)e^{-j2\pi ck/N}. \tag{3.30}$$

Note that the expression for $U_c(k)$ is actually for the FFT of the tail of the combined impulse response. In terms of ICI, [78] shows that the ISI and ICI have the same power spectral density. Therefore, the noise level of ICI is equal to that of the ISI. Thus, the interference power for the VC receiver system can be derived as:

$$\mathbb{E}[N_{\mathrm{So}}(k)^2] = \sigma^2 + \sum_{a=1}^{\gamma-1} \mathbb{E}\left[X(aK+k)^2\right] \cdot \mathbb{E}[|W_{\mathrm{cn}}(aK+k)|^2] + 2\sigma^2 \sum_{c=L_{\mathrm{CP}}+1}^{L_{\mathrm{com}}-1} |U_c(k)|^2. \tag{3.31}$$

Therefore, the expression of the average SINR for the case where the CP is much shorter than combined response can be written as:

$$\rho_{\mathrm{So}}(k) = \frac{\mathbb{E}\left[X(k)^2\right] \cdot \mathbb{E}[|W_{\mathrm{cn}}(k)|^2]}{\sigma^2 + \sum_{a=1}^{\gamma-1} \mathbb{E}\left[X(aK+k)^2\right] \cdot \mathbb{E}[|W_{\mathrm{cn}}(aK+k)|^2] + 2\sigma^2 \sum_{c=L_{\mathrm{CP}}+1}^{L_{\mathrm{com}}-1} |U_c(k)|^2}. \tag{3.32}$$

3.4.4 Asynchronous ISI Analysis

In the previous sections, we assumed the received signals are perfectly synchronised and sampled at the correct timing. This sub-section will analyse the ISI effects caused by asynchronism. Here we define τ_{Err} as the timing error in samples, which we assume is positive. Thus, interference to the first OFDM symbol $x_1(t)$ is caused by the first τ_{Err} samples from the second OFDM symbol $x_2(t)$. Then, we can write the interference term as:

$$i_{\text{Err}} = \sum_{t=0}^{\tau_{\text{Err}}-1} x_2(t) \otimes b(t).$$

(3.33)

Thus, the interference term on the kth sub-carrier can be rewritten using the Fourier transform as:

$$i_{\text{Err}}(k) = \sum_{k=0}^{N-1} \sum_{n=0}^{\tau_{\text{Err}}-1} X_2(n)B(n)e^{-j2\pi nk/N},$$

(3.34)

where $X_2(n)$ is the nth FFT output for $x_2(t)$. Then the ISI noise for timing error denoted as N_{IErr}, for the VC receiver with sampling reduction ratio of γ can be derived as:

$$\mathbb{E}\left[N_{\text{IErr}}(k)^2\right] = \sum_{a=0}^{\gamma-1} \sum_{n=0}^{\tau_{\text{Err}}-1} \mathbb{E}\left[X_2(aK+k)^2\right] \cdot \mathbb{E}[|B(aK+k)|^2].$$

(3.35)

Note that equation (3.35) represents an extra timing error interference term which can be added to the denominator for our SINR equations to compute the theoretical SINR values when a specified timing error is present.

3.4.5 BER Analysis

In terms of comparing the VC receiver BER performance with the standard OFDM receiver system, this chapter will use the three BER basic LTE standard modulation schemes, including 4PSK, 16QAM and 64QAM for both the AWGN channel and the Rayleigh fading multipath channel.

3.4.5.1 BER Analysis For the AWGN Channel

The ratio of energy per bit (E_{b}) to the spectral noise density (N_0) is defined as:

$$E_{\mathrm{b}}/N_0 = \frac{\overline{\rho}}{N_{\mathrm{b}}}, \tag{3.36}$$

where N_{b} is the number of bits per sample. The theoretical BER value of the standard OFDM receiver is computed as [44]:

$$P_{\mathrm{QPSK}} = \frac{1}{2} \cdot \mathrm{erfc}\left(\sqrt{\frac{E_{\mathrm{b}}}{N_0}}\right), \tag{3.37}$$

$$P_{\mathrm{16QAM}} \approx \frac{3}{8} \cdot \mathrm{erfc}\left(\sqrt{\frac{2}{5} \cdot \frac{E_{\mathrm{b}}}{N_0}}\right), \tag{3.38}$$

$$P_{\mathrm{64QAM}} \approx \frac{7}{24} \cdot \mathrm{erfc}\left(\sqrt{\frac{1}{7} \cdot \frac{E_{\mathrm{b}}}{N_0}}\right), \tag{3.39}$$

where $\mathrm{erfc}(.)$ denotes the complementary error function.

3.4.5.2 Standard OFDM BER Analysis Under the Rayleigh Multipath Channel

The theoretical BER value of normal OFDM system over the Rayleigh multipath channel is computed as [44] [45]:

$$P_{\mathrm{QPSK}} = \frac{1}{2}\left(1 - \sqrt{\frac{E_{\mathrm{b}}/N_0}{1 + E_{\mathrm{b}}/N_0}}\right), \tag{3.40}$$

$$P_{\mathrm{16QAM}} = \frac{1}{2}\left(1 - \frac{3}{4}\sqrt{\frac{4 \cdot E_{\mathrm{b}}/N_0}{5/2 + 4 \cdot E_{\mathrm{b}}/N_0}} - \frac{1}{2}\sqrt{\frac{4 \cdot E_{\mathrm{b}}/N_0}{5/18 + 4 \cdot E_{\mathrm{b}}/N_0}} + \frac{1}{4}\sqrt{\frac{4 \cdot E_{\mathrm{b}}/N_0}{1/10 + 4 \cdot E_{\mathrm{b}}/N_0}}\right). \tag{3.41}$$

For the 64QAM modulation, the BER expression is [79]:

$$P_{\mathrm{64QAM}} = \sum_{i=1}^{28} \omega_i I_{\mathrm{ir}}(v_i^1, v_i^2, \overline{\gamma}, r, \varrho), \tag{3.42}$$

where $\overline{\gamma}$ is the average SNR per symbol and coefficients ω_i, v_i^1, v_i^2 and ϱ are listed in a table in [79] and I_{ir} is the integral representation:

$$I_{\mathrm{ir}}(z) = \frac{1}{\pi} \int_{-(\pi/2)}^{(\pi/2)} e^{-z \cdot \sin\phi} d\phi. \tag{3.43}$$

Simulation Parameters						
Bandwidth	N	Transmitted f_s	L_CP	IIR Filter Order	Type of Filter	Attenuation
20 MHz	2048	30.72 MHz	144	4	Butterworth	3 dB
Equivalent FIR Filter Order						
γ	1/2	1/4	1/8	1/16	1/32	1/64
L_F	24	35	67	132	208	332

Table 3.2: *Common Simulation Parameters.*

Now we can compute the theoretical BER value by taking the SINR closed form expression ρ for the VC system into the BER equations as above.

3.5 Numerical Results

This section will firstly evaluate the bandwidth efficiency performance and the energy saving performance by using the VC receiver system rather than a full bandwidth OFDM receiver. Then theoretical and simulation results for the SINR and BER performance will be described. According to the LTE downlink specification [16], the thesis considers LTE downlink bandwidth of 20 MHz with sampling rate of 30.72 MHz, which is matching the FFT size of 2048. The length of CP is chosen as the LTE CP short standard of 144 samples. Common parameters for simulations are listed in Table 3.2.

3.5.1 LTE Downlink Efficiency Performance

An additional physical control format indicator channel carries on specific resource elements in the first OFDM symbol of each subframe, which is used to indicate the number of OFDM symbols used for the PDCCH, i.e. 1, 2 or 3 symbols are possible in the LTE downlink specification [16], depending on the number of users in a cell and signalling formats conveyed on PDCCH. The number of PDCCH is also dependent on the bandwidth, e.g. for a 1.4 MHz bandwidth the minimum number of PDCCH symbols is always 2 according to the LTE specification [16]. The result for the LTE downlink capacity for one 10 ms LTE radio frame with the number of PDCCH transmissions is shown in Figure 3.4. The LTE bandwidth efficiency is computed as Equation (3.11) and it is obvious that whether one or two PDCCH symbols is used, the percentage capacity of 20 MHz bandwidth is much higher than other options, and the least efficient is the 1.4 MHz bandwidth carrier. We can conclude that compared with the SC and CA meth-
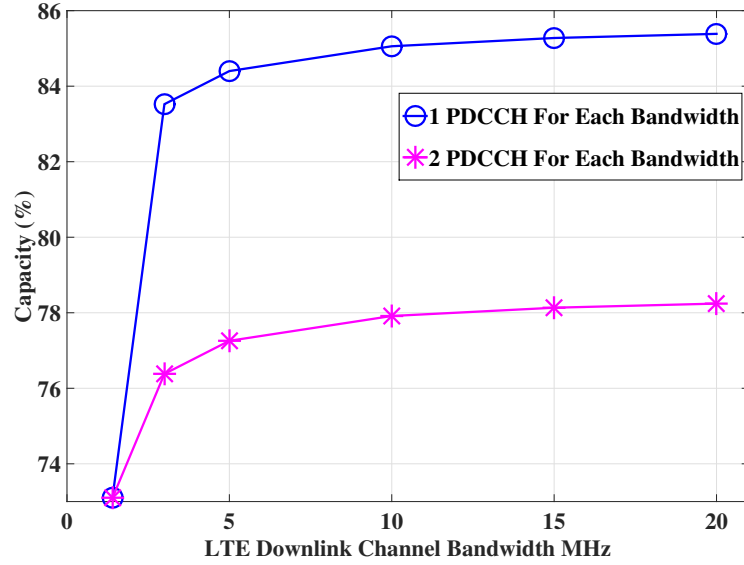
Figure 3.4: *LTE Downlink Capacity Vs. Channel Bandwidth.*

Sampling Rate (f_s)	FFT Size (N)	Normalised ADC Power (W)	FFT Computational Complexity (Ops)
30.72 MHz	2048	1	11264
15.36 MHz	1024	1/2	5120
7.68 MHz	512	1/4	2304
3.84 MHz	256	1/8	1024
1.92 MHz	128	1/16	448
0.96 MHz	64	1/32	192

Table 3.3: *Energy Saving Performance of the VC System for the 20 MHz LTE Channel From Equations (3.14) and (3.15).*

ods, using a virtual carrier mapped into a 20 MHz LTE band can improve bandwidth efficiency significantly.

3.5.2 Energy Saving Performance for the VC Receiver

Compared with the 20 MHz LTE standard receiver, the ADC dissipation performance and the computational complexity of the FFT block for the virtual carrier receiver system is shown in Table 3.3. In order to compare the cost-efficiency, we defined the energy cost of processing the full 20 MHz bandwidth to be normalised to 1. By reducing the sampling rate of a MTC receiver, the ADC power dissipation and the computational complexity are reduced significantly. If
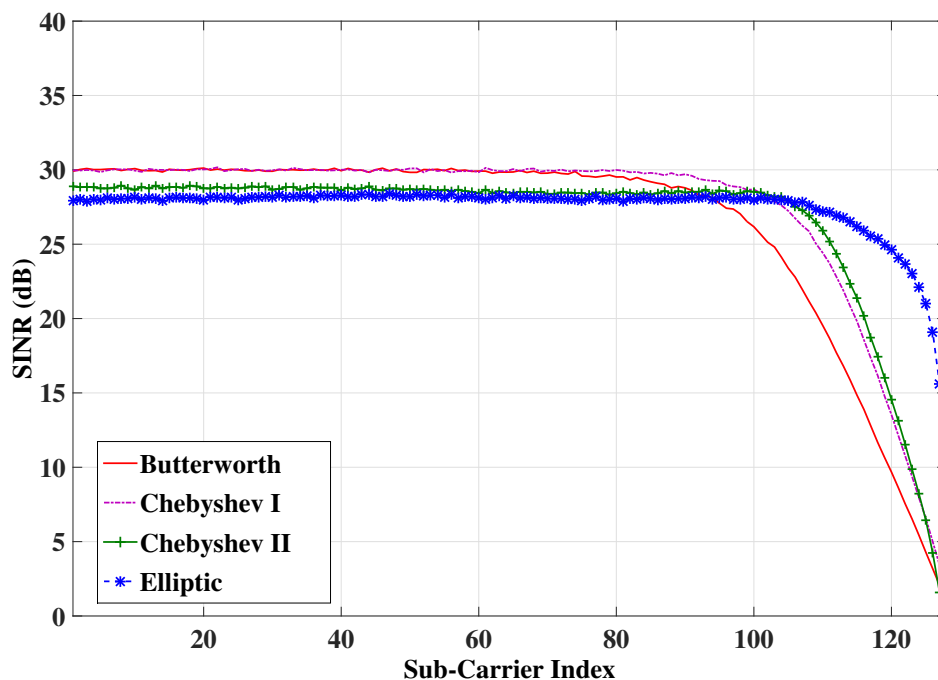
Figure 3.5: *SINR Performance over Different IIR Filters, AWGN channel 30 dB, $N = 2048$, $L_{\mathrm{CP}} = 144$, $\gamma = 8$, 16-QAM.*

a MTC terminal device only needs to decode 64 sub-carriers, by using a low pass filter and sampling rate at 0.96 MHz, it only costs 1/32 of the ADC operations compared with decoding the whole 20 MHz band and the FFT computation is reduced from 11264 operations to 192.

3.5.3 SINR Performance

The SINR performance of the VC receiver system over the AWGN channel with four types of IIR analogue filter (Butterworth, Chebyshev I, Chebyshev II and Elliptic filters [51]) with $\gamma = 8$ is shown in Figure 3.5. The passband ripple for Chebyshev I is set to 1 dB and the stopband attenuation for Chebyshev II is set to 40 dB. In the case of the Elliptic filter, the passband ripple and the stopband attenuation are set to 1 dB and 40 dB in order to provide fair comparison. We plot the SINR value for the first 128 sub-carriers in Figure 3.5 and it shows that the sub-carriers near the cut-off frequency band present significant SINR loss. It also shows that both the Butterworth and the Chebyshev I filters achieve higher SINR performance in the passband compared with Chebyshev II and Elliptic filters. However, the Chebyshev I filter has a worse phase response because of group delay variations at the band edges. Therefore, in order to
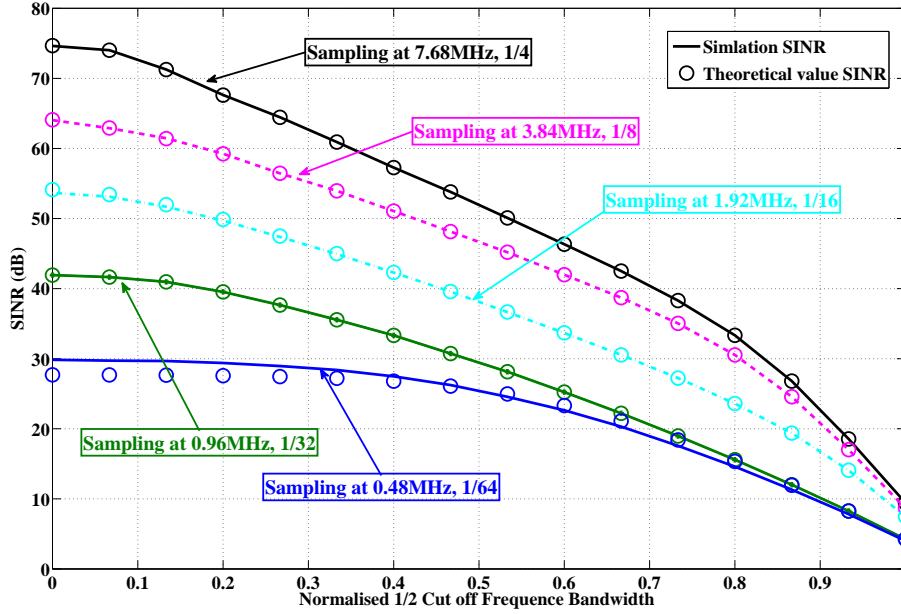
Figure 3.6: *SINR Performance for Different Sampling Rate, $g(t) = 0$, $h(t) = 0$, $N = 2048$, $L_{\mathrm{CP}} = 144$, 16-QAM.*

achieve a high SINR performance in the pass band frequency, this chapter will focus on the Butterworth IIR filter in the remaining simulations.

The SINR performance for different sampling reduction ratios is shown in Figure 3.6 with the assumption of a 16-QAM modulation scheme and no background noise, and there is perfect time synchronisation. When γ is 64, L_{F} is much larger than L_{CP}. Thus we computed the ISI and ICI noise power using equation (3.31) for $\gamma = 64$ to obtain the theoretical value of the SINR which is computed from equation (3.23). The theoretical results show a perfect match with the simulations. If the MTC receiver samples at 0.48 MHz (about 1/64 of transmitted sampling rate, the IIR cut-off frequency is set to 0.3125 MHz in order to match with the sampling reduction ratio), the SINR value of the first 65% of all sub-carriers is still above 20 dB. It also indicates that the VC receiver system is able to decode the transmitted low data rate MTC messages mapped into a normal LTE band, even if we reduced the sampling rate by 64 times. The basic reason for the SINR performance with $\gamma = 32$ and $\gamma = 64$ being much poorer than other cases is the non-integer sampling reduction of the CP.

The SINR degradation performance of the VC receiver system without timing error over the

59
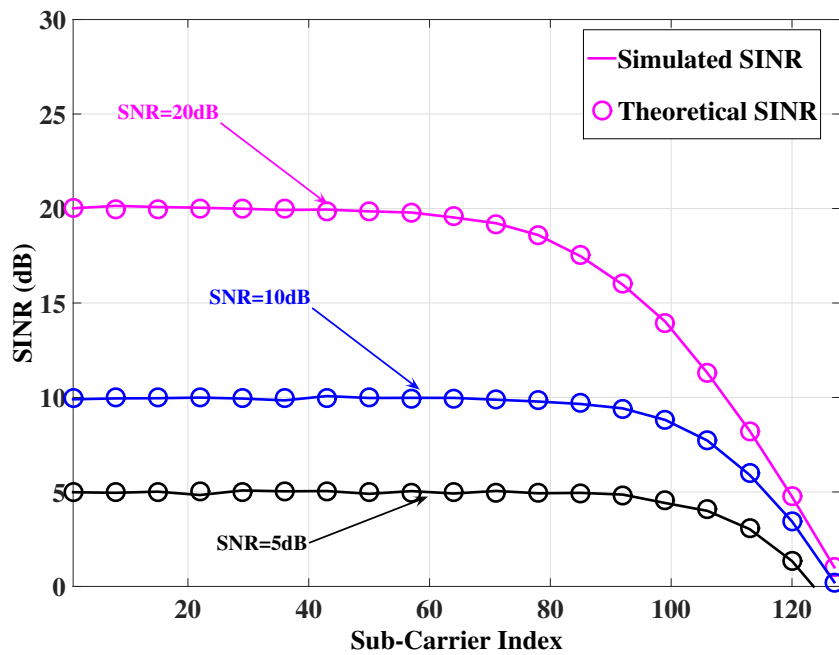
(a) Without Timing Error
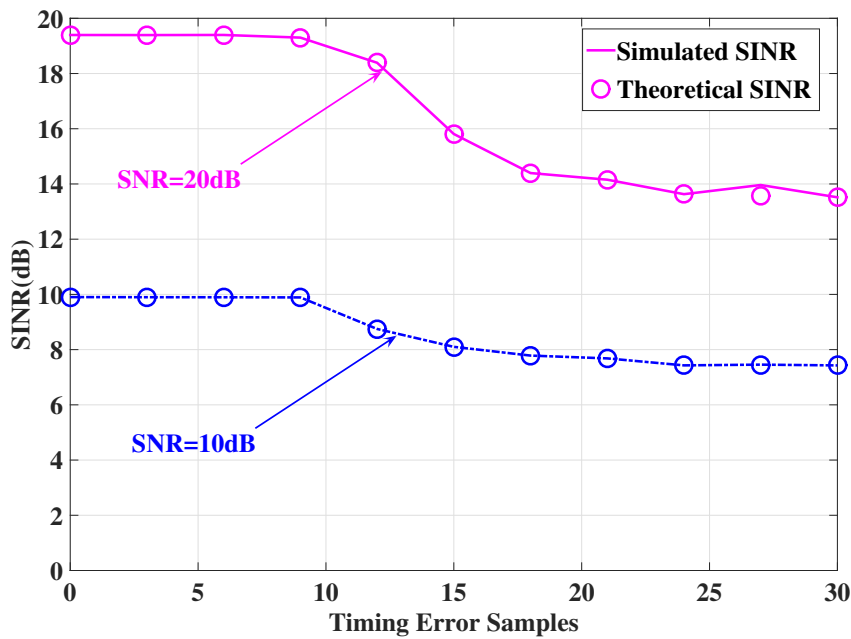
(b) With Timing Error

Figure 3.7: *SINR Performance over the AWGN channel, Butterworth, QPSK, $N = 2048$, $L_{\mathrm{CP}} = 144$, $\gamma = 8$.*
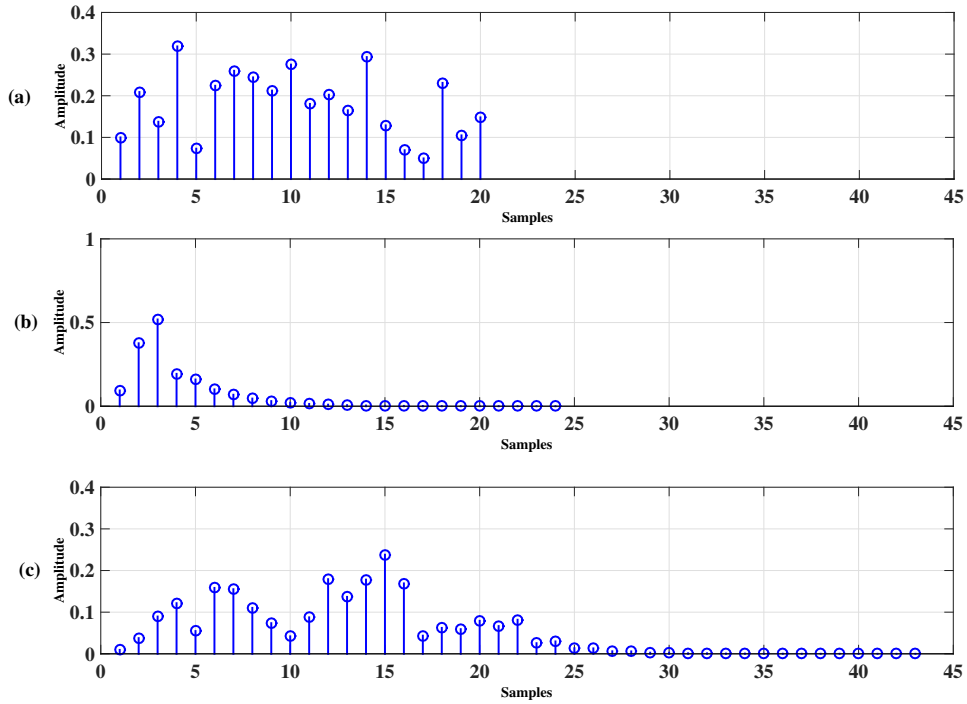
Figure 3.8: *Overall Receiver Impulse Response: (a) Channel Impulse Response, (b) Receiver Filter Impulse Response, (c) Combined Impulse Response.*

AWGN channel is shown in Figure 3.7(a). The transmitted SNR is set to 20 dB, 10 dB and 5 dB. The theoretical SINR value is computed using (3.25) and it is closely matched with simulations. The AWGN channel does not significantly affect the SINR performance of the VC receiver. If the input SNR is 20 dB, the SINR degradation becomes apparent at sub-carrier number 80, where there is about 2 dB SINR loss. By reducing the transmitted SNR, the SINR degradation in the VC receiver mores closer to half the cut-off frequency. In terms of the first 60-70 sub-carriers, the VC receiver system presents high SINR performance.

The SINR performance versus timing error τ_{Err} is shown in Figure 3.7(b). The ISI of timing error is computed using (3.35), and added to the denominator of (3.25) to compute the theoretical SINR, which perfectly matches the simulations. When τ_{Err} is larger than 9 samples, the SINR performance is significantly reduced.

One example of a combined $h(t)$ and $b(t)$ impulse response is shown in Fig. 3.8, and it clearly shows that the receiver filter $b(t)$ increases the delay spread of the channel filter $h(t)$. There-

fore, when the CP length in samples is shorter than the combined impulse w_{cn}, ISI and ICI interference will be introduced.

The SINR degradation performance over the Rayleigh multipath channel is shown in Figure 3.9. Assuming the VC receiver has received the signal over a $L_H = 20$ tap Rayleigh fading channel, the length of CP is longer than the combined impulse response and the ADC sampling follows perfect timing, the SINR performance is shown in Figure 3.9(a). The theoretical value of the SINR is computed using equation (3.28), and similar to the AWGN channel case, the Rayleigh fading channel does not significantly affect the average SINR in the passband. Now we increase the length of channel to 300 taps, i.e. the "long channel". Thus, the CP is not long enough to prevent ISI and ICI interference as shown in Figure 3.9(b), where the theoretical value is computed using equation (3.32). It is obvious that there is a significant SINR degradation in the passband due to the ISI and ICI. For a received signal with 20 dB SNR over a 300 tap multipath channel, the average SINR of the down-sampled signal is reduced to 13 dB in the passband. Therefore, the performance of the VC receiver can be limited by increases in the number of channel taps L_H.

3.5.4   BER Performance

In terms of testing the BER performance of the VC receiver system, we assume the transmitted MTC messages are mapped in to the first 90 sub-carriers over a 20 MHz LTE channel. According to Figure 3.7(a), the SINR values of sub-carriers 1-90 would not be affected significantly by using sampling reduction ratio of $\gamma = 8$. Therefore, in this section, we will examine the BER performance of sub-carriers from 1 to 90.

The BER performance of the VC receiver over the AWGN channel is shown in Figure 3.10, we compared the theoretical value of the normal OFDM system derived from equation (3.37) - (3.39) and the simulated value of the VC system. It is obvious that the VC receiver system can achieve the same BER performance compared with the traditional LTE receiver even when reducing the receiver ADC sampling rate.

The BER performance of the Rayleigh fading channel is shown in Figure 3.11. The BER performance of the VC receiver system is closely matched with the normal OFDM receiver performance obtained from equation (3.40) - (3.42). There are slightly higher BER values for E_b/N_0 between 25 dB to 30 dB. The reason for that is the VC receiver system causes a
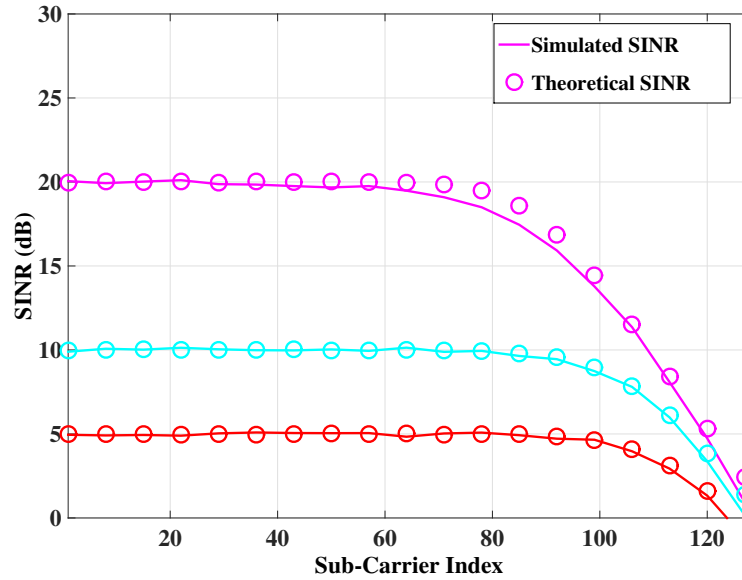
(a) SINR for 20 Taps Multipath Channel
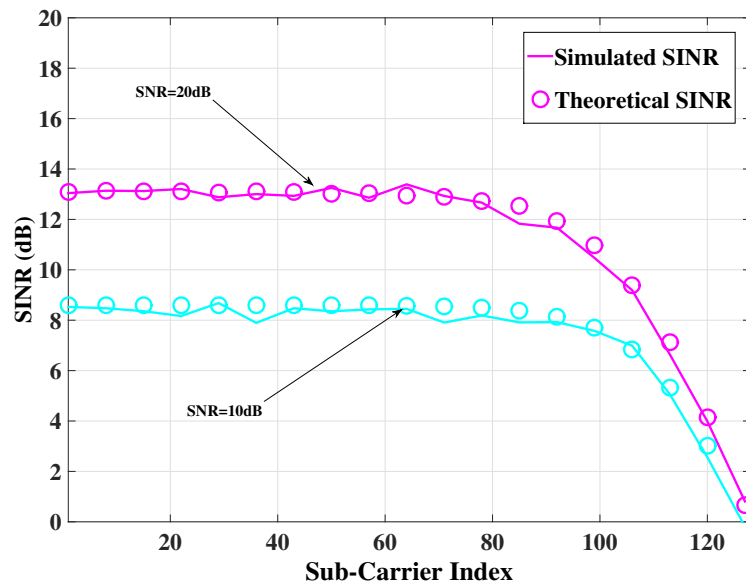
(b) SINR for 300 Taps Multipath Channel

Figure 3.9: *SINR Degradation Caused by a Rayleigh Fading Channel, Butterworth, QPSK, $N = 2048$, $L_{\mathrm{CP}} = 144$, $\gamma = 8$.*

63
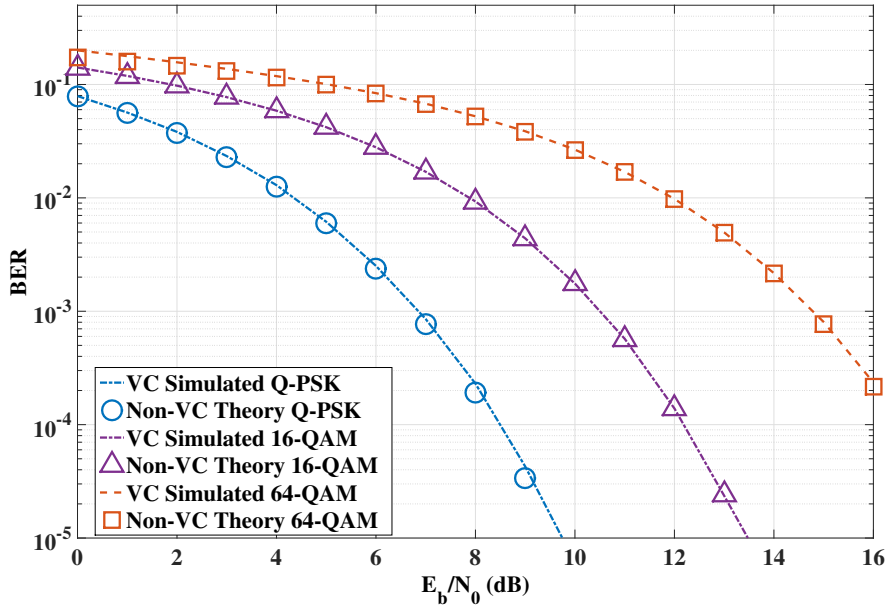
Figure 3.10: *BER Performance of the Virtual Carrier System over the AWGN Channel, $N = 2048$, $L_{CP} = 144$, $\gamma = 8$.*

small SINR degradation around sub-carrier 90, especially for high input SNR. However, the VC receiver system still can perfectly decode the transmitted low data rate MTC messages without significant BER degradation by using only 1/8 of the ADC power and reducing the computational complexity from 11264 operations to 1024.

A measure of the delay spread depicted in the channel power delay profile is useful since the ISI which causes higher BER. The delay profile is the expected power per unit of time received with a certain excess delay. In order to measure the BER performance of the VC receiver affected by both ISI and ICI, this chapter now considers a very dispersive channel. Thus we increase the multipath Rayleigh fading channel taps to 200, 300 and 500 with $L_{CP} = 144$ and the result is shown in Figure 3.12. It is obtained by averaging a large set of impulse responses. The theoretical BER value is computed by substituting the SINR value from equation (3.32) into equation (3.41), which closely matches with simulations. It clearly indicates that by increasing the length channel impulse response in samples, the BER degradation will increase significantly due to the presence of ICI and ISI. Compared with 200 taps, the BER performance significantly degrades with increasing the number of channel taps to 300 or 500. When the channel taps increased to 500, the gap between the OFDM system and the VC system becomes small. This means the CP is no longer able to protect the received signal against ICI and ISI. Compared
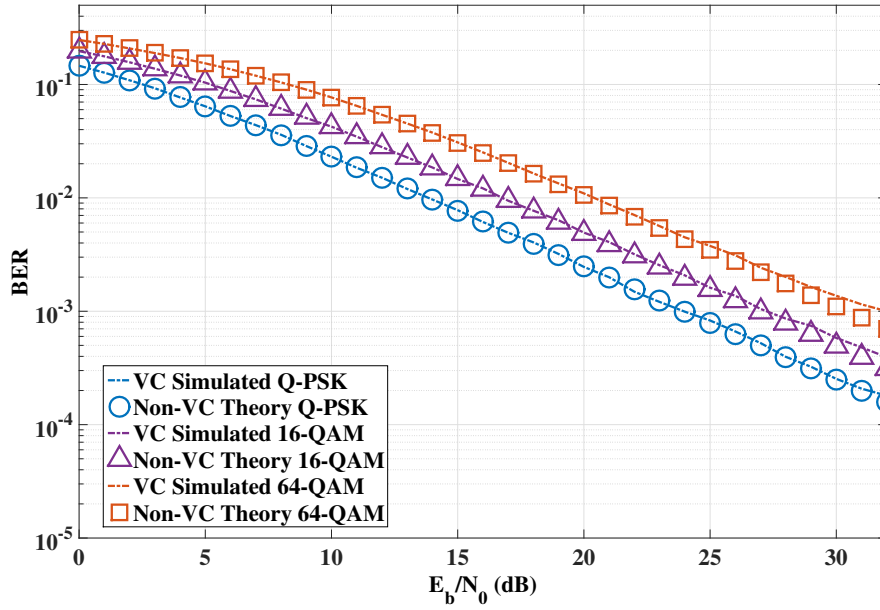
Figure 3.11: *BER Performance of the Virtual Carrier System over the Rayleigh fading Channel, Channel Taps=20.*

with the standard OFDM receiver, the VC receiver is more sensitive to the number of channel taps L_{H}. Therefore, the VC receiver system might not be suitable for some very poor channel conditions, so future studies might focus on how to reduce the ISI and ICI effects while at the same time reducing the cost of the receiver.

3.6 Conclusion

In this chapter, a practical virtual carrier receiver system is proposed that uses a narrow band analogue filter and a much lower sampling rate ADC in order to extract the low data rate MTC signals while significantly reducing the ADC power consumption and the computational complexity. In order to modify the existing LTE communication systems to support low data rate MTC devices, the VC receiver can significantly improve the LTE bandwidth efficiency and cost-efficiency. At the same time, it provides high SINR and BER performance close to a full sample rate OFDM receiver for the sub-carriers of interest. Secondly, this chapter has derived the theoretical analysis of the VC receiver performance, which perfectly match with simulations. The theoretical equations account for the effect of aliasing spread on the sub-carrier location, and this helps to the system designer to evaluate what kind of filters and receiver
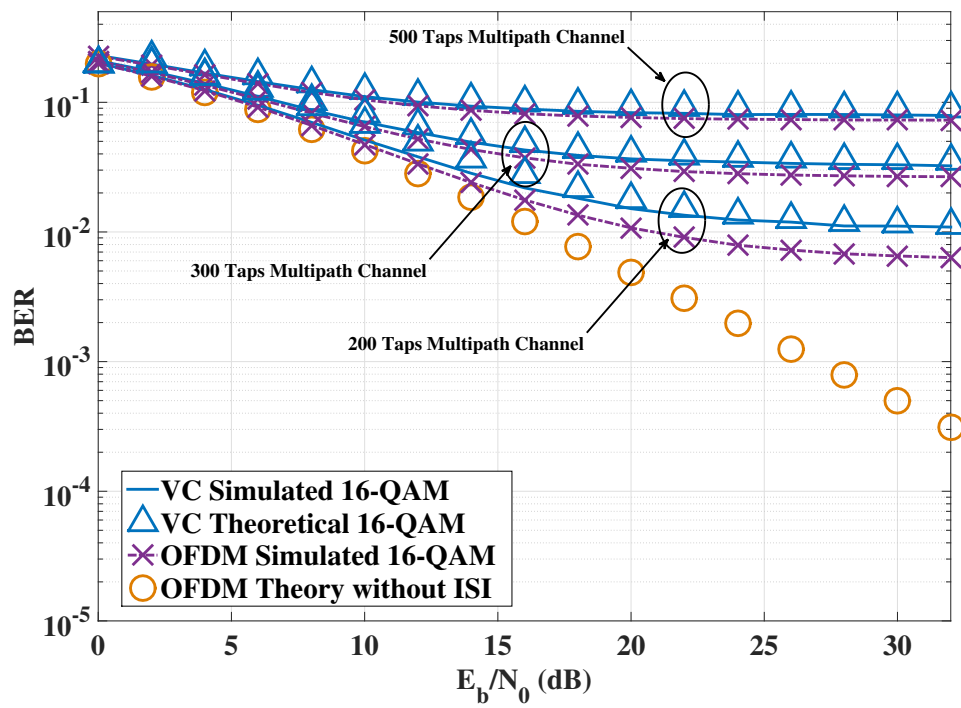
Figure 3.12: *BER Performance over a much longer Rayleigh flat fading multipath channel, 16-QAM, $\gamma = 8$, $L_{CP} = 144$.*

sampling rate can be used to balance the energy cost and detection performance. This chapter highlights that the VC receiver system could be a suitable solution to support the MTC based on the LTE standard.

In Chapter 4, we will provide the analysis and performance of the 5G Uplink waveform design to address the ICI caused by asynchronous. The purpose is to relax the synchronism requirements can significantly improve operational capabilities, bandwidth efficiency and even battery lifetime for the low data rate MTC devices. The performance of several candidate waveforms will be presented in the next chapter.

Chapter 4
Compare and Contrast the Performance of Several Multi-user Waveform Designs For the Asynchronous MTC

The MTC (or IoT) extends the internet as we know it today by attaching a multitude of sensors/actors (e.g. smart meters) with access to the wireless network. The cost on the wireless transmission is a critical issue, as the devices are not necessarily connected to the electrical supply, e.g., in the case of sensor devices. In Chapter 3, we concentrated on the virtual carrier receiver system, which aimed to reduce the maximum bandwidth and the ADC sampling rate of LTE to reduce the processing cost for the MTC downlink.

In this chapter, we are concentrating on the uplink channel for supporting the massive MTC devices carrying the data via wireless. One key aspect of user-centric processing in the fifth generation (5G) communications is for devices to be connected to multiple access points typically. The dynamic changes in distance between the devices and all access points are required a flexible synchronised processing. So a similarly tight synchronisation as used in LTE, appears not to be cost-effective or even possible for a multi-user system in 5G. Relaxing the synchronisation requirements by reducing the OFDM side-lobes is one solution for the 5G uplink. This chapter analyses the sidelobe reduction performance for 6 candidate multi-carrier waveforms, which are CP-OFDM, zero-padding (ZP-OFDM), weighted overlap and add (WOLA-OFDM), polynomial cancellation coded (PCC-OFDM), universal filtered multi-carrier (UFMC) and infinite impulse response (IIR-UFMC). We are initially attracted to IIR-UFMC in terms of its models computational complexity. Our results indicate that both PCC and UFMC can provide better frequency roll-off than CP/ZP-OFDM and WOLA. PCC is more easier to implement and performs strongly against ICI with cost of losing spectral efficiency and a PAPR. UFMC is more robust to very dispersive multipath channels but with cost of increasing computational complexity. Compared with FIR-UFMC, IIR-UFMC achieves less ICI cancellation performance in terms of BER, but it is still better than CP-OFDM.

The chapter is organised as follows: Section 4.1 introduces the background and motivation of this chapter. Section 4.2 specifies the system model of the 6 candidate waveforms. The filter design for UFMC and WOLA is shown in Section 4.3. The waveform sidelobe reduction performance and the simulation numerical results are shown in Section 4.4 and Section 4.5. Section 4.6 concludes the chapter.

4.1   Introduction

A mix of high and low data rates for multiple users is the main aim of the fifth generation (5G) of the wireless communications systems. A previous study [80] highlighted one of the fundamental functions for 5G will be to support for IoT, which is synonymous with MTC and exponential growth in MTC traffic is expected in the near future. One of the major challenges for future MTC is the scalability problem when many MTC systems are using the air interface.

As mentioned in Chapter 3, the current 4G wireless network is based on the OFDM waveform, which is well understood and documented in many papers, e.g. in [81]. In OFDMA, each user is allocated a subset of sub-carriers, to present the ICI, the users signal much be synchronised at the receiver's input [53]. However, there are several challenging problems for the application of OFDMA cellular systems supporting the massive MTC in the 5G uplink. First, the orthogonality is based on strict synchronisation between each sub-carriers, and as soon as the orthogonality is lost by multi-cell or multiple access transmission or through time-offsets between transmitters, interference between sub-carriers can become significant in OFDM [80]. Second, one of the significant purposes of 5G is able to support efficiently multiple traffic types. It should be able to deal both high and low volume data requirements and with synchronous or asynchronous transmissions [82]. Third, one key aspect of user-centric processing is for devices to be connected to multiple access points typically. The dynamic changes in distance between the devices and all access points require flexible synchronised processing. The tight synchronisation, as required in LTE, appears not to be cost-effective or even possible for a multi-user system in the future [83].

MTC devices will not use synchronous signal transmission. They often send only a few bytes, which makes the overhead for synchronisation is too high. Instead in the 5G systems, MTC traffic is to be removed from standard uplink traffic to minimise the signalling overhead [84]. By doing this, relaxing the synchronism requirements can significantly improve the operational

capabilities, bandwidth efficiency and even battery lifetime for the low data rate MTC devices [85]. There are several approaches to deal with asynchronous and non-orthogonal transmissions, where the reduced side-lobe levels of the waveform seek to minimise ISI and ICI.

First, the zero padding (ZP-OFDM) is designed for the highly dispersive channels, an OFDM receiver is more efficient for capturing multipath energy than an equivalent single-carrier system using the same total bandwidth [86]. ZP has been recently mentioned as an alternative to the CP in 5G transmissions [87].

Second, the 5GNOW project [80] has defined a new intermediate frame structure to support both high and low synchronisation requirements, which is called the unified frame layout. This aims to handle the very heterogeneous services and devices communicating over a 5G wireless access frame structure. In order to deal with the ISI and ICI, which are caused by the time and frequency offsets, several techniques can be used to reduce the OFDM side-lobes, e.g. filter bank multi-carrier (FBMC) [53], with a prototype filter designed for a superior frequency selectivity. FBMC systems achieve signal separation through filtering in terms of the perfect carrier synchronisation. Due to the very narrow sub-carrier filters needed in FBMC, the filter length could be very long. Therefore, 5GNOW studies an alternative version, universal filtered multi-carrier (UFMC) [80], which designs filters for each sub-band with a very narrow band. Compared with the sub-carrier filter, the sub-band filter reduces the processing cost by reducing the impulse response length.

Third, the weighted overlap and add (WOLA-OFDM) is a filtered CP-OFDM waveform proposed in [88], which is a similar process compared with UFMC. The differences is overlapping several samples together between the nearby time domain filtered signals to reduce the transmitted signal length.

Fourth, the polynomial cancellation coded (PCC-OFDM) [89] is a coding technique for OFDM in which the data to be transmitted is mapped onto weighted groups of sub-carriers. PCC-OFDM has been shown to be much less sensitive than OFDM to frequency offset and Doppler spread. However, one of the drawbacks of PCC-OFDM is the spectral efficiency is at best approximately half of that for OFDM as each data symbol is mapped to at last two sub-carriers. A previous study [90] has shown that the PAPR for PCC-OFDM is much higher than OFDM, and proposed that the symmetric cancellation coding (SCC) to reduce the PAPR compared with PCC-OFDM. However, the BER performance over a multipath fading channel of SCC

[90] is significantly poorer than PCC, especially when the carrier frequency offset (CFO) is large. Secondly, SCC does not improve the frequency roll-off in order to reduce the time offset effects, unlike PCC.

To the best of our knowledge, there is no paper providing a detail analysis and comparison on the OFDM side-lobe reduction performance between the waveforms as mentioned above and there is no previous paper implementing the IIR filter for UFMC. We summaries the main contributions of this chapter: Firstly, we provide the first study of the time offset performance for UFMC with the analogue IIR filters (IIR-UFMC). Secondly, we provide a detailed comparison between CP/ZP-OFDM, WOLA-OFDM, PCC-OFDM, UFMC and IIR-UFMC, including different filter designs, PSD, SINR, BER, overlapping effects, computational complexity and PAPR.

4.2 System Model of the Uplink Waveform

This section briefly introduces 6 candidate waveforms for the system performance comparison, including CP-OFDM, ZP-OFDM, PCC-OFDM, WOLA-OFDM, UFMC and IIR-UFMC. A multi-user uplink transmission model is shown in Figure 4.1, where each user transmits using K sub-carriers over a bandwidth with N-point FFT in the frequency domain. The total number of users is defined as U, and u is the user index. In order to simplify, we start to analyse the each single user transmission model. Moreover, in order to provide a fair comparison, we set the transmitted sample length for all candidate waveforms equal to L in the time domain.
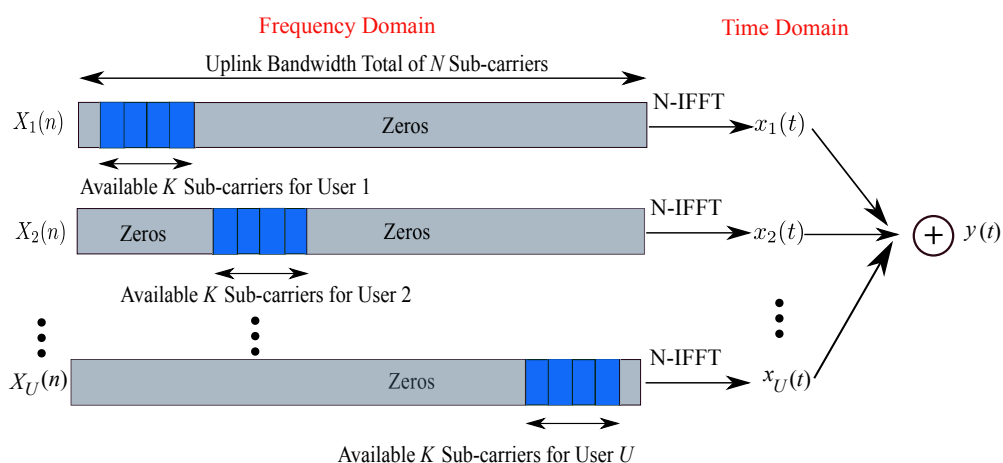
Figure 4.1: *Multi-user Uplink Transmission Model.*

4.2.1 CP-OFDM

Assume that, $X(n)$ denotes modulation symbol to be transmitted on the nth sub-carrier. The baseband CP-OFDM data signal after the N-point IFFT and adding the CP with length of L_{CP} can be expressed as:

$$x(t) = \frac{1}{\sqrt{N}} \sum_{n=0}^{N-1} X(n) \cdot e^{j2\pi nt/N}, \ t \in [0, L-1], \tag{4.1}$$

where X is the N-point FFT of x. Then the received signal over the Rayleigh multipath channel h with the length of L_{H} and AWGN noise $g(t)$ can be defined as:

$$y(t) = x(t) \otimes h(t) + g(t), \tag{4.2}$$

where $\otimes$ denotes the convolution operation and a power spectral density $N_0/2$ is assumed for the noise samples $g(t)$.

4.2.2 ZP-OFDM

ZP-OFDM uses the zero-padding to guard instead of the cyclic prefix in the time domain. It has recently been proposed as an appealing alternative to the traditional CP-OFDM to ensure symbol recovery regardless of the channel zero locations [86]. The advantage of adding a ZP is that the transmitter requires less power back-off at the analogue amplifier. In Reference [91], both CP-OFDM and ZP-OFDM are studied to delineate their relative merits in wireless systems where channel knowledge is not available at the transmitter and it is found that in terms of the power amplifier induced clipping effects, ZP introduces slightly more non-linear distortions and needs increased power back off compared with CP. Therefore, in terms of the power saving performance, this thesis considers ZP as a potential waveform design for the time and frequency synchronisations.

This chapter consider its ICI cancellation performance due to the time offsets. We set the length of ZP equals to L_{CP}. We now define the length of zeros samples is L_{ZP} and $\frac{L_{\mathrm{ZP}}}{2}$ zero samples guard in the front and end of each OFDM symbol.

4.2.3 WOLA-OFDM

The principle of WOLA-OFDM [88] is that passing the baseband time domain CP-OFDM symbol through the narrow band FIR filter is replaced by a pulse with soft edges at both sides, which results in much sharper side-lope decay in frequency domain. The soft edges at the beginning and end of the filter response effectively gives a better contained prototype filter in frequency domain. Overlap two transmitted filtered symbols to justify the transmitted symbol length as shown in Figure 4.2. Two adjacent symbols (Symbol 1 and 2) are overlapped together in the time domain. Here we define the length of the overlapped samples is L_{OL}, the processing of windows function is similar with UFMC, we will introduce it later.
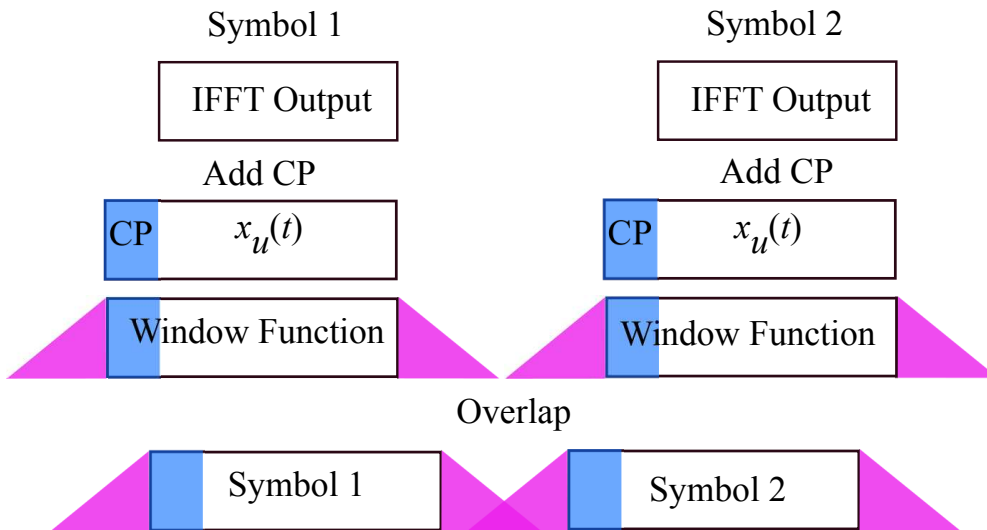
Figure 4.2: *WOLA Transmission Model.*

4.2.4 PCC-OFDM

PCC is a coding technique for OFDM in which the data to be transmitted is mapped onto weighted groups of sub-carriers. Reference [89] has shown PCC-OFDM to be much less sensitive than OFDM to frequency offset and Doppler spread. The block diagram of a PCC-OFDM system is shown in Figure 4.3 (a), the baseband low data rate signal $A_0...A_{N/2-1}$ will pass through a PCC-OFDM modulator. In this case, pairs of sub-carriers have a relative weighting of $+1, -1$, and the input IFFT signal thus can be organised as $A_0, -A_0..., A_{N/2-1}, -A_{N/2-1}$.

After the N-point IFFT, the time domain samples $a(t)$ can be expressed as:

$$a(t) = \frac{1}{\sqrt{N}} \sum_{n=0}^{N-1} A(n) \cdot e^{j2\pi nt/N}. \tag{4.3}$$

The received signal over the Rayleigh multipath fading channel is then expressed as:

$$r^{\text{PCC}}(t) = a(t) \otimes h(t) + g(t). \tag{4.4}$$

At the receiver, the data is recovered from the FFT outputs $R^{\text{PCC}}(0)...R^{\text{PCC}}(N-1)$. The mapping of data onto pairs of sub-carriers indicate that the ICI caused by one sub-carrier is substantially cancelled by the ICI caused by the other sub-carrier in the pair. Therefore, in the receiver, pairs of sub-carriers are combined by applying the weighting and then summing:

$$Y^{\text{PCC}}(n) = \frac{R^{\text{PCC}}(2n) - R^{\text{PCC}}(2n+1)}{2} (n = 0, 1, 2, ..., N/2 - 1). \tag{4.5}$$

One of the disadvantages of PCC-OFDM is the spectral efficiency is approximately half of that for OFDM as each data symbol is mapped to two carriers. For MTC, many MTC devices require only low data rate transmission. Therefore, in terms of reducing ICI effects, PCC-OFDM is another option for supporting the low data rate MTC devices in the 5G networks.

4.2.5 UFMC

The block diagram of UFMC is shown in Figure 4.3 (b). Unlike OFDM, the principle of UFMC is grouping a number of sub-carriers into a sub-band (each sub-band transmitted for each user). Here we define the bandpass filter impulse response as $b(t)$ with the length of L_{F}. Then, the time domain UFMC signal at the output of the filter can be expressed as $s(t)$:

$$s(t) = \frac{1}{\sqrt{N}} \sum_{n=0}^{N-1} X(n) e^{j2\pi nt/N} \otimes b(t),\ t \in [0, L-1], L = N + L_{\text{F}} - 1 = N + L_{\text{CP}} \tag{4.6}$$

Note that each sub-band filter is designed as a bandpass filter, and then we design each filter's centre frequency to match with each sub-band's (or user) centre frequency. The received signal will be passed though a $2N$-point FFT to convert the time domain signal into the frequency domain. Then, we retain only even sub-carriers which correspond to a data carrier [83]. UFMC does not use a cyclic prefix (but still is able to further improve on intersymbol-interference
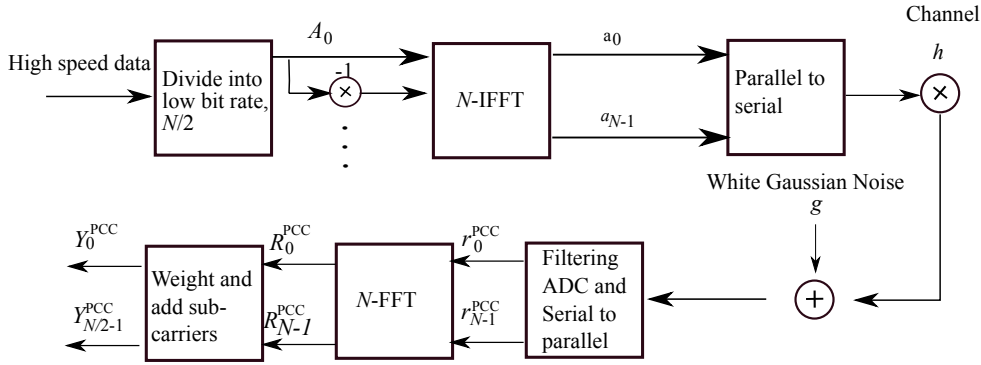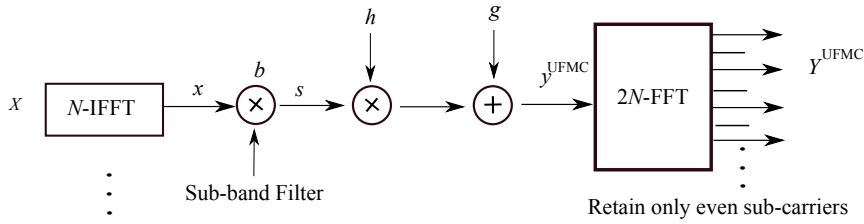
Figure 4.3: *Block Diagram of (a) PCC-OFDM and (b) UFMC.*

protection).

4.2.6 IIR-UFMC

One of the drawbacks of UFMC is increasing the computational complexity significantly by applying digital FIR filters to achieve a faster frequency roll-off than required in CP-OFDM. The computational complexity is directly related to power consumption and raises practical implementation issues [48], which do not match with the desire to achieve energy efficient 5G terminals. Thus, we propose the UFMC with the analogue prototype IIR filter banks. The IIR-UFMC processing is shown in Table 4.1.

IIR-UFMC Transmission Steps
Step 1: The baseband signal $X(n)$ passes through the N-point IFFT into the time domain
Step 2: Time domain signal passes through a narrow band IIR filter, s^{IIR}
Step 3: Truncate the length of the IIR filter output to L, $s^{\text{IIR}}(t)$, $t \in [0, L-1]$,
Step 4: Transmit through the wireless channel

Table 4.1: *IIR-UFMC Processing Steps.*
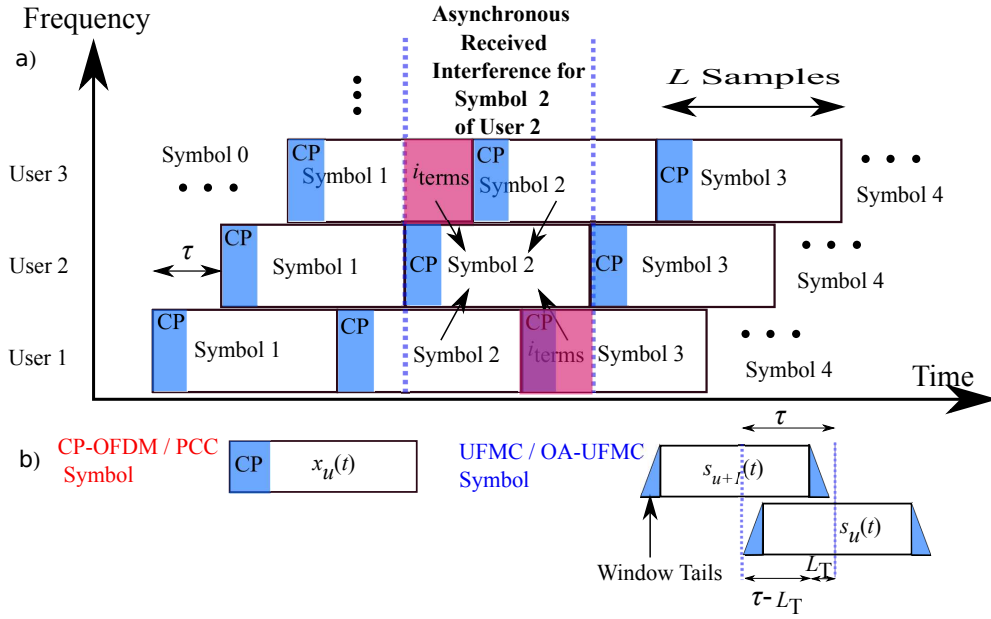
Figure 4.4: *Time Offset Model.*

4.2.7   System Model for Time offset

As mentioned above, the future 5G system for the MTC should allow to transmit with the relaxed synchronisation conditions regarding time misalignments. Therefore, we assume the received MTC signal is asynchronous and it suffers from time-offsets. The system model for time offset is shown in Figure 4.4. Previous UFMC papers are often based on long OFDM symbol transmission, where the FFT size is chosen as 1024 [26], [80] and [92]. In this chapter, we concentrate on the performance of a short OFDM symbol which is affected by a significant time offset due to asynchronous transmission of different MTC users. Here we assume the uplink bandwidth is 1.25 MHz and the sub-carrier spacing is 15 kHz, where the FFT size is 128 and it supports up to 7 users. Each user's transmission occupies 15 sub-carriers in the frequency domain, and the users are spaced by one blank sub-carrier. In this chapter, the number of transmitting users is set to $U = 3$ or $U = 5$. The scalar τ is the relative delay between two adjacent users as shown in Figure 4.4. The 2nd time OFDM symbol of user 2 is affected by four relative parts, two of them from the same time period and two of them from the adjacent time period, as shown in Figure 4.4.

4.3   Filter Design

In order to achieve a low side-lobe attenuation without significant attenuation of the carrier in the pass-band, we consider several filter designs. The ratio γ_{ro} between the number of sub-carriers per user K and the total number of available sub-carriers N can be defined as:

$$\gamma_{\mathrm{ro}} = \frac{K}{N} = \frac{15}{128} = 0.1172. \tag{4.7}$$

The normalised cut-off frequency f_{cf} should be bigger than γ_{ro}, especially for the IIR filters. Unlike FIR filters, their phase characteristic is not linear which can cause a problem to the systems which need phase linearity [93]. For this reason, we design the cut-off frequency to be wider than the sub-band bandwidth to achieve an almost linear phase in the passband. Note that each sub-band filter is designed as a band pass FIR filter in FIR-UFMC and WOLA, whose centre frequency matches with each sub-band's centre frequency. The filter impulse response after operating FFT in the frequency domain can be expressed as:

$$B(j\omega) = \int_{-\infty}^{\infty} b(t)\, e^{-j\omega t}\, \mathrm{d}t. \tag{4.8}$$

If we shift the centre frequency to ω_0, the filter impulse response for ω_0 can then be written as:

$$b(t)e^{j\omega_0 t} = \int_{-\infty}^{\infty} b(t)e^{j\omega_0 t}e^{-j\omega t}\, \mathrm{d}t = \underbrace{\int_{-\infty}^{\infty} b(t)e^{-j(\omega-\omega_0)t}\, \mathrm{d}t}_{B(j(\omega-\omega_0))}. \tag{4.9}$$

4.3.1   FIR Filter Design

Since the choice of the cost function is unlimited, many designs are possible. For the sake of simplicity, we limit our discussion to the use of the common window functions that are often used to design FIR digital filters. Previous UFMC papers focus on the Dolph-Chebyshev filter. However, as mentioned in Chapter 2, the Hamming and the Blackman windows are the other well-known approaches to reduce the side-lobe structure [94]. The Hamming window is optimised to minimise the maximum side-lobe, giving it a height of about one-fifth that of the Hann window. The Blackman window is similar to Hamming and Hann windows with resulting spectrum has a wide peak.

In this subsection, we design FIR filters using the Matlab "**fir1**" equation and consider three
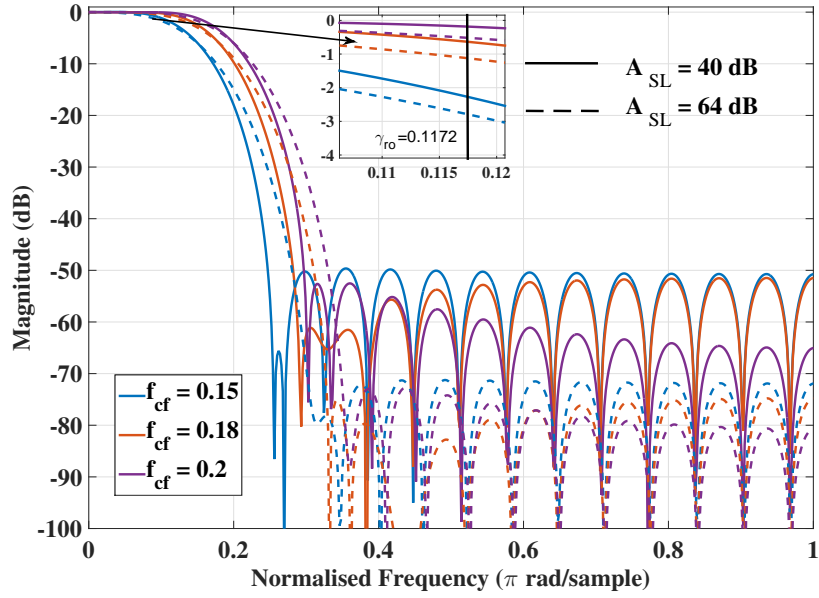
(a) FIR Dolph-Chebyshev
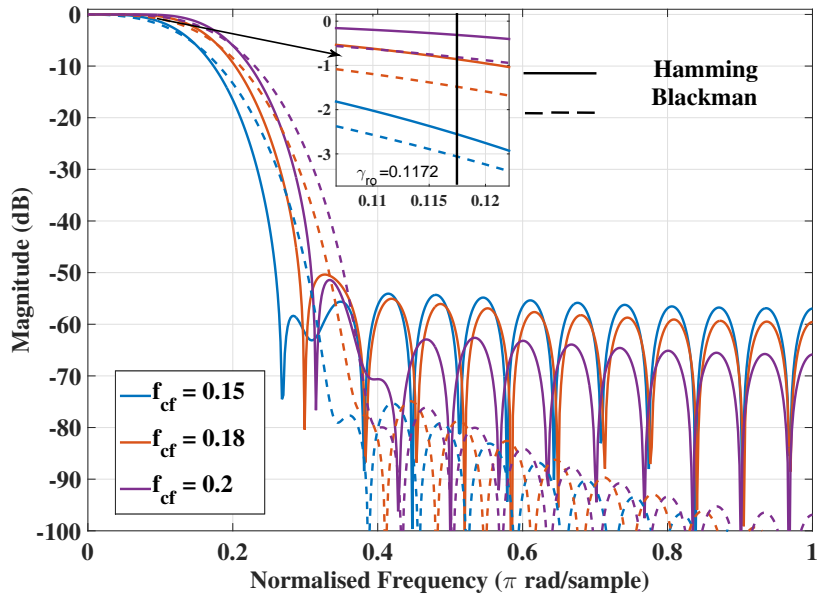
(b) Hamming and Blackman

Figure 4.5: *FIR Filter Magnitude Response.*

cut-off frequencies for the UFMC filter as $f_{cf} = 0.15, 0.18$ and 0.2, where the sub-band was normalised to $\gamma_{ro} = 0.1172$. The length of the filter is set to $L_F = 31$ samples. In order to provide a fair comparison, the length of the CP in OFDM and PCC-OFDM is set to $L_{CP} = 30$ samples to ensure they have a same transmission OFDM sample length. The side-lobe attenuation A_{SL} is chosen as 40 dB and 64 dB.

The FIR Dolph-Chebyshev filter magnitude response is shown in Figure 4.5(a). If we set the fixed $L_F = 31$, with increasing f_{cf}, the stopband attenuation reduces. Meanwhile, the stopband will move further away from the pass-band. Here we consider two conditions, an accurate passband and fast roll-off. In terms of the accurate passband, three combinations of $f_{cf} = 0.18$ with $A_{SL} = 40$ dB, $f_{cf} = 0.2$ with $A_{SL} = 40$ or 64 dB present slightly better than others. Among these three combinations, $f_{cf} = 0.18$ with $A_{SL} = 40$ dB presents the best frequency roll-off performance. Even $f_{cf} = 0.18$ with $A_{SL} = 64$ dB can achieve a much low attenuation, due to its poor frequency roll-off and poor accurate bandwidth performance, this chapter consider the Dolph-Chebyshev window with $f_{cf} = 0.18$ and $A_{SL} = 40$ dB.

The performance of FIR Hamming and Blackman filter magnitude response is shown in Figure 4.5(b). Same as above, we consider both the accurate passband and fast roll-off performance. Thus, both Blackman windows with $f_{cf} = 0.15$, $f_{cf} = 0.18$, and Hamming window with $f_{cf} = 0.15$ are not the suitable filter designs. In terms of the frequency roll-off performance, Hamming with with $f_{cf} = 0.15$ presents the best performance compared with the remaining designs. The aim of the narrow band filter is to achieve a very narrow passband at the meanwhile fast frequency roll-off and low stopband attenuation. We will then examine their side-lobe reduction performance in the next sections.

4.3.2   IIR Filter Design

This sub-section focus the Chebyshev Type I (or ChebyshevI) IIR analogue prototype filter with order of 4, 8, and 12. In terms of the smooth passband, we set the passband ripple to $A_{PB} = 0.15$ dB. According to the FIR filter design, we set the normalised cut-off frequency equals $f_{cf} = 0.18$, which is much wider than $\gamma_{ro} = 0.1172$ in terms of the almost linear phase in the passband as shown in Figure 4.6(a). It clearly shows that the non-linear phase change starts from about 0.17 of the normalised frequency bandwidth, which can obtain there is an approximate linear phase within user's bandwidth.

The performance of ChebyshevI Filter magnitude frequency response is shown in Figure 4.6(b). With increasing the filter order, the passband ripple becomes more smooth and the transmission width reduces, which achieves faster frequency roll-off. Although IIR filter with the order of 12 presents the best performance in both passband ripple and stopband attenuation. There are two reasons this chapter consider the order of 4. First, the high order filter requires high operation costs, which does not meet with the main purposes of the low costs MTC devices. Digital filters design works fairly well and has been generally accepted. When we come to the design of a IIR prototype filter, the lowest filter order should be strictly imposed [95], which can maximumly reduce the operation costs, especially for MTC. Second, in terms of the fair comparison and limit the transmitted sample length, we truncated all IIR filter output equals to only L samples. With increasing the filter order, the first truncated L samples will provide a less accurate signal representation.

4.4   Sidelobe Reduction Performance on PSD

This section simulates the power spectral distance for the different candidate waveforms likely to be used 5G communications. As mentioned above, OFDMA designed to used in the network downlink of a base station, where all of the sub-carriers are transmitted from the same base station and it can be easily synchronised and experiences the same Doppler frequency shift before reaching each receiver. However, synchronisation is not trivial in the uplink where a number of MTC devices are transmitting separately from different physical locations. In this section, the sidelobe reduction performance of different waveforms is compared.

4.4.1   OFDM Sidelobe PSD

The side-lobe behaviour performance of the OFDM system with $U = 7$ users is shown in Figure 4.7(a). Here we assume, each user has 15 sub-carriers over the 1.25 MHz channel with the FFT of 128, i.e. the 1st OFDM symbol shares sub-carriers from 9 to 23, the 2nd symbol shares sub-carriers from 25 to 39 and etc. There is one blank sub-carrier between each user. OFDM spectrum has high sidelobe levels resulted from the rectangular pulse in time domain. This causes ICI and performance degradation, and the orthogonality between sub-carriers collapses. The OFDM wide side-lobe significantly affects sub-carriers nearby, especially for the adjacent users, e.g. the 4th user interferes to the 3nd and 5th users. Its side-
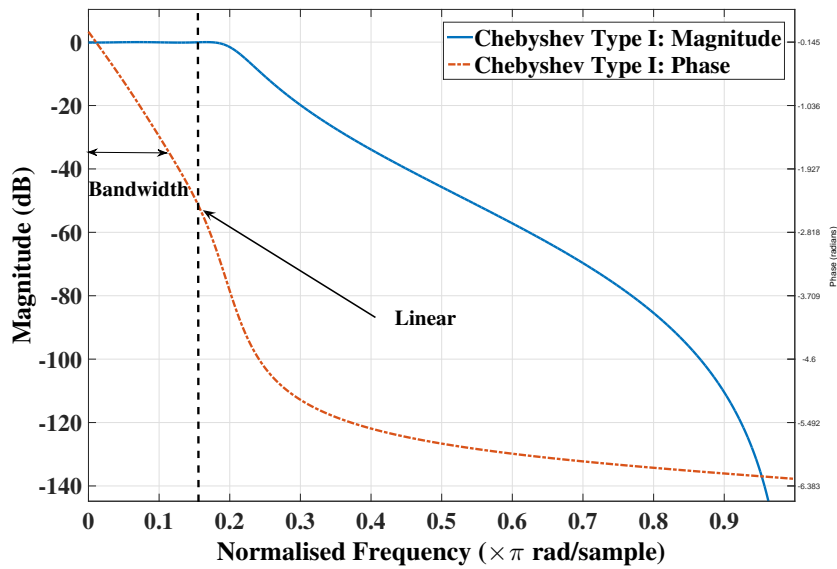
(a) IIR Magnitude Response and Phase Response.
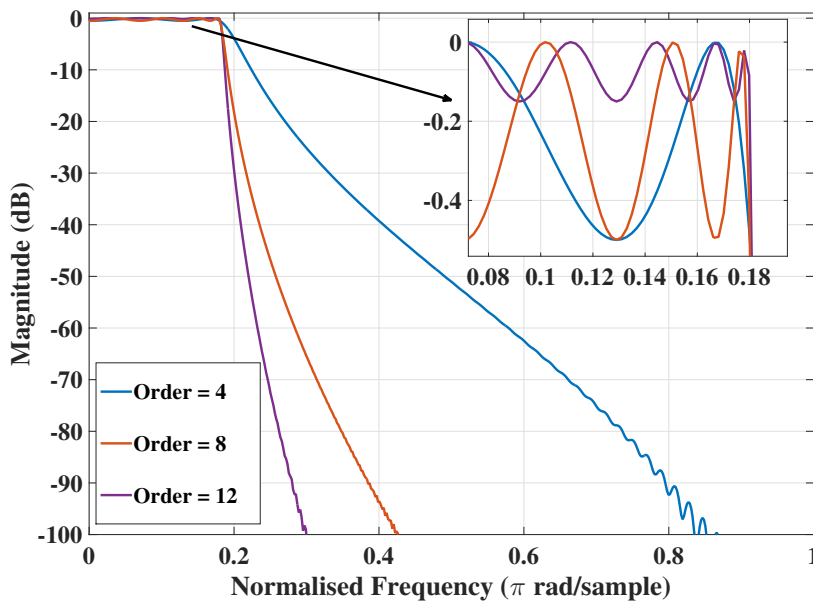
(b) IIR ChebyshevI Filter Magnitude Response.

Figure 4.6: *Chebyshev Type I Magnitude Response.*

lobe attenuation in the roll-off region crosses from -11 dB to -25 dB for the 3nd and 5th users, which are placed at the adjacent sub-bands. Moreover, its side-lobe attenuation for the 2nd and 6th user bands continuously reduces from 25 dB to 30 dB, which still can cause significant interference.

4.4.2   Sidelobe Reduction of the Candidate Waveforms

The PSD performance of CP-OFDM, ZP-OFDM, UFMC and PCC-OFDM for the 4th user is shown in Figure 4.7(b). First, compared with CP-OFDM, there is only little difference for adding zero samples in the time domain. Thus, in the next sections, we will not consider further the ZP-OFDM as an candidate waveform due to its poor sidelobe behaviour. Second, both UFMC and PCC-OFDM can reduce the side-lobe level significantly compared with CP-OFDM. Moreover, PCC-OFDM provides a better ICI protection due to its very rapid side-lobe roll-off. Considering the roll-off width, sub-carriers from 50 to 55 or 73 to 78, PCC significantly reduces the side-lobe attenuation from -30 dB to -50 dB, UFMC reduces the side-lobe attenuation from -17 dB to -30 dB and slightly than OFDM, which is -14 dB to 20 dB in this band. However, considering the end of the roll-off region, the side-lobe attenuation of UFMC downs to -50 dB at the 46th or 81th sub-carrier, which is much superior to OFDM in this case. We thus conclude that even UFMC cannot provide a similar fast frequency roll-off performance with PCC, it is still significantly fast than OFDM, especially at the band-edge.

The PSD performance of different windows is shown in Figure 4.8(a). Here we compare the Dolph-Chebyshev window with $A_{\mathrm{SL}} = 40$ dB and $A_{\mathrm{SL}} = 64$ dB, the Hamming and Blackman windows, and the WOLA-OFDM. First, in terms of the Dolph-Chebyshev window, the side-lobe reduction performance of 40 dB is superior to 64 dB, same as our previous FIR filter magnitude response results as in Figure 4.5(a), i.e. the 49th sub-carrier, the side-lobe attenuation has reduced about 3 dB. Second, the Hamming window achieves a similar side-lobe reduction performance with the Dolph-Chebyshev window of $A_{\mathrm{SL}} = 40$ dB, both of them provide fast frequency roll-off performance and they are slightly better than $A_{\mathrm{SL}} = 64$ dB or the Blackman window. In the next simulations, this chapter will focus on the Hamming filter. Moreover, compared with UFMC, WOLA-OFDM presents inferior performance on the side-lobe reduction, especially in the adjacent bands. Thus, we can conclude that the WOLA-OFDM should not be considered for supporting the massive MTC devices in the 5G with the poor time synchronisation.

The PSD performance of UFMC with the analogue prototypes IIR filter is shown in Figure 4.8(b). In terms of the fair comparison, we truncate all IIR filter outputs equal to L. The normalised cut-off frequency is set to $f_{\mathrm{cf}} = 0.18$ as before. We assume the available sub-carriers for transmission is from 57 to 71, which is exact 15 sub-carriers and $\gamma_{\mathrm{ro}} = 0.1172$. Figure 4.8(b) clearly shows that IIR filters with order of 8 and 12 provide slightly superior frequency roll-off performance at the centre of adjacent sub-carriers, i.e. from sub-carrier 48 to 57, compared with the FIR and IIR filter with order of 4. However, with increasing the filter order, the truncated L samples will provide a less accurate signal representation, i.e. sub-carriers locate at 1 to 48. Moreover, as mentioned in Chapter 3, with increasing the filter order, the operation cost increases too. Therefore, this chapter will consider the ChebyshevI IIR filter with order of 4 in the next simulations.
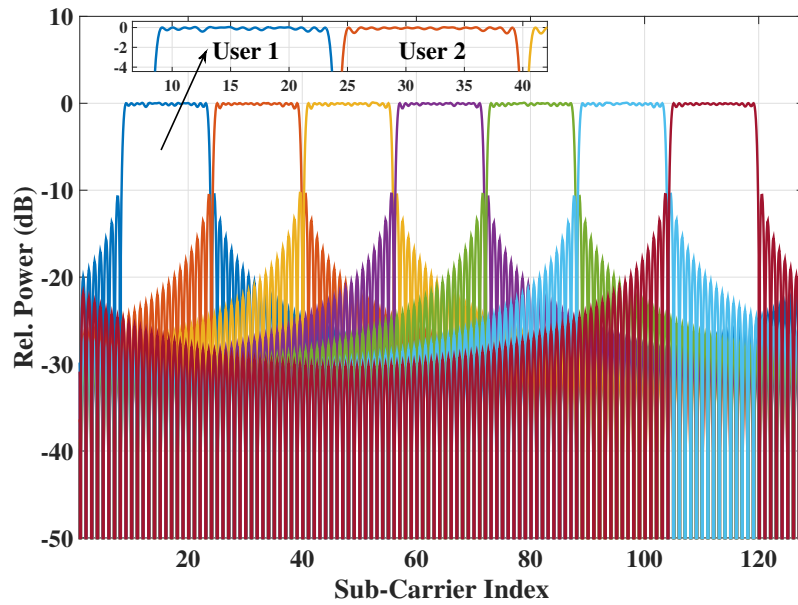
(a) Superimposed Spectrum of 7 Different OFDM Resource Blocks
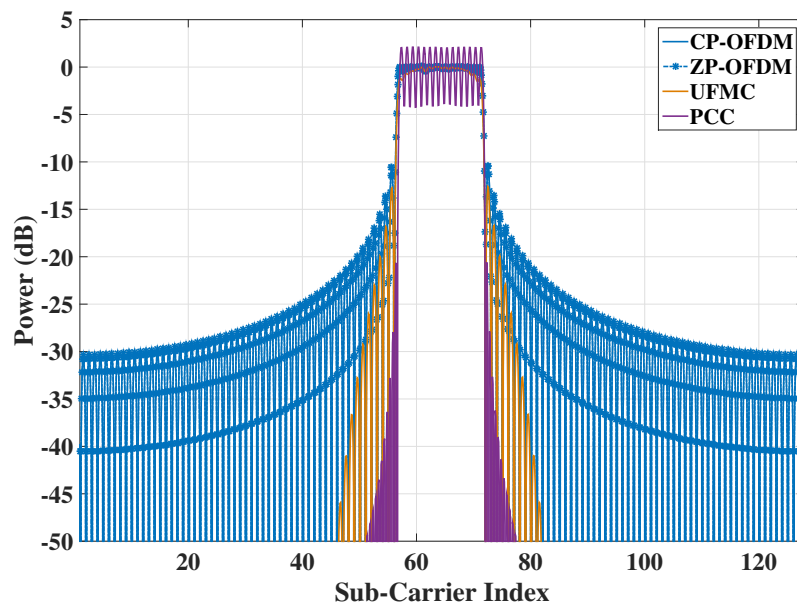
(b) PSD of CP/ZP-OFDM, FIR-UFMC, and PCC-OFDM

Figure 4.7: *OFDM Resource Blocks with 15 Sub-carriers Each, Carrying Random QPSK Data Symbols.*
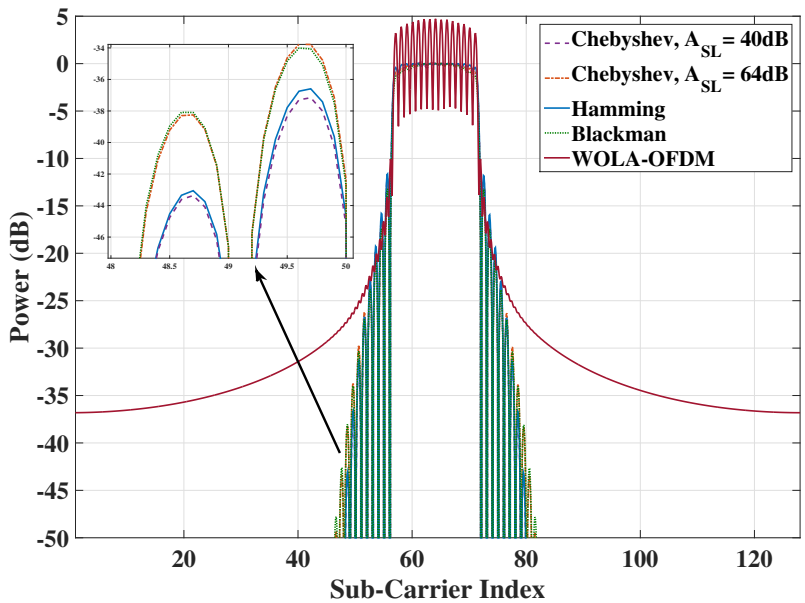
(a) PSD of FIR-UFMC with Different Filters and WOLA-OFDM
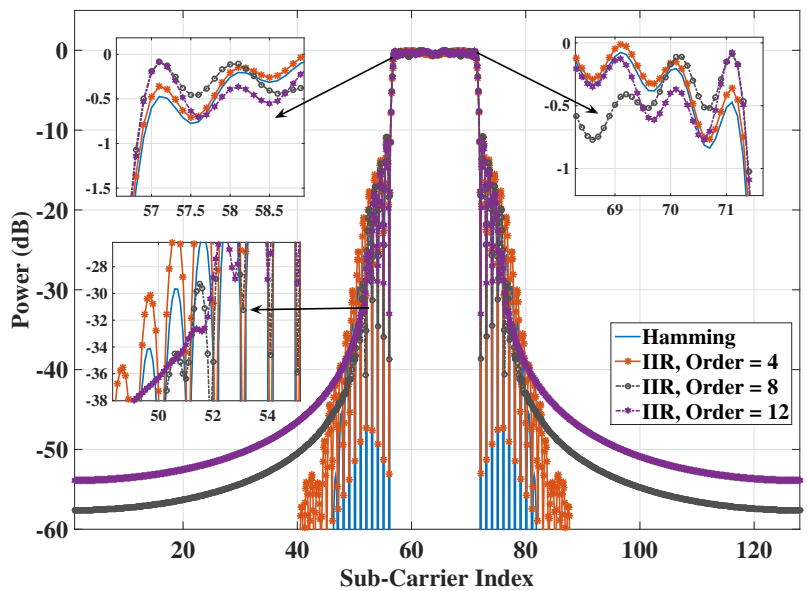
(b) PSD of IIR-UFMC, Truncated the Output to L

Figure 4.8: *Side-lobe Reduction Performance on PSD, $N = 128$, $L_{\text{F}} = 31$, $L_{\text{CP}} = 30$.*

4.5 Numerical Results

As we discussed in Section 4.4, firstly, ZP-OFDM has the similar sidelobe behaviour compared with CP-OFDM. Secondly, WOLA-OFDM is the inferior performance on the side-lobe reduction, moreover, it has the same high computational complexity operations compared with UFMC. Thus, both ZP and WOLA-OFDM waveforms are not been further considered in this chapter. Both UFMC and PCC-OFDM systems have a superior side-lobe reduction performance, which protects against the ICI caused by the multi-user time offsets. In this section, we thus consider OFDM, UFMC and PCC-OFDM as the candidate waveforms for the 5G asynchronous channel.

In terms of the fair comparison, L_F is set to 31 samples and L_{CP} is set to 30 samples to ensure they have a same transmission length. The transmitted signal power E_b for OFDM, UFMC and PCC-OFDM are the same. For the OFDM and UFMC systems, BPSK and QPSK will be used. Because the spectral efficiency of PCC-OFDM is half of the OFDM system, the corresponding constellation schemes for PCC-OFDM are chosen as QPSK or 16-QAM. The total number of MTC users is set to 3 or 5. As in Section 4.3, the sub-carrier ratio $\gamma_{ro} = 0.1172$, the normalised cut-off frequencies f_{cf} is set to 0.18 and the side-lobe attenuation A_{SL} is set to 40 dB in the next simulations.

4.5.1 SINR Performance of the Time-offset Model

The SINR performance over the AWGN channel with a SNR of 15 dB is shown in Figure 4.9. Same as before, the 1st user transmits sub-carriers 9 to 23, the 2nd user is 25 to 30 and the 3nd user is 41 to 55. First, when the time offset τ is 10 samples, there is no significant SINR degradation for both the UFMC and PCC-OFDM systems. For the OFDM system, the SINR of user 1 is almost the same as the transmitted SNR. However, the SINR initial front sub-carriers of the 2nd user and the 3nd user are significantly reduced by ICI. Second, now we let the time offsets τ is larger than L_{CP}, i.e. $\tau = 40$ samples, there is a significant SINR degradation for both the OFDM and UFMC systems, especially for the sub-carriers located at the adjacent bands. Moreover, compared with OFDM, UFMC slightly improves the SINR performance (about 2 dB higher SINR) but still inferior to PCC. Third when we set $\tau = 70$ samples, there is no significant difference among OFDM, UFMC and PCC-OFDM compared with the case of $\tau = 40$ samples. PCC-OFDM still provides the highest SINR performance for sub-carriers
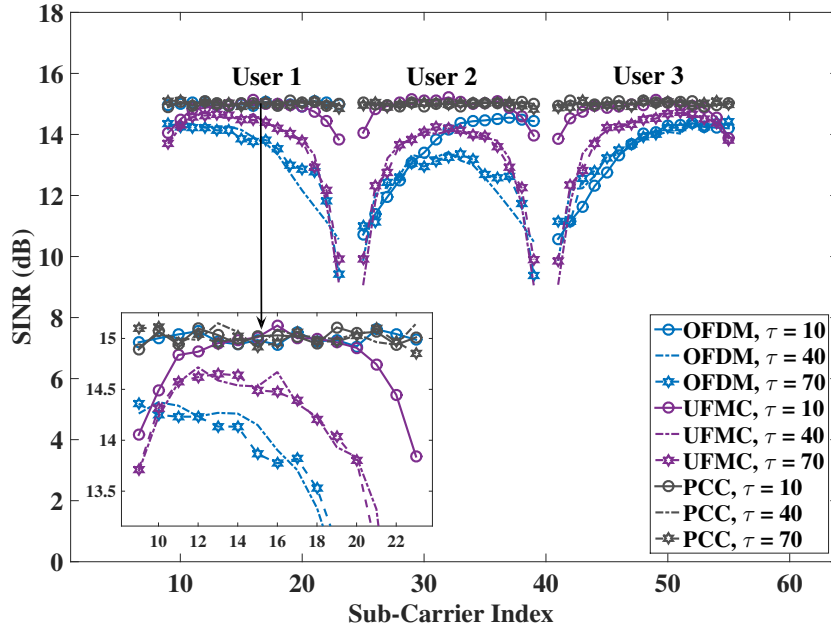
Figure 4.9: *SINR Performance with AWGN (SNR = 15 dB), UFMC with Hamming Filter.*

located in both the middle transmission band and the adjacent bands. The nearby sub-carriers of both OFDM and UFMC are significantly affected by ICI. We thus can conclude that in terms of the SINR performance, PCC provides the best ICI cancellation performance, UFMC is inferior but still slightly superior to OFDM. In order to measure a significant poor time offset scenario, in the the next simulations, we will consider $\tau = 70$ samples time offsets.

The SINR performance of the UFMC Chebyshev window with different filter settings over the $\tau = 70$ samples time offset is shown in Figure 4.10. Here we compare 6 combinations same as before, which are $f_{cf} = 0.15,\ 0.18$ and 0.2, and among $A_{SL} = 40$ or 60 dB. Same as our FIR frequency response results was shown in Figure 4.5(a), when we set the normalised cut-off frequency to $f_{cf} = 0.15$, even the SINR performance at the middle range of the user's transmission bands is slightly higher than other combinations, the signal energy at the filter's band edge will be significantly attenuated due to the very narrow pass-band. Both the combinations of $f_{cf} = 0.18\ \&\ A_{SL} = 40$ dB and $f_{cf} = 0.2\ \&\ A_{SL} = 64$ dB present slightly superior SINR performance compared with others. Moreover, considering the passband SINR performance, $f_{cf} = 0.18\ \&\ A_{SL} = 40$ dB is slightly better than $f_{cf} = 0.2\ \&\ A_{SL} = 64$ dB. This result is same as before, we thus can conclude that for the FIR Dolph-Chebyshev window designs, the

88
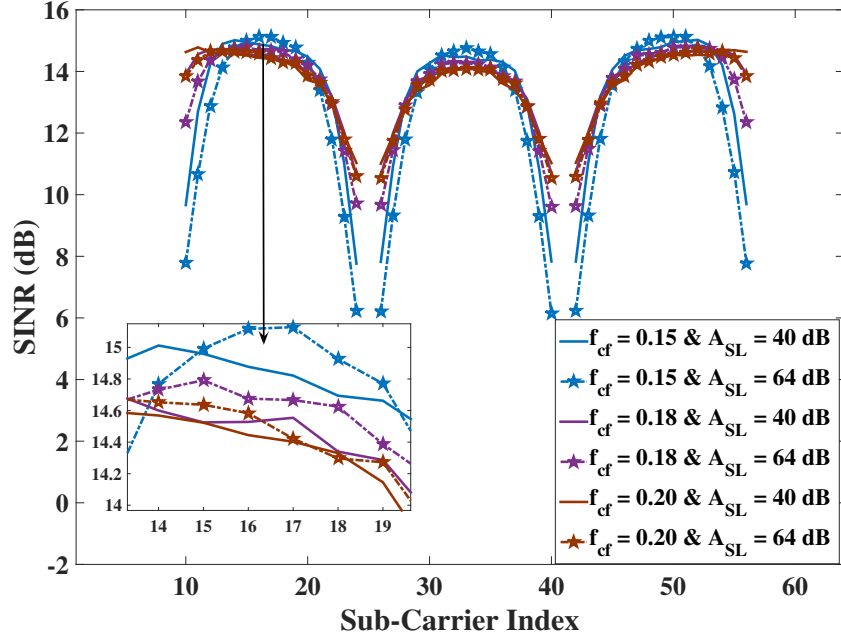
Figure 4.10: *Filter's Cut-off Frequency Effects: AWGN 15 dB, Chebyshev, $\tau = 70$.*

combination of $f_{cf} = 0.18$ & $A_{SL} = 40$ dB provides the best performance in terms of high SINR in the passband and small SINR degradation in the band-edge.

Now, in terms of saving the transmission cost, we reduce the transmitted signal length by overlapping L_{ol} samples from the adjacent two UFMC symbols. The SINR degradation performance for overlapping the nearby two transmitted UFMC symbols over a 20 taps Rayleigh multipath channel is shown in Figure 4.11. Where the overlap factor is computed as the number of overlapped samples L_{ol} divided by the number of baseband sub-carrier length N as below:

$$\alpha_{ol} = \frac{L_{ol}}{N}. \tag{4.10}$$

Here we measure 4 cases, which are $\tau = 0, 20, 50$ or 70 samples time offset. In terms of $\tau = 0$, the SINR significantly degrades from $\alpha_{ol} = 0.4$. For $\tau = 20$, the SINR smoothly reduces between $\alpha_{ol} = 0.1$ and $\alpha_{ol} = 0.5$ and significantly degrades after $\alpha_{ol} > 0.5$. For the case of $\tau = 50$ or 70 samples time offset, between $0 < \alpha_{ol} < 0.4$ the SINR reduces from 30 dB to 21 dB and then significantly reduces when $\alpha_{ol} > 0.5$. From Figure 4.10, we thus conclude that the overlapping technique can be generally used in MTC and through adjusting the overlap factor α_{ol} to satisfy the decoding requirements.
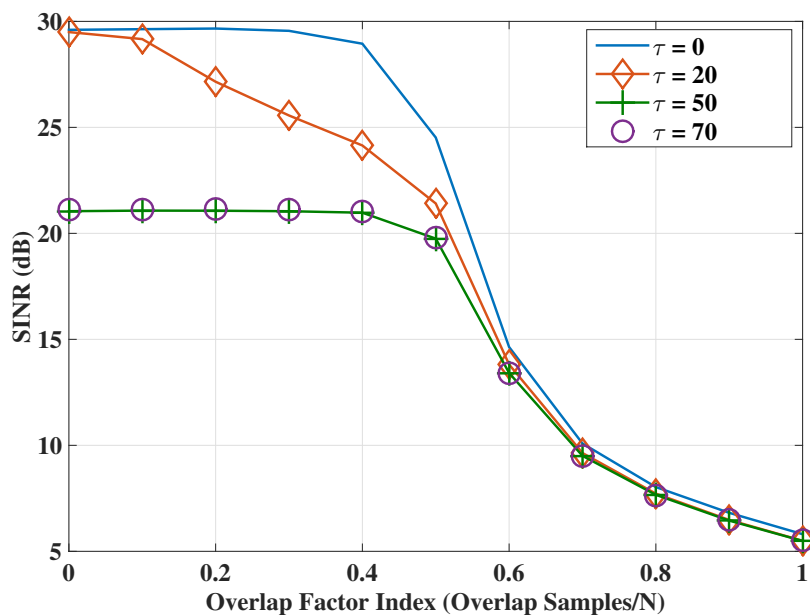
Figure 4.11: *SINR Performance for Overlapping (SINR for the centre sub-carrier of the second user), AWGN = 30 dB, Rayleigh $L_H = 20$, $L_F = 31$.*

4.5.2 BER Performance of OFDM, UFMC and PCC-OFDM

The BER performance for the AWGN channel is shown in Figure 4.12. The results are plotted for E_b/N_0 and every multiple access scheme has the same transmitted signal power. Again L_{CP} is set to 30 samples, L_F is set to 31 samples, and τ is 70 samples. The Hamming filter with $f_{cf} = 0.18$ is used for UFMC. The results are similar with the SINR curves, for low data rate requirements, QPSK PCC-OFDM presents the best performance in terms of BER. When the BER is 10^{-3}, PCC-OFDM saves about 0.7 dB E_b/N_0 compared with UFMC and is about 1.5 dB better than OFDM. However, it will incur the poorest E_b/N_0 efficiency when increasing the data rate via the use of 16-QAM modulation as compared to QPSK for OFDM and UFMC. Compared with FIR-UFMC, IIR-UFMC presents less ICI cancellation performance, it increases 0.3 dB E_b/N_0 when the BER is 10^{-3}, however, it still better than CP-OFDM.

Now, we assume the number of the overall transmitted users is $U = 5$ as shown in Figure 4.13. For UFMC and OFDM, the ICI of the 1st user and the 5th user is slightly small than the 3nd user. This closely matches with our SINR results, where the sub-carriers allocated at the middle of the frequency band will be significantly interfered by adjacent users. As the number of interfering users increases, the ICI will also be increased. However, for PCC-OFDM, there
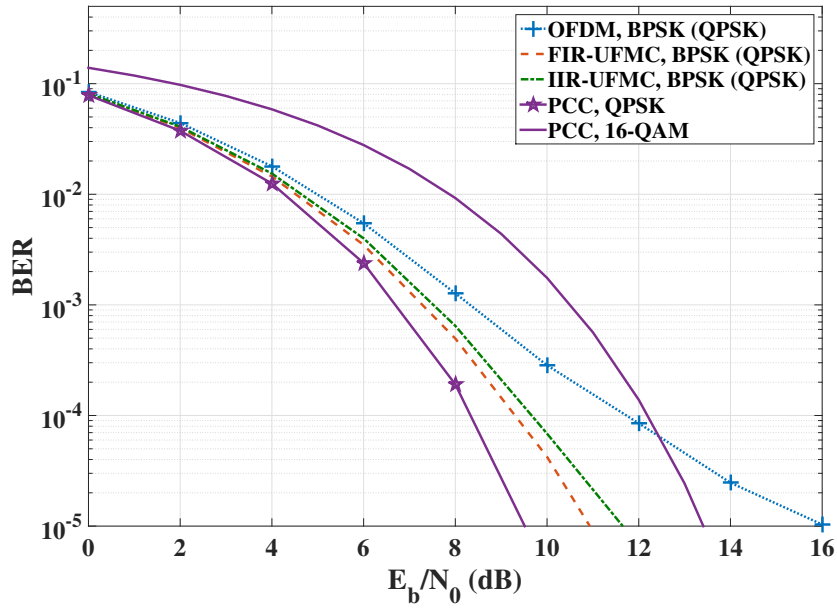
Figure 4.12: *BER: AWGN, $\tau = 70$, Hamming $f_{\text{cf}} = 0.18$, $L_{\text{CP}} = 30$, $L_{\text{F}} = 31$, $U = 3$, Spectral Efficiency = 1 or 2 bit/s/Hz.*
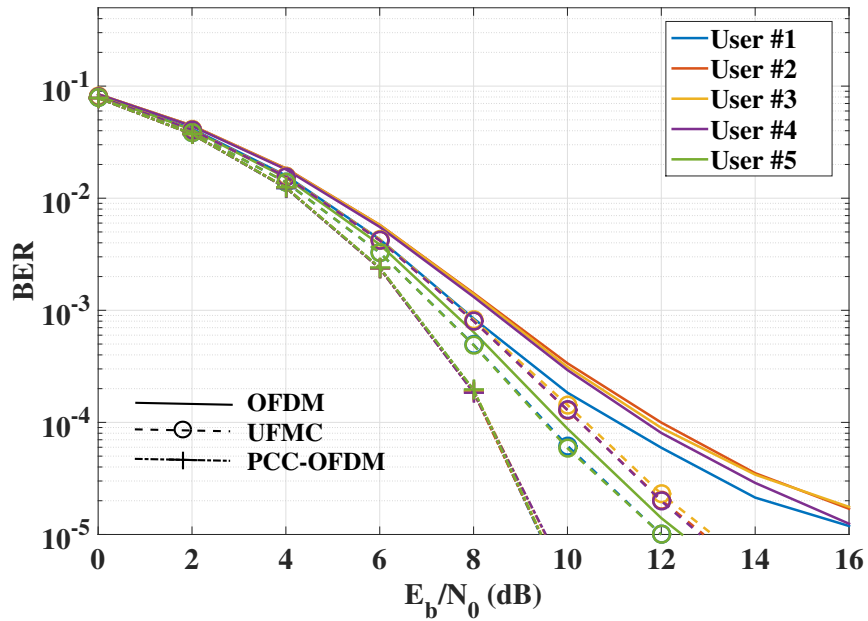
Figure 4.13: *BER: AWGN, $\tau = 70$, Hamming $f_{\text{cf}} = 0.18$, $L_{\text{CP}} = 30$, $L_{\text{F}} = 31$, $U = 5$, Spectral Efficiency = 2 bit/s/Hz.*
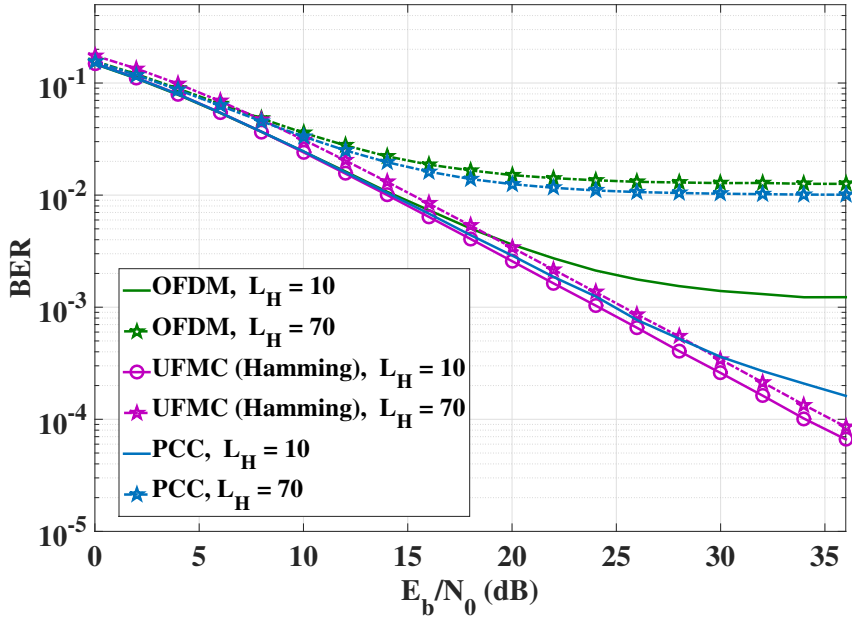
Figure 4.14: *BER: Rayleigh Multipath Channel Length= 10, 70, $\tau = 10$, Hamming $f_{cf} = 0.18$, $L_{CP} = 47$, $L_F = 48$, Spectral Efficiency = 2 bit/s/Hz.*

is still no significant BER degradation even we increase the number of interfering users. In terms of the 3nd user BER performance, PCC-OFDM saves about 2dB E_b/N_0 compared with UFMC and saves about 1.7 dB E_b/N_0 compared with CP-OFDM at the BER of 10^{-4}.

The BER performance for $\tau = 10$ samples over the Rayleigh multipath channel is shown in Figure 4.14, where L_{CP} is 47 samples and L_F is 48 samples. The channel tap lengths are set to 10 and 70 samples and the modulation scheme for OFDM and UFMC is BPSK while for PCC-OFDM it is QPSK. The Hamming filter is used for the UFMC system with f_{cf} normalised to 0.18. When the number of channel taps is smaller than L_F and L_{CP}, both UFMC and PCC-OFDM can present better BER performance than OFDM. When the number of channel taps is 70 (much longer than L_{CP}), UFMC presents the best performance in terms of BER.

The BER performance for $\tau = 70$ samples over the Rayleigh multipath channel is shown in Figure 4.15. It clearly shows that when the number of taps is smaller than L_{CP} or L_F, PCC-OFDM presents the best performance in terms of BER. When the number of taps is longer than L_{CP}, PCC-OFDM is no longer robust to the ISI effect. UFMC presents a slightly better BER performance when the number of channel taps is 70. Compared with UFMC, PCC-OFDM is
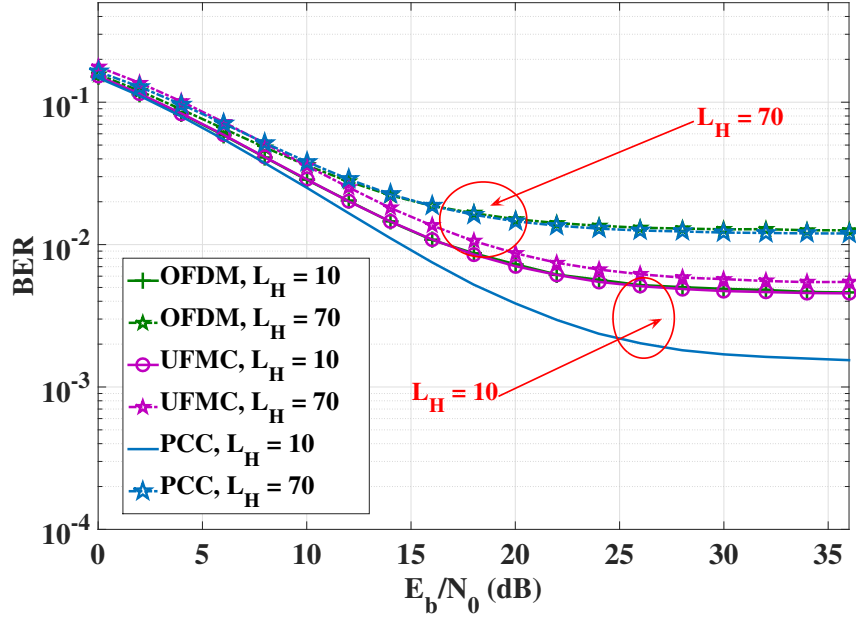
Figure 4.15: *BER: Rayleigh Multipath Channel Length= 10, 70, $\tau = 70$, Hamming $f_{\mathrm{cf}} = 0.18$, $L_{\mathrm{CP}} = 47$, $L_{\mathrm{F}} = 48$, Spectral Efficiency = 2 bit/s/Hz.*

more sensitive to the multipath channel effects.

According to Figure 4.14 and Figure 4.15, we thus conclude that PCC-OFDM provides the best performance to reduce the interference affected by large time-offsets (or very poor time synchronisation scenario) but it suffered by the large number of multipath channel propagation delay. In terms of the UFMC, even it has slightly less performance of time offsets compared with PCC, but it still much better than OFDM. Moreover, UFMC is more robust to very dispersive multipath channels compared with the PCC-OFDM and CP-OFDM.

4.5.3 Computational Complexity and PAPR

Waveform	Transmitter Complexity (Ops.)	Receiver Complexity (Ops.)
CP-OFDM	448	448
PCC-OFDM	448	448
UFMC/WOLA-OFDM, $L_{\mathrm{F}} = 31$	4416	1024
UFMC/WOLA-OFDM, $L_{\mathrm{F}} = 48$	6592	1024

Table 4.2: *Computational Complexity Comparisons, N=128.*
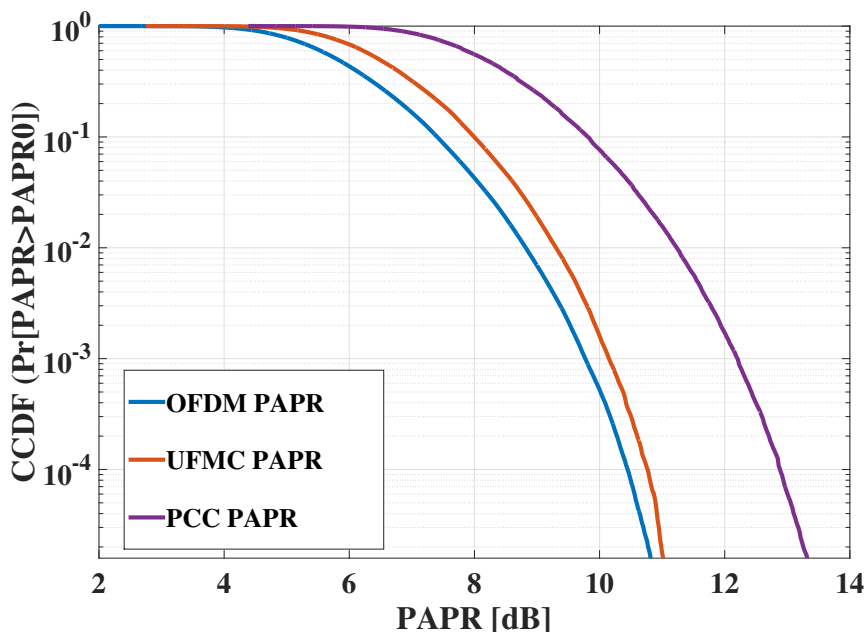
Figure 4.16: *The PAPR Performance, $N = 128$, $f_{\mathrm{cf}} = 0.18$, $L_{\mathrm{F}} = 31$.*

The computational complexity performance is shown in Table 4.2. It clearly shows that the transmitter IFFT computational complexity of UFMC (for transmission the main cost is the filter convolution operations and for the receiver it is the $2N$ point FFT) is significantly higher than OFDM and PCC-OFDM (3968 operations more than OFDM and PCC-OFDM). When the filter length is increased, the IFFT computational complexity will be increased significantly.

The PAPR performance is shown in Figure 4.16. Both UFMC and PCC-OFDM increase the PAPR compared with OFDM. The PAPR of PCC-OFDM is about 2.1 dB higher than OFDM and 1.7 dB higher than UFMC at a complementary cumulative distribution function (CCDF) value of 10^{-2}. The results is similar with [90], the reason could be that the complementary cumulative distribution function of PAPR is derived for PCC with Gaussian approximation and is shown to have a prolonged tail. Its characteristic as a matched windowing scheme as shown in Figure 4.7(b). Thus, for PCC-OFDM, the sidelobe reduction comes at the cost of a slightly higher PAPR. This will require a higher power amplifier for the same signal coverage, assuming that the PAPR leads an increased amplifier back-off.

4.6   Conclusion

In this chapter, a detailed waveform side-lobe reduction performance comparison between CP/ZP-OFDM, WOLA-OFDM, PCC-OFDM, UFMC and IIR-UFMC was presented. This chapter concentrated on the practical analysis of the time offset estimation in the 5G uplink system. Our results shown that: first, compared with CP-OFDM, there is no significant side-lobe reduction on ZP-OFDM in terms of PSD. Second, WOLA-OFDM presented the same computational complexity performance but with inferior side-lobe reduction performance. Third, PCC is easier to implement and can strongly mitigate against ICI at the cost of halving the spectral efficiency and incurring higher PAPR. In the AWGN channel with a BER of 10^{-3} and a time offset of 70 samples, the E_b/N_0 of PCC-OFDM was about 0.7 dB better than UFMC and 1.5 dB better than OFDM. Fourth, UFMC slightly improved the performance in very dispersive multipath channel scenarios. However, it significantly increased the computational complexity due to the transmit filter banks and the $2N$ point FFT that is required at the receiver. Fifth, compared with FIR, IIR-UFMC presented the slightly superior performance in terms of BER and removes the need for the convolution operation (lower operating cost than FIR), but still is much better than OFDM.

Thus, we can conclude that both ZP-OFDM and WOLA might not be a successful waveform design for 5G. Both UFMC and PCC-OFDM achieve better frequency roll-off than OFDM in terms of supporting low data rate asynchronous 5G MTC. Compared with PCC, UFMC slightly improves the performance in very dispersive multipath channel scenarios with higher computational complexity. PCC can be used when channel conditions are good and the data requirement is low. UFMC can be used more widely in supporting 5G MTC.

In Chapter 5, we will mathematically analyse the interference caused by the integer time offset and derive the closed-form expressions for the SINR, the Shannon capacity and the BER based on the waveforms we analysed in Chapter 4. We will also propose the overlap and add UFMC (OA-UFMC) system which reduces the computational complexity of the IFFT.

Chapter 5

Interference and Complexity Analysis for the Time Offset In 5G Uplink

In Chapter 3, We concentrated on the VC receiver system to reduce the maximum bandwidth in the downlink. In Chapter 4, we compared different candidate waveforms to reduce the OFDM side-lobe levels in terms of relaxing the synchronism requirements. A key result in Chapter 4 has shown that UFMC presented a better performance in terms of ICI and ISI with the cost of significantly increasing the computational complexity. In this chapter, we extend the study to significantly reduce the operation complexity for UFMC and mathematically analyse the interference, which is caused by the integer time offsets.

This chapter provides a closed form expression for the interference arising in such a case for both OFDM, PCC-OFDM, UFMC and IIR-UFMC. We also derive theoretical analysis for the SINR, capacity and BER. In order to reduce the complexity, this chapter proposes the overlap and add UFMC (OA-UFMC) system. Our results show that both OA-UFMC and IIR-UFMC reduce the complexity significantly compared with conventional UFMC and meanwhile, OA-UFMC provides a similar waveforms. For IIR-UFMC, it achieves a similar performance in terms of SINR, the Shannon capacity and BER, especially when there is a large time offset.

The chapter is organised as follows. Section 5.1 introduces the motivation and contribution of the chapter. Section 5.2 specifies the system models and proposes the OA-UFMC system. Section 5.3 analyses the computational complexity. The closed form expression for ICI, ISI, SINR and BER in an integer time offset system is analysed in Section 5.4. Section 5.5 shows the numerical results, and Section 5.6 concludes the chapter.

5.1 Introduction

As mentioned in Chapter 4, each sub-carrier in an OFDM system is shaped using a rectangular window in time domain and leading to sinc-shaped sub-carriers in frequency domain.

Consequently, the large side-lobes occur the ICI of the adjacent sub-carriers in the legacy systems. OFDM suffers from high out-of-band radiation caused by side-lobes of the modulated sub-carriers [96]. In 4G LTE, the time and frequency synchronisation and control signalling are linked to the cell [83] for supporting the OFDM systems, which are sensitive to the time/frequency errors [97].

Chapter 4 showed that PCC-OFDM presented the best ICI cancellation performance due to its very rapid sidelobe roll-off in the frequency at the cost of the halving spectral efficiency and high PAPR. UFMC improved the performance in both large time-offset and very dispersive multipath channel scenarios. However, UFMC increased the computational complexity significantly due to the transmit filter banks and the $2N$ point FFT that is required at the receiver. Considering the main drawback of high complexity for UFMC, this chapter now extends the study to reduce its computational complexity and then analyse the ICI caused by time offsets.

There are few newest papers on UFMC: in Reference [98], a timing-offset-tolerant UFMC passive optical network (PON) was experimentally verified as a proof-of-concept for asynchronous multi-services over fiber. They concluded that the effective bit rate of UFMC were improved about 30% and UFMC could be a promising solution for multi-services transmission in the most asynchronous cases.

In Reference [99], a fairly comparison between the UFMC, FBMC, and legacy LTE waveforms was presented and a bit loading algorithm is proposed to cope with the non-uniform distribution of the interference across the carriers in order to increase the spectral efficiency.

In Reference [100], several approaches for the space-time coding for UFMC was presented, such as the space time block codes (STBC), which was widely used in the multiple-input multiple-output (MIMO) system. And other recent published references studied on the comparison between UFMC and FBMC as shown in [101], [102] and [103].

As above recent studies on the UFMC systems, to the best of our knowledge, there is no study on reducing the computational complexity for the UFMC and for closed-form expressions for ICI and ISI in the UFMC time offset system.

We now summarise the main contributions of this chapter. First, we propose the overlap and add UFMC (OA-UFMC) system which reduces the computational complexity of the IFFT, especially for a longer filter impulse response. Second, we derive closed-form expressions for

the different types of interference caused by the integer time offset. Our closed-form expressions can be easily derived for the SINR, the Shannon capacity and the BER. It can be used in both simple and complex time-offset transmission scenarios. Third, we provide a detailed comparison and analysis including SINR, capacity, BER, and computational complexity. We also measure the time offset performance when varying the number of zero sub-carriers between the adjacent users. Fourth, we propose and analyse for the first time on the ICI cancellation performance for IIR-UFMC in both the analytical and simulation results.

5.2 System Model of OA-UFMC

In this chapter, we start with a simple uplink system. There are U users, which are allocated to different frequency carriers and transmit simultaneously to a BS. There are a total of N sub-carriers, which are divided among the U users (or sub-bands). Each user has a total of K available sub-carriers. Here we define L_{CP} as the length of CP in samples. Then the BS will sum all the received signals and process it to decode the message for all U users.

5.2.1 State of the Art

Assume that $X_u(n)$ denotes that modulation symbol to be transmitted on the nth sub-carrier by the uth user. The baseband OFDM data signal at the output of the N-point IFFT and after adding the CP can be expressed as:

$$x_u(t) = \frac{1}{\sqrt{N}} \sum_{n=0}^{N-1} X_u(n) \cdot e^{j2\pi nt/N}, \ t \in [0, L-1], L = N + L_{\mathrm{CP}} \tag{5.1}$$

where X is the FFT of x. In order to simplify our analysis, we assume the length of channel taps for each user is same as L_{H}. Then the received signal over the multipath channel h (each channel tap l_{H} follows the quasi-static Rayleigh distribution) and the AWGN $g(t)$ can be defined as:

$$y(t) = \sum_{u=1}^{U} x_u(t) \otimes h_u(t) + g(t), \tag{5.2}$$

where $\otimes$ denotes the convolution operation and a power spectral density $\sigma = N_0/2$ is assumed for the noise samples $g(t)$.

Unlike OFDM, the principle of UFMC is the grouping a number of sub-carriers into a sub-band
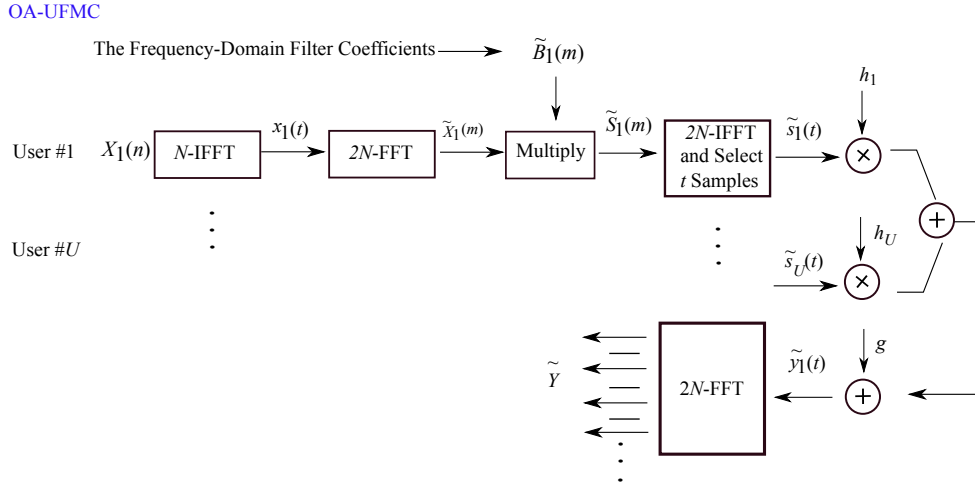
Figure 5.1: *Block Diagram of the OA-UFMC System.*

(each sub-band transmitted for each user). Here we define the bandpass filter impulse response as $b_u(t)$ with the length of L_F. Then, the time domain UFMC signal for the uth user at the output of the filter can be expressed as $s_u(t)$:

$$s_u(t) = \frac{1}{\sqrt{N}} \sum_{n=0}^{N-1} X_u(n)e^{j2\pi nt/N} \otimes b_u(t),\ t \in [0, L-1], L = N + L_F - 1 = N + L_{CP} \quad (5.3)$$

5.2.2 Overlap and Add UFMC (OA-UFMC) Model

As mentioned in Chapter 4, one of the major drawbacks of UFMC is that the computational complexity is significantly increased by applying digital FIR filters to achieve a faster frequency roll-off than required in CP-OFDM. The computational complexity is directly related to power consumption and raises practical implementation issues [48], which do not match with the desire to achieve energy efficient 5G terminals. Thus, we propose the OA-UFMC system by applying the multiplication operation in frequency domain in place of time domain convolution.

The block diagram of OA-UFMC is shown in Figure 5.1, using the overlap and add technique [104] instead of the time domain convolution operation to reduce the computational complexity. We increase the number of samples in the frequency domain by using a $2N$-point FFT then multiply carrier by carrier with the frequency-domain filter coefficients. The OA-UFMC system transmission processing as shown in Table 5.1.

Note that there is a good reason why we do not implement directly the product $(X_u(n) \cdot B_u(n))$,

OA-UFMC Transmission Steps
Step 1: The baseband signal $X_u(n)$ passes through the N-point IFFT block, $x_u(t)$
Step 2: Appends N samples zeros on to x_u to obtain $x_u(t^{OA})$, $t^{OA} \in [0, 2N-1]$
Step 3: Passes $x_u(t^{OA})$ through the $2N$-point FFT block, $\tilde{X}_u(m)$
Step 4: Multiplication $\tilde{S}_u(m) = \tilde{X}_u(m) \cdot \tilde{B}_u(m)$
Step 5: The baseband signal $\tilde{S}_u(m)$ then passes through the $2N$-point IFFT block

Table 5.1: *OA-UFMC Transmission Processing Steps*

where $B_u(n)$ is the N-point FFT of $b_u(t)$. This is because we need to ensure the transmitted samples are exactly the same as $s_u(t)$ with the length of L. The signal after the $2N$-point FFT block in the frequency domain can be expressed as:

$$\tilde{X}_u(m) = \sum_{m=0}^{2N-1} x_u(t^{OA})e^{-j2\pi t^{OA}m/2N}, t^{OA} \in [0, 2N-1] \tag{5.4}$$

thus, frequency domain multiplication processing can be expressed as:

$$\tilde{S}_u(m) = \tilde{X}_u(m) \cdot \tilde{B}_u(m), \ m \in [0, L-1] \tag{5.5}$$

where $\tilde{B}_u(m)$ is the first L samples of the $2N$-point FFT of $b_u(t)$. After transforming $\tilde{S}_u(m)$ into the time domain through the $2N$-point IFFT, truncate the first L samples to achieve the same time domain sequence as:

$$\tilde{s}_u(t) = s_u(t), \ t \in [0, L-1]. \tag{5.6}$$

5.2.3 Efficient N-FFT

In this sub-section, we study the Efficient FFT to implement a N-point FFT to generate an $2N$ point sequence samples in the frequency domain. The main processing of the efficient FFT is shown in Table 5.2.

The time domain sequence between the convolution-UFMC, OA-UFMC and Efficient FFT is shown in Figure 5.2. It clearly shows that the OA-UFMC can achieve the similar time domain sequence as the time domain convolution operation. The efficient N-point FFT approach only can achieve the similar time domain sequence for the middle N transmitted samples and lose the accurate signal representation during the window tail range.

Efficient FFT Steps
Step 1: The baseband signal $X_u(n)$ passes through the N-point IFFT block, $x_u(t)$
Step 2: Frequency domain extra sequence samples as $X^{\mathrm{E}} = \sum\limits_{n=0}^{N-1} X(n)\mathrm{sinc}(x)$
Step 3: Set $X^{\mathrm{Total}} = [X(0), X^{\mathrm{E}}(0), X(1), X^{\mathrm{E}}(1), ..., X(N-1), X^{\mathrm{E}}(N-1)]$
Step 4: Multiplication $S_u^{\mathrm{E}}(m) = X^{\mathrm{Total}}(m) \cdot \tilde{B}_u(m)$
Step 5: The baseband signal $S_u^{\mathrm{E}}(m)$ passes through the $2N$-point IFFT block

Table 5.2: *Efficient N-FFT Transmission Processing Steps*
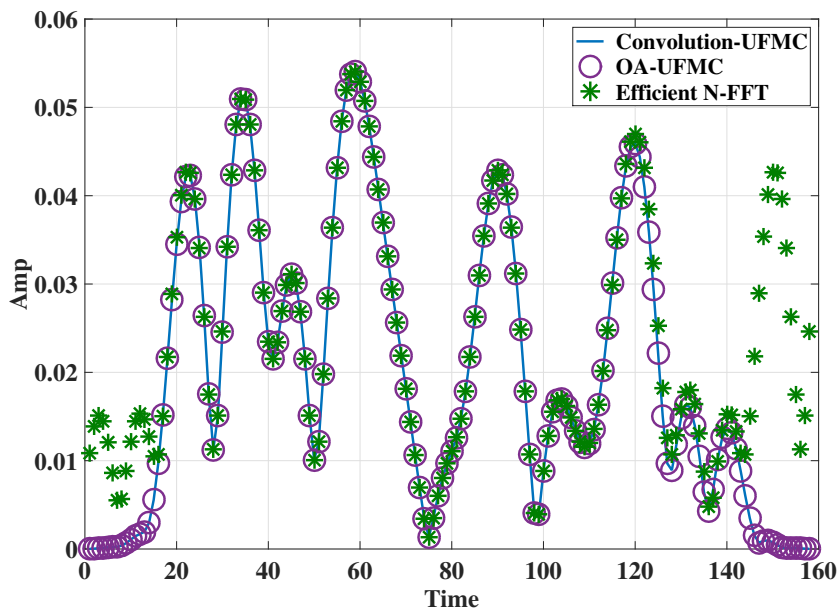
Figure 5.2: *Time Domain Signal Sequence Between the Convolution-UFMC, OA-UFMC, and Efficient N-FFT*

5.3 Computational Complexity Analysis

As mentioned in Chapter 4, the main computational complexity is dominated by the number of multiplication operations that are performed. Thus, the computational complexity equations for the UFMC (or WOLA) transmitter can be written as $\Gamma^{\mathrm{UFMC/WOLA}}$:

$$\Gamma^{\mathrm{UFMC}} = \underbrace{\frac{N}{2}\log_2(N)}_{N-\text{point IFFT}} + (N \cdot L_{\mathrm{F}}), \tag{5.7}$$

where the term of $(N \cdot L_F)$ determines the number of multiplications during the time domain

convolution operation. The computational complexity for OA-UFMC transmitter can be written as Γ^{OA}:

$$
\begin{aligned}
\Gamma^{\mathrm{OA}} &= \underbrace{\frac{N}{2}\log_2(N)}_{N\text{–point IFFT}} + \underbrace{2\frac{2N}{2}\log_2(2\cdot N)}_{2N\text{–point FFT} + 2N\text{–point IFFT}} + L \\
&= \frac{N}{2}\log_2(N) + 2N\left(1 + \log_2(N)\right) + N + L_{\mathrm{F}} - 1 \\
&= \frac{5N}{2}\log_2(N) + 3N + L_{\mathrm{F}} - 1.
\end{aligned}
\tag{5.8}
$$

Compared with UFMC, OA-UFMC can reduce the computational complexity by:

$$
\Gamma^{\mathrm{OA}} - \Gamma^{\mathrm{UFMC}} = (L_{\mathrm{F}} - 3)N - 2N\log_2(N) - L_{\mathrm{F}} + 1,
\tag{5.9}
$$

operations, and the benefit increases when increasing L_{F}.

This chapter also considers IIR filters, such as Chebyshev Type I [51], to determine the ICI performance in terms of reducing the computational complexity caused by the time domain convolution operation. IIR prototype filters with a few number of filter orders L_{Or} can achieve a similar performance compared to FIR, i.e. $L_{\mathrm{Or}} = 4$, if we consider the IIR filter with the Direct Form I, the overall filter coefficients (both feedforward and feedback) is $(2L_{\mathrm{Or}} + 1)$. Thus, in this case, the computational complexity for IIR-UFMC can be significantly reduced as:

$$
\Gamma^{\mathrm{IIR\text{–}UFMC}} = \underbrace{\frac{N}{2}\log_2(N)}_{N\text{–point IFFT}} + \underbrace{L\cdot(2L_{\mathrm{Or}} + 1)}_{L \text{ samples and IIR process}} \quad, L_{\mathrm{Or}} < L_{\mathrm{F}}.
\tag{5.10}
$$

As mentioned in Chapter 2, the computational complexity for CP/ZP-OFDM and PCC-OFDM be expressed as:

$$
\Gamma^{\mathrm{CP/ZP/PCC\text{–}OFDM}} = \frac{N}{2}\log_2(N).
\tag{5.11}
$$

5.4 Time Offset Interference Analysis

The time domain signals of UFMC and OA-UFMC are very similar as shown in (5.6). This chapter considers CP-OFDM (CP-OFDM processing is very similar to PCC-OFDM as both of

103
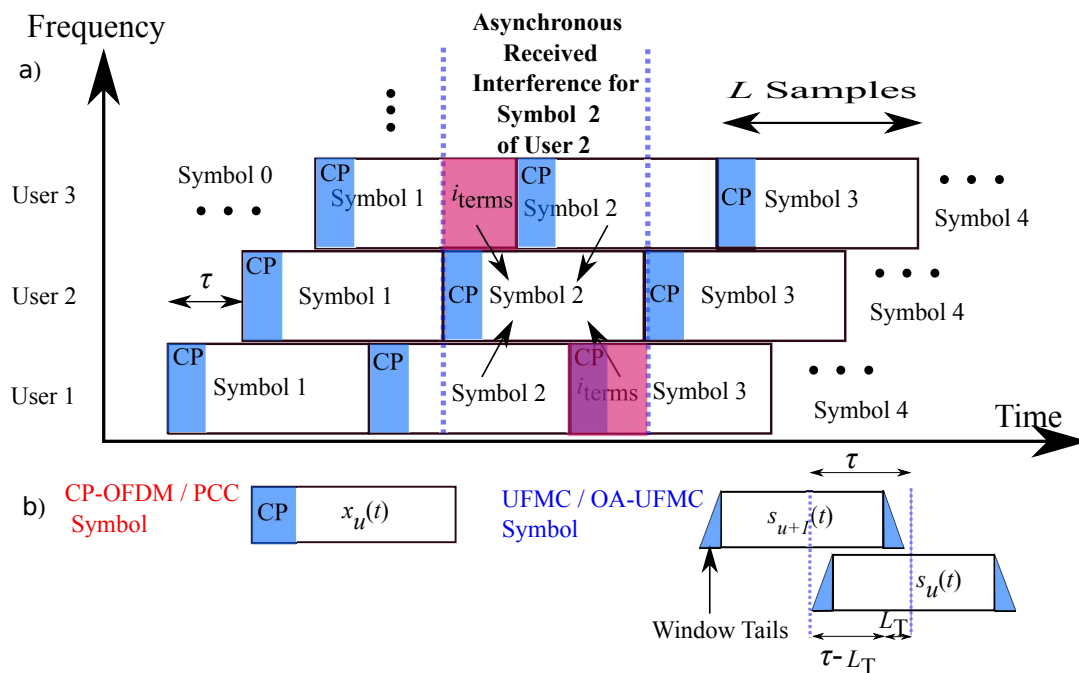
Figure 5.3: *Time Offset Interference Model*

them add a CP guard interval [105]) and UFMC for the interference analysis. In this section, we use a simple time-offset model to analyse the interference caused by asynchronism and we also consider the ISI effect by the Rayleigh multipath fading channel.

5.4.1 Time-offset Model

We assume that the received MTC signals from the U users are asynchronous and suffer from time-offsets at the base station. The time-frequency representation for time offset is shown in Figure 5.3. To simplify our analysis we starts by considering $U = 3$ users where each user transmits 3 OFDM symbols. The scalar τ is the relative delay in timing samples between adjacent users. In addition, we assume that the time offsets between each pair of adjacent users are the same. This chapter focuses on decoding the 2nd OFDM symbol for each user. Here we define $x_{u,i}$ to note the time domain transmitted symbol for the ith OFDM symbol of the uth user, which is following the notation in Figure 5.3.

5.4.2 ICI Analysis Caused by Time Offset

This subsection analyses the ICI interference for both the CP-OFDM and the UFMC system.

5.4.2.1 CP-OFDM (or PCC-OFDM) System ICI Analysis

The ICI interference for each user is caused by the OFDM side-lobes of the adjacent asynchronous users. As shown in Figure 5.3(a), the interference terms for the 2nd symbol of user 2, $x_{2,2}(t)$, are separated into four parts: two of them arise from the adjacent time periods and two of them arise from the same time period. First, the interference of $x_{2,2}(t)$ from the adjacent time periods is dominated by the first τ samples from $x_{1,3}(t)$ and the tail τ samples from $x_{3,1}(t)$ as shown in red in Figure 5.3(a). Thus, the time domain interference terms to the 2nd user ($u = 2$), which are caused from the different time periods can be computed as:

$$i_2^{\text{Diff}}(t) = \sum_{l=0}^{\tau-1} x_{1,3}(t)\delta(t-l) + \sum_{l=L-\tau}^{L-1} x_{3,1}(t)\delta(t-l), \ t \in [0, L-1], \qquad (5.12)$$

Second, the remaining samples of $x_{1,2}(t)$ and $x_{3,2}(t)$ are nearly orthogonal with $x_{2,2}(t)$, which are transmitted in the same time period. If there is no time offsets, $x_{1,2}(t)$, $x_{2,2}(t)$ and $x_{3,2}(t)$ are orthogonal. Then, the dot product of $x_{1,2}(t)$ and $x_{2,2}(t)$ can be expressed as:

$$\sum_{l=0}^{L-1} x_{1,2}(t)e^{-j2\pi lt/N} \cdot x_{2,2}(t)e^{-j2\pi lt/N} = 0, \qquad (5.13)$$

thus,

$$\sum_{l=0}^{\tau-1} x_{1,2}(t)e^{-j2\pi lt/N} \cdot x_{2,2}(t)e^{-j2\pi lt/N} + \sum_{l=\tau}^{L-1} x_{1,2}(t)e^{-j2\pi lt/N} \cdot x_{2,2}(t)e^{-j2\pi lt/N} = 0,$$

$$(5.14)$$

and then,

$$\sum_{l=\tau}^{L-1} x_{1,2}(t)e^{-j2\pi lt/N} \cdot x_{2,2}(t)e^{-j2\pi lt/N} = \sum_{l=0}^{\tau-1} -x_{1,2}(t)e^{-j2\pi lt/N} \cdot x_{2,2}(t)e^{-j2\pi lt/N}. \quad (5.15)$$

Now, similarly, the interference terms for $x_{2,2}(t)$, which are caused from the same time period can be computed as:

$$i_2^{\text{Same}}(t) = \sum_{l=0}^{\tau-1} -x_{1,2}(t)\delta(t-l) + \sum_{l=L-\tau}^{L-1} -x_{3,2}(t)\delta(t-l). \tag{5.16}$$

Finally, according to (5.12) and (5.16), we can write the total interference terms for $x_{2,2}(t)$ in the time domain as:

$$i_2^{\text{OFDM}}(t) = \sum_{l=0}^{\tau-1} x_{1,3}(t)\delta(t-l) + \sum_{l=L-\tau}^{L-1} x_{3,1}(t)\delta(t-l) \tag{5.17}$$
$$+ \sum_{l=0}^{\tau-1} -x_{1,2}(t)\delta(t-l) + \sum_{l=L-\tau}^{L-1} -x_{3,2}(t)\delta(t-l).$$

After removing the CP, we can rewrite (5.17) as:

$$i_2^{\text{OFDM}}(n) = \sum_{l=0}^{\tau-1} \left(-x_{1,2}(n) + x_{1,3}(n)\right)\delta(n-l) \tag{5.18}$$
$$+ \sum_{l=N-\tau+L_{\text{CP}}}^{N-1} \left(-x_{3,2}(n) + x_{3,1}(n)\right)\delta(n-l).$$

Similarly, the interference for the 2nd symbol of user 1, $x_{1,2}(t)$, after removing CP is:

$$i_1^{\text{OFDM}}(n) = \sum_{l=N-\tau+L_{\text{CP}}}^{N-1} \left(-x_{2,2}(n) + x_{2,1}(n)\right)\delta(n-l) \tag{5.19}$$
$$+ \sum_{l=N-2\tau+L_{\text{CP}}}^{N-1} \left(-x_{3,2}(n) + x_{3,1}(n)\right)\delta(n-l),$$

and for user 3, $x_{3,2}(t)$, is:

$$i_3^{\text{OFDM}}(n) = \sum_{l=0}^{2\tau-1} \left(-x_{1,2}(n)+x_{1,3}(n)\right)\delta(n-l) + \sum_{l=0}^{\tau-1} \left(-x_{2,2}(n)+x_{2,3}(n)\right)\delta(n-l). \tag{5.20}$$

Now, the time domain interference term on the kth sub-carrier can be rewritten using the Discrete Fourier transform as $I_u(k)$:

$$I_1^{\text{OFDM}}(k) = \sum_{k=0}^{K-1} \sum_{n=N-\tau+L_{\text{CP}}}^{N-1} \big(-x_{2,2}(n) + x_{2,1}(n) \big) e^{-j2\pi nk/N} \tag{5.21}$$

$$+ \sum_{k=0}^{K-1} \sum_{n=N-2\tau+L_{\text{CP}}}^{N-1} \big(-x_{3,2}(n) + x_{3,1}(n) \big) e^{-j2\pi nk/N},$$

$$I_2^{\text{OFDM}}(k) = \sum_{k=0}^{K-1} \sum_{n=0}^{\tau-1} \big(-x_{1,2}(n) + x_{1,3}(n) \big) e^{-j2\pi nk/N} \tag{5.22}$$

$$+ \sum_{k=0}^{K-1} \sum_{n=N-\tau+L_{\text{CP}}}^{N-1} \big(-x_{3,2}(n) + x_{3,1}(n) \big) e^{-j2\pi nk/N},$$

$$I_3^{\text{OFDM}}(k) = \sum_{k=0}^{K-1} \sum_{n=0}^{2\tau-1} \big(-x_{1,2}(n) + x_{1,3}(n) \big) e^{-j2\pi nk/N} \tag{5.23}$$

$$+ \sum_{k=0}^{K-1} \sum_{n=0}^{\tau-1} \big(-x_{2,2}(n) + x_{2,3}(n) \big) e^{-j2\pi nk/N}.$$

We can conclude that the CP only can reduce the interference in the front of L_{CP} sample time-offsets as shown in (5.21), where $(L_{\text{CP}} - \tau)$ error samples have been considered. When the interference is located in the final τ samples, CP-OFDM would no longer to be robust to the ICI, as shown in (5.22) and (5.23), e.g. as τ or 2τ error samples are considered as the interference.

5.4.2.2 UFMC / OA-UFMC System ICI Analysis

Unlike CP-OFDM, the side-lobe attenuation of UFMC is much smaller due to filtering. The narrow band filter used at the transmitter can significantly reduce the interference caused by the time-offset between the transmitting users. Similar to (5.17), we can write the interference terms on uth user of UFMC as $i_u^{\text{UFMC}}(t)$:

$$i_2^{\text{UFMC}}(t) = \sum_{l=0}^{\tau-1} \big(-s_{1,2}(t) + s_{1,3}(t) \big) \delta(t-l) + \sum_{l=L-\tau}^{L-1} \big(-s_{3,2}(t) + s_{3,1}(t) \big) \delta(t-l), \tag{5.24}$$

thus, the kth sub-carrier can be rewritten using the Fourier transform as:

$$I_2^{\text{UFMC}}(k) = \sum_{k=0}^{K-1} \sum_{t=0}^{\tau-1} \big(-s_{1,2}(t) + s_{1,3}(t) \big) e^{-j2\pi tk/N} \tag{5.25}$$
$$+ \sum_{k=0}^{K-1} \sum_{t=L-\tau}^{L-1} \big(-s_{3,2}(t) + s_{3,1}(t) \big) e^{-j2\pi tk/N}.$$

Now, we define L_{T} is the transmitted signal tail length which is located at both the front and the end of the UFMC samples, and $L_{\text{T}} = \frac{L_{\text{F}}-1}{2}$. Then, the first term of (5.25) can be expanded as:

$$\sum_{k=0}^{K-1} \sum_{t=0}^{\tau-1} \big(-s_{1,2}(t) + s_{1,3}(t) \big) e^{-j2\pi tk/N} \tag{5.26}$$
$$= \sum_{k=0}^{K-1} \left(\sum_{t=0}^{L_{\text{T}}-1} \big(-s_{1,2}(t) + s_{1,3}(t) \big) + \sum_{t=L_{\text{T}}}^{\tau-1} \big(-s_{1,2}(t) + s_{1,3}(t) \big) \right) e^{-j2\pi tk/N},$$

and the second term of (5.25) can be rewritten as:

$$\sum_{k=0}^{K-1} \sum_{t=L-\tau}^{L-1} \big(-s_{3,2}(t) + s_{3,1}(t) \big) e^{-j2\pi tk/N} \tag{5.27}$$
$$= \sum_{k=0}^{K-1} \left(\sum_{t=L-\tau}^{L-L_{\text{T}}-1} \big(-s_{3,2}(t) + s_{3,1}(t) \big) + \sum_{t=L-L_{\text{T}}}^{L-1} \big(-s_{3,2}(t) + s_{3,1}(t) \big) \right) e^{-j2\pi tk/N}.$$

Note that, each filter is designed with the narrow bandwidth, such as Chebyshev or Hamming [106], the magnitude of $b_u(t)$ at the band-edge should be very small. After removing the tail samples (window tails) which are located at ($t \in [0, L_{\text{T}}-1]$, $t \in [L-\text{T}, L-1]$) as shown in Figure 5.3(b), the equation (5.25) can be summed from (5.26) and (5.27) then be approximated as:

$$I_2^{\text{UFMC}}(k) \approx \sum_{k=0}^{K-1} \sum_{t=L_{\text{T}}}^{\tau-1} \big(-s_{1,2}(t) + s_{1,3}(t) \big) e^{-j2\pi tk/N} \tag{5.28}$$
$$+ \sum_{k=0}^{K-1} \sum_{t=L-\tau}^{L-L_{\text{T}}-1} \big(-s_{3,2}(t) + s_{3,1}(t) \big) e^{-j2\pi tk/N}.$$

Similarly, the interference on the kth sub-carrier of the 1st user in the frequency domain can be written as:

$$I_1^{\text{UFMC}}(k) = \sum_{k=0}^{K-1} \sum_{t=L-\tau}^{L-1} \left(- s_{2,2}(t) + s_{2,1}(t) \right) e^{-j2\pi tk/N} \tag{5.29}$$

$$+ \sum_{k=0}^{K-1} \sum_{t=L-2\tau}^{L-1} \left(- s_{3,2}(t) + s_{3,1}(t) \right) e^{-j2\pi tk/N}$$

$$= \sum_{k=0}^{K-1} \left(\sum_{t=L-\tau}^{L-L_{\text{T}}-1} \left(- s_{2,2}(t) + s_{2,1}(t) \right) + \sum_{t=L-L_{\text{T}}}^{L-1} \left(- s_{2,2}(t) + s_{2,1}(t) \right) \right) e^{-j2\pi tk/N}$$

$$+ \sum_{k=0}^{K-1} \left(\sum_{t=L-2\tau}^{L-L_{\text{T}}-1} \left(- s_{3,2}(t) + s_{3,1}(t) \right) + \sum_{t=L-L_{\text{T}}}^{L-1} \left(- s_{3,2}(t) + s_{3,1}(t) \right) \right) e^{-j2\pi tk/N}$$

$$\approx \sum_{k=0}^{K-1} \sum_{t=L-\tau}^{L-L_{\text{T}}-1} \left(- s_{2,2}(t) + s_{2,1}(t) \right) e^{-j2\pi tk/N}$$

$$+ \sum_{k=0}^{K-1} \sum_{t=L-2\tau}^{L-L_{\text{T}}-1} \left(- s_{3,2}(t) + s_{3,1}(t) \right) e^{-j2\pi tk/N},$$

and for the 3th user can be written as:

$$I_3^{\text{UFMC}}(k) = \sum_{k=0}^{K-1} \sum_{t=0}^{2\tau-1} \left(- s_{1,2}(t) + s_{1,3}(t) \right) e^{-j2\pi tk/N} \tag{5.30}$$

$$+ \sum_{k=0}^{K-1} \sum_{t=0}^{\tau-1} \left(- s_{2,2}(t) + s_{2,3}(t) \right) e^{-j2\pi tk/N}$$

$$= \sum_{k=0}^{K-1} \left(\sum_{t=0}^{L_{\text{T}}-1} \left(- s_{1,2}(t) + s_{1,3}(t) \right) + \sum_{L_{\text{T}}}^{2\tau-1} \left(- s_{1,2}(t) + s_{1,3}(t) \right) \right) e^{-j2\pi tk/N}$$

$$+ \sum_{k=0}^{K-1} \left(\sum_{t=0}^{L_{\text{T}}-1} \left(- s_{2,2}(t) + s_{2,3}(t) \right) + \sum_{L_{\text{T}}}^{\tau-1} \left(- s_{2,2}(t) + s_{2,3}(t) \right) \right) e^{-j2\pi tk/N}$$

$$\approx \sum_{k=0}^{K-1} \sum_{t=L_{\text{T}}}^{2\tau-1} \left(- s_{1,2}(t) + s_{1,3}(t) \right) e^{-j2\pi tk/N}$$

$$+ \sum_{k=0}^{K-1} \sum_{t=L_{\text{T}}}^{\tau-1} \left(- s_{2,2}(t) + s_{2,3}(t) \right) e^{-j2\pi tk/N}.$$

The narrow band triangle filter reduces the power amplitude at the band-edge, which directly reduces the ICI caused by the time offset overlapped samples. Note that, in terms of the multipath channel, this paper considers that the sum of the mean power values for all channel taps

is equal to 1. The interference terms for the multipath channel can be easily computed as using $x_{u,i}(t) \otimes h_u(t)$ or $s_{u,i}(t) \otimes h_u(t)$ instead of $x_{u,i}(t)$ or $s_{u,i}(t)$ in the above equations, which can be used for the case of any of the multipath channels.

5.4.3 ISI Analysis Caused by Channel

This chapter also considers the analysis of ISI when the length of channel impulse response in samples L_{H} is longer than L_{CP} or L_{F}.

5.4.3.1 CP-OFDM System ISI Analysis

Reference [78] proved that when $(L_{\mathrm{H}} > L_{\mathrm{CP}})$, a part of one signal will then be ISI from the previous symbol and the ISI causes interference at the tail of the channel impulse response that are not covered by the CP. Thus, the residual ISI of the uth user on the kth sub-carrier after removing the CP in the frequency domain can be expressed as $Z_u(k)$ [78]:

$$
\begin{aligned}
Z_u^{\mathrm{OFDM}}(k) &= \sum_{n=L_{\mathrm{CP}}}^{L_{\mathrm{H}}-1} x_{u-1}(n) \sum_{t=n}^{L_{\mathrm{H}}-1} h_u(t) e^{-j2\pi(t-n)k/N} \\
&= \sum_{n=L_{\mathrm{CP}}}^{L_{\mathrm{H}}-1} x_{u-1}(n) e^{j2\pi nk/N} \sum_{t=n}^{L_{\mathrm{H}}-1} h_u(t) e^{-j2\pi tk/N},
\end{aligned} \tag{5.31}
$$

then the PSD of ISI for the CP-OFDM system can be determined as P_{ISI}:

$$
\begin{aligned}
P_{\mathrm{ISIu}}^{\mathrm{OFDM}}(k) &= \mathbb{E}\left(Z_u^{\mathrm{OFDM}}(k) Z_u^{\mathrm{OFDM}*}(k)\right) \\
&= \mathbb{E}\left(x_{u-1}(n) x_{u-1}^*(n)\right) e^{-j2\pi(n-n)k/N} \\
&\quad \cdot \sum_{n=L_{\mathrm{CP}}}^{L_{\mathrm{H}}-1} \sum_{t=n}^{L_{\mathrm{H}}-1} h_u(t) e^{-j2\pi tk/N} \sum_{n=L_{\mathrm{CP}}}^{L_{\mathrm{H}}-1} \sum_{t=n}^{L_{\mathrm{H}}-1} h_u^*(t) e^{-j2\pi tk/N} \\
&= \sigma^2 \sum_{n=L_{\mathrm{CP}}}^{L_{\mathrm{H}}-1} \left| \sum_{t=n}^{L_{\mathrm{H}}-1} h_u(t) e^{-j2\pi tk/N} \right|^2.
\end{aligned} \tag{5.32}
$$

5.4.3.2 UFMC System ISI Analysis

Following a similar analysis to the CP-OFDM system, the residual ISI of the uth user on the kth sub-carrier for UFMC is:

$$
\begin{aligned}
Z_u^{\mathrm{UFMC}}(k) &= \sum_{n=L_{\mathrm{T}}}^{L_{\mathrm{H}}-1} s_{u-1}(n) e^{j2\pi nk/N} \sum_{t=n}^{L_{\mathrm{H}}-1} h_u(t) e^{-j2\pi tk/N} \\
&= \sum_{n=L_{\mathrm{T}}}^{L_{\mathrm{H}}-1} x_{u-1}(n) b_{u-1}(n) e^{j2\pi nk/N} \sum_{t=n}^{L_{\mathrm{H}}-1} h_u(t) e^{-j2\pi tk/N}.
\end{aligned} \tag{5.33}
$$

Thus, the PSD of ISI for the UFMC system can be determined as:

$$
\begin{aligned}
P_{\mathrm{ISI}u}^{\mathrm{UFMC}}(k) &= \mathbb{E}\left(x_{u-1}(n) x_{u-1}^*(n)\right) e^{-j2\pi(n-n)k/N} \\
&\cdot \sum_{n=L_{\mathrm{T}}}^{L_{\mathrm{H}}-1} \sum_{t=n}^{L_{\mathrm{H}}-1} b_u(t) h_u(t) e^{-j2\pi tk/N} \sum_{n=L_{\mathrm{T}}}^{L_{\mathrm{H}}-1} \sum_{t=n}^{L_{\mathrm{H}}-1} b_u^*(t) h_u^*(t) e^{-j2\pi tk/N} \\
&= \sigma^2 \sum_{n=L_{\mathrm{T}}}^{L_{\mathrm{H}}-1} \left| \sum_{t=n}^{L_{\mathrm{T}}-1} b_u(t) h_u(t) e^{-j2\pi tk/N} \right|^2.
\end{aligned} \tag{5.34}
$$

5.4.4 SINR Analysis and Capacity

The SINR of the received signal on kth sub-carrier can is defined as $\rho_u(k)$:

$$
\rho_u(k) = \frac{\mathbb{E}[X_u(k)^2]}{\sigma^2 + \mathbb{E}[I_u(k)^2] + P_{\mathrm{ISI}u}(k)}, \tag{5.35}
$$

where $\mathbb{E}[X_u(k)^2]$ denotes the transmitted signal power. Inserting (5.21), (5.22), (5.23) and (5.32) into (5.35), the closed-form expression of SINR for the uth user CP-OFDM can be expressed as:

$$
\rho_u^{\mathrm{OFDM}}(k) = \frac{\mathbb{E}[X_u(k)^2]}{\sigma^2 + \mathbb{E}[(I_u^{\mathrm{OFDM}}(k))^2] + \sigma^2 \sum_{n=L_{\mathrm{CP}}}^{L_{\mathrm{H}}-1} \left| \sum_{t=n}^{L_{\mathrm{H}}-1} h_u(t) e^{-j2\pi tk/N} \right|^2}. \tag{5.36}
$$

Inserting (5.29), (5.28), (5.30) and (5.34) into (5.35), the closed-form expression of SINR for the uth user UFMC can be expressed as:

$$\rho_u^{\text{UFMC}}(k) = \frac{\mathbb{E}[S_u(k)^2]}{\sigma^2 + \mathbb{E}[(I_u^{\text{UFMC}}(k))^2] + \sigma^2 \sum_{n=L_{\text{T}}}^{L_{\text{H}}-1} \left| \sum_{t=n}^{L_{\text{T}}-1} b_u(t)h_u(t)e^{-j2\pi tk/N} \right|^2}. \tag{5.37}$$

Now, we can compute an estimate of the Shannon capacity $C_u(k)$ for the kth sub-carrier of the uth user based on our SINR equations as:

$$C_u^{\text{OFDM}}(k) = \log_2(1 + \rho_u^{\text{OFDM}}(k)), \tag{5.38}$$

$$C_u^{\text{UFMC}}(k) = \log_2(1 + \rho_u^{\text{UFMC}}(k)). \tag{5.39}$$

5.4.5 BER Analysis

This section now considers the performance for a 4PSK modulation scheme. As in [45] and [107], we can express the theoretical BER values for the time-offset model under the AWGN channel as:

$$P_{\text{4PSK}u}^{\text{OFDM}} = \frac{1}{2}\text{erfc}\left(\sqrt{\overline{\rho_u^{\text{OFDM}}/N_{\text{bs}}}} \right), \tag{5.40}$$

$$P_{\text{4PSK}u}^{\text{UFMC}} = \frac{1}{2}\text{erfc}\left(\sqrt{\overline{\rho_u^{\text{UFMC}}/N_{\text{bs}}}} \right), \tag{5.41}$$

where $\text{erfc}(\cdot)$ represents the complementary error function, $\overline{\rho_u}$ is the average value of SINR and N_{bs} is the number of bits per sample. For the Rayleigh multipath channel, according to [45] and [107], the BER equations are given:

$$P_{\text{4PSK}u}^{\text{OFDM}} = \frac{1}{2}\text{erfc}\left(1 - \sqrt{\frac{\overline{\rho_u^{\text{OFDM}}/N_{\text{bs}}}}{1 + \overline{\rho_u^{\text{OFDM}}/N_{\text{bs}}}}} \right), \tag{5.42}$$

$$P_{\text{4PSK}u}^{\text{UFMC}} = \frac{1}{2}\text{erfc}\left(1 - \sqrt{\frac{\overline{\rho_u^{\text{UFMC}}/N_{\text{bs}}}}{1 + \overline{\rho_u^{\text{UFMC}}/N_{\text{bs}}}}} \right). \tag{5.43}$$

5.5 Numerical Results

In this section, various simulations are conducted to confirm our theoretical analysis. The common simulation parameters are listed in Table 5.3, Each user's transmission occupies 13

Simulation Parameters							
Uplink Bandwidth	No. of N-FFT	Sub-carriers K	Total U	CP L_{CP}	Filter L_{F}	Channel L_{H}	Modulation Scheme
1.25 MHz	128	13	3 or 7	30	31	10 or 70	4PSK
Filter Parameters							
FIR Filter			IIR Filter				
Window	Normalised f_{cf}		Filter Type	f_{cf}	Orders		A_{PB}
Hamming	0.18		Chebyshev I	0.18	4, 8, 12		0.15 dB

Table 5.3: *COMMON SIMULATION PARAMETERS*

sub-carriers in the frequency domain, and the users are spaced by 2 blank sub-carriers. We set the normalised cut-off frequency to $f_{\text{cf}} = 0.18$, which is wider than the ratio between the number of sub-carriers per user K and the total number of available sub-carriers N, $\gamma_{\text{ro}} = 13/128 = 0.1016$. A_{SL} is the side-lobe attenuation and A_{PB} is the passband ripple. In the BER simulations, we elected to measure the middle user's performance, e.g. when $U = 3$, we measure the 2nd user and when $U = 7$, we measure the 4th user.

5.5.1 Computational Complexity Performance

The relative computational complexity performance is shown in Figure 5.4 using (5.7), (5.8) and (5.11). Both CP-OFDM and PCC-OFDM require significantly fewer operations than time domain UFMC and OA-UFMC. When $L_{\text{F}} < 17$ samples, time domain UFMC requires fewer operations than OA-UFMC. As L_{F} increases, the number of operations for UFMC significantly increases. In this case, OA-UFMC reduces the computational complexity significantly for larger values of L_{F}. IIR-UFMC, with a filter order of 4, only slightly increases the complexity compared with OFDM and PCC, but it significantly reduces the number of operations compared with UFMC and OA-UFMC.

5.5.2 SINR and Capacity Performance

The SINR performance over the AWGN channel with a SNR of 30 dB is shown in Figure 5.5(a) and we assume τ is a 50 sample time offset, which is much longer than $L_{\text{CP}} = 30$ or $L_{\text{F}} = 31$. The theoretical SINR analysis values are computed from (5.36) and (5.37), which perfectly match with the simulations. The 1st user occupies sub-carriers from 11 to 23, similarly 26 to
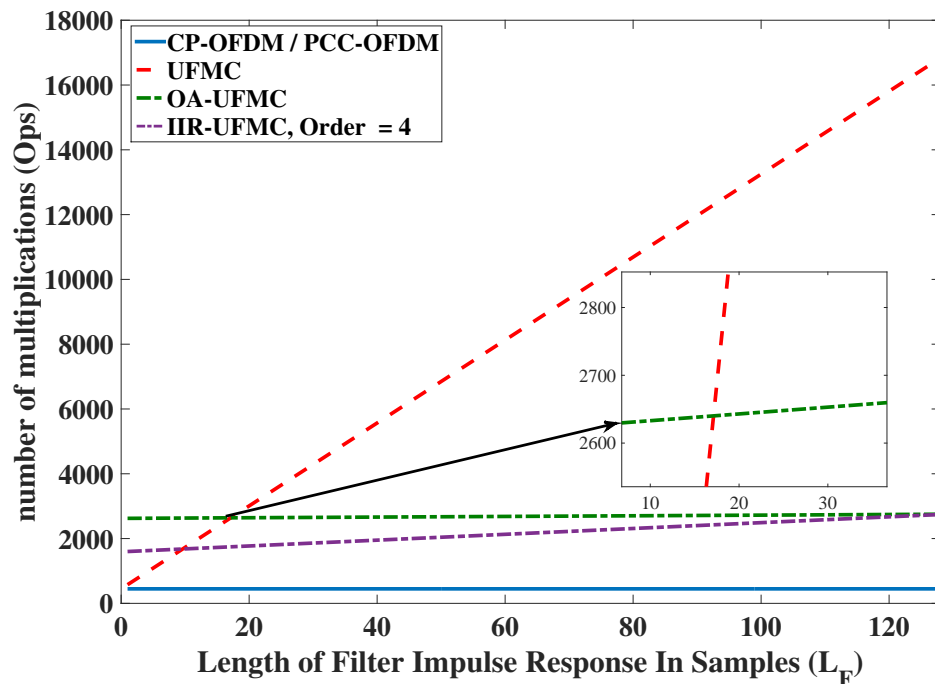
Figure 5.4: *Comparison of Computational Complexity, N=128*

38 for the 2nd user and 41 to 52 for the 3rd user. Note in Figure 5.5(a) how the SINR performance degrades due to interference between users 1&2 and also 2&3 except for PCC. From the Figure 5.5(a), we notice that: first, compared with OFDM, UFMC and IIR-UFMC, PCC-OFDM presents the best performance. Second, the nearby sub-carriers of both OFDM, UFMC, and IIR-UFMC are significantly affected by ICI, especially for the second user. Third, both UFMC and IIR-UFMC can perform slightly better than OFDM (about 3.5 dB higher SINR), but they still have an inferior SINR to PCC-OFDM. There is no significant performance difference between UFMC and IIR-UFMC.

The impact of the number of blank sub-carriers in the frequency domain between each user is shown in Figure 5.5(b). Increasing the number of blank sub-carriers at the user band-edge, the SINR performance of both OFDM, UFMC and IIR-UFMC improves significantly at the cost of reducing the available bandwidth for data transmission. Moreover, if the sub-user spacing is 4 blank sub-carriers, UFMC achieves about 0.5 dB higher SINR than IIR-UFMC and about 2.6 dB higher SINR than OFDM. PCC still provide the best performance compared with the other schemes. It can also be seen that the result from the analysis matches very well with the
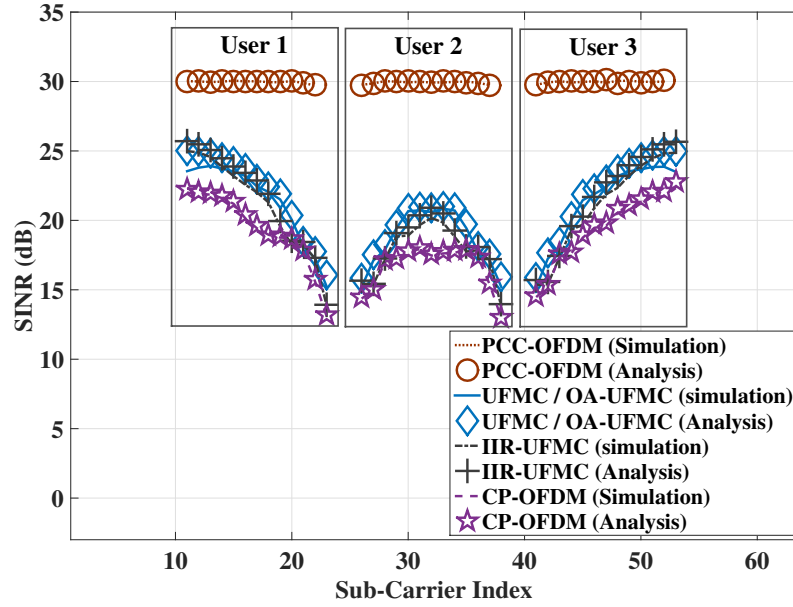
(a) SINR Performance with $\tau = 50$
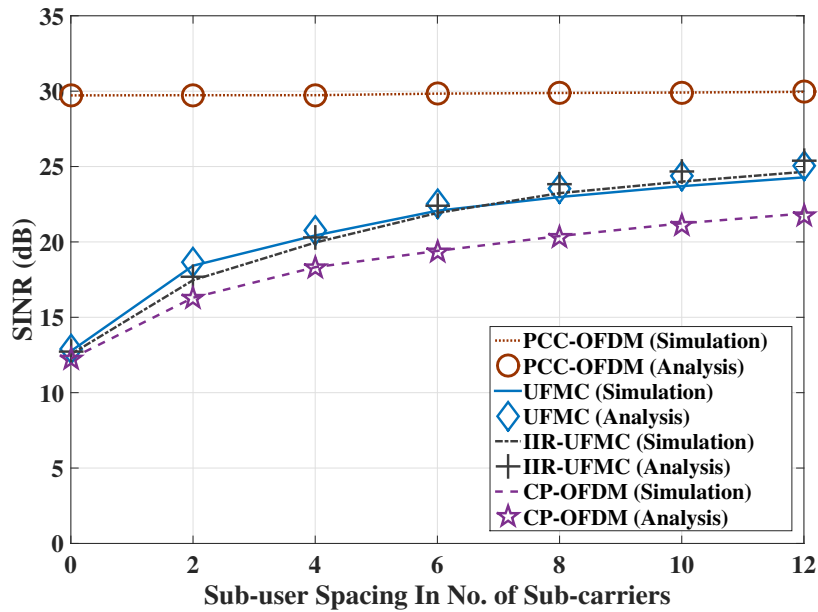
(b) SINR Performance with Blank Sub-carriers

Figure 5.5: *SINR Performance, 4PSK, AWGN (SNR =30 dB), $N = 128$, $L_{\mathrm{CP}} = 30$, $L_{\mathrm{F}} = 31$, $U = 3$.*

simulations.

The capacity performance with the time offset factor (τ/L) is shown in Figure 5.6(a). The theoretical capacity values are computed from (5.38) and (5.39), and the results from our derived expressions and the simulations match perfectly. It can be seen that firstly, PCC-OFDM provides the poorest capacity performance because of its reduced spectral efficiency, even though it can achieve the highest SINR performance in Figure 5.5. Secondly, with increasing τ, the capacity performance of UFMC, IIR-UFMC and OFDM significantly reduces due to the ICI. However, when $\tau = L = 158$ samples, there is no significant capacity degradation as there is no relative time-offsets between the adjacent users. Thirdly, if there is a small time offset, i.e. $\tau = 5\%$ of the transmitted symbol length, both UFMC and IIR-UFMC are more robust to ICI compared with OFDM. In detail, the capacity degradation for UFMC and IIR-UFMC significantly reduces when $\tau > 10\%$ (or 15 samples) of the transmitted symbol length, which is approximately the window tail length L_{T}. The capacity degradation for OFDM starts with when $\tau > 5\%$ of the transmitted symbol length and then stays at a constant value of 6.3 bit/sec/Hz until $\tau > 20\%$ (or 30 samples), which is approximately the CP length. Fourthly, if $\tau > 20\%$ of the transmitted symbol length, both UFMC, IIR-UFMC and OFDM provide an approximately constant capacity. Both UFMC and IIR-UFMC achieve 1 bit/sec/Hz higher capacity than OFDM. Finally, there is no significant difference between UFMC and IIR-UFMC when $\tau > 20\%$.

When $U = 3$, UFMC can directly reduce the ICI caused by the adjacent sub-carriers attenuation whether located in the front or in the end when τ is very small. Unlike UFMC, OFDM only can protect ICI caused by the 3rd user and cannot protect ICI caused by the 1st user, as we proved in Figure 5.6(b). As we discussed before in Figure 5.3, in terms of the interference for $x_{2,2}(t)$, when we removed the CP, the L_{CP} sample time offset has been removed from $x_{3,1}(t)$ and the remaining samples from $x_{1,2}(t)$, $x_{1,3}(t)$ and $x_{3,2}(t)$ still significantly interfere to $x_{2,2}(t)$. Thus, the SINR of the 2nd user of OFDM presents low in front and high in end. Moreover, in terms of the UFMC, the maximum relative τ for $s_{2,2}(t)$ is only 10 samples, which is smaller than L_{T}. For the $s_{1,2}(t)$ or $s_{3,2}(t)$, the maximum relative time offset becomes $\tau = 20$ samples due to the jump adjacent between users. However, if we increase U e.g. to $U = 7$, the middle user of UFMC $u = 4$ will present a more constant value. It will be affected not only by the adjacent users, but also by the users in adjacent the frequency bands.

In terms of a more realistic case, the SINR performance for the random time offsets over the
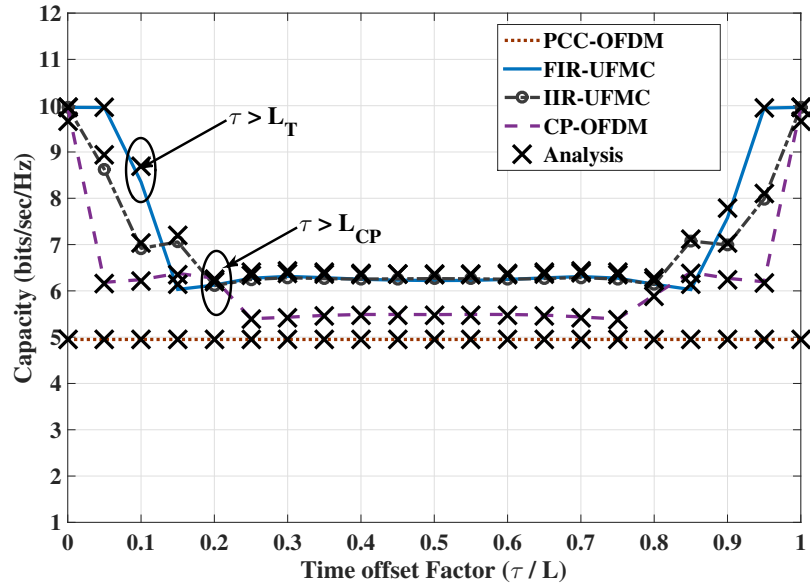
(a) Capacity Performance, 4PSK, AWGN (SNR = 30 dB)
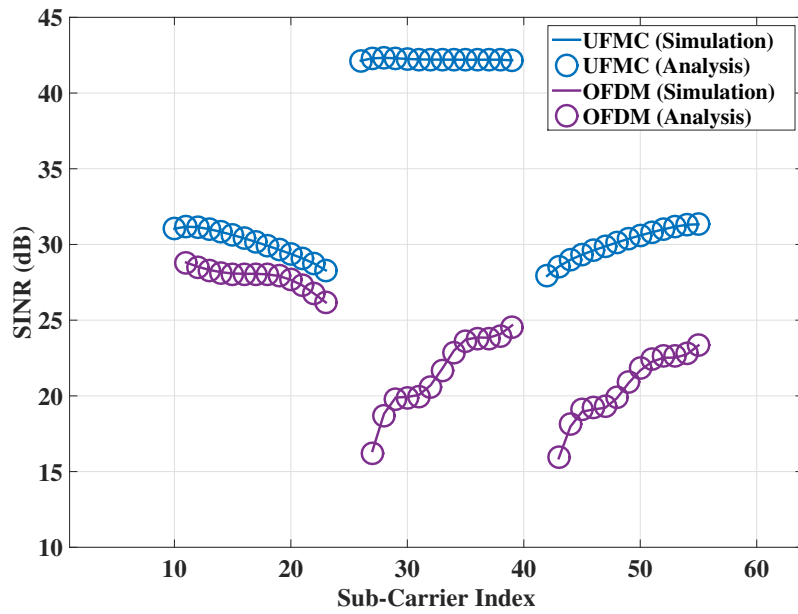
(b) SINR Performance $\tau = 10$, AWGN (SNR = 50 dB)

Figure 5.6: *Capacity and SINR Performance, $U = 3$, $N = 128$, $L_{CP} = 30$, $L_F = 31$, $U = 3$.*

AWGN channel with 30 dB is shown in Figure 5.7. Now we assume that the time delay τ is taking values over a random vector from 0 to 50 samples for adjacent users. Figure 5.7 shows that first, for the first user, UFMC can improve about 0.5 dB higher SINR compared with OFDM. The results is similar with Figure 5.6(b), the cyclic prefix of OFDM can protect against the ICI caused by the 2nd user and 3rd user. Second, in terms of the SINR performance of the 2nd user, UFMC can improve about 3 dB SINR higher compared with OFDM. The CP is no longer to protect against the interference caused by the 1st user. Similarly, for the 3rd user of the OFDM system, the CP is hard to reduce the interference caused by both the 1st and 2nd user. Third, the analytical results closely match with simulations.
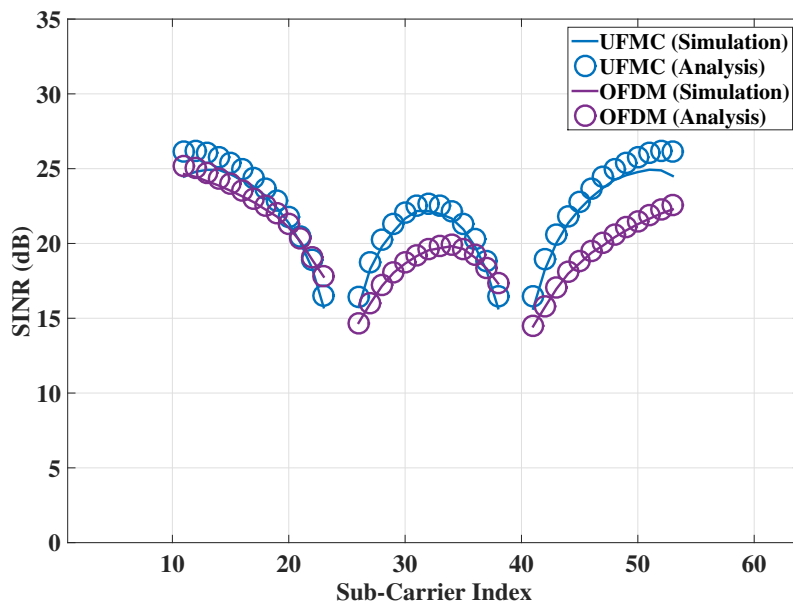
Figure 5.7: *SINR Performance for the Random Time Offsets, $\tau \in [0, 50]$ samples, with AWGN (SNR = 30 dB), $U = 3$, $N = 128$, $L_{\mathrm{CP}} = 30$, $L_{\mathrm{F}} = 31$, $U = 3$.*

5.5.3 BER Performance

The approximate BER for the OFDM and UFMC systems employing 4PSK modulation (for PCC-OFDM, 16-QAM is been simulated due to its reduced spectral efficiency) for AWGN and Rayleigh fading channels are shown in Figure 5.8(a) and Figure 5.8(b). The time offset scenarios of $\tau = 10$ are $\tau = 50$ are considered. The theoretical BER results are obtained using the proposed equations as (5.40), (5.41), (5.42) and (5.43). Again, the agreement between the
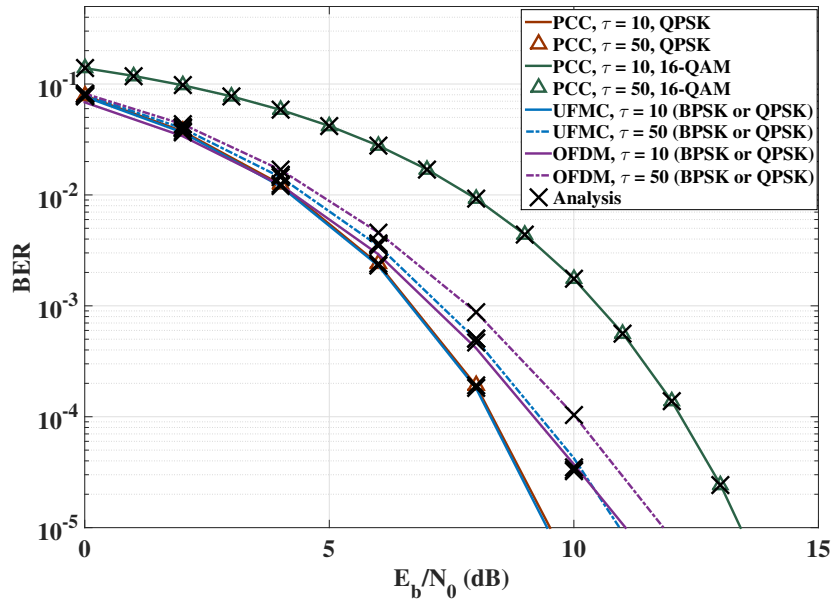
(a) AWGN BER
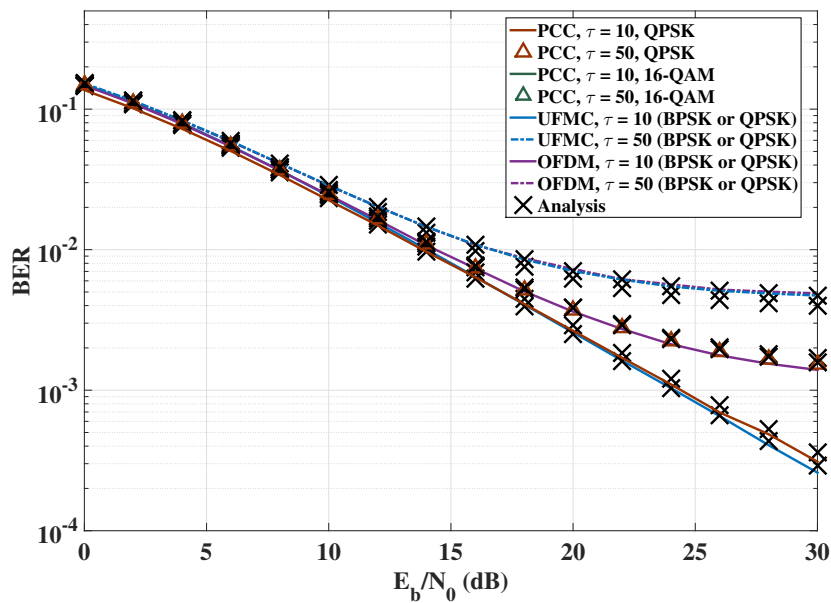
(b) Rayleigh Fading BER, without ISI

Figure 5.8: *Approximate BER Performance for AWGN and Rayleigh Fading Channels, $L_H = 10$, $U = 3$.*

analytical and simulation results is clear. The BER results show similar trends to the previous SINR results. Firstly, there is no significant BER degradation for PCC even if there is a 50 samples time offset, which means PCC-OFDM can significantly mitigate against the ICI. However, if we consider the spectral efficiency is $\eta = 2$ bit/sec/Hz, PCC will no longer to provide superior BER performance due to the requirement to use a higher order modulation scheme i.e. 16QAM. Secondly, when $\tau < L_{CP}$ or $L_F - 1$, there is no significant BER degradation for UFMC, especially when the time offset is less than 15 samples. Even when $\tau = 50$, UFMC saves about 1.1 dB E_b/N_0 compared with OFDM at a BER of 10^{-4} in the AWGN channel. Figure 5.8(b) shows that if L_H=10 and $\tau = 10$, UFMC saves about 5 dB E_b/N_0 at the BER is $10^{-2.9}$. If the τ increases to 50 samples, the BER performance of both UFMC and OFDM will degrade to the same curve.
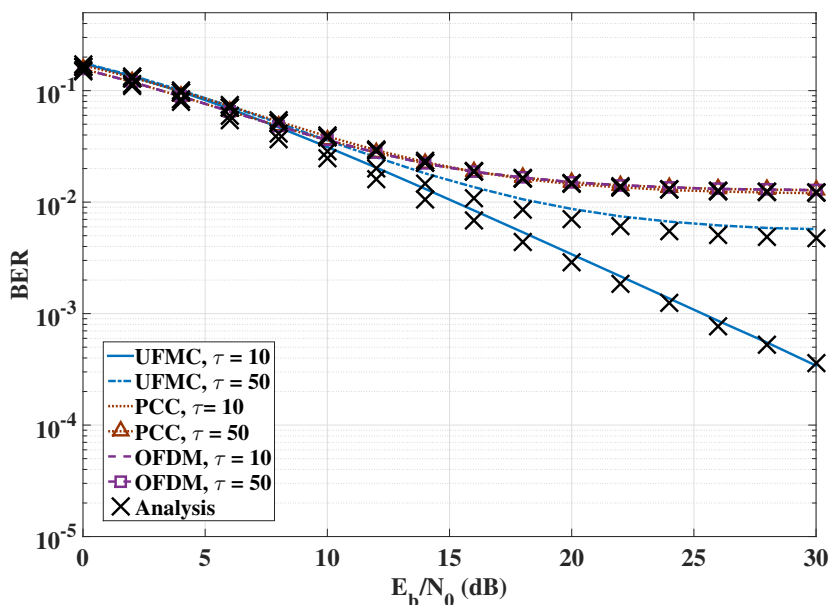
Figure 5.9: *Approximate BER and ISI Performance the Rayleigh Fading Channels, $L_H = 70$, $U = 3$, $L_{CP} = 47$ and $L_F = 48$.*

The approximate BER for the OFDM and UFMC systems in a Rayleigh fading channels with $L_H = 70$ channel taps is shown in Figure 5.9. The theoretical ISI interference is computed using (5.32) and (5.34), and simulations closely match with the analytical results. It can be seen that UFMC is more robust to very dispersive multipath channels compared with CP-OFDM especially when τ is small, i.e. $\tau = 10$ samples, UFMC provides the BER of 10^{-2} at the cost of 15 dB E_b/N_0. However, CP-OFDM hardly achieves it even increasing the E_b/N_0 to

infinity. Figure 5.9 also shows that if L_H is much longer than L_{CP}, ISI becomes the dominant interference for OFDM and the ICI caused by the time offset is somewhat smaller than ISI, i.e. when $L_H = 70$ and $L_{CP} = 47$, there is no significant differences between $\tau = 10$ and $\tau = 50$ for the OFDM systems.

Now we measure the BER performance of IIR-UFMC, as mentioned above, we use the IIR ChebyshevI filter with order of 4 and $f_{cf} = 0.18$. Here, we increase the number of transmitting users to $U = 7$ and measure the 4th user performance. The approximate BER performance over the AWGN channel with $\tau = 50$ samples and the Rayleigh fading channel for UFMC with the FIR and IIR filters are shown in Figure 5.10(a) and Figure 5.10(b). The analytical values are computed similarly as before, which the interference is analysed as the over-lapped sub-carriers from the adjacent users. The results shows that the BER performance of IIR-UFMC is slightly less than for the FIR. The reason is that we truncated the output length of IIR to equal L in terms of a fair comparison. Compared with OFDM, the BER performance of IIR-UFMC is significantly improved, especially for the Rayleigh multipath channel with the short impulse response and small τ. Again, the theoretical analysis closely matches with the Monte Carlo simulations.

5.6 Conclusion

This chapter has provided a complete time offset interference analysis for both CP/PCC-OFDM and UFMC systems and shown that firstly, PCC using a frequency guard interval significantly protect against the time offsets at the cost of reduced spectral efficiency. Secondly, UFMC provides a superior performance to OFDM (at the cost of high operational complexity) in terms of SINR, capacity and BER, especially for the Rayleigh fading multipath channel. In particular, if the time offset is less than 10 samples, there is no significant degradation in both SINR and BER for the UFMC system. Further we have proposed two methods to reduce the computational complexity. OA-UFMC provides a much lower complexity than UFMC when the filter impulse response is larger. For IIR-UFMC, the complexity is significantly reduced, while it provides a similar SINR, capacity and BER performance compared with UFMC, especially with a larger time offset.

In conclusion, even though PCC-OFDM and UFMC offered the most efficient computational performance for protecting against ICI, IIR-UFMC is attractive as it provides superior BER
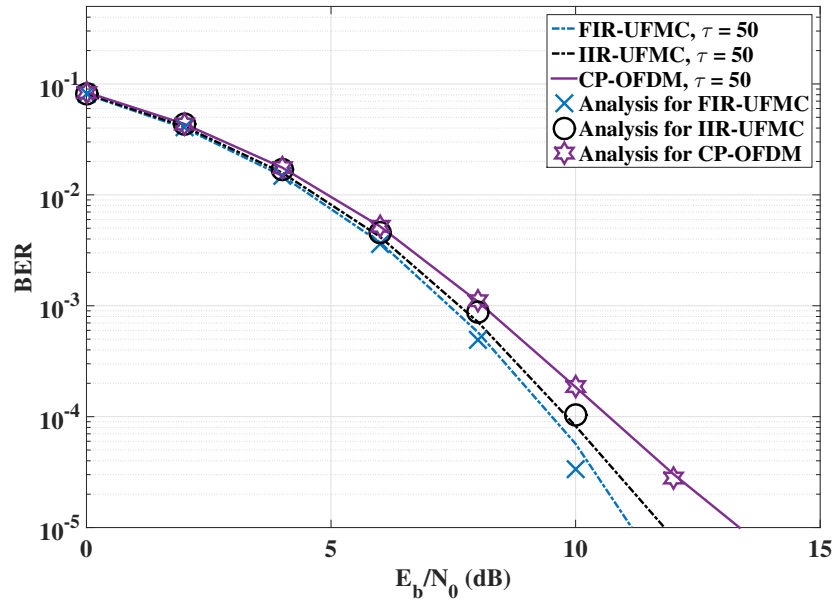
(a) AWGN BER
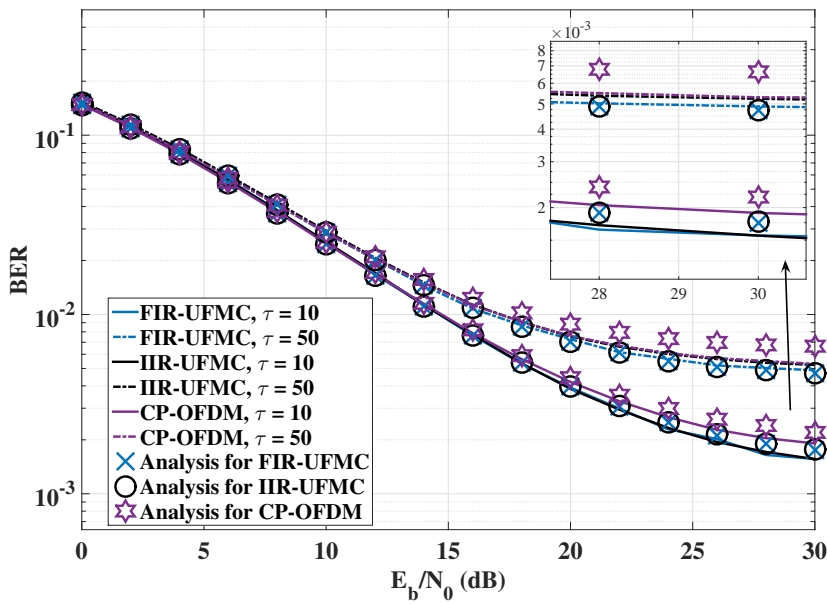
(b) Rayleigh Fading BER, without ISI

Figure 5.10: *Approximate BER Performance for FIR and IIR-UFMC, $U = 7$, $L_{\text{H}} = 10$.*

performance to CP-OFDM. IIR-UFMC achieved lower computational complexity compared with FIR-UFMC and without additional cost on spectral efficiency. We thus conclude that IIR-UFMC might be a potential waveform design for the massive machine 5G MTC scenario to support low data rate, low energy consumption and low latency transmissions.

In Chapter 6, we will summarise the key findings and contributions of this thesis. Then we will list several limitations of the thesis and several possible research areas for the future studies.

Chapter 6
Conclusions and Future Work

This thesis has contributed to both the theoretical performance analysis and the practical designs in order to achieve the cost-efficient communication systems for machine type communications (MTC). In this concluding chapter, Section 6.1 will summarise the key contributions of the thesis. Several limitations of the work and same possible suggestions for the future work will be presented in Section 6.2.

6.1 Conclusions

This thesis has studied cost-efficient MTC transmitter and receiver design for low cost MTC devices. In term of the downlink scenario, we investigated the virtual carrier (VC) receiver system in order to reduce the maximum transmission bandwidth and the number of subsequent processing operations for the low data rate MTC devices. In terms of the massive machine type communications uplink scenario, we compared and contrasted several candidate waveform designs for supporting asynchronous MTC devices. We also proposed the overlap and add universal filtered multi-carrier (OA-UFMC) and infinite impulse response (IIR)-UFMC systems in terms of reducing the high computational complexity for the UFMC transmitters. The key findings of this thesis are summarised in the following sub-sections.

6.1.1 Evaluation of Virtual Carrier Receiver Systems for Downlink

We now summarise the evaluation of the overall system performance for the VC receiver from three aspects as below :

- In terms of the bandwidth efficiency performance, our results clearly show that compared with the LTE carrier aggregation technique, the VC receiver system could provide more than 10 % bandwidth capacity improvement. Because whether a 1.4 MHz or 20 MHz channel bandwidth has been used in LTE, the number of sub-carriers for synchronisation

signals, reference signals and the physical downlink channel is very similar. We thus extracted only sub-carriers of interest using the VC receiver, which could significantly improve the bandwidth capacity.

- In terms of the energy consumption performance, we found that compared with the standard OFDM receiver, the VC receiver system significantly reduces the number of processing operations by reducing the ADC sampling rate. If an MTC terminal device only needs to decode 64 sub-carriers, the VC receiver would only consume 1/32 of the ADC operation costs compared with decoding the whole 20 MHz band, moreover, the FFT computation reduced from 11264 to only 192 operations.

- In terms of the aliasing interference protection performance, we found that a suitable filter design can reduce the aliasing interference caused by the sampling rate reduction technique used in VC. In such a case of that if we only decode the first 90 sub-carriers out of 2048, which are transmitted for the MTC devices, the VC receiver with the sampling reduction ratio of 8 provided high SINR and BER performance close to a full sample rate standard OFDM receiver.

Considering the VC receiver system has the advantages of the bandwidth capacity improvement performance, low complexity and significant protection against aliasing interference performance, we thus conclude that it could be a suitable receiver system design for supporting low data rate MTC devices.

6.1.2 Evaluation of Waveform Designs for Uplink

This compared several waveform designs for the 5G uplink scenario and we list the overall performance by a ranking table in Table 6.1. This thesis considered the performance of the side-lobe behaviour, complexity, SINR, BER and spectral efficiency. We now summarise the key findings as:

- ZP-OFDM and WOLA-OFDM systems do not provide suitable performance for the 5G uplink waveform. In terms of ZP-OFDM, it provided the very similar side-lobe levels compared with CP-OFDM (5th ranking in the table). WOLA-OFDM has the same level of complexity and provided inferior side-lobe reduction performance compared with UFMC.

	Side-lobe Behaviour	Computational Complexity	SINR	BER AWGN	BER Multipath	Spectral Efficiency
CP-OFDM	5th	1st	4th	4th	4th	Same
ZP-OFDM	5th	1st	-	-	-	Same
WOLA-OFDM	4th	5th	-	-	-	Same
PCC-OFDM	1st	1st	1st	1st	3nd	Half
FIR-UFMC	2nd	5th	2nd	2nd	1st	Same
IIR-UFMC	3nd	4th	2nd	2nd	1st	Same

Table 6.1: *Thesis Relative Waveform Performance Summary*

- Both PCC-OFDM and UFMC systems are more suitable compared with other state of the art candidate waveform designs, but are still not perfect choices. More specifically, PCC-OFDM achieves the best performance against ICI caused by timing offset errors (1st ranking for SINR and BER in the AWGN channel) at the cost of at least halving the spectral efficiency and also suffering from high PAPR. Low spectral efficiency is not desirable for MTC devices and high PAPR increases the transmitter amplifier requirements, which does not meet the low cost requirements for MTC. UFMC improves the performance for both ICI and ISI (1st ranking for BER in multipath channel) at the cost of high computational complexity (5th ranking for the complexity), which is again not desirable for low cost MTC devices.

- Both OA-UFMC and IIR-UFMC, as the our alternative implementations of UFMC, improve the computational complexity performance. Although OA-UFMC can significantly reduce the number of complexity operations when the filter impulse response is very long, it is still much higher than standard OFDM systems. For IIR-UFMC, the complexity is significantly reduced as it provides a similar SINR, capacity and BER performance compared with UFMC, especially with a larger time offset.

Considering the overall performance of the IIR-UFMC system, it provides similar spectral efficiency and better ICI protection performance compared with OFDM, moreover, it significantly reduces the complexity operations compared with UFMC. We thus conclude that IIR-UFMC might be a potential waveform for massive machine 5G communications scenarios providing low data rates, low cost and low latency.

6.1.3 Contributions on Theoretical Analysis

In this thesis, we derived the closed-form expressions for the aliased interference caused by reducing the sampling rate at the VC receiver and also derived the closed-form expressions for the ICI caused by asynchronous time offsets. First, our interference equations can be easily used in SINR, BER and capacity equations, where the results were perfectly matched with simulations. Second, our theoretical equations accounted for the interference at each sub-carrier location, which helps system designers to evaluate the parameter designs (i.e. cut-off frequency, passband ripple, stopband attenuation, filter order and sampling rate) in order to balance the energy cost and system detection performance.

We can thus conclude that this thesis has analytically and numerically studied the system transmitter and receiver design for supporting the low data rate MTC devices in future communication systems. The VC receiver system, as the bandwidth reduction technique, could be one option for the MTC downlink channel. Simultaneously, the IIR-UFMC approach is a new potential waveform design, which could be used for the uplink channel.

6.2 Future Work

Due to the limited time and space, there are several limitations of this thesis. Thus, in the end of this thesis, we introduce several potential research areas for moving forward into future study.

6.2.1 Analyse the Set-up Costs of The VC System

In Chapter 3, we only provided an ideal synchronisation scheme for the VC system, which aimed to enable users to be synchronised at the subframe level. The VC control signal (VCCS) would map into the sub-carriers and provide the VC carrier locations, filter parameters and sampling reduction ratio. However, this thesis did not study the required number of sub-carriers needed for VCCS and its costs. Moreover, this thesis did not consider the analogue processing required for the VC system. In terms of a more reliable and realistic performance analysis, we might pay more attention to realistic algorithms for the VC synchronisation scheme and analyse the IIR operation costs.

6.2.2 Analyse the Quantisation Noise for the VC System

In Chapter 3, in terms of simplicity, we did not consider in detail the effects of the quantisation noise. For a realistic system, the effect of uniform quantisation can often be modelled by an additive noise term due to the ADC quantisation processing. In terms of a more accurate result, it will be necessary to extend the analysis of relationship between the quantisation noise, sampling rate and cut-off frequency.

6.2.3 Use a More Accurate Power Model

Power consumption is very critical for efficient deployment of MTC, especially in case of massive MTC. In order to simplify our results, the thesis has not considered a realistic and more accurate power consumption model for the MTC receiver and transmitter system designs, such as the power consumption of the synchronisation activities and the decoding costs during. Reference [108] proposes a low-complexity method for symbol synchronisation based on the LTE system. A thorough analysis is conducted for all possible sampling frequencies that reduce the computational complexity of LTE cell search. Several papers focus on the power consumption during the data transmission, e.g. the power amplifier costs and the relationship between modelling accuracy and the number of samplings is mentioned in Reference [109] and a detailed power consumption model of the MTC is listed in Reference [110]. Therefore, future studies could analyse the overall VC receiver and IIR-UFMC systems performance based on those power models in order to provide a more accurate power saving evaluation.

6.2.4 Optimise the Bandwidth and the Number of Sub-carriers For MTC

Future studies should focus on the optimisation between the number of sub-carriers and the bandwidth based on the current LTE downlink or uplink channel. In the thesis, we assumed a fixed number of sub-carriers for all the transmitted users, i.e. in Chapter 4 & 5, all MTC devices transmit a fixed number of sub-carriers (such as 13 sub-carriers) through a 1.4 MHz uplink bandwidth. However, this is not realistic for the data transmissions. Future studies could focus on the optimisation between the bandwidth efficiency and the number of sub-carriers for each user. A basic algorithm can be proposed as: first, detect the required data rate and the channel condition. Second, compute the number of sub-carriers in order to achieve a signal quality requirement, i.e. the number of sub-carriers for the synchronisation, the number of sub-

carriers for achieving the bit rate and the number of sub-carriers for the channel estimation, etc. Third, assign individual channels to individual MTC devices.

6.2.5 Normalise a More Realistic Distribution for the Time Offset Model
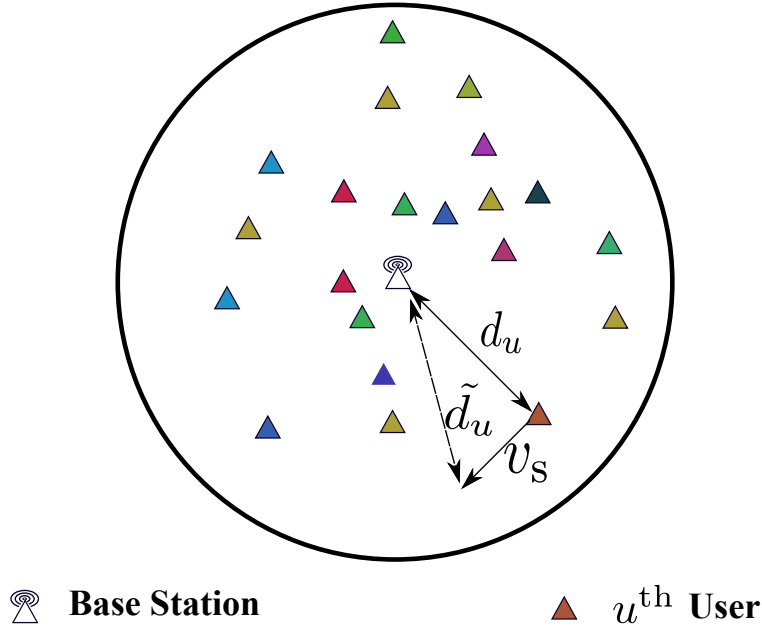
Figure 6.1: *Enhanced Time Offset Model for the Multi-users Transmission*

In Chapter 4 and 5, we studied the interference, which arises for significant time offsets. In detail, we assumed the transmitted signal length in samples in the time domain is $L = N + L_{CP} = 128 + 30 = 158$ samples, then a large time offset between each user is set to be $\tau = 50$ or 70 samples. Thus, we considered a fixed integer time-offset in samples and aimed to analyse the worse case. However, it is not realistic.

An example of our potential enhanced time offset scenario is shown in Figure 6.1. The triangles with different colours represent different users. First, for a simpler time offset scenario we may assume that each user is stationary. The distance d_u between the uth MTC terminal device and the base station can be measured statistically. Thus we can normalise the distance distribution in order to extend the normalised time offset distribution. Second, if considering a more complex scenario, it might also be necessary to account for the velocity v_s. Different type of MTC devices could have variable velocity, which can cause more complex time offset interactions. If this can be analysed, our interference analysis will be more useful for system design.

Appendix A
Original Publications

The list comprises publications that have been published or submitted.

A.1 Journal papers

- S. Wang and J. S. Thompson, "Performance analysis of VC receiver systems for M2M communications using orthogonal frequency-division multiple access," *IET Communications*, vol. 10, no. 16, pp. 20612070, 2016.

- S. Wang, J. S. Thompson, and P. M. Grant, "Closed-Form Expressions for ICI/ISI in Filtered OFDM Systems for Asynchronous 5G Uplink," has been submitted to *IEEE Transactions on Communications*, Under Review

A.2 Conference papers

- S. Wang and J. S. Thompson, "Signal Processing Implementation of Virtual Carrier for Supporting M2M systems Based on LTE," *2015 IEEE 81st Vehicular Technology Conference (VTC Spring)*, Glasgow, UK, pp. 1-5, May. 2015.

- S. Wang, J. Armstrong, and J. S. Thompson, "Waveform Performance for Asynchronous Wireless 5G Uplink Communications," *2016 IEEE 27th Annual International Symposium on Personal, Indoor, and Mobile Radio Communications (PIMRC) Workshops*, Valencia, Spain, pp. 1-6, Sept. 2016.

The accepted and published original publications are included in the following pages.

Performance analysis of VC receiver systems for M2M communications using orthogonal frequency-division multiple access

Shendi Wang ✉, *John S. Thompson*

Institute for Digital Communications, Joint Research Institute for Signal and Image Processing, The University of Edinburgh, Edinburgh, UK, EH9 3JL
✉ E-mail: Shendi.Wang@ed.ac.uk

Abstract: With increasing demand for machine-to-machine (M2M) communications, modifying existing orthogonal frequency-division multiple access communication systems such as the long-term evolution (LTE) system to successfully support low-data rate M2M devices has become an important issue. In LTE Release 12 and beyond, the reduction of maximum bandwidth, the reduction of transmission power and the reduction of downlink transmission model should be studied for supporting low-data rate M2M communications. This paper will address one solution based on the virtual carrier (VC) concept, which aims to improve the bandwidth efficiency and cost-efficiency, using analogue filters to extract only sub-carriers of interest. This will reduce the sampling rate at the M2M analogue-to-digital converter (ADC) leading to improvements in ADC power consumption and the computational complexity. Our results indicate that the VC system can provide significant high signal-to-interference-plus-noise ratio performance without significant bit error rate degradation.

1 Introduction

Wireless communication technologies have been rapidly developing in recent years, and mobile communication has become a basic tool for modern society. The current fourth generation networks, as known as the long-term evolution (LTE) standards [1], it provides high spectrum efficiency by combining advanced multi-antenna techniques and implements the orthogonal frequency-division multiple access (OFDMA) scheme in the downlink (DL) from the base station to the mobile terminals. In terms of supporting synchronisation, LTE uses a subset of carriers to transmit DL control information in the physical DL control channel (PDCCH) [2]. With increasing the number of PDCCH, the sub-carrier efficiency will decrease. Projections for the growth machine type communication devices range up to 50 billion in the next few decades, compared with the 2 billion devices which are directly connected to the wireless communication network [3]. The communication network will shift from the existing human-to-human communication mode to the machine-to-machine (M2M) communication mode.

1.1 Motivation and related work

With the growth of automated systems such as e-health, the smart grid, smart homes and smart cites M2M communications will experience exponential growth in the next generation of mobile communication systems [4]. M2M communications is one of the most promising solutions for revolutionising [5] future intelligent wireless applications. The major idea of M2M communication system is allowing M2M terminal devices or components to be interconnected, networked and controlled remotely [6], with the advantages of low-cost, scalable and reliable technologies.

One of the major challenges for supporting M2M communications using LTE is how to reduce the processing cost to maximise the battery life of M2M terminal devices. For instance, the LTE DL channel can provide up to 20 MHz bandwidth. However, M2M communications usually require low-data rate transmission, for instance, an M2M terminal device may only be allocated 1 MHz out of the 20 MHz LTE DL channel. In this case, most of the

sub-carriers are not relevant to the M2M device. Therefore, how to reduce the energy and processing cost of LTE in order to support M2M low-cost devices with increasing the bandwidth efficiency will be a major issue for standardisation beyond Release 12 of LTE [2]. This paper will study how reduced sampling rates in M2M receiver devices can improve their energy efficiency without losing performance.

To the best of our knowledge, there are no previous works which studied reducing the LTE bandwidth in order to support low-data rate M2M communications. Reference [7] only proposes a possible solution: insert an M2M low-data rate message into the LTE DL channel and design a virtual carrier (VC) to contain the message. This VC can be separately scheduled to support low-bandwidth M2M devices and the remaining sub-carriers are designed to support high-data rate services as normal. However, [7] did neither describe a detailed system structure nor how to extract the low-data rate VC messages at the receiver.

1.2 Contributions

Considering the LTE DL capacity, we reduce the analogue-to-digital converter (ADC) costs and computational complexity by reducing the sampling rate. Our main contributions are as follows:

(i) Propose a novel reduced sample rate VC receiver system. Compared with the current LTE carrier aggregation (CA) technique, it significantly improves the bandwidth efficiency.
(ii) The VC system significantly reduces the ADC cost and computational complexity while providing high signal-to-interference-and-noise ratio (SINR) and low bit error rate (BER) performance to support low-data rate M2M devices.
(iii) Drive a closed-form expression for SINR which includes the additional interference caused by aliasing effects. Our previous study [8] shows that aliasing effects caused by the filter and the lower sampling rate ADC can reduce the VC system performance. First, our SINR analysis includes the effect of the filter cut-off frequency, the receiver ADC sampling rate and the sampling reduction ratio. Second, the BER can also be evaluated in closed

form to show the trade-off between system parameter choices and detection performance.

(iv) Drive a closed-form expression for the effect of intersymbol interference (ISI) caused by asynchronism. We also consider several cases including: very dispersive multipath channel effects on ISI and interchannel interference (ICI) plus the additional interference caused by sample timing errors.

The rest of this paper is organised as follows: Section 2 introduces the state of the art. We discuss the VC receiver system model and derive the performance analysis in Sections 3 and 4, respectively. The LTE bandwidth efficiency and analytical results comparing with different SINR and BER performance are shown in Section 5 and Section 6 concludes this paper.

2 Orthogonal frequency-division multiplexing (OFDM) system: state of the art

This section will provide a brief introduction of the standard OFDM transmitter and receiver and introduce three options to support reduced bandwidth transmissions in OFDMA for M2M devices.

2.1 Standard OFDM system

(i) *Transmitter for OFDM:* OFDM inherently provides good protection against ISI due to the long symbol cyclic prefix (CP), where the length of CP in samples is defined as L_{CP}, and it is used in cellular systems such as LTE and worldwide interoperability for microwave access [9]. Assume that the message bits are to be transmitted using OFDM modulation with N sub-carriers. Denote the frequency domain symbols by X_m, $m = 0$, 1, ..., $N - 1$. Then, the baseband signal for an OFDM symbol can be expressed as

$$x(t) = \frac{1}{N} \sum_{m=0}^{N-1} X(m) \cdot e^{j2\pi mt/N} (m = 0, 1, \ldots, N - 1), \quad (1)$$

where $X(m)$ is the fast Fourier transform (FFT) of x. The signal $x(t)$ is up-converted to radio frequency, transmitted and propagates through the wireless channel.

(ii) *Model for the standard OFDM receiver:* The transmitted signals will go through a wireless channel and the impulse response can be
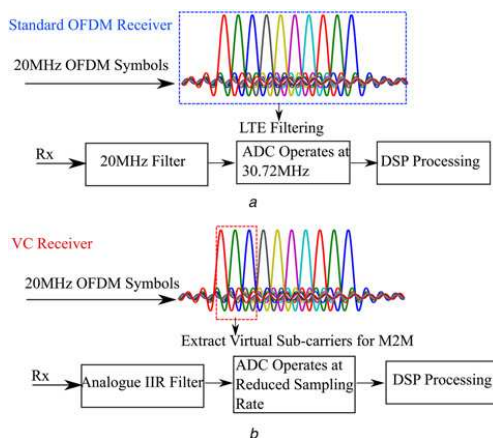
modelled as

$$h_i = \sum_{j=0}^{J-1} h_{ij} \delta(t - jT_s), \quad (2)$$

where i is the time index, and each channel tap h_{ij} follows the Rayleigh distribution, T_s is the sample period, and $\delta(t)$ is the Dirac delta function [For the additive white Gaussian noise (AWGN) channel without multipath, $J = 1$, $h_{ij} = 1$.]. The received signal over the Rayleigh multipath channel and AWGN channel can be defined as $y(t)$

$$y(t) = x(t) \otimes h_i + g_o(t), \quad (3)$$

where $\otimes$ denotes the convolution operation and $g_o(t)$ represents AWGN with power spectral density $N_0/2$ is assumed. For a standard OFDM receiver as shown in Fig. 1*a*, the received signal is match filtered and sampled at frequency f_s. After removing the CP and applying the FFT, the frequency domain signal can be expressed as

$$Y(m) = X(m) \cdot \boldsymbol{H}(m) + G_o(m), \quad (4)$$

where $\boldsymbol{H}(m)$ is the FFT of the vector $[h_{i0}, h_{i1}, \ldots, h_{i,J-1}]$ and G_o is the FFT of the noise sequence g_o in the frequency domain. Finally, to decode the transmitted messages, zero forcing equalisation [10] can be used to estimate the transmitted data.

2.2 Options to reduce OFDMA bandwidth for M2M devices

To support low-data rate communications, the maximum bandwidth of OFDMA systems such as LTE should be reduced. Reference [7] lists three possible solutions including separate carrier (SC), CA and VC:

(i) *Separate carrier:* The easiest way to reduce the maximum bandwidth is to separate a high-bandwidth carrier into several narrower band carriers to support low-bandwidth M2M devices. For instance, a 20 MHz bandwidth carrier can be split into several 1.4 and 3 MHz carriers. Low-bandwidth M2M devices transmit and receive messages on each SC and all narrow bandwidth M2M devices share the same OFDMA channel. However, the SC option will no longer support full bandwidth 20 MHz data transmissions and data capacity will be limited by the maximum bandwidth carrier.

(ii) *Carrier aggregation:* One of the key features for LTE-advanced is the CA technique [11]. It allows a user equipment to receive data on multiple carriers simultaneously. To support low-data rate M2M communication devices in LTE, one 20 MHz band can be formed by component carriers of bandwidths 1.4, 3 and 15 MHz. The low bandwidths support M2M communications, and the high-bandwidth carriers such as 15 MHz can support high-data rate transmissions. However, CA does not improve the bandwidth efficiency, as each sub-band still needs several carriers to support synchronisation of the DL channel.

(iii) *VC:* Here the transmitter insets a VC to carry the M2M messages into a 20 MHz DL OFDMA channel to support low-cost devices. High-data rate devices can still use the remaining carriers.

In Section 5, it will be shown that compared with SC and CA, by using a VC mapped into a 20 MHz band the transmitter obtains the highest bandwidth efficiency but the receiver ADC power cost reduces linearly with reduced sampling rate. In the following sections, this paper will study the VC receiver system in detail.

Fig. 1 *Standard OFDM receiver and VC system receiver*

133

3 Virtual carrier system

This section will introduce the proposed VC receiver system then analyse the LTE DL efficiency and the ADC energy cost performance. We assume that the filter information has been transmitted through the PDCCH channel to each terminal devices.

3.1 Sub-sampling receiver for VC option

To improve OFDMA bandwidth efficiency, this paper studies a novel receiver system supporting M2M communications. The principle of the VC receiver is shown in Fig. 1*b*. With the assumption that the standard OFDMA receiver received a set of messages over a 20 MHz channel bandwidth, the signal will pass through a 20 MHz analogue circuit filter and then be passed to an ADC with a higher sampling rate, e.g. 30.72 MHz as in LTE. Unlike the traditional OFDMA receiver, the major feature of the VC receiver system is improving the bandwidth efficiency by integrating both low-data rate M2M messages and high-data rate wideband messages in one DL channel. M2M receivers can reduce the ADC processing cost by reducing the receiver's bandwidth to capture only the M2M sub-carriers of interest and filter out other sub-carriers. Therefore, a VC receiver implements one or more narrowband infinite impulse response (IIR) filters to extract the transmitted M2M signals from the received OFDMA signal. It operates the ADC at a much lower sample rate to reduce the power consumption and the number of subsequent digital signal processing computations to decode the signal. The scenario where an M2M receiver has received a 20 MHz bandwidth LTE signal but only a few sub-carriers (e.g. 70 carriers) are used for this terminal device is shown in Fig. 1*b*. A standard 20 MHz LTE bandwidth maps to an FFT size of 2048 with a sampling rate of 30.72 MHz. Therefore, the useful sub-carrier rate R_U for the M2M device can be calculated as the number of VC sub-carriers (70) divided by the total number of sub-carriers (2048), which is $\sim 1/32$ in this case. Thus, a 0.625 MHz low-pass filter (LPF) can be designed to extract the relevant sub-carriers from the 20 MHz bandwidth signal. A correspondingly lower sampling rate ADC is used at the LPF output; in this case, we can choose a 0.96 MHz sampling frequency ADC instead of 30.72 MHz.

3.2 Mathematical model of the VC receiver

The VC receiver block diagram is shown in Fig. 2. The major function of the VC receiver system is to demodulate only sub-carriers of interest. Therefore, the major difference of the VC receiver compared with a standard OFDM receiver is that the received signals are passed to a narrowband IIR filter which separates the VCs from the rest of the OFDM sub-carriers, then samples those carriers using a much lower sample frequency ADC. To determine the SINR performance, the narrowband IIR filter can be approximately expressed as a finite impulse response (FIR) filter with the impulse response written as b_l with length of L_F. Denote the composite effect of the multipath channel and the

IIR filter by $w_{cn}(t)$

$$w_{cn}(t) \simeq h_i \otimes b_l = \sum_{z=0}^{Z-1} w_{cn}(z)\delta(t - zT_s), \tag{5}$$

where Z is the length of the combined channel impulse response. In the rest of this paper, every combined filter is approximated as being FIR. The received signal after an IIR filter can be designed as r_{LPF}

$$\begin{aligned} r_{LPF}(t) &= \{x(t) \otimes h_i + g_o(t)\} \otimes b_l \\ &= x(t) \otimes w_{cn}(t) + g_o'(t) + i_A(t) + q(t). \end{aligned} \tag{6}$$

Equation (6) shows that the receiver filter b_l may increase the delay spread of the channel filter h_i. The scalar $i_A(t)$ is the aliasing noise (due to the effect of the narrowband filter and the reduced sample rate processing) and $q(t)$ is the quantisation noise. For a realistic system, the effect of uniform quantisation can often be modelled by an additive noise term due to quantisation noise, which is uncorrelated with the input signal and has zero mean and a variance of $q^2/12$, where q is the quantisation step size [12]. To simplify the analysis results, this paper will assume that the aliasing effect dominates over the quantisation noise. Transforming w_{cn} into the frequency domain yields the following expression for the frequency response of sub-carrier m

$$W_{cn}(m) = \sum_{n=o}^{Z-1} w_{cn}(n) \cdot e^{-j2\pi mn/N}. \tag{7}$$

In terms of reducing the ADC cost and the number of subsequent digital signal processing computations, the VC receiver system employs a much lower sampling rate f_{vc} rather than the standard sampling rate f_s, thus the sampling reduction ratio γ can be defined as

$$\gamma = \frac{f_s}{f_{vc}}. \tag{8}$$

With the effect of the analogue IIR filter and reduced sampling rate ADC, the number of operating sub-carriers has been reduced to $K = N/\gamma$, which means the VC receiver FFT size is reduced to N/γ. Assuming that the length of the CP in samples is longer than combined channel and filter response, and the signal is sampled with the correct timing, the received M2M signal in the frequency domain after CP is removed can be denoted as

$$\begin{aligned} R(k) &= \beta \cdot X(k) \cdot W_{cn}(k) + \beta \cdot G_o(k) + I_A(k) \\ &(k = 0, 1, \ldots, N/\gamma - 1). \end{aligned} \tag{9}$$

where I_A is the aliasing term and the term β is the scaling mismatch factor between the transmitter and the receiver and reflects the different sample rates and FFT sizes at these two devices. Given that this scaling mismatch factor affects both the signal and
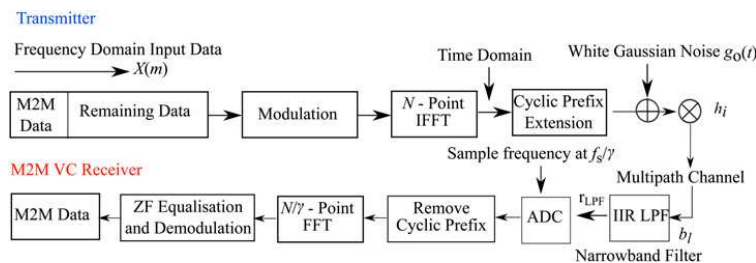

Fig. 2 *Block diagram of the VC receiver system*

the noise equally, then we can neglect it and assume $\beta = 1$ without loss of generality. The transmitted M2M signal in the frequency domain $\hat{X}(k)$ can be estimated using zero forcing equalisation as

$$\hat{X}(k) = \frac{R(k)}{W_{\mathrm{cn}}(k)}. \tag{10}$$

3.3 LTE DL efficiency

The LTE DL bandwidth directly relates to the overall transmission efficiency of the system as this determines the proportion of data sub-carriers in a radio frame. In the LTE DL channel, in terms of providing good signal synchronisation performance, it uses several synchronisation channels such as the primary synchronisation channel, the secondary synchronisation channel and the PDCCH channel. However, those SCHs will share lots of sub-carriers. To estimate the LTE DL channel bandwidth efficiency, the percentage capacity of the LTE frequency-division duplex DL channel is computed as

$$C = \frac{N_{\mathrm{A}}}{N_{\mathrm{T}}} \times 100\%, \tag{11}$$

where we assume that a 10 ms radio frame is divided into 20 equal size slots of 0.5 ms [13]. A subframe consists two consecutive slots, and therefore one 10 ms radio frame contains ten subframes. *CSC* is the capacity of one 10 ms LTE FDD radio frame, N_{A} is the number of available sub-carriers and N_{T} is the number of total occupied sub-carriers in one frame, which can be computed from [14]. The standard LTE DL channel bandwidth is 1.4, 3, 5, 10, 15 or 20 MHz.

3.4 Synchronisation for the VC system

As mentioned above, cell synchronisation is the very first step when an M2M device wishes to connect to a cell. LTE users first find the primary synchronisation signal (PSS) [2] which is located in the last OFDM symbol of first time slot of the first subframe as shown in Fig. 3. This enables users to be synchronised at the subframe level. In the next step, the terminal finds the SS signal (SSS) which determines the physical layer cell identity group number. To decode the VC message, a VC control signal (VCCS) should be included in the VC carrier as shown in Fig. 3. The VCCS includes the VC carrier locations, filter parameters and sampling reduction ratio. When the VCCS has been decoded, the M2M terminal devices can easily decode the received signals intended for it. The VCCS can be also mapped into the VC carrier to assist the M2M receiver in maintaining accurate symbol timing. The VC system decoding processing is as below.
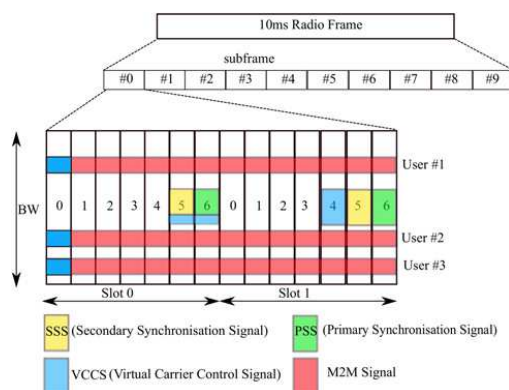
Fig. 3 *VC synchronisation signals*

Processing 1: *VC synchronisation steps*:

Step 1: Search for the PSS and the SSS.
Step 2: Decode the VCCS to identify VC carrier location.
Step 3: Set filter parameters and receiver sampling rate.
Step 4: Decode received M2M messages from the specified VC location.

3.5 Energy saving for the VC receiver

The basic motivation for the VC system is the fact that for an ADC, the power dissipation is a linear function of the sampling rate. A previous study [15] derived the power dissipation of an ADC as P_{o}

$$P_{\mathrm{o}} = 48 k_{\mathrm{B}} T_{\mathrm{Temp}} \cdot 2^{2V} \cdot f_{s}, \tag{12}$$

where k_{B} is Boltzmann's constant, T_{Temp} is the temperature, f_{s} is the sampling frequency and V is the signal-to-noise ratio (SNR)-bits, which is given by [15]

$$V = \frac{\mathrm{SNR[dB]} - 1.76}{6.02}. \tag{13}$$

Therefore, the ADC power dissipation presents a linear reduction by reducing the sampling frequency.

In terms of the FFT computational complexity, compared with the standard OFDM system, the VC receiver also reduces the number of subsequent digital signal processing computations. The computational complexity for the standard OFDM receiver C_{OFDM} can be defined as [16]

$$C_{\mathrm{OFDM}} = \frac{N}{2} \log_2 N, \tag{14}$$

where N is the size of FFT for the original OFDM receiver. In terms of the VC receiver system, the received M2M low-data rate messages after filtering with a lower sampling rate ADC, the FFT size can be decreased to N/γ. Therefore, the computational complexity for the VC receiver system can be defined as

$$C_{\mathrm{VC}} = \frac{N/\gamma}{2} \log_2 (N/\gamma). \tag{15}$$

4 Performance analysis

In terms of computing the overall SINR performance of the VC receiver system, this paper will focus on three distinct channel scenarios to evaluate system performance. This paper will not consider the effect of time or frequency offset, thus, we make the assumption of the perfect sampling timing.

4.1 No channel effect SINR analysis

First, we evaluate a simple scenario, in order to evaluate only the effects of filter aliasing in $i_{\mathrm{A}}(t)$, which is computed by the analogue filter response and the reduced sampling rate ADC in the VC receiver (see Fig. 2). We assume the received M2M message $y_{\mathrm{F}}(t)$ is not corrupted by background noise ($G_{\mathrm{o}} = 0$) or multipath channel effects. The received signal can be expressed as

$$y_{\mathrm{F}}(t) = x(t) \otimes b_i(t). \tag{16}$$

With the assumptions of perfect sampling timing, a sampling reduction rate of γ and the case that the CP duration is longer than filter impulse response $b_i(t)$, then we can write down an expression for the FFT output of $y_{\mathrm{F}}(t)$, after the CP is removed. The mth

135

frequency bin can be denoted as [17]

$$y_F(m) = \sum_{n=0}^{N-1} X(n) \cdot B(n) \cdot e^{-j2\pi nm/K}$$
$$= \sum_{k=0}^{K-1} \left(\sum_{a=0}^{\gamma-1} X(aK+k) \cdot B(aK+k) \right) \cdot e^{-j2\pi km/K}, \quad (17)$$

where $B(n)$ is the nth bin of the Fourier transform of the filter impulse response b_i. Therefore, the received k sub-carrier signal after reducing the sampling rate in the frequency domain can be written as

$$R_F(k) = \sum_{a=0}^{\gamma-1} X(aK+k) \cdot B(aK+k). \quad (18)$$

After reducing the sampling rate at the receiver, there are γ copies of the original OFDM signal centred at frequencies 0, f_s/γ, $2f_s/\gamma$, ..., $(\gamma-1)f_s/\gamma$. The 0 frequency term is the desired spectrum of the transmitted signal $x(t)$ while the remaining frequencies represent undesired aliased components. Thus, (18) can be re-written as

$$R_F(k) = X(k) \cdot B(k) + \sum_{a=1}^{\gamma-1} X(aK+k) \cdot B(aK+k), \quad (19)$$

The aliasing term can be expressed as

$$I_A(k) = \sum_{a=1}^{\gamma-1} X(aK+k) \cdot B(aK+k), \quad (20)$$

and it represents all the aliased interference present in the received signal.

The SINR value for the signal can be computed as

$$\text{SINR}(k) = \frac{E[S(k)^2]}{E[N_I(k)^2]}, \quad (21)$$

where $E[\cdot]$ denotes statistical expectation, $S(k)^2$ is the received signal power over at the output of the IIR filter and $N_I(k)^2$ is the interference power arising from the $(\gamma-1)$ aliased terms. Thus, the interference power for no channel effect case N_{IF} can be written as

$$E[N_{IF}(k)^2] = E\left[|R_F(k) - X(k) \cdot B(k)|^2 \right]$$
$$= \sum_{a=1}^{\gamma-1} E[X(aK+k)^2] \cdot |B(aK+k)|^2. \quad (22)$$

Thus, the theoretical SINR value at the output of the VC receiver without channel effects can be derived as

$$\text{SINR}_F(k) = \frac{E[X(k)^2] \cdot |B(k)|^2}{\sum_{a=1}^{\gamma-1} E[X(aK+k)^2] \cdot |B(aK+k)|^2}. \quad (23)$$

4.2 AWGN channel effect SINR analysis

Assume now the transmitted M2M signals go through an AWGN channel where the noise has mean zero and a noise standard deviation of $\sigma = \sqrt{f_s N_{0/2}}$. Similar to (4) and (19), the received M2M messages from the AWGN channel in the frequency domain

can be expressed as

$$R_A(k) = X(k) \cdot B(k) + \sum_{a=1}^{\gamma-1} X(aK+k) \cdot B(aK+k) + G_o(k). \quad (24)$$

Thus, the theoretical SINR value of VC receiver at k sub-carrier for the AWGN channel can be derived as

$$\text{SINR}_A(k) = \frac{E[X(k)^2] \cdot |B(k)|^2}{\sigma^2 + \sum_{a=1}^{\gamma-1} E[X(aK+k)^2] \cdot |B(aK+k)|^2}. \quad (25)$$

4.3 Multipath channel SINR analysis

This section is devoted to address the effect of multipath channels by analysing the combined impulse response w_{cn} of both the multipath Rayleigh channel and the analogue filter in (5). We consider two cases when the length of combined response is both longer and shorter than the CP length in samples:

(i) *CP longer than combined response:* Assume that an M2M receiver has received the signals over a Rayleigh multipath channel and an IIR filter has been applied at the receiver. The CP length L_{CP} is longer than the combined response and we assume the received signal is sampled with the correct timing. According to (7) and (17), the received signal in the frequency domain can be expressed as

$$y_{Lo}(m) = \sum_{n=0}^{N-1} X(n) \cdot W_{cn}(n) \cdot e^{-j2\pi nm/K} + g(m)$$
$$= \sum_{k=0}^{K-1} \left(\sum_{a=0}^{\gamma-1} X(aK+k) \cdot W_{cn}(aK+k) \right) \cdot e^{-j2\pi km/K} + g(m).$$
$$\quad (26)$$

The kth received sub-carrier in the frequency domain can be derived as

$$R_{Lo}(k) = X(k) \cdot W_{cn}(k) + \sum_{a=1}^{\gamma-1} X(aK+k) \cdot W_{cn}(aK+k)$$
$$+ G_o(k). \quad (27)$$

Thus, the average SINR value of the VC receiver over the Rayleigh fading multipath channel can be expressed as

$$\text{SINR}_{Lo}(k) = \frac{E[X(k)^2] \cdot E[|W_{cn}(k)|^2]}{\sigma^2 + \sum_{a=1}^{\gamma-1} E[X(aK+k)^2] \cdot E[|W_{cn}(aK+k)|^2]}. \quad (28)$$

(ii) *CP much shorter than combined response:* The major function of the CP is that it removes the ISI and ICI. To address the impact of the case when CP is shorter than the channel response in the VC receiver system, we need to compute both the ISI and ICI noise terms. According to a previous study [18], the ISI and ICI cause interference at the tail of the impulse response. On the basis of [18], the ISI noise for the VC receiver, in the case that the L_{CP} is shorter than the length (Z) of combined channel and filter impulse response, can be expressed as

$$N_{ISI}(k) = \sigma^2 \sum_{c=L_{CP}+1}^{Z-1} |U_c(k)|^2, \quad (29)$$

136

where $U_c(k)$ is defined as

$$U_c(k) = \sum_{c=L_{CP}+1}^{Z-1} w_{cn}(c)\,e^{-j2\pi ck/N}. \tag{30}$$

Note that the expression for $U_c(k)$ is actually for the FFT of the tail of the combined impulse response. In terms of ICI, Henkel *et al.* [18] show that the ISI and ICI have the same power spectral density. Therefore, the noise level of ICI is equal to that of the ISI. Thus, the interference power for the VC receiver system can be derived as

$$E[N_{So}(k)^2] = \sigma^2 + \sum_{a=1}^{\gamma-1} E[X(aK+k)^2]\cdot E[|W_{cn}(aK+k)|^2]$$
$$+ 2\sigma^2 \sum_{c=L_{CP}+1}^{Z-1} |U_c(k)|^2. \tag{31}$$

Therefore, the expression of the average SINR for the case where the CP is much shorter than combined response can be written as (see (32))

4.4 Asynchronous ISI analysis

In the previous sections, we assumed the received signals are perfectly synchronised and sampled at the correct timing. This section will analyse the ISI effects caused by asynchronism. Here we define τ_{Err} as the timing error in samples, which we assume is positive. Thus, interference to the first OFDM symbol $x_1(t)$ is caused by the first τ_{Err} samples from the second OFDM symbol $x_2(t)$. Then, we can write the interference term as

$$i_{Err} = \sum_{t=0}^{\tau_{Err}-1} x_2(t) \otimes b(t). \tag{33}$$

Thus, the interference term on the kth sub-carrier can be re-written using the Fourier transform as

$$i_{Err}(k) = \sum_{k=0}^{N-1} \sum_{n=0}^{\tau_{Err}-1} X_2(n)B(n)\,e^{-j2\pi nk/N}, \tag{34}$$

where $X_2(n)$ is the nth FFT output for $x_2(t)$. Then the ISI noise for timing error denoted as N_{IErr}, for the VC receiver with sampling reduction ratio of γ can be derived as

$$E[N_{IErr}(k)^2] = \sum_{a=0}^{\gamma-1} \sum_{n=0}^{\tau_{Err}-1} E[X_2(aK+k)^2]\cdot E[|B(aK+k)|^2]. \tag{35}$$

Note that (35) represents an extra timing error interference term which can be added to the denominator for our SINR equations to compute the theoretical SINR values when a specified timing error is present.

4.5 BER analysis

In terms of comparing the VC receiver BER performance with the standard OFDM receiver system, this paper will use the three BER basic LTE standard modulation schemes including quadrature phase shift keying (QPSK), 16-quadrature amplitude modulation (QAM) and 64-QAM for both the AWGN channel and the Rayleigh fading multipath channel:

(i) *Standard OFDM BER analysis under the AWGN channel:* The theoretical BER value of the standard OFDM receiver is computed as [19]

$$\mathrm{BER}_{QPSK} = \frac{1}{2}\cdot \mathrm{erfc}\left(\sqrt{\frac{E_b}{N_o}}\right), \tag{36}$$

$$\mathrm{BER}_{16\text{-}QAM} \simeq \frac{3}{8}\cdot \mathrm{erfc}\left(\sqrt{\frac{2}{5}\cdot\frac{E_b}{N_o}}\right), \tag{37}$$

$$\mathrm{BER}_{64\text{-}QAM} \simeq \frac{7}{24}\cdot \mathrm{erfc}\left(\sqrt{\frac{1}{7}\cdot\frac{E_b}{N_o}}\right), \tag{38}$$

where erfc(.) denotes the complementary error function. The relationship between E_b/N_o and SINR can be presented as

$$E_b/N_o = \frac{\overline{\mathrm{SINR}}}{N_{bs}}, \tag{39}$$

where N_{bs} is the number of bits per sample.
(ii) *Standard OFDM BER analysis under the Rayleigh multipath channel:* The theoretical BER value of normal OFDM system over the Rayleigh multipath channel is computed as [19, 20]

$$P_{QPSK} = \frac{1}{2}\left(1 - \sqrt{\frac{E_b/N_o}{1+E_b/N_o}}\right), \tag{40}$$

(see (41))

For the 64-QAM modulation, the BER expression is

$$P_{64\text{-}QAM} = \sum_{i=1}^{28} \omega_i I(a_i,\ b_i,\ \bar{\gamma},\ r,\ \rho), \tag{42}$$

where $\bar{\gamma}$ is the average SNR per symbol and coefficients ω_i, a_i, b_i are listed in a table in [21] and I is the integral representation

$$I(z) = \frac{1}{\pi}\int_{-(\pi/2)}^{(\pi/2)} e^{-z\sin\phi}\,d\phi. \tag{43}$$

5 Simulation results

This section will first evaluate the bandwidth efficiency performance and the energy saving performance by using the VC receiver system rather than a full bandwidth OFDM receiver. Then theoretical and

$$\mathrm{SINR}_{So}(k) = \frac{E[X(k)^2]\cdot E[|W_{cn}(k)|^2]}{\sigma^2 + \sum_{a=1}^{\gamma-1} E[X(aK+k)^2]\cdot E[|W_{cn}(aK+k)|^2] + 2\sigma^2 \sum_{c=L_{CP}+1}^{Z-1} |U_c(k)|^2}. \tag{32}$$

$$P_{16\text{-}QAM} = \frac{1}{2}\left(1 - \frac{3}{4}\sqrt{\frac{4\cdot E_b/N_o}{5/2+4\cdot E_b/N_o}} - \frac{1}{2}\sqrt{\frac{4\cdot E_b/N_o}{5/18+4\cdot E_b/N_o}} + \frac{1}{4}\sqrt{\frac{4\cdot E_b/N_o}{1/10+4\cdot E_b/N_o}}\right). \tag{41}$$

Table 1 Common simulation parameters

Simulation parameters						
Bandwidth	N	Transmitted f_s	L_{CP}	IIR filter order	Type of filter	Attenuation
20 MHz	2048	30.72 MHz	144	4	Butterworth	3 dB
Approximate filter impulse response						
γ	1/2	1/4	1/8	1/16	1/32	1/64
L_F	24	35	67	132	208	332
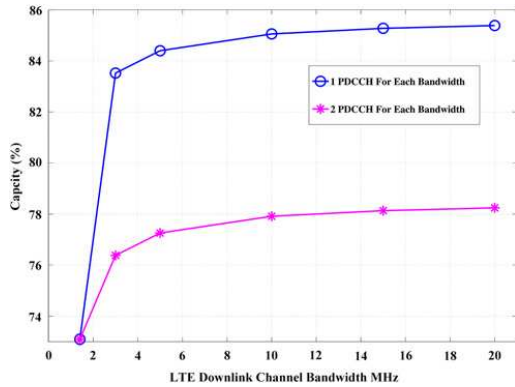
Fig. 4 *LTE DL capacity against channel bandwidth*

Fig. 5 *SINR performance over different IIR filters, AWGN channel 30 dB,*
$N = 2048$, $L_{CP} = 144$, $\gamma = 8$, 16-QAM

sub-carriers, by using an LPF and sampling rate at 0.96 MHz, it only costs 1/32 of the ADC operations compared with decoding the whole 20 MHz band and the FFT computation is reduced from 11,264 operations to 192.

5.3 SINR performance

The SINR performance of the VC receiver system over the AWGN channel with four types of IIR analogue filter (Butterworth, Chebyshev I, Chebyshev II and Elliptic filters [22]) with $\gamma = 8$ is shown in Fig. 5. The passband ripple for Chebyshev I is set to 1 dB and the stopband ripple for Chebyshev II is set to 40 dB. In the case of the Elliptic filter, the passband and stopband ripples are set to 1 and 40 dB in order to provide fair comparison. We plot the SINR value for the first 128 sub-carriers in Fig. 5 and it shows that the sub-carriers near the cut-off frequency band present significant SINR loss. It also shows that both the Butterworth and the Chebyshev I filters achieve higher SINR performance in the

Table 2 Energy saving performance of the VC system for the 20 MHz LTE channel from (14) and (15)

Sampling rate (f_s), MHz	FFT size, N	Normalised ADC power, W	FFT computational complexity, Ops
30.72	2048	1	11,264
15.36	1024	1/2	5120
7.68	512	1/4	2304
3.84	256	1/8	1024
1.92	128	1/16	448
0.96	64	1/32	192

simulation results for the SINR and BER performance will be described. Common parameters for simulations are listed in Table 1.

5.1 LTE DL efficiency performance

The result for the LTE DL capacity for one 10 ms LTE radio frame with the number of PDCCH transmissions is shown in Fig. 4. The LTE bandwidth efficiency is computed as (11) and it is obvious that whether one or two PDCCH symbols are used, the percentage capacity of 20 MHz bandwidth is much higher than other options, and the least efficient is the 1.4 MHz bandwidth carrier. We can conclude that compared with the SP and CA methods, using a VC mapped into a 20 MHz LTE band can improve bandwidth efficiency significantly.

5.2 Energy saving performance for the VC receiver

Compared with the 20 MHz LTE standard receiver, the ADC dissipation performance and the computational complexity of the FFT block for the VC receiver system is shown in Table 2. To compare the cost-efficiency, we defined the energy cost of processing the full 20 MHz bandwidth to be normalised to 1. By reducing the sampling rate of an M2M receiver, the ADC power dissipation and the computational complexity are reduced significantly. If an M2M terminal device only needs to decode 64
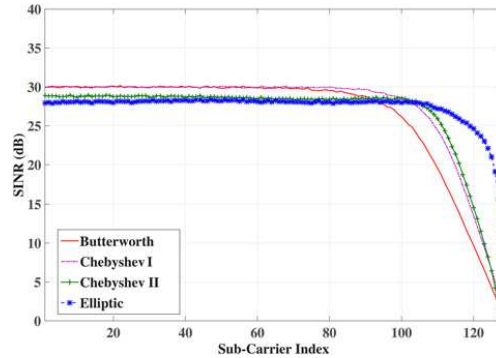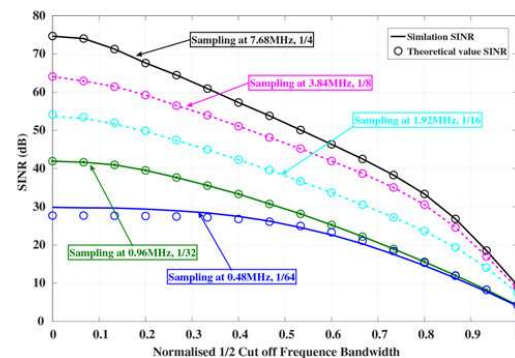

Fig. 6 *SINR performance for different sampling rate, $G_o = 0$, $h_i = 0$,*
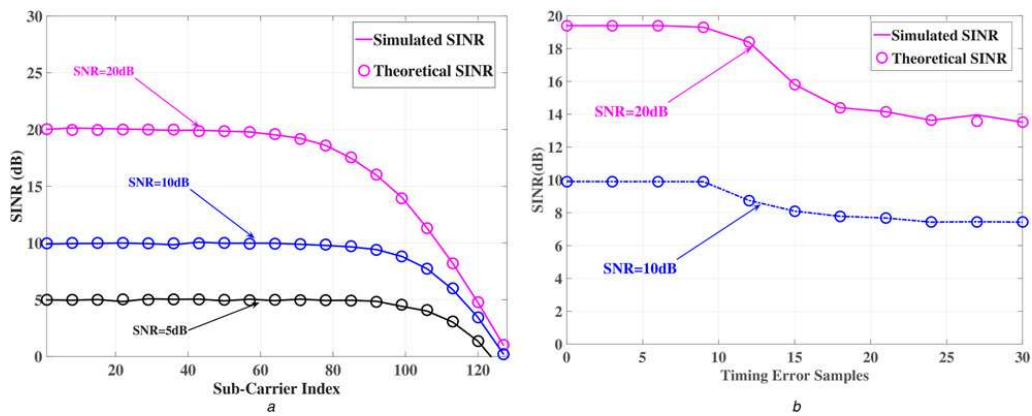*$N = 2048$, $L_{CP} = 144$, 16-QAM*

Fig. 7 *SINR performance over the AWGN channel, Butterworth, QPSK, N = 2048, L_{CP} = 144, γ = 8*

a None timing error
b With timing error

passband compared with Chebyshev II and Elliptic filters. However, the Chebyshev I filter has a worst phase response because of group delay variations at the band edges. Therefore, in order to achieve a high SINR performances in the pass band frequency, this paper will focus on the Butterworth IIR filter in the remaining simulations.

The SINR performance for different sampling reduction ratios is shown in Fig. 6 with the assumption of a 16-QAM modulation scheme and no background noise, and there is perfect time synchronisation. When γ is 64, L_F is much larger than L_{CP}. Thus, we computed the ISI and ICI noise power using (31) for γ = 64 to obtain the theoretical value of the SINR which is computed from (23). The theoretical results show a perfect match with the simulations. If the M2M receiver samples at 0.48 MHz (about 1/64 of transmitted sampling rate), the IIR cut-off frequency is set to 0.3125 MHz in order to match with the sampling reduction ratio), the SINR value of the first 65% of all sub-carriers is still above 20 dB. It also indicates that the VC receiver system is able to decode the transmitted low-data rate M2M messages mapped into a normal LTE band, even if we reduced the sampling rate by 64 times. The basic reason for the SINR performance with γ = 32 and 64 being much poorer than other cases is the non-integer sampling reduction of the CP.

The SINR degradation performance of the VC receiver system without timing error over the AWGN channel is shown in Fig. 7a. The transmitted SNR is set to 20, 10 and 5 dB. The theoretical SINR value is computed using (25) and it is closely matched with simulations. The AWGN channel does not significantly affect the SINR performance of the VC receiver. If the input SNR is 20 dB, the SINR degradation becomes apparent at sub-carrier number 80, where there is about 2 dB SINR loss. By reducing the transmitted SNR, the SINR degradation in the VC receiver moves closer to half the cut-off frequency. In terms of the first 60–70 sub-carriers, the VC receiver system presents high SINR performance. The SINR performance against timing error τ_{Err} is shown in Fig. 7b. The ISI of timing error is computed using (35), and added to the denominator of (25) to compute the theoretical SINR, which perfectly matches the simulations. When τ_{Err} is larger than nine samples, the SINR performance is significantly reduced.

The SINR degradation performance over the Rayleigh multipath channel is shown in Fig. 8. Assuming the VC receiver has received the signal over a J = 20 tap Rayleigh fading channel, the length of CP is longer than the combined impulse response and the ADC sampling follows perfect timing, the SINR performance is shown in Fig. 8a. The theoretical value of the SINR is computed using (28),
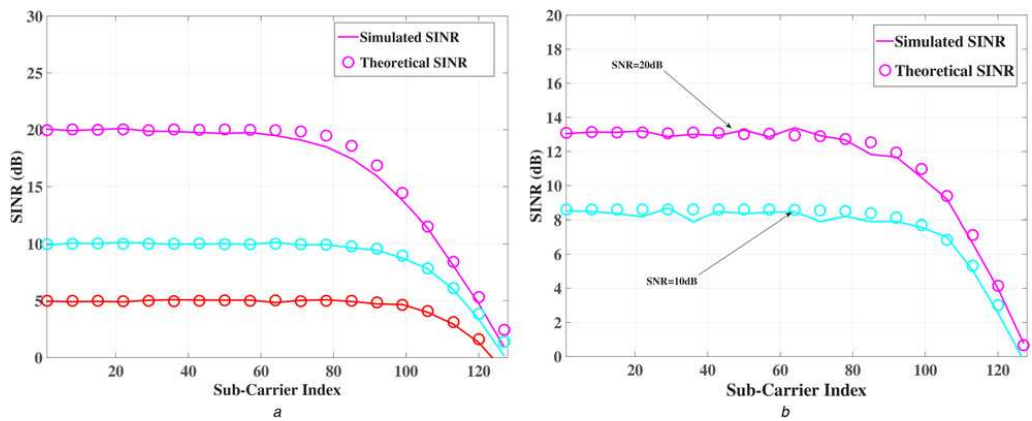

Fig. 8 *SINR degradation caused by a Rayleigh fading channel, Butterworth, QPSK, N = 2048, L_{CP} = 144, γ = 8*

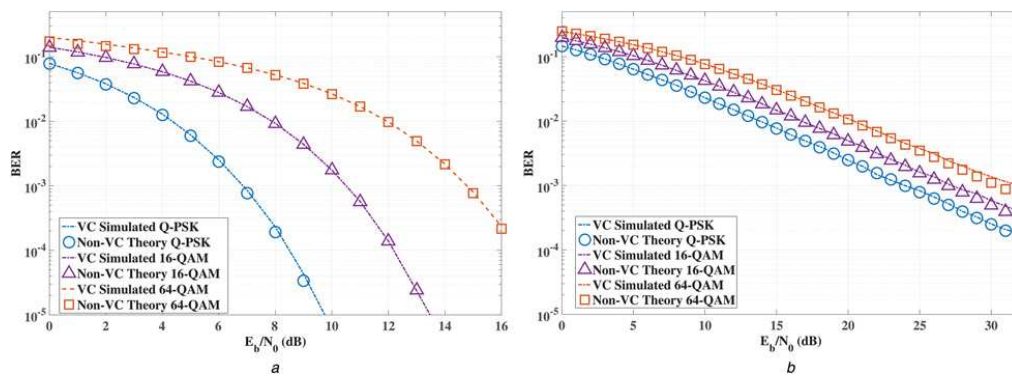*a* SINR for channel taps: 20
b SINR for channel taps: 300

Fig. 9 *BER performance of VC receiver system, Butterworth, N = 2048, L_{CP} = 144, γ = 8*
a BER performance of the VC system over the AWGN channel
b BER performance of the VC system over the Rayleigh fading channel, channel taps = 20

and similar to the AWGN channel case, the Rayleigh fading channel does not significantly affect the average SINR in the passband. Now, we increase the length of channel to 300 taps, i.e. the 'long channel'. Thus, the CP is not long enough to prevent ISI and ICI interferences as shown in Fig. 8*b*, where the theoretical value is computed using (32). It is obvious that there is a significant SINR degradation in the passband due to the ISI and ICI. For a received signal with 20 dB SNR over a 300 tap multipath channel, the average SINR of the down-sampled signal is reduced to 13 dB in the passband. Therefore, the performance of the VC receiver can be limited by increases in the number of channel taps *J*.

5.4 BER performance

In terms of testing the BER performance of the VC receiver system, we assume the transmitted M2M messages are mapped into the first 90 sub-carriers over a 20 MHz LTE channel. According to Fig. 7*a*, the SINR values of sub-carriers 1–90 would not be affected significantly by using sampling reduction ratio of γ = 8. Therefore, in this section, we will examine the BER performances of sub-carriers from 1 to 90.

The BER performance of the VC receiver over the AWGN channel is shown in Fig. 9*a*, we compared the theoretical value of the normal OFDM system derived from (36) to (38) and the simulated value of the VC system. It is obvious that the VC receiver system can achieve the same BER performance compared

with the traditional LTE receiver even when reducing the receiver ADC sampling rate. The BER performance of the Rayleigh fading channel is shown in Fig. 9*b*. The BER performance of the VC receiver system is closely matched with the normal OFDM receiver performance obtained from (40) to (42). There are slightly higher BER values for SNRs between 25 and 30 dB. The reason for that is the VC receiver system causes a small SINR degradation around sub-carrier 90, especially for high-input SNR. However, the VC receiver system still can perfectly decode the transmitted low-data rate M2M messages without significant BER degradation by using only 1/8 of the ADC power and reducing the computational complexity from 11,264 operations to 1024.

To measure the BER performance of the VC receiver affected by both ISI and ICI, this paper increased the multipath Rayleigh fading channel taps 200, 300 and 500 with L_{CP} = 144 and the result is shown in Fig. 10. The theoretical BER value is computed by substituting the SINR value from (32) into (41), which closely matches with simulations. It clearly indicates that by increasing the number of channel taps, the BER degradation will increase significantly due to the presence of ICI and ISI. When the channel taps increased to 500, the gap between the OFDM system and the VC system becomes small. This means the CP is no longer to protect the received signal against ICI and ISI. Compared with the standard OFDM receiver, the VC receiver is more sensitive to the number of channel taps *J*. Therefore, the VC receiver system might not be suitable for some very bad channel conditions, so future studies might focus on how to reduce the ISI and ICI effects while at the same time reducing the cost of the receiver.
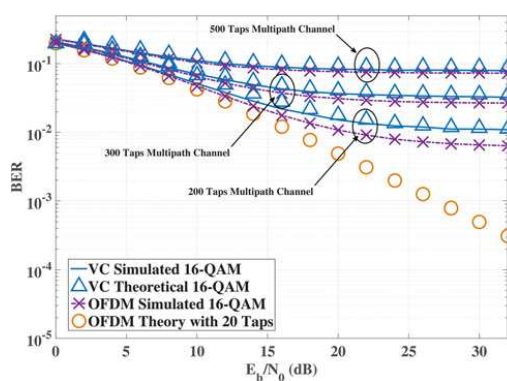
6 Conclusion

In this paper, a practical VC receiver system is proposed that uses a narrowband analogue filter and a much lower sampling rate ADC in order to extract the low-data rate M2M signals while significantly reducing the ADC power consumption and the computational complexity. To modify the existing LTE communication systems to support low-data rate M2M devices, the VC receiver can significantly improve the LTE bandwidth efficiency and cost-efficiency. At the same time, it provides high SINR and BER performance close to a full sample rate OFDM receiver for the sub-carriers of interest. Second, this paper has derived the theoretical analysis of the VC receiver performance, which perfectly match with simulations. The theoretical equations account for the effect of aliasing spread on the sub-carrier location, and this helps to the system designer to evaluate what kind of filters and receiver sampling rate can be used to balance the energy cost and detection performance. This paper highlights

Fig. 10 *BER performance over a much longer Rayleigh flat fading multipath channel, 16-QAM, γ = 8, L_{CP} = 144*

that the VC receiver system could be a suitable solution to support the M2M communications based on the LTE standard.

7 References

1 Abdullah, M.F.L., Yonis, A.Z.: 'Performance of LTE release 8 and release 10 in wireless communications'. CyberSec Conf., 2012, pp. 236–241

2 *3GPP TR 36.888, Study on Provision of Low-Cost Machine-Type Communications (MTC) User Equipments (UEs) Based on LTE*

3 Dhillon, H.S., Huang, H.C., Viswanathan, H., *et al.*: 'Power-efficient system design for cellular-based machine-to-machine communications', *IEEE Trans. Wirel. Commun.*, 2013, **12**, (11), pp. 5740–5753

4 Michailow, N., Matthe, M., Gaspar, I., *et al.*: 'Generalized frequency division multiplexing for 5th generation cellular networks', *IEEE Trans. Commun.*, 2014, **62**, (9), pp. 3045–3061

5 Lu, R., Li, X., Liang, X., *et al.*: 'GRS: the green, reliability, and security of emerging machine to machine communications', *IEEE Commun. Mag.*, 2011, **49**, (4), pp. 28–35

6 Niyato, D., Xiao, L., Wang, P.: 'Machine-to-machine communications for home energy management system in smart grid', *IEEE Commun. Mag.*, 2011, **49**, (4), pp. 53–59

7 Beale, M.: 'Future challenges in efficiently supporting M2M in the LTE standards'. WCNC Workshops, 2012, pp. 186–190

8 Wang, S., Thompson, J.: 'Signal processing implementation of virtual carrier for supporting M2M systems based on LTE'. IEEE Vehicular Technology Conf. (VTC Spring), May 2015, pp. 1–5

9 Elayoubi, S.-E., Ben Haddada, O., Fourestie, B.: 'Performance evaluation of frequency planning schemes in OFDMA based networks', *IEEE Trans. Wirel. Commun.*, 2008, **7**, (5), pp. 1623–1633

10 Au, E., Wang, C., Sfar, S., *et al.*: 'Error probability for MIMO zero forcing receiver with adaptive power allocation in the presence of imperfect channel state information', *IEEE Trans. Wirel. Commun.*, 2007, **6**, (4), pp. 1523–1529

11 Pedersen, K., Frederiksen, F., Rosa, C., *et al.*: 'Carrier aggregation for LTE-advanced: functionality and performance aspects', *IEEE Commun. Mag.*, 2011, **49**, (6), pp. 89–95

12 Widrow, B., Kollar, I., Liu, M.-C.: 'Statistical theory of quantization', *IEEE Trans. Instrum. Meas.*, 1996, **45**, (2), pp. 353–361

13 Gessner, M.K.C., Roessier, A.: 'UMTS long term evolution (LTE) – technology introduction application note. 3GPP', July 2012. Available at http://www.cdn.rohde-schwarz.com/pws/dldownloads/dlapplication/applicationnotes/1ma111/1MA1114ELTEtechnologyintroduction.pdf

14 LTE resource grid. LG Space. Available at http://www.niviuk.free.fr/lteresourcegrid.html

15 Sundstrom, T., Murmann, B., Svensson, C.: 'Power dissipation bounds for high-speed Nyquist analog-to-digital converters', *IEEE Trans. Circuits Syst. I, Regul. Pap.*, 2009, **56**, (3), pp. 509–518

16 Parhi, K., Ayinala, M.: 'Low-complexity Welch power spectral density computation', *IEEE Trans. Circuits Syst. I, Regul. Pap.*, 2014, **61**, (1), pp. 172–182

17 Mulgrew, B., Grant, P., Thompson, J.: 'Digital signal processing: concepts and applications' (Ed. Palgrave Macmillan, Basingstoke, 2002, 2nd edn.)

18 Henkel, W., Taubock, G., Odling, P., *et al.*: 'The cyclic prefix of OFDM/DMT – an analysis'. Proc. Int. Seminar on Broadband Communications, Access, Transmission, Networking, Zurich, 2002, pp. 22–1–22–3

19 Thompson, J., Smokvarski, A.: 'Bit error ratio performance of a receiver diversity scheme with channel estimation', *IET Commun.*, 2007, **1**, (1), pp. 92–100

20 Adachi, F.: 'BER analysis of 2PSK, 4PSK, and 16QAM with decision feedback channel estimation in frequency-selective slow Rayleigh fading', *IEEE Trans. Veh. Technol.*, 1999, **48**, (5), pp. 1563–1572

21 Tang, X., Alouini, M.-S., Goldsmith, A.: 'Effect of channel estimation error on M-QAM BER performance in Rayleigh fading', *IEEE Trans. Commun.*, 1999, **47**, (12), pp. 1856–1864

22 Losada, R., Pellisier, V.: 'Designing IIR filters with a given 3 db point', *IEEE Signal Process. Mag.*, 2005, **22**, (4), pp. 95–98

Closed-Form Expressions for ICI/ISI in Filtered OFDM Systems for Asynchronous 5G Uplink

Shendi Wang, *Student Member,* John S. Thompson, *Fellow, IEEE,*

and Peter M. Grant, *Fellow, IEEE*

Abstract

One of the major purposes for fifth generation (5G) communications waveform design is to relax the synchronisation requirements for supporting efficient massive machine type communications (MTC). Polynomial cancellation coded orthogonal frequency-division multiplexing (PCC-OFDM) and universal filtered multi-carrier (UFMC) are designed to reduce the side-lobes of the orthogonal frequency division multiplexing (OFDM) waveform to protect against intercarrier interference (ICI) in the 5G uplink. To the best of our knowledge, there is no analysis of the effect of ICI for the UFMC system with time offset transmissions that many arise in MTC scenarios. Furthermore, there is no study on reducing the computational complexity of the UFMC system. This paper provides closed form expressions for time offset interference in such a case for OFDM, PCC-OFDM and UFMC. This paper also presents theoretical analysis for the signal-to-interference-plus-noise ratio (SINR), capacity and bit error ratio (BER) performance. The results show that PCC-OFDM significantly protects against ICI at the cost of halving the spectral efficiency. UFMC improves the ICI and ISI protection performance, especially when the length of time offset is very small, at the cost of significantly increasing the computational complexity. Finally, this paper proposes the overlap and add UFMC (OA-UFMC) and a variant of UFMC using infinite impulse response prototype filter banks (IIR-UFMC) to reduce the processing complexity.

I. INTRODUCTION

Wireless communications researchers are developing a vision for beyond the long-term evolution (LTE), or the fourth generation of wireless communication systems (4G), to enable the roll-out of the fifth generation (5G) standard [1], which will support both human-centric and machine type communications (MTC) [2]. In addition, 5G wireless communication systems will have to be able to deal with a very diverse variety of traffic types ranging from regular high-rate traffic (e.g. mobile data downloading applications), sporadic low data rates (e.g. smart meters) and urgent low latency transmissions (e.g. real time vehicle traffic information) [3].

Orthogonal frequency division multiplexing (OFDM) has been widely used in 4G [4]. However, there are several challenging problems in the application of OFDM cellular systems to support a large number of MTC devices in the 5G uplink. First, in OFDM, the orthogonality is based on strict synchronisation between each sub-carriers, and as soon as the orthogonality is lost by multi-cell or multiple access transmission or through time-offsets between transmitters, interference between sub-carriers can become significant [5]. Second, one significant design goal for 5G is to be able to support efficiently multiple traffic types. It should be able to deal both high and low volume data transmission requirements and with synchronous or asynchronous communications [3]. Third, one key aspect of user-centric processing is for devices to be connected to multiple access points simultaneously [6]. The dynamic changes in distance between the devices and all access points require a flexible synchronised processing environment. Thus tight synchronisation, as required in LTE, appears not to be cost-effective or even possible for a multi-user 5G system for supporting thousands of subscribers in one cell [6]. Relaxing the synchronism requirements can significantly improve operational capabilities, bandwidth efficiency and even battery lifetime particularly for supporting low data rate MTC devices [5].

A. Motivation and Related Work

In order to relax the synchronisation requirements, there are several approaches to deal with asynchronous and non-orthogonal transmission, in order that the reduced side-lobe levels of the waveform will minimise intersymbol interference (ISI) and intercarrier interference (ICI).

First, polynomial cancellation coded orthogonal frequency-division multiplexing (PCC-OFDM) [7] is a frequency coding technique in which the data to be transmitted is mapped onto weighted groups of sub-carriers. PCC-OFDM has been shown to be much less sensitive than OFDM to frequency offset and Doppler spread but the spectral efficiency is at best approximately half of that for OFDM as each data symbol is mapped to at least two sub-carriers [7].

Second, filter bank multi-carrier (FBMC) is designed with a prototype filter which improves frequency selectivity. Separation of each sub-carrier through a filtering process also avoids the need for any timing synchronisation between the users [8]. If a filter is designed for each sub-carrier in FBMC, the filter impulse response length could be very long, which increases the symbol duration. Practically, this significantly increases the computational complexity, which mitigates against achieving a low cost 5G implementation.

Third, universal filtered multi-carrier (UFMC) [5], an alternative version of FBMC, groups a number of sub-carriers into a sub-band and passes the sub-band signal though a narrow sub-band finite impulse response (FIR) filter. Compared with FBMC, the processing complexity of UFMC is significantly reduced [9], but our previous paper [10] has shown that the complexity is still much higher than OFDM.

Fourth, weighted overlap and add (WOLA)-OFDM is a filtered cyclic prefix (CP) CP-OFDM waveform proposed for 3GPP in [11], which is a similar to UFMC. WOLA overlaps several samples together between the nearby time domain filtered signals to reduce the transmitted signal

144

length. However, [11] has shown that WOLA has a inferior side-lobe reduction performance compared to UFMC while requiring a similar level of complexity due to the filter banks.

B. Contributions

Previous studies have performed several comparison simulations to assess the achievable UFMC side-lobe reduction performance [12]–[14]. However, there is no paper on reducing the computational complexity for UFMC or for developing closed-form expressions for ICI and ISI in a UFMC time offset system. Moreover, there is not a detailed analysis and comparison between CP-OFDM, PCC-OFDM and UFMC waveforms to measure the overall time-offset performance. The main contributions in this paper can be summarised as follows:

1) We propose the overlap and add UFMC (OA-UFMC) system which reduces the computational complexity of the inverse fast Fourier transform (IFFT), especially for longer filter impulse responses.

2) We derive closed-form expressions for the interference caused by time offsets between adjacent unsynchronised MTC users. First, our closed-form expressions can be easily used to compute the signal-to-interference-plus-noise ratio (SINR), the theoretical Shannon capacity and the bit error ratio (BER). Second, our closed-form expressions can be used in both additive white Gaussian noise and multipath transmission scenarios.

3) We provide a detailed comparison and analysis for different filter designs, considering power spectral density (PSD), SINR, capacity, BER and computational complexity. We also measure the time offset performance when varying the number of zero sub-carriers between adjacent users.

4) We provide for the first time the ICI cancellation performance for infinite impulse response (IIR) prototype filter UFMC (IIR-UFMC) systems, using both analytical and simulation

results.

The rest of this paper is organised as follows. Section II introduces the state of the art. Section III proposes the OA-UFMC and IIR-UFMC system, and analyses the computational complexity. In Section IV, a time offset model is provided and the interference is analysed. Section V presents the numerical results and Section VI concludes the paper. In this paper, $\mathbb{E}[\cdot]$ represents the expectation operation, $\otimes$ represents the convolution operation and $(\cdot)^*$ represents the complex conjugate operation.

II. STATE OF THE ART

This section introduces the uplink scenario and the 3 basic candidate waveforms including OFDM, PCC-OFDM and UFMC transmission models. We focus on the effect of poor time synchronisation on the ICI experienced in such systems.

A. Uplink Model

We start with a simple uplink system as shown in Fig. 1. There are U users, which are allocated to different frequency carriers and they transmit simultaneously to a base station (BS). There are a total of N sub-carriers, which are divided among U users in sub-bands. Each user has a total of K available sub-carriers. Here we define L_{CP} as the length of the cyclic prefix (CP) in samples. Then the BS will receive the sum of all the transmitted signals and process it to decode the messages for all U users.

B. OFDM Transmission Model

Assume that $X_u(n)$ denotes that modulation symbol to be transmitted on the nth sub-carrier by the uth user as shown in Fig. 1(a). The baseband OFDM data signal at the output of the
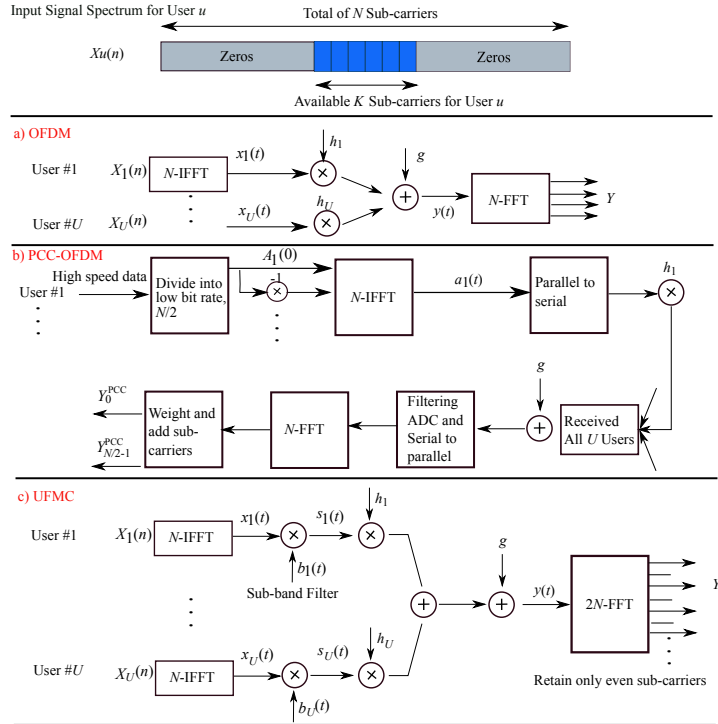
Fig. 1.   Multi-user Uplink Transmission Models for (a) OFDM, (b) PCC and (c) UFMC.

N-point IFFT and after adding the CP can be expressed as:

$$x_u(t) = \frac{1}{\sqrt{N}} \sum_{n=0}^{N-1} X_u(n) \cdot e^{j2\pi nt/N}, \ t \in [1, L-1], L = N + L_{\text{CP}} \tag{1}$$

where X is the fast Fourier transform (FFT) of x. A wireless Rayleigh multipath channel impulse response h with L_{H} taps is defined as:

$$h_u(t) = \sum_{l_{\text{H}}=0}^{L_{\text{H}}-1} h_{u,l_{\text{H}}} \cdot \delta(t - l_{\text{H}} T_{\text{s}}), \tag{2}$$

where T_{s} is the sample period and $\delta(t)$ is the Dirac delta function and each channel tap l_{H} follows the quasi-static Rayleigh distribution. Note that to simplify our analysis, we assume the number of channel taps L_{H} for each user is same. Then the received signal over the multipath

channel h in the presence of additive white Gaussian noise (AWGN), $g(t)$, can be defined as:

$$y(t) = \sum_{u=1}^{U} x_u(t) \otimes h_u(t) + g(t), \tag{3}$$

where a power spectral density $\sigma^2 = N_0/2$ is assumed for the noise samples $g(t)$.

C. PCC-OFDM Transmission Model

PCC is a frequency coding technique for OFDM in which the data to be transmitted is mapped onto weighted groups of sub-carriers. Reference [7] has shown PCC-OFDM to be much less sensitive than OFDM to frequency offset and Doppler spread. The block diagram of a PCC-OFDM system is shown in Fig. 1(b), where the baseband symbols for the uth user $A_u(0)...A_u(N/2-1)$ will pass through a PCC-OFDM modulator. In this case, pairs of sub-carriers have a relative weighting of $+1$, -1, and the input IFFT signal is organised as $A_u(0), -A_u(0)..., A_u(N/2-1), -A_u(N/2-1)$. After the N-point IFFT, the time domain samples for the uth user $a_u(t)$ can be expressed as:

$$a_u(t) = \frac{1}{\sqrt{N}} \sum_{n=0}^{N-1} A(n) \cdot e^{j2\pi nt/N}. \tag{4}$$

The received signal over the Rayleigh multipath fading channel is then expressed as:

$$r^{\text{PCC}}(t) = \sum_{u=1}^{U} a_u(t) \otimes h_u(t) + g(t). \tag{5}$$

At the receiver, the data is recovered from the FFT outputs $R^{\text{PCC}}(0)...R^{\text{PCC}}(N-1)$. The mapping of data onto pairs of sub-carriers indicate that the ICI caused by one sub-carrier is substantially cancelled by the ICI caused by the other sub-carrier in the pair. Therefore, in the receiver, pairs of sub-carriers are combined by applying the weightings and then summing:

$$Y^{\text{PCC}}(n) = \frac{R^{\text{PCC}}(2n) - R^{\text{PCC}}(2n+1)}{2}, \ (n = 0, 1, 2, ..., N/2 - 1). \tag{6}$$
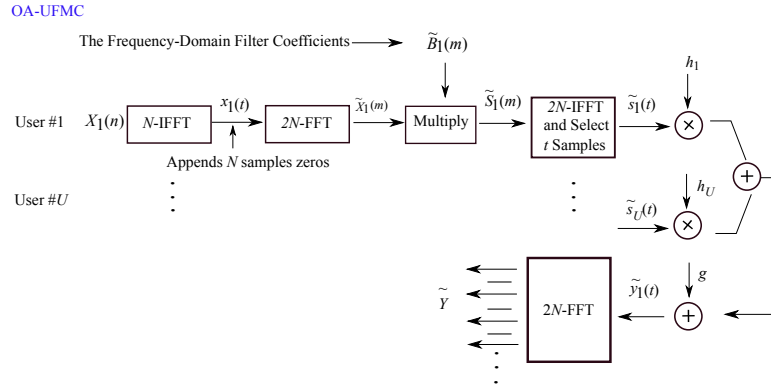
Fig. 2. Block Diagram of the OA-UFMC System.

D. UFMC Transmission Model

The block diagram of standard UFMC [6] is shown in Fig. 1. Unlike OFDM, the principle of UFMC is passing each sub-band signal through a narrow band filter. Here we define the bandpass filter impulse response as $b_u(t)$ with the number of filter taps denoted as L_{F}. Then, the time domain UFMC signal at the output of the filter can be expressed as $s_u(t)$:

$$s_u(t) = \frac{1}{\sqrt{N}} \sum_{n=0}^{N-1} X_u(n) e^{j2\pi nt/N} \otimes b_u(t), \ t \in [0, L-1], L = N + L_{\mathrm{F}} - 1 = N + L_{\mathrm{CP}}. \quad (7)$$

Note that each sub-band filter is designed as a bandpass filter, and then we design each filter's centre frequency to match the sub-band's (or user's) centre frequency. The received signal will be passed though a $2N$-point FFT to convert the time domain signal into the frequency domain. Then, we retain only even sub-carriers whose frequencies correspond to those of the transmitted data carriers [6].

III. IMPROVEMENT OF THE COMPUTATIONAL COMPLEXITY: OA-UFMC, IIR-UFMC

As mentioned above, one of the drawbacks of UFMC is that the computational complexity is significantly increased by applying digital FIR filters to achieve a faster frequency roll-off than

is required in CP-OFDM. Computational complexity is directly related to power consumption and raises practical implementation issues [15], which do not match with the desire to achieve energy efficient 5G MTC terminals. Thus, we propose the OA-UFMC system by applying the multiplication operation in the frequency domain in place of time domain convolution. We also propose the IIR-UFMC which makes use of IIR prototype filter banks. This section will now analyse the computational complexity for those two methods and compare them with standard UFMC, PCC and OFDM approaches.

A. Overlap and Add UFMC (OA-UFMC) Model

The block diagram of OA-UFMC is shown in Fig. 2, using the overlap and add technique [16] instead of the time domain convolution operation. We increase the number of samples in the frequency domain by using a $2N$-point FFT then multiply carrier-by-carrier with the frequency-domain filter coefficients. The OA-UFMC system transmission processing is shown in Algorithm 1 with a 5 step process.

Algorithm 1 *OA-UFMC Transmission Steps*

Step 1: The baseband signal $X_u(n)$ passes through the N-point IFFT block, $x_u(t)$

Step 2: Appends N samples zeros on to x_u to obtain $x_u(t^{\mathrm{OA}})$, $t^{\mathrm{OA}} \in [0, 2N-1]$

Step 3: Passes $x_u(t^{\mathrm{OA}})$ through the $2N$-point FFT block, $\tilde{X}_u(m)$

Step 4: Multiplication $\tilde{S}_u(m) = \tilde{X}_u(m) \cdot \tilde{B}_u(m)$, $m \in [0, L-1]$

Step 5: The baseband signal $\tilde{S}_u(m)$ then passes through the $2N$-point IFFT block

---

Note that there is a good reason why we do not implement directly the product $(X_u(n) \cdot B_u(n))$, where $B_u(n)$ is the N-point FFT of $b_u(t)$. This is because we need to ensure the transmitted samples are exactly the same length as $s_u(t)$ in equation (7) with a length of L samples. The

signal after the $2N$-point FFT block in the frequency domain can be expressed as:

$$\tilde{X}_u(m) = \sum_{m=0}^{2N-1} x_u(t^{\mathrm{OA}})e^{-j2\pi t^{\mathrm{OA}}m/2N}, \tag{8}$$

thus, frequency domain multiplication processing can be expressed as:

$$\tilde{S}_u(m) = \tilde{X}_u(m) \cdot \tilde{B}_u(m), \ m \in [0, L-1] \tag{9}$$

where $\tilde{B}_u(m)$ is the first L samples of the $2N$-point FFT of $b_u(t)$. After transforming $\tilde{S}_u(m)$ into the time domain through the $2N$-point IFFT, we select the first L samples to achieve the same time domain sequence as,

$$\tilde{s}_u(t) = s_u(t), \ t \in [0, L-1]. \tag{10}$$

B. IIR-UFMC

In this paper, we use IIR prototype filters instead of the FIR to reduce the processing cost. Note that, unlike linear phase FIR filters, the phase characteristic of the IIR filter is not linear [17], which can cause a signal distortion. For this reason, we design the cut-off frequency to be wider than the sub-band bandwidth to achieve an almost linear phase in the passband. The processing steps of IIR-UFMC is shown in Algorithm 2.

Algorithm 2 *IIR-UFMC Transmission Steps*

Step 1: The baseband signal $X(n)$ passes through the N-point IFFT into the time domain

Step 2: Time domain signal passes through a narrow band IIR filter

Step 3: Truncate the first L samples of the IIR filter output match $s_u(t)$ in equation (7)

Step 4: Transmit through the wireless channel

C. Computational Complexity Analysis

The main computational complexity is dominated by the number of multiplication operations that are performed. Thus, the computational complexity equations for the UFMC transmitter can be written as Γ^{UFMC}:

$$\Gamma^{\text{UFMC}} = \underbrace{\frac{N}{2}\log_2(N)}_{N\text{–point IFFT}} + (N \cdot L_{\text{F}}),\tag{11}$$

where the term of $(N \cdot L_F)$ determines the number of multiplications during the time domain convolution operation. The computational complexity for the OA-UFMC transmitter can be written as Γ^{OA}:

$$\Gamma^{\text{OA}} = \underbrace{\frac{N}{2}\log_2(N)}_{N\text{–point IFFT}} + \underbrace{2\frac{2N}{2}\log_2(2 \cdot N)}_{2N\text{–point FFT + }2N\text{–point IFFT}} + L$$

$$= \frac{N}{2}\log_2(N) + 2N\left(1 + \log_2(N)\right) + N + L_{\text{F}} - 1$$

$$= \frac{5N}{2}\log_2(N) + 3N + L_{\text{F}} - 1.\tag{12}$$

Compared with UFMC, OA-UFMC can reduce the computational complexity by:

$$\Gamma^{\text{OA}} - \Gamma^{\text{UFMC}} = (L_{\text{F}} - 3)N - 2N\log_2(N) - L_{\text{F}} + 1,\tag{13}$$

operations, and the benefit increases when increasing L_{F}.

This paper also considers IIR filters, such as Chebyshev Type I [18], to determine the ICI performance in terms of reducing the computational complexity caused by the time domain convolution operation. IIR prototype filters with a low filter order L_{Or} can achieve a similar performance compared to FIR filter, i.e. $L_{\text{Or}} = 4$. If we consider the IIR filter with the Direct Form I [19], the overall filter coefficients (both feedforward and feedback) is $(2L_{\text{Or}} + 1)$. Thus,

in this case, the computational complexity for IIR-UFMC can be significantly reduced as:

$$\Gamma^{\text{IIR}-\text{UFMC}} = \underbrace{\frac{N}{2}\log_2(N)}_{N-\text{point IFFT}} + \underbrace{L \cdot (2L_{\text{Or}} + 1),}_{L \text{ samples and IIR process}} \qquad L_{\text{Or}} < L_{\text{F}}. \tag{14}$$

Due to a similar processing required for both PCC-OFDM and CP-OFDM, the N-point IFFT computational complexity can be expressed as:

$$\Gamma^{\text{CP/PCC}-\text{OFDM}} = \frac{N}{2}\log_2(N). \tag{15}$$

IV. TIME OFFSET INTERFERENCE ANALYSIS

The time domain signal of UFMC and OA-UFMC are very similar as shown in (10). This paper considers CP-OFDM (CP-OFDM processing is very similar to PCC-OFDM as both of them add a CP guard interval [7]) and UFMC for the interference analysis. In this section, we use a simple time-offset model to analyse the interference caused by asynchronism and also consider the ISI caused in the case that the channel impulse response L_{H} is longer than the cyclic prefix length L_{CP}.

A. Time-offset Model

We assume that the received MTC signals from the U users are asynchronous and suffer from time-offsets at the base station. The time-frequency representation for time offset is shown in Fig. 3(a). To simplify our analysis we start by considering $U = 3$ users where each user transmits 3 OFDM symbols. The scalar τ is the relative delay in timing samples between adjacent users. In addition, we assume that the time offsets between each pair of adjacent users are the same. This paper focuses on decoding the 2nd OFDM symbol for each user. Here we define #1, #2 and #3 as the 1st, 2nd and 3th OFDM symbol following the notation in Fig. 3(a).
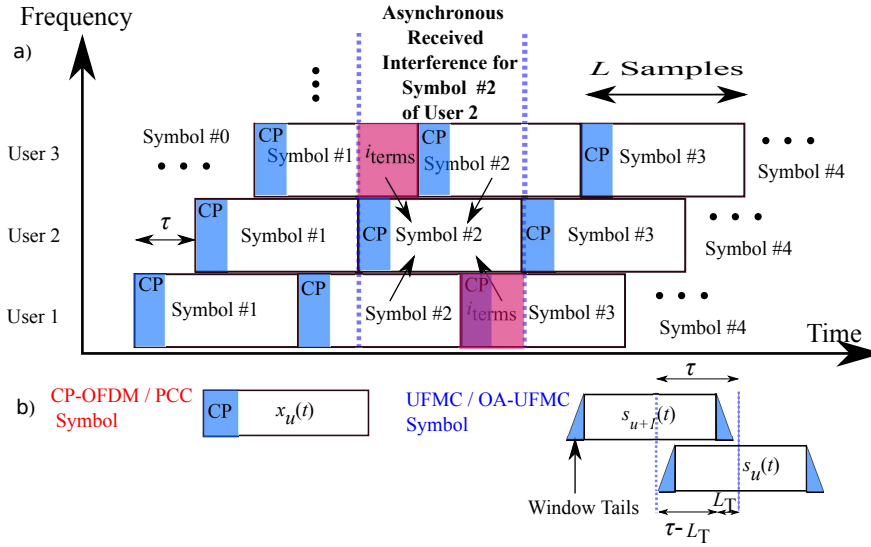
Fig. 3. (a) Time-Frequency Representation of the Time Offset Interference Model, (b) Time Domain Waveforms for CP/PCC-OFDM and UFMC.

B. ICI Analysis Caused by Time Offset

This subsection analyses the ICI interference for both the CP/PCC-OFDM and UFMC systems.

1) CP-OFDM (or PCC-OFDM) System ICI Analysis: The ICI interference for each user is caused by the OFDM side-lobes of the adjacent asynchronous users. As shown in Fig. 3(a), the interference terms for the 2nd symbol of user 2, $x_2^{\#2}(t)$, are separated into four parts: two of them arise from the adjacent time periods and two of them arise from the same time period. First, the interference of $x_2^{\#2}(t)$ from the adjacent time periods is dominated by the first τ samples from $x_1^{\#3}(t)$ and the tail τ samples from $x_3^{\#1}(t)$ as shown in red in Fig. 3(a). Thus, the time domain interference terms to the 2nd user ($u = 2$), which are caused from the different time

periods can be computed as:

$$i_2^{\text{Diff}}(t) = \sum_{l=0}^{\tau-1} x_1^{\#3}(t)\delta(t-l) + \sum_{l=L-\tau}^{L-1} x_3^{\#1}(t)\delta(t-l), \ t \in [0, L-1], \qquad (16)$$

where l is a sample index. Second, the remaining samples of $x_1^{\#2}(t)$ and $x_3^{\#2}(t)$ are nearly orthogonal with $x_2^{\#2}(t)$, which are transmitted in the same time period. If there is no time offsets, $x_1^{\#2}(t)$, $x_2^{\#2}(t)$ and $x_3^{\#2}(t)$ are orthogonal. Then, the dot product of $x_1^{\#2}(t)$ and $x_2^{\#2}(t)$ can be expressed as:

$$\sum_{l=0}^{L-1} x_1^{\#2}(t)e^{-j2\pi lt/N} \cdot x_2^{\#2}(t)e^{-j2\pi lt/N} = 0, \qquad (17)$$

thus,

$$\sum_{l=0}^{\tau-1} x_1^{\#2}(t)e^{-j2\pi lt/N} \cdot x_2^{\#2}(t)e^{-j2\pi lt/N} + \sum_{l=\tau}^{L-1} x_1^{\#2}(t)e^{-j2\pi lt/N} \cdot x_2^{\#2}(t)e^{-j2\pi lt/N} = 0, \qquad (18)$$

and then,

$$\sum_{l=\tau}^{L-1} x_1^{\#2}(t)e^{-j2\pi lt/N} \cdot x_2^{\#2}(t)e^{-j2\pi lt/N} = \sum_{l=0}^{\tau-1} -x_1^{\#2}(t)e^{-j2\pi lt/N} \cdot x_2^{\#2}(t)e^{-j2\pi lt/N}. \qquad (19)$$

Now, similarly, the time domain interference terms for $x_2^{\#2}(t)$, which are caused from the same time period can be computed as:

$$i_2^{\text{Same}}(t) = \sum_{l=0}^{\tau-1} -x_1^{\#2}(t)\delta(t-l) + \sum_{l=L-\tau}^{L-1} -x_3^{\#2}(t)\delta(t-l). \qquad (20)$$

Finally, according to (16) and (20), we can write the total interference terms for $x_2^{\#2}(t)$ in the time domain as:

$$i_2^{\text{OFDM}}(t) = \sum_{l=0}^{\tau-1} x_1^{\#3}(t)\delta(t-l) + \sum_{l=L-\tau}^{L-1} x_3^{\#1}(t)\delta(t-l) + \sum_{l=0}^{\tau-1} -x_1^{\#2}(t)\delta(t-l) + \sum_{l=L-\tau}^{L-1} -x_3^{\#2}(t)\delta(t-l). \qquad (21)$$

After removing the CP, we can rewrite (21) as:

$$i_2^{\text{OFDM}}(n) = \sum_{l=0}^{\tau-1} \big(-x_1^{\#2}(n) + x_1^{\#3}(n)\big)\delta(n-l) + \sum_{l=N-\tau+L_{\text{CP}}}^{N-1} \big(-x_3^{\#2}(n) + x_3^{\#1}(n)\big)\delta(n-l). \qquad (22)$$

Similarly, the time domain interference for the 2nd symbol of user 1, $x_1^{\#2}(t)$, after removing the

CP is:

$$i_1^{\text{OFDM}}(n) = \sum_{l=N-\tau+L_{\text{CP}}}^{N-1} \left(-x_2^{\#2}(n) + x_2^{\#1}(n)\right)\delta(n-l) + \sum_{l=N-2\tau+L_{\text{CP}}}^{N-1} \left(-x_3^{\#2}(n) + x_3^{\#1}(n)\right)\delta(n-l),$$

$$(23)$$

and for user 3, $x_3^{\#2}(t)$, is:

$$i_3^{\text{OFDM}}(n) = \sum_{l=0}^{2\tau-1} \left(-x_1^{\#2}(n) + x_1^{\#3}(n)\right)\delta(n-l) + \sum_{l=0}^{\tau-1} \left(-x_2^{\#2}(n) + x_2^{\#3}(n)\right)\delta(n-l). \quad (24)$$

Now, the frequency domain interference for the uth user can be rewritten using the Discrete

Fourier transform as I_u:

$$I_1^{\text{OFDM}} = \sum_{k=0}^{K-1} \sum_{n=N-\tau+L_{\text{CP}}}^{N-1} \left(-x_2^{\#2}(n) + x_2^{\#1}(n)\right)e^{-j2\pi nk/N} \quad (25)$$

$$+ \sum_{k=0}^{K-1} \sum_{n=N-2\tau+L_{\text{CP}}}^{N-1} \left(-x_3^{\#2}(n) + x_3^{\#1}(n)\right)e^{-j2\pi nk/N},$$

$$I_2^{\text{OFDM}} = \sum_{k=0}^{K-1} \sum_{n=0}^{\tau-1} \left(-x_1^{\#2}(n) + x_1^{\#3}(n)\right)e^{-j2\pi nk/N} \quad (26)$$

$$+ \sum_{k=0}^{K-1} \sum_{n=N-\tau+L_{\text{CP}}}^{N-1} \left(-x_3^{\#2}(n) + x_3^{\#1}(n)\right)e^{-j2\pi nk/N},$$

$$I_3^{\text{OFDM}} = \sum_{k=0}^{K-1} \sum_{n=0}^{2\tau-1} \left(-x_1^{\#2}(n) + x_1^{\#3}(n)\right)e^{-j2\pi nk/N} \quad (27)$$

$$+ \sum_{k=0}^{K-1} \sum_{n=0}^{\tau-1} \left(-x_2^{\#2}(n) + x_2^{\#3}(n)\right)e^{-j2\pi nk/N}.$$

We can conclude that the CP only can reduce the interference in the front of L_{CP} sample

time-offsets as shown in (25), where $(L_{\text{CP}} - \tau)$ error samples have been considered. When the

interference is located in the final τ samples, CP-OFDM would no longer to be robust to the

ICI, as shown in (26) and (27), e.g. as τ or 2τ error samples are considered as the interference.

2) UFMC / OA-UFMC System ICI Analysis: Unlike CP-OFDM, the side-lobe attenuation of UFMC is much smaller due to the time domain filtering. The narrow band filter used at the transmitter can significantly reduce the interference caused by the time-offset between the transmitting users. Similar to (21), we can write the time domain interference terms to uth user of UFMC as $i_u^{\mathrm{UFMC}}(t)$:

$$i_2^{\mathrm{UFMC}}(t) = \sum_{l=0}^{\tau-1} \big(- s_1^{\#2}(t) + s_1^{\#3}(t) \big) \delta(t-l) + \sum_{l=L-\tau}^{L-1} \big(- s_3^{\#2}(t) + s_3^{\#1}(t) \big) \delta(t-l), \quad (28)$$

thus, the frequency domain interference can be rewritten using the Discrete Fourier transform as:

$$I_2^{\mathrm{UFMC}} = \sum_{k=0}^{K-1} \sum_{t=0}^{\tau-1} \big(- s_1^{\#2}(t) + s_1^{\#3}(t) \big) e^{-j2\pi tk/N} + \sum_{k=0}^{K-1} \sum_{t=L-\tau}^{L-1} \big(- s_3^{\#2}(t) + s_3^{\#1}(t) \big) e^{-j2\pi tk/N}. \quad (29)$$

Now, we define L_{T} is the transmitted signal tail length which is located at both the front and the end of the UFMC samples, and $L_{\mathrm{T}} = \frac{L_{\mathrm{F}}-1}{2}$. Then, the first term of (29) can be expanded as:

$$\sum_{k=0}^{K-1} \sum_{t=0}^{\tau-1} \big(- s_1^{\#2}(t) + s_1^{\#3}(t) \big) e^{-j2\pi tk/N} \quad (30)$$
$$= \sum_{k=0}^{K-1} \left(\sum_{t=0}^{L_{\mathrm{T}}-1} \big(- s_1^{\#2}(t) + s_1^{\#3}(t) \big) + \sum_{t=L_{\mathrm{T}}}^{\tau-1} \big(- s_1^{\#2}(t) + s_1^{\#3}(t) \big) \right) e^{-j2\pi tk/N},$$

and the second term of (29) can be rewritten as:

$$\sum_{k=0}^{K-1} \sum_{t=L-\tau}^{L-1} \big(- s_3^{\#2}(t) + s_3^{\#1}(t) \big) e^{-j2\pi tk/N} \quad (31)$$
$$= \sum_{k=0}^{K-1} \left(\sum_{t=L-\tau}^{L-L_{\mathrm{T}}-1} \big(- s_3^{\#2}(t) + s_3^{\#1}(t) \big) + \sum_{t=L-L_{\mathrm{T}}}^{L-1} \big(- s_3^{\#2}(t) + s_3^{\#1}(t) \big) \right) e^{-j2\pi tk/N}.$$

Note that, each filter is designed with the narrow bandwidth, such as Chebyshev or Hamming [20], the magnitude of $b_u(t)$ at the band-edge should be very small. After removing the tail samples (window tails) which are located at ($t \in [0, L_{\mathrm{T}} - 1]$, $t \in [L - \mathrm{T}, L - 1]$) as shown in

Fig. 3(b), the equation (29) can be summed from (30) and (31) then be approximated as:

$$I_2^{\text{UFMC}} \approx \sum_{k=0}^{K-1} \sum_{t=L_{\text{T}}}^{\tau-1} \left(-s_1^{\#2}(t) + s_1^{\#3}(t) \right) e^{-j2\pi tk/N} + \sum_{k=0}^{K-1} \sum_{t=L-\tau}^{L-L_{\text{T}}-1} \left(-s_3^{\#2}(t) + s_3^{\#1}(t) \right) e^{-j2\pi tk/N}.$$

(32)

Similarly, the interference of the 1st user in the frequency domain can be written as:

$$I_1^{\text{UFMC}} = \sum_{k=0}^{K-1} \sum_{t=L-\tau}^{L-1} \left(-s_2^{\#2}(t) + s_2^{\#1}(t) \right) e^{-j2\pi tk/N} + \sum_{k=0}^{K-1} \sum_{t=L-2\tau}^{L-1} \left(-s_3^{\#2}(t) + s_3^{\#1}(t) \right) e^{-j2\pi tk/N}$$

$$\approx \sum_{k=0}^{K-1} \sum_{t=L-\tau}^{L-L_{\text{T}}-1} \left(-s_2^{\#2}(t) + s_2^{\#1}(t) \right) e^{-j2\pi tk/N} + \sum_{k=0}^{K-1} \sum_{t=L-2\tau}^{L-L_{\text{T}}-1} \left(-s_3^{\#2}(t) + s_3^{\#1}(t) \right) e^{-j2\pi tk/N},$$

(33)

and for the 3th user can be written as:

$$I_3^{\text{UFMC}} = \sum_{k=0}^{K-1} \sum_{t=0}^{2\tau-1} \left(-s_1^{\#2}(t) + s_1^{\#3}(t) \right) e^{-j2\pi tk/N} + \sum_{k=0}^{K-1} \sum_{t=0}^{\tau-1} \left(-s_2^{\#2}(t) + s_2^{\#3}(t) \right) e^{-j2\pi tk/N}$$

$$\approx \sum_{k=0}^{K-1} \sum_{t=L_{\text{T}}}^{2\tau-1} \left(-s_1^{\#2}(t) + s_1^{\#3}(t) \right) e^{-j2\pi tk/N} + \sum_{k=0}^{K-1} \sum_{t=L_{\text{T}}}^{\tau-1} \left(-s_2^{\#2}(t) + s_2^{\#3}(t) \right) e^{-j2\pi tk/N}.$$

(34)

The narrow band triangle filter reduces the power amplitude at the band-edge, which directly reduces the ICI caused by the time offset overlapped samples. Note that, in terms of the multipath channel, this paper considers that the sum of the mean power values for all channel taps is equal to 1. The interference terms for the multipath channel can be easily computed as using $x_u^{\#}(t) \otimes h_u(t)$ or $s_u^{\#}(t) \otimes h_u(t)$ instead of $x_u^{\#}(t)$ or $s_u^{\#}(t)$ in the above equations, which can be used for the case of any of the multipath channels.

C. ISI Analysis Caused by Channel

This paper also considers the analysis of ISI when the length of channel impulse response in samples L_{H} is longer than L_{CP} or L_{F}.

1) CP-OFDM System ISI Analysis: Reference [21] proved that when $(L_{\mathrm{H}} > L_{\mathrm{CP}})$, a part of one signal will then be the ISI from the previous symbol and this causes interference at the tail of the channel impulse response that is not covered by the CP. Thus, the residual ISI of the uth user on the kth sub-carrier after removing the CP in the frequency domain can be expressed as $Z_u(k)$ [21]:

$$
\begin{aligned}
Z_u^{\mathrm{OFDM}}(k) &= \sum_{n=L_{\mathrm{CP}}}^{L_{\mathrm{H}}-1} x_{u-1}(n) \sum_{t=n}^{L_{\mathrm{H}}-1} h_u(t) e^{-j2\pi(t-n)k/N} \\
&= \sum_{n=L_{\mathrm{CP}}}^{L_{\mathrm{H}}-1} x_{u-1}(n) e^{j2\pi nk/N} \sum_{t=n}^{L_{\mathrm{H}}-1} h_u(t) e^{-j2\pi tk/N},
\end{aligned} \tag{35}
$$

then the PSD of ISI for the CP-OFDM system can be determined as P_{ISI}:

$$
\begin{aligned}
P_{\mathrm{ISI}u}^{\mathrm{OFDM}}(k) &= \mathbb{E}\left(Z_u^{\mathrm{OFDM}}(k) Z_u^{\mathrm{OFDM}*}(k) \right) \\
&= \mathbb{E}\left(x_{u-1}(n) x_{u-1}^*(n) \right) e^{-j2\pi(n-n)k/N} \\
&\quad \cdot \sum_{n=L_{\mathrm{CP}}}^{L_{\mathrm{H}}-1} \sum_{t=n}^{L_{\mathrm{H}}-1} h_u(t) e^{-j2\pi tk/N} \sum_{n=L_{\mathrm{CP}}}^{L_{\mathrm{H}}-1} \sum_{t=n}^{L_{\mathrm{H}}-1} h_u^*(t) e^{-j2\pi tk/N} \\
&= \sigma^2 \sum_{n=L_{\mathrm{CP}}}^{L_{\mathrm{H}}-1} \left| \sum_{t=n}^{L_{\mathrm{H}}-1} h_u(t) e^{-j2\pi tk/N} \right|^2 .
\end{aligned} \tag{36}
$$

2) UFMC System ISI Analysis: Following a similar analysis to the CP-OFDM system, the residual ISI of the uth user on the kth sub-carrier for UFMC is:

$$
\begin{aligned}
Z_u^{\mathrm{UFMC}}(k) &= \sum_{n=L_{\mathrm{T}}}^{L_{\mathrm{H}}-1} s_{u-1}(n) e^{j2\pi nk/N} \sum_{t=n}^{L_{\mathrm{H}}-1} h_u(t) e^{-j2\pi tk/N} \\
&= \sum_{n=L_{\mathrm{T}}}^{L_{\mathrm{H}}-1} x_{u-1}(n) b_{u-1}(n) e^{j2\pi nk/N} \sum_{t=n}^{L_{\mathrm{H}}-1} h_u(t) e^{-j2\pi tk/N} .
\end{aligned} \tag{37}
$$

Thus, the PSD of ISI for the UFMC system can be determined as:

$$P_{\text{ISI}u}^{\text{UFMC}}(k) = \mathbb{E}\left(x_{u-1}(n)x_{u-1}^*(n)\right)e^{-j2\pi(n-n)k/N}$$

$$\cdot \sum_{n=L_{\text{T}}}^{L_{\text{H}}-1}\sum_{t=n}^{L_{\text{H}}-1}b_u(t)h_u(t)e^{-j2\pi tk/N}\sum_{n=L_{\text{T}}}^{L_{\text{H}}-1}\sum_{t=n}^{L_{\text{H}}-1}b_u^*(t)h_u^*(t)e^{-j2\pi tk/N}$$

$$= \sigma^2\sum_{n=L_{\text{T}}}^{L_{\text{H}}-1}\left|\sum_{t=n}^{L_{\text{T}}-1}b_u(t)h_u(t)e^{-j2\pi tk/N}\right|^2. \tag{38}$$

D. SINR Analysis and Capacity

The SINR of the received signal on kth sub-carrier can be defined as $\rho_u(k)$:

$$\rho_u(k) = \frac{\mathbb{E}[X_u(k)^2]}{\sigma^2 + \mathbb{E}[I_u(k)^2] + P_{\text{ISI}u}(k)}, \tag{39}$$

where $\mathbb{E}[X_u(k)^2]$ denotes the transmitted signal power. Inserting (25), (26), (27) and (36) into (39), the closed-form expression of SINR for the uth user CP-OFDM can be expressed as:

$$\rho_u^{\text{OFDM}}(k) = \frac{\mathbb{E}[X_u(k)^2]}{\sigma^2 + \mathbb{E}[(I_u^{\text{OFDM}}(k))^2] + \sigma^2\sum_{n=L_{\text{CP}}}^{L_{\text{H}}-1}\left|\sum_{t=n}^{L_{\text{H}}-1}h_u(t)e^{-j2\pi tk/N}\right|^2}. \tag{40}$$

Inserting (32), (33), (34) and (38) into (39), the closed-form expression of SINR for the uth user UFMC can be expressed as:

$$\rho_u^{\text{UFMC}}(k) = \frac{\mathbb{E}[S_u(k)^2]}{\sigma^2 + \mathbb{E}[(I_u^{\text{UFMC}}(k))^2] + \sigma^2\sum_{n=L_{\text{T}}}^{L_{\text{H}}-1}\left|\sum_{t=n}^{L_{\text{T}}-1}b_u(t)h_u(t)e^{-j2\pi tk/N}\right|^2}. \tag{41}$$

Now, we can compute an estimate of the Shannon capacity $C_u(k)$ for the kth sub-carrier of the uth user based on our SINR equations as:

$$C_u^{\text{OFDM}}(k) = \log_2(1 + \rho_u^{\text{OFDM}}(k)), \tag{42}$$

$$C_u^{\text{UFMC}}(k) = \log_2(1 + \rho_u^{\text{UFMC}}(k)). \tag{43}$$

E. BER Analysis

This paper now considers the performance for a 4PSK modulation scheme. As in [22] and [23], we can express the theoretical BER values for the time-offset model under the AWGN channel as:

$$P_{4\text{PSK}u}^{\text{OFDM}} = \frac{1}{2}\text{erfc}\left(\sqrt{\overline{\rho_u^{\text{OFDM}}/N_{\text{bs}}}}\right), \tag{44}$$

$$P_{4\text{PSK}u}^{\text{UFMC}} = \frac{1}{2}\text{erfc}\left(\sqrt{\overline{\rho_u^{\text{UFMC}}/N_{\text{bs}}}}\right), \tag{45}$$

where $\text{erfc}(\cdot)$ represents the complementary error function, $\overline{\rho_u}$ is the average value of SINR and N_{bs} is the number of bits per sample. For the Rayleigh multipath channel, according to [22] and [23], the BER equations are given:

$$P_{4\text{PSK}u}^{\text{OFDM}} = \frac{1}{2}\text{erfc}\left(1 - \sqrt{\frac{\overline{\rho_u^{\text{OFDM}}/N_{\text{bs}}}}{1 + \overline{\rho_u^{\text{OFDM}}/N_{\text{bs}}}}}\right), \tag{46}$$

$$P_{4\text{PSK}u}^{\text{UFMC}} = \frac{1}{2}\text{erfc}\left(1 - \sqrt{\frac{\overline{\rho_u^{\text{UFMC}}/N_{\text{bs}}}}{1 + \overline{\rho_u^{\text{UFMC}}/N_{\text{bs}}}}}\right). \tag{47}$$

For the higher order modulation scheme required in PCC, i.e. 16-QAM is required for PCC in terms of achieving spectral efficiency $\eta = 2$ bit/sec/Hz, the standard theoretical BER equations can be found in [22]. Inserting our SINR equations into the formulas given in [22] allows us to compute the 16-QAM theoretical BER values.

V. NUMERICAL RESULTS

In this section, various simulations are conducted to confirm our theoretical analysis. The common simulation parameters are listed in Table I. Each MTC user's transmission occupies 13 sub-carriers in the frequency domain, and the users are spaced by 2 blank sub-carriers. We set the normalised cut-off frequency to $f_{\text{cf}} = 0.18$, which is wider than the ratio between the number of sub-carriers per user K and the total number of available sub-carriers N, $\gamma_{\text{ro}} = 13/128 = 0.1016$.

TABLE I

COMMON SIMULATION PARAMETERS

Simulation Parameters							
Uplink Bandwidth	No. of FFT (N)	Sub-carriers per user (K)	Total Users (U)	CP Length (L_{CP})	Filter Length (L_F)	Channel Length (L_H)	Modulation Scheme
1.25 MHz	128	13	3 or 7	30	31	10 or 70	4PSK
Filter Parameters							
FIR Filter		IIR Filter					
FIR Window	Normalised cut-off frequency (f_{cf})	Type of Filter	f_{cf}	Filter Order	Passband Ripple (A_{PB})		
Hamming	0.18	Chebyshev Type I	0.18	4, 8, 12	0.15 dB		

A_{SL} is the side-lobe attenuation and A_{PB} is the passband ripple. In the BER simulations, we elected to measure the middle user's performance, e.g. when $U = 3$, we measure the 2nd user and when $U = 7$, we measure the 4th user.

A. Computational Complexity Performance

The relative computational complexity is shown in Fig. 4 using (11), (12) and (15). Both CP-OFDM and PCC-OFDM require significantly fewer operations than time domain UFMC and OA-UFMC. When $L_F < 17$ samples, the standard UFMC requires fewer operations than OA-UFMC. As L_F increases, the number of operations for UFMC significantly increases. In this case, OA-UFMC reduces the computational complexity significantly for larger values of L_F. IIR-UFMC, with a filter order of 4, only slightly increases the complexity compared with OFDM and PCC, but it significantly reduces the number of operations compared with UFMC.
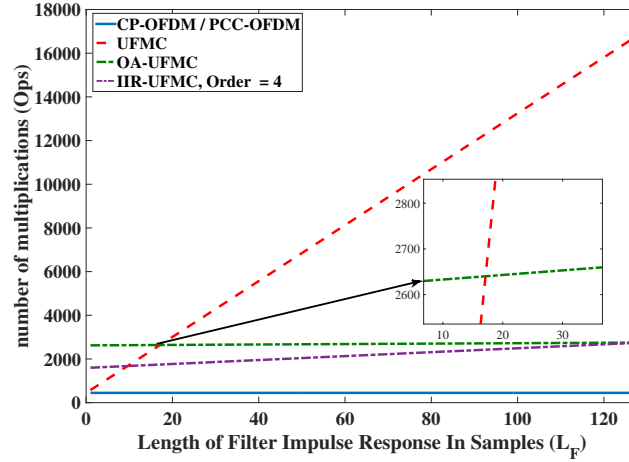
Fig. 4. Comparison of Computational Complexity, $N = 128$

B. PSD Performance

The PSD performance of CP-OFDM, PCC-OFDM and UFMC with different types of FIR filters is shown in Fig. 5(a). Firstly, both UFMC and PCC-OFDM significantly reduce the side-lobe level compared to CP-OFDM. Among these, PCC-OFDM provides the best ICI protection due to its very rapid side-lobe roll-off. Secondly, in terms of the Dolph-Chebyshev filter, compared with $A_{\text{SL}} = 64$ dB, the PSD performance of $A_{\text{SL}} = 40$ dB is better, as it achieves a slightly lower side-lobe attenuation in the roll-off region. Both the Dolph-Chebyshev filter with $A_{\text{SL}} = 40$ dB and the Hamming filter present better frequency roll-off performance than the Blackman filter. Moreover, there are no significant differences between Dolph-Chebyshev and Hamming. Thus, this paper will focus on the Hamming filter in the next simulations.

The PSD performance of IIR-UFMC is shown in Fig. 5(b). In terms of a fair comparison, we truncated the lengths of all IIR filtered signal outputs equal to L. The normalised cut-off frequency is set to $f_{\text{cf}} = 0.18$, which is much wider than $\gamma_{\text{ro}} = 0.1016$ to achieve an almost
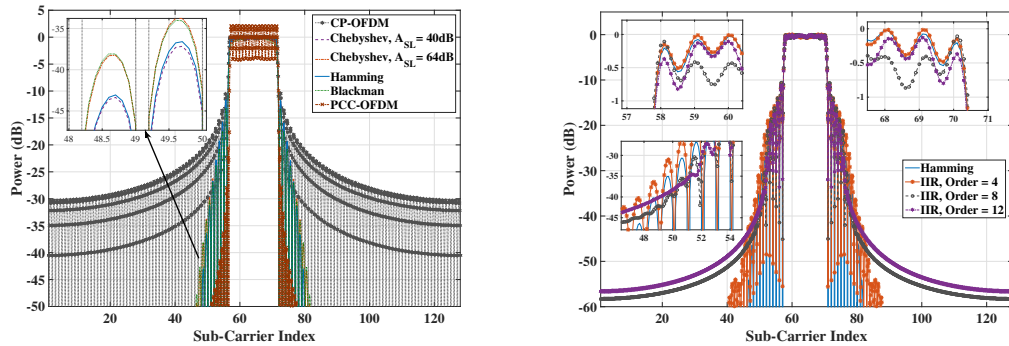
(a) CP-OFDM, UFMC with Different Filters, PCC-OFDM

(b) IIR-UFMC, Truncating the Filter Outputs to L Samples.

Fig. 5. PSD Performance of the Side-lobe Reduction.

linear phase in passband. We assume the available sub-carriers for transmission is from 58 to 70, i.e. 13 sub-carriers. Fig. 5(b) clearly shows that IIR filters with order of 8 and 12 provide slightly superior frequency roll-off performance at the centre of adjacent sub-carriers (from 48 to 58) to the FIR Hamming window and IIR with order of 4. However, when increasing the filter order, the truncated L samples will no longer accurately represent the original signal and also introduce increased computational cost. Therefore, this paper will consider the ChebyshevI IIR filter with order 4 for the IIR-UFMC system in the next simulations.

C. SINR and Capacity Performance

The SINR performance over the AWGN channel with a signal to noise ratio (SNR) of 30 dB is shown in Fig. 6(a) and we assume τ is a 50 sample time offset, which is larger than $L_{CP} = 30$ or $L_F = 31$. The theoretical SINR analysis values are computed from (40) and (41), which perfectly match with the simulations. The 1st user occupies sub-carriers from 11 to 23, sub-carriers 26 to 38 are for the 2nd user and 41 to 53 are for the 3nd user. Note in Fig. 6(a) how the SINR performance degrades due to interference between users 1&2 and also 2&3 for
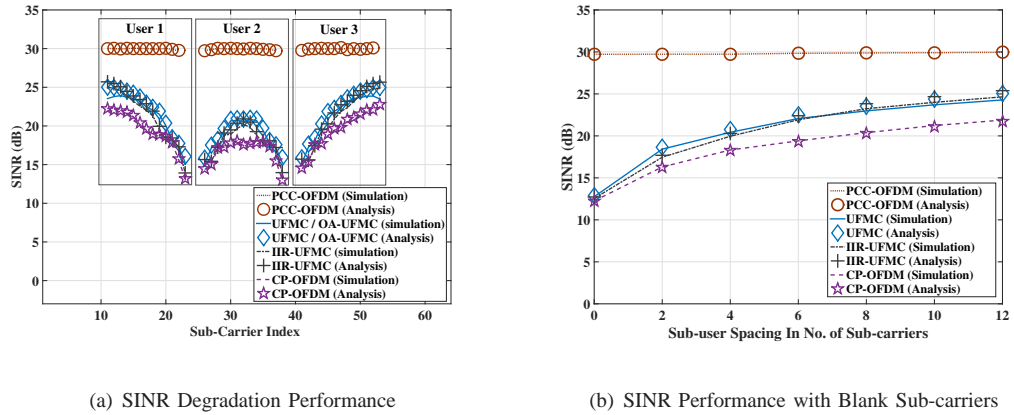
(a) SINR Degradation Performance

(b) SINR Performance with Blank Sub-carriers

Fig. 6. SINR Performance, AWGN (SNR =30 dB), $N = 128$, $L_{\text{CP}} = 30$, $L_{\text{F}} = 31$, $L_{\text{Or}} = 4$, $\tau = 50$, $U = 3$.

OFDM, UFMC and IIR-UFMC. From the Fig. 6(a), we notice that first, compared with OFDM, UFMC and IIR-UFMC, PCC-OFDM presents the best performance. Second, the nearby sub-carriers of both OFDM, UFMC, and IIR-UFMC are significantly affected by ICI, especially for the second user. Third, both UFMC and IIR-UFMC can perform slightly better than OFDM (about 3.5 dB higher SINR), but they still have an inferior SINR to PCC-OFDM. There is no significant performance difference between UFMC and IIR-UFMC.

The impact of the number of zero sub-carriers in the frequency domain between each user is shown in Fig. 6(b). Increasing the number of blank sub-carriers at the user band-edge, the SINR performance of both OFDM, UFMC and IIR-UFMC improves significantly at the cost of reducing the available bandwidth for data transmission. Moreover, if the sub-user spacing is 4 blank sub-carriers, UFMC achieves about 0.5 dB higher SINR than IIR-UFMC and about 2.6 dB higher SINR than OFDM. PCC still provides the best performance compared with the other schemes. It can also be seen that the result from the analysis matches very well with the simulations.
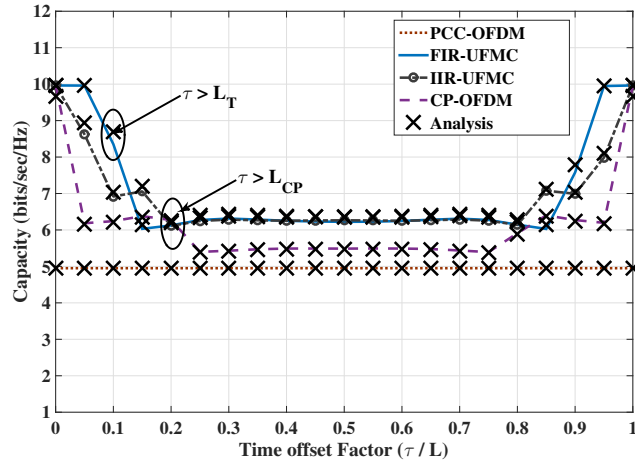
Fig. 7. Capacity and SINR Performance, AWGN (SNR = 30 dB), $U = 3$, $N = 128$, $L_{CP} = 30$, $L_F = 31$, $L_T = 15$, $U = 3$.

The capacity performance with the time offset factor (τ/L) is shown in Fig. 7. The theoretical capacity values are computed from (42) and (43), and the results from our derived expressions and the simulations match perfectly. It can be seen that firstly, PCC-OFDM provides the poorest capacity performance because of its reduced spectral efficiency, even though it can achieve the highest SINR performance in Fig. 6. Secondly, with increasing τ, the capacity performance of UFMC, IIR-UFMC and OFDM significantly reduces due to the ICI. However, when $\tau = L = 158$ samples, there is no significant capacity degradation as there are no relative time-offsets between the adjacent users. Thirdly, if there is a small time offset, i.e. $\tau = 5\%$ of the transmitted symbol length, both UFMC and IIR-UFMC are more robust to ICI compared with OFDM. In detail, the capacity degradation for UFMC and IIR-UFMC significantly reduces when $\tau > 10\%$ (or 15 samples) of the transmitted symbol length, which is approximately the window tail length L_T. The capacity degradation for OFDM starts with when $\tau > 5\%$ of the transmitted symbol
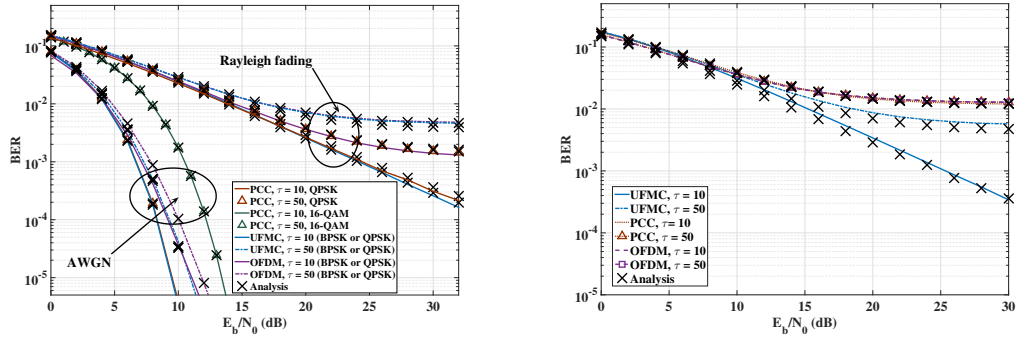
(a) Approximate BER Performance, $L_H = 10$.

(b) Approximate BER and ISI Performance, $L_H = 70$.

Fig. 8.   BER Performance for AWGN and Rayleigh Multipath Channel, $U = 3$, $N = 128$, $L_{CP} = 30$, $L_F = 31$, $\eta = 1$ or 2 bit/sec/Hz.

length and then stays at a constant value of 6.3 bit/sec/Hz until $\tau > 20\%$ (or 30 samples), which is approximately the CP length. Fourthly, if $\tau > 20\%$ of the transmitted symbol length, both UFMC, IIR-UFMC and OFDM provide an approximately constant capacity. Both UFMC and IIR-UFMC achieve 1 bit/sec/Hz higher capacity than OFDM. Finally, there is no significant difference between UFMC and IIR-UFMC when $\tau > 20\%$.

D. BER Performance

The average BER for the OFDM, UFMC and PCC systems for AWGN and Rayleigh fading channels is shown in Fig. 8(a). The time offset scenarios of $\tau = 10$ or $\tau = 50$ samples are considered. The theoretical BER results are obtained using the proposed equations as (44), (45), (46) and (47). Again, the agreement between the analytical and simulation results is clear. The BER results show similar trends to the previous SINR results. Firstly, there is no significant BER degradation for PCC even if there is a 50 samples time offset, which means PCC-OFDM can significantly mitigate against the ICI. However, if we consider the spectral efficiency is $\eta = 2$

bit/sec/Hz, PCC will no longer provide superior BER performance due to the requirement to use a higher order modulation scheme i.e. 16QAM. Secondly, when $\tau < L_{\text{CP}}$ or $L_{\text{F}} - 1$, there is no significant BER degradation for UFMC, especially when the time offset is less than 15 samples. Even when $\tau = 50$, UFMC saves about 1.1 dB E_{b}/N_0 compared with OFDM at a BER of 10^{-4} in the AWGN channel. Fig. 8(a) also shows that if L_{H}=10 and $\tau = 10$, UFMC saves about 5 dB E_{b}/N_0 at the BER is $10^{-2.9}$. If the τ increases to 50 samples, the BER performance of both UFMC and OFDM will degrade to the same curve.

The approximate BER for the OFDM, UFMC and PCC systems in a Rayleigh fading channel with $L_{\text{H}} = 70$ channel taps is shown in Fig. 8(b). The theoretical ISI interference is computed using (36) and (38), and simulations closely match with the analytical results. It can be seen that UFMC is more robust to very dispersive multipath channels compared with CP-OFDM and PCC-OFDM, especially when τ is small. Fig. 8(b) also shows that if L_{H} is much longer than L_{CP}, ISI becomes the dominant interference for both OFDM and PCC-OFDM systems. In this case, the ICI caused by the time offset is somewhat smaller than ISI.

Now we measure the BER performance of IIR-UFMC, using the ChebyshevI filter with order of 4 and $f_{\text{cf}} = 0.18$. Here, we increase the number of transmitting users to $U = 7$ and measure the 4th user's performance. The competitive BER performance for UFMC with the FIR and IIR filters is shown in Fig. 9. The analytical values are computed similarly as before, with the interference analysed using the sub-carriers from the adjacent users. Fig. 9 shows that the BER performance of IIR-UFMC is slightly less than for the FIR. The reason is that we truncated the output length of IIR to equal L in terms to ensure a fair comparison. Compared with OFDM, the BER performance of IIR-UFMC is significantly improved, especially for the Rayleigh multipath channel with the short impulse response $L_{\text{H}} = 10$ taps and small $\tau = 10$ samples. Again, the theoretical analysis closely matches with the Monte Carlo simulations. Moreover, for PCC-
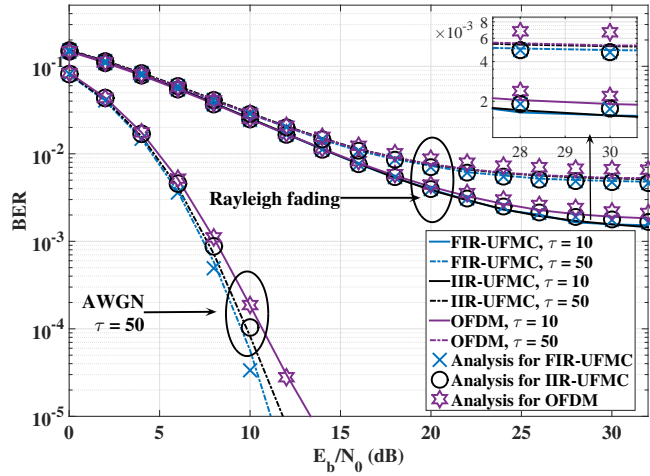
Fig. 9.   Approximate BER Performance for UFMC with FIR and IIR Filter When Receiving $U = 7$ Users, $L_{\mathrm{H}} = 10$.

OFDM, our previous paper [10] has shown that one of another drawback is the high peak-to-average power ratio (PAPR), which increases the transmitter amplifier requirements and might cause the power assumption issues for low data rate MTC devices.

VI. CONCLUSION

We have provided a complete time offset interference analysis for both CP/PCC-OFDM and UFMC systems and shown that firstly, PCC using a frequency guard interval significantly protects against co-channel interference from time offsets at the cost of reduced spectral efficiency. Secondly, UFMC provides a superior performance to OFDM (at the cost of high operational complexity) in terms of SINR, capacity and BER, especially for the Rayleigh fading multipath channel. In particular, if the time offset is less than 10 samples, there is no significant degradation in both SINR and BER for the UFMC system. Further we have proposed two methods to reduce the computational complexity. OA-UFMC provides a much lower complexity than UFMC when

the filter impulse response is larger. For IIR-UFMC, the complexity is significantly reduced, while it provides a similar SINR, capacity and BER performance compared to UFMC, especially with a larger time offset.

In conclusion, even though PCC-OFDM and UFMC offer the most efficient computational performance for protecting against ICI, IIR-UFMC is attractive as it provides superior BER performance to CP-OFDM. IIR-UFMC achieved lower computational complexity compared with FIR-UFMC and without any cost in spectral efficiency. We thus conclude that IIR-UFMC might be a potential waveform design for the massive machine 5G MTC scenario to support low data rate, low energy consumption and low latency transmissions.

REFERENCES

[1] E. Hossain *et al*, "Evolution toward 5G multi-tier cellular wireless networks: An interference management perspective," *IEEE Wireless Communications*, vol. 21, no. 3, pp. 118–127, June 2014.

[2] J. G. Andrews *et al*, "What will 5G be?" *IEEE J. Sel. Areas Commun.*, vol. 32, no. 6, pp. 1065–1082, June 2014.

[3] E. Hossain and M. Hasan, "5G cellular: key enabling technologies and research challenges," *IEEE Instrum. Meas. Mag.*, vol. 18, no. 3, pp. 11–21, June 2015.

[4] M. O. Pun *et al*, "Maximum-likelihood synchronization and channel estimation for OFDMA uplink transmissions," *IEEE Trans. Commun.*, vol. 54, no. 4, pp. 726–736, April 2006.

[5] G. Wunder *et al*, "5GNOW: non-orthogonal, asynchronous waveforms for future mobile applications," *IEEE Commun. Mag.*, vol. 52, no. 2, pp. 97–105, February 2014.

[6] F. Schaich and T. Wild, "Waveform contenders for 5G, OFDM vs. FBMC vs. UFMC," in *International Symposium on communications, Control and Signal Processing (ISCCSP)*, May 2014, pp. 457–460.

[7] J. Armstrong, "Analysis of new and existing methods of reducing intercarrier interference due to carrier frequency offset in OFDM," *IEEE Trans. Commun.*, vol. 47, no. 3, pp. 365–369, Mar 1999.

[8] B. Farhang-Boroujeny, "OFDM versus filter bank multicarrier," *IEEE Signal Process. Mag.*, vol. 28, no. 3, pp. 92–112, May 2011.

[9] F. Schaich, T. Wild, and Y. Chen, "Waveform contenders for 5G - suitability for short packet and low latency transmissions," in *IEEE Vehicular Technology Conference (VTC Spring)*, May 2014, pp. 1–5.

[10] S. Wang, J. Armstrong, and J. S. Thompson, "Waveform performance for asynchronous wireless 5G uplink communications," in *2016 IEEE 27th Annual International Symposium on Personal, Indoor, and Mobile Radio Communications Workshops (IRACON)*, Valencia, Spain, Sep. 2016.

[11] *3GPP, TSG-RAN WG184b, R1-162199, Waveform Candidates*, URL:http://www.ee.iitm.ac.in/ giri/pdfs/EE5141/R1-162199-Waveform-Candidates.docx.

[12] X. Wang *et al*, "Universal filtered multi-carrier with leakage-based filter optimization," in *European Wireless Conference, Proceedings of European Wireless*, May 2014, pp. 1–5.

[13] A. Aminjavaheri *et al*, "Impact of timing and frequency offsets on multicarrier waveform candidates for 5G," in *IEEE Signal Processing and Signal Processing Education Workshop (SP/SPE)*, Aug 2015, pp. 178–183.

[14] S. M. Kang *et al*, "Timing-offset-tolerant universal- filtered multicarrier passive optical network for asynchronous multiservices-over-fiber," *IEEE J. Opt. Commun. Netw.*, vol. 8, no. 4, pp. 229–237, April 2016.

[15] Y. Fan and J. S. Thompson, "Mimo configurations for Relay channels: Theory and practice," *IEEE Trans. Wireless Commun.*, vol. 6, no. 5, pp. 1774–1786, May 2007.

[16] M. J. Narasimha, "Modified overlap-add and overlap-save convolution algorithms for real signals," *IEEE Signal Process. Lett.*, vol. 13, no. 11, pp. 669–671, Nov 2006.

[17] S. Holford and P. Agathoklis, "The use of model reduction techniques for designing IIR filters with linear phase in the passband," *IEEE Trans. Signal Process.*, vol. 44, no. 10, pp. 2396–2404, Oct 1996.

[18] R. Losada and V. Pellisier, "Designing IIR filters with a given 3-dB point," *IEEE Signal Process. Mag.*, vol. 22, no. 4, pp. 95–98, July 2005.

[19] B. Mulgrew, P. M. Grant, and J. S. Thompson, *Digital Signal Processing: Concepts and Applications*, 2nd Edition edition, Ed. Palgrave Macmillan, 2002.

[20] K. K. Wojcicki and K. K. Paliwal, "Importance of the dynamic range of an analysis windowfunction for phase-only and magnitude-only reconstruction of speech," in *2007 IEEE International Conference on Acoustics, Speech and Signal Processing - ICASSP '07*, vol. 4, April 2007, pp. IV–729–732.

[21] W. Henkel *et al*, "The cyclic prefix of OFDM/DMT - an analysis," in *in Proc. International Seminar on Broadbond Communicalions, Access, Transmission, Networking, Zurich*, 2002, pp. 22–1–22–3.

[22] F. Adachi, "BER analysis of 2PSK, 4PSK, and 16QAM with decision feedback channel estimation in frequency-selective slow Rayleigh fading," *IEEE Trans. Veh. Technol.*, vol. 48, no. 5, pp. 1563–1572, Sep 1999.

[23] S. Wang and J. S. Thompson, "Performance analysis of virtual carrier system receivers for M2M communications using OFDMA," *IET Communications*, 2016.

Signal Processing Implementation of Virtual Carrier for Supporting M2M Systems Based on LTE

Shendi Wang, and John S. Thompson

Institute for Digital Communications, Joint Research Institute for Signal and Image Processing
School of Engineering, The University of Edinburgh, EH9 3JL, Edinburgh, UK
Email: Shendi.Wang@ed.ac.uk, John.Thompson@ed.ac.uk

Abstract—**Machine-to-Machine (M2M) communications normally require low data transmission rates and low cost devices. Thus, how to modify existing cellular systems such as the Long Term Evolution (LTE) system to successfully support low cost M2M devices will become a major issue for industry. This paper will address one solution based on the virtual carrier system, which improves bandwidth efficiency and reduces the power dissipation dramatically on the LTE downlink. Our results indicate that the virtual carrier system provides a high Signal-to-Interference-and-Noise Ratio (SINR) performance without significant Bit Error Rate (BER) degradation.**

I. INTRODUCTION

Wireless communication technologies have been rapidly improved, especially in the last decade. Systems have progressed from 1G, the analogue telecommunications standards radio system in 1980s, through to current 4G networks (LTE) [1]. LTE takes advantage of high spectrum efficiency to provide high data rate communication and reduced data latency. It implements the orthogonal frequency division multiple access (OFDMA) scheme in the downlink and single carrier frequency division multiple access (SC-FDMA) in the uplink. With the focus to achieve high data rate transmission techniques, there is a blind spot which has received less attention. About 80% of the population has been connected by using a mobile network worldwide. However the development of the cellular network market will face a bottleneck in the next few years. There is predicted to be 50 billion machines and only 6 billion people in the world [2]. Therefore, communication networks will shift from the existing Human to Human (H2H) communication mode to the Machine-to-Machine (M2M) communication mode.

M2M will be experience exponential growth in the next generation of communication networks due to the demand for automated systems such as e-health, smart grid and smart homes [3]. M2M systems cannot be simply defined as one terminal device communicating with another device through a network. It is a more advanced and highly intelligent network system. For instance, a smart medical sensor is placed on a patient in order to collect physical data, such as temperature, blood pressure or heart rate. If these measurements change significantly, the smart sensor will transmit the results to a medical centre and request an automatic medical response [4].

Unlike H2H, M2M communication systems normally require low data rates, low cost and low energy consumption, and minimal human intervention to be viable for sensors and monitoring purposes. Currently, many M2M applications are implemented by using the General Packet Radio Service (GPRS) infrastructure. However, this will not satisfy the future requirements of network operators, who aim to limit the maintenance cost by reducing the number of access technologies in the network. LTE is replacing GPRS system at present [5] and could provide a better platform for M2M applications with higher spectrum efficiency and a wide range of signal coverage and network operation functions. In addition, there will be a large number of devices supporting LTE in the near future. LTE provides high signal quality, and wide bandwidth, which increases cost. However, M2M usually only requires a narrow bandwidth carrier to transmit occasional data packets. If an M2M device receives at a low data rate (for example 1MHz) on a LTE 20MHz bandwidth carrier, a large number of sub-carriers do not need to be processed. How to reduce the energy and processing cost of LTE for supporting M2M communications with reduced bandwidth will be investigated for standardisation beyond Release 12 of LTE [6].

In order to improve LTE bandwidth efficiency, [5] illustrates a possible solution: the M2M messages can be transmitted on a virtual carrier in the LTE downlink within the bandwidth of the host carrier. This virtual carrier (VC) can be separately scheduled to low bandwidth receivers. However [5] did not consider in detail methods to decode the VC signal at the receiver. This study will focus how to extract the virtual carrier messages with better Signal-to-Interference-and-Noise Ratio (SINR) performance. We study a practical VC system receiver, which uses a reduced bandwidth analogue filter to extract the virtual carriers of interest and a low sampling rate analogue-to-digital converter (ADC) to decrease energy cost and subsequent computation for an M2M receiver. We highlight the key contributions of the paper as follows:

- Propose a novel reduced sample rate VC receiver system.
- Performance evaluation of the receiver in terms of the Bit Error Rate (BER) and the reduction in complexity.

This paper is organised as follows: Section II presents the system model for the VC system. The analytical SINR and
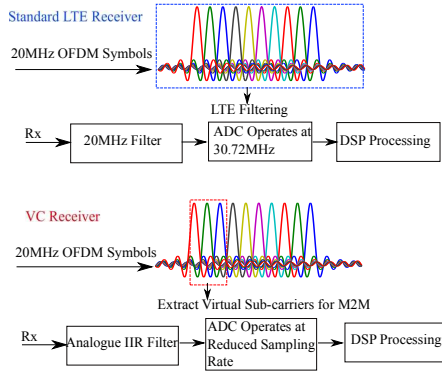
Fig. 1. Standard LTE Receiver and VC System Receiver

BER performance simulation results are shown in Section III, and Section IV concludes the paper.

II. SYSTEM MODEL OF THE VIRTUAL CARRIER RECEIVER

A. Principle of the VC System

The standard OFDM receiver is shown in Fig. 1. We assume that if it received a set of messages over a 20MHz bandwidth channel, it would pass a 20MHz filter and a ADC with a sampling rate of 30.72MHz as in LTE. In order to reduce the cost of the ADC processing, this paper studies a lower sampling rate VC receiver which is shown in Fig. 1. Unlike the standard OFDM receiver, the principle of the VC receiver is to employ one or more narrow band Infinite Impulse Response (IIR) analogue filters to extract the transmitted M2M signals over a downlink channel. It operates the ADC at a much lower sample rate to reduce the power consumption and the number of subsequent digital signal processing computations.

Assume that an M2M receiver has received a 20 MHz bandwidth LTE signal but only a few sub-carriers (for example only 70 sub-carriers) are used for this M2M device, which are mapped into the first baseband sub-carriers as shown in Fig. 1. In order to save energy, it does not need to sample the whole bandwidth signal. The standard 20MHz LTE bandwidth contains up to 1201 occupied sub-carriers. We can calculate that the useful sub-carriers rate R_U is approximately 1/16, i.e. the number of M2M sub-carriers divided by the total number of sub-carriers. Then we can use a 1.25MHz low pass filter (LPF) analogue filter to extract the relevant signals. The original LTE sampling rate is 30.72MHz for a 20MHz bandwidth channel, and R_U is 1/16 , therefore, a 1.92MHz sample rate ADC could be used in this case.

B. VC System Receiver Model

In the transmission block, the input M2M message is mapped to the virtual carriers and combined with the remaining data, which designed for standard LTE receivers. Then the data is transmitted as in a normal OFDM system and propagates through the wireless channel. The baseband signal in an OFDM symbol can be expressed as

$$x(t) = \frac{1}{\sqrt{N}} \sum_{m=0}^{N-1} X_m \cdot e^{j2\pi mt/N} (m = 0, 1, ..., N - 1), \quad (1)$$

where N is the number of sub-carriers, and X_m is the baseband input signal. The wireless channel impulse response is $h_i = \sum_{j=0}^{J-1} h_{ij}\delta(t - jT_s)$ each h_{ij} follows Rayleigh distribution, T_s is the sample period and $\delta(t)$ is the Dirac delta function. The transmitted signal over the channel can be defined as $y(t)$:

$$y(t) = x(t) \otimes h_i + n_o(t), \quad (2)$$

where $n_o(t)$ is the background Gaussian noise then the received signal over a matched filter and remove cyclic prefix (CP) in frequency domain can be expressed as:

$$Y(m) = X(m) \cdot H(m) + N_o(m), \quad (3)$$

where X, H and N_o are the x, h_i and n_o in frequency domain.

The major function of the VC receiver is to decode only sub-carriers of interest. Therefore, in the VC receiver block, the received signal is passed to an IIR filter which separates the virtual carriers from the rest of the OFDM sub-carriers. In order to simulate the SINR and BER performances, this IIR filter can be approximately expressed as an finite impulse response (FIR) filter with impulse response of b_l with length of l, and B denotes filter impulse response in frequency domain. Therefore, the received data passes an IIR low pass filter can be designed as r_{LPF}:

$$r_{LPF}(t) = \{x(t) \otimes h_i + n_o(t)\} \otimes b_l$$
$$= x(t) \otimes (h_i \otimes b_l) + n'_o(t). \quad (4)$$

The receiver noise is due to both thermal noise n_o and aliasing effects from other sub-carriers. The effective channel at the receiver comprises both the RF channel h_i and the filter impulse response b_l is defined as $w_{cn}(t) = h_i \otimes b_l$. Thus the equation (4) can be rewritten as:

$$r_{LPF}(t) = x(t) \otimes w_{cn}(t) + n'_o(t). \quad (5)$$

In order to save energy, we operate the filtered data at the reduced sampling rate of f_{vc} for the VC receiver, which is less than the standard receiver sampling rate f_s. Therefore, the sampling reduction ratio γ can be defined as:

$$\gamma = \frac{f_s}{f_{vc}}. \quad (6)$$

Assuming that the length of CP is longer than combined channel and filter response, then the received signal of the M2M receiver in the frequency domain can be denoted as $R(k)$:

$$R(k) = \hat{X}(k) \cdot W_{cn}(k)(k = 0, 1, ..., N/\gamma - 1), \quad (7)$$

where $\hat{X}(k)$ and $W_{cn}(k)$ are the Fourier transform of $x(k)$ and $w_{cn}(k)$. Due to the lower sample rate ADC, the number of sub-carriers is reduced to N/γ, which means the FFT size

TABLE I
ENERGY SAVING PERFORMANCE OF THE VC SYSTEM FOR THE 20MHZ
LTE CHANNEL FROM EQUATIONS (9) AND (10)

Sampling Rate (f_s)	FFT Size (N)	Normalised ADC Power (W)	FFT Computational Complexity (Ops)
30.72MHz	2048	1	11264
15MHz	1024	1/2	5120
7.68MHz	512	1/4	2304
3.84MHz	256	1/8	1024
1.92MHz	128	1/16	448
0.96MHz	64	1/32	192

in a VC receiver is reduced to N/γ. Then the transmitted M2M signal $\hat{X}(k)$ can be estimated using zero forcing [7] equalisation as:

$$\hat{X}(k) = \frac{R(k)}{W_{\mathrm{cn}}(k)}. \tag{8}$$

C. Energy Saving For the VC System

The basic motivation for the VC system is the fact that for an ADC, the power dissipation is a linear function of the sampling rate. Previous study [8] analysed the power dissipation as P,

$$P = 2^V \cdot f_s, \tag{9}$$

where, V is the number of bits per sample for the ADC, and f_s is the sampling rate. By using a lower sampling rate ADC, the power dissipation can be reduced significantly for M2M devices.

A second point of VC is to reduce the complexity of FFT processing of the received signal. In terms of FFT computational complexity, the VC system provides lower FFT computation compared with the standard OFDM system. For a 20MHz LTE bandwidth, the FFT size is 2048. Therefore, the computational complexity for the traditional OFDM receiver C_{OFDM} is defined as [9]:

$$C_{\mathrm{OFDM}} = \frac{N}{2} \cdot \log_2 N. \tag{10}$$

For the VC system receiver, after filtering and operating a lower sampling rate ADC, the size of the FFT is reduced to (N/γ). Therefore, the computational complexity for the VC system receiver can be computed as:

$$C_{\mathrm{VC}} = \frac{N/\gamma}{2} \cdot \log_2(N/\gamma). \tag{11}$$

The numerical results for energy saving performance is shown in Table I. The standard 20MHz LTE FDD bandwidth uses a sampling frequency of 30.72MHz, the number of FFT size is 2048 and we defined the normalised ADC power dissipation for the LTE receiver as 1. When reducing the sampling rate at the VC receiver, the FFT size, power dissipation and computational complexity are reduced significantly, e.g. by using a 1.92MHz ADC instead of 30.72MHz, the FFT size is 128, the ADC power cost reduced to 1/16 and the computational complexity decreased to from 11264 to 448 operations.
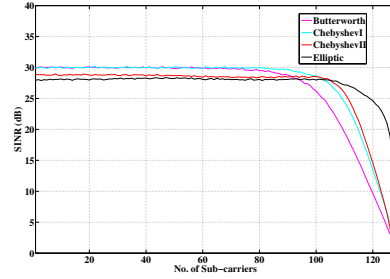

Fig. 2.   SINR Performances over Different IIR Filters

III.   SIMULATION RESULTS

We have demonstrated the energy saving performance of the VC system receiver, therefore, it would important to evaluate its SINR and BER performance after operating a much lower sampling rate ADC. In this section, we present the SINR and BER performance of a VC receiver by assuming that a M2M receiver received the transmitted messages over a 20MHz LTE bandwidth channel with FFT size of 2048. The cyclic prefix (CP) length is 144 samples and the Q-PSK, 16-QAM and 64-QAM as used in LTE. The order of all analogue IIR filters is 8 in order to provide fair comparison and we assume perfect time and frequency synchronisations in this paper. The number of channel taps J is set to 40 and the power for all Rayleigh fading channel taps is the same (flat channel profile).

A. SINR Performance of VC

The SINR performance of the VC system receiver with 16-QAM modulation through the 30dB Additive White Gaussian Noise (AWGN) channel, under four typical low pass IIR analogue filters (Butterworth, ChebyshevI, ChebyshevII and Elliptic filters), is shown in Fig. 2. The channel bandwidth is 20MHz, and the filter cut-off frequency is set to 2.5MHz in order to allow a sampling rate of 3.84MHz. Therefore, the sampling reduction ratio is 8 (30.72MHz/3.84MHz). For ChebyshevI, the passband ripple is set to 1dB and the stopband ripple of ChebyshevII is set to 40dB. For the Elliptic filter, the passband ripple and stopband are also set to 1dB and 40dB. Fig. 2 plots the first 128 sub-carriers and shows that sub-carriers near the cut-off frequency band experience significant SINR loss: for the Butterworth filter the SINR degradation begins at sub-carrier 90. While the ChebyshevII and Elliptic filters present better SINR performances. However, in the pass-band, due to the filter aliasing effects, there is about 2dB SINR loss between sub-carrier 1 to sub-carrier 100 by using ChebyshevII and Elliptic filters. Compared with the Butterworth, the Chebyshev filter has an equal-ripple response in the passband with better stop-band roll off but worse phase response because of group delay variations at the band edges. Therefore, in order to achieve a higher SINR performance at the pass band frequency, this paper will focus on the Butterworth IIR filter in the remaining simulations.
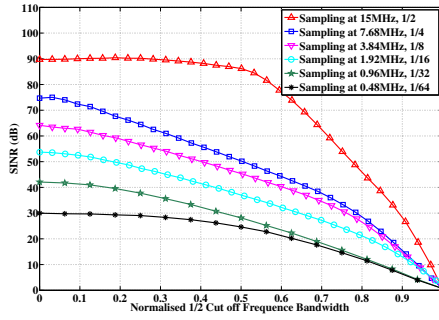
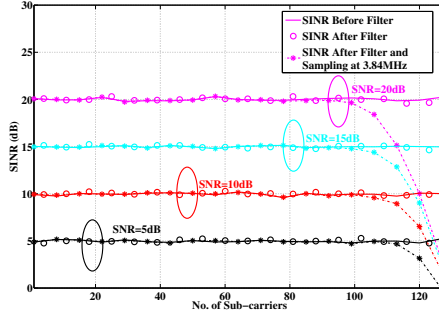Fig. 3.   SINR Performance for Different Sampling Rate

Fig. 4.   Rayleigh Fading Channel SINR Performances

The SINR performance for different sampling rate ADCs with 16-QAM modulation and without added background noise is shown in Fig. 3. We assume that the transmitted signal uses a 20MHz LTE channel, the sampling frequency is 30.72MHz and the perfect time synchronisation. In the VC receiver, we use different sampling rate ADCs to test the SINR degradation performance. The result shows that by reducing the sampling rate at the VC receiver, the SINR of received signal decreased significantly. If using a 0.48MHz ADC (about 1/64 of transmitted sampling frequency, and the IIR cut-off frequency is set to 0.3125MHz in this case) in the VC receiver, the SINR of sub-carriers, which are allocated in the front of pass band frequency, is still above 20dB. This indicates the VC receiver is able to decode the transmitted messages even if we reduced the sampling rate by 64 times. However, the SINR performances of sampling reduction rate at 1/32 and 1/64 are much lower than others. The basic reason that causes this is the non-integer sampling reduction of the CP. In this case, the CP length is chosen as 144, when γ is 1/32 or 1/64, the CP cannot be divided as an integer and it may cause inter-symbol interference (ISI) and inter-carrier interference (ICI).

In Fig. 4, we investigate the impact of SINR degradations by a low pass IIR filter (Butterworth) and a lower sampling rate ADC over the Rayleigh fading channels with 16-QAM modulation. The VC receiver sampling rate is 3.84MHz and the half cut-off frequency is 1.25MHz, which matches sub-

carrier 128. The initial SNR values of the transmitted signal are set to 20dB, 15dB, 10dB and 5dB. The received signal over the Rayleigh multipath fading channel is shown in equation (2). The SINR value is computed by using:

$$SINR(k) = \frac{S_{\mathrm{Rx}}(k)^2}{N_{\mathrm{I}}^2(k)}, \qquad (12)$$

where $S_{\mathrm{Rx}}(k)$ is the received signal in kth sub-carrier and $N_{\mathrm{I}}^2(k)$ only determines the interference noise power at kth sub-carrier:

$$E[N_{\mathrm{I}}^2(k)] = E\left[|S_{\mathrm{Rx}}(k) - \alpha S_{\mathrm{Tx}}(k)|^2\right], \qquad (13)$$

where S_{Tx}^2 is the power of transmitted signal. Dividing (12) by the number of bits per symbol yields the $E_{\mathrm{b}}/N_{\mathrm{o}}$ value.

This paper compares the SINR performance of the received signal before and after the IIR analogue filter. The result shows the IIR filter does not affect the SINR performance significantly for the Rayleigh fading channel. After operating at a sample rate of 3.84MHz, the SINR degradation only occurs at near half cut-off frequency. If the SNR of transmitted signal at 20dB, the SINR degradation of received signal appears from sub-carrier number 90. If reducing the SNR of transmitted signal, the SINR degradation in the VC receiver mores closer to half the cut-off frequency. However, in the pass band, the VC system receiver provides good SINR performance, which means a VC system receiver is able to decode the transmitted messages reliably.

B. BER Performance of VC

The BER performance of the VC system uses Q-PSK, 16-QAM and 64-QAM modulation schemes and the CP length is 144 samples (LTE CP short standard). We assume that the bandwidth of the transmitted signal is 20MHz and the transmission sampling rate is 30.72MHz. The received signal firstly passes a Butterworth low pass filter with 2.5MHz cut-off frequency and the ADC sampling rate is 3.84MHz (1/8 of transmitted sampling frequency). According to the result of Fig. 4, if the SNR of transmitted signal is 20dB, the SINR performance of sub-carriers from 1 to 90 would not be affected by setting the sampling reduction ratio γ at 8. Therefore, we assume the VC receiver only decodes the messages located from sub-carriers 1 to 90.

The BER performance of the VC system over the AWGN channel is shown in Fig. 5, where the theoretical value of non-VC system (traditional LTE receiver) is computed as [10]:

$$\mathrm{BER}_{\mathrm{QPSK}} = \frac{1}{2} \cdot \mathrm{erfc}\left(\sqrt{\frac{E_{\mathrm{b}}}{N_{\mathrm{o}}}}\right), \qquad (14)$$

$$\mathrm{BER}_{16-\mathrm{QAM}} \approx \frac{3}{8} \cdot \mathrm{erfc}\left(\sqrt{\frac{2}{5} \cdot \frac{E_{\mathrm{b}}}{N_{\mathrm{o}}}}\right), \qquad (15)$$

$$\mathrm{BER}_{64-\mathrm{QAM}} \approx \frac{7}{24} \cdot \mathrm{erfc}\left(\sqrt{\frac{1}{7} \cdot \frac{E_{\mathrm{b}}}{N_{\mathrm{o}}}}\right), \qquad (16)$$

Fig. 5. BER Performance of the Virtual Carrier System over the AWGN Channel
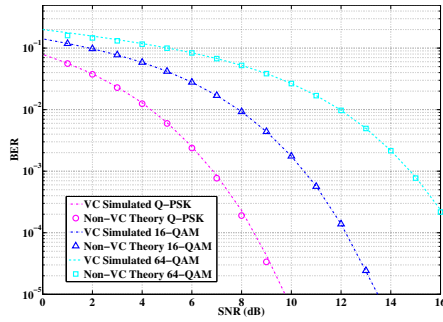

Fig. 6. BER Performance of the Virtual Carrier System over the Rayleigh Fading Channel

where $\mathrm{erfc}(.)$ denotes the complementary error function. It is obvious that comparing with the traditional LTE receiver, reducing the sampling rate at the VC receiver does not significantly affect on the BER performance. The VC receiver achieves almost the same BER performance on the AWGN channel.

Fig.6 shows the BER performance of VC system over the Rayleigh Fading channel and the theory value of the non-VC systems is computed as [10] [11]:

$$P_{\mathrm{QPSK}} = \frac{1}{2}\left(1 - \sqrt{\frac{E_{\mathrm{b}}/N_{\mathrm{o}}}{1 + E_{\mathrm{b}}/N_{\mathrm{o}}}}\right), \qquad (17)$$

$$P_{16-\mathrm{QAM}} = \frac{1}{2}\left(1 - \frac{3}{4}\sqrt{\frac{4 \cdot E_{\mathrm{b}}/N_{\mathrm{o}}}{5/2 + 4 \cdot E_{\mathrm{b}}/N_{\mathrm{o}}}}\right.$$
$$\left. - \frac{1}{2}\sqrt{\frac{4 \cdot E_{\mathrm{b}}/N_{\mathrm{o}}}{5/18 + 4 \cdot E_{\mathrm{b}}/N_{\mathrm{o}}}} + \frac{1}{4}\sqrt{\frac{4 \cdot E_{\mathrm{b}}/N_{\mathrm{o}}}{1/10 + 4 \cdot E_{\mathrm{b}}/N_{\mathrm{o}}}}\right). \quad (18)$$

For the 64-QAM modulation, the BER expression as:

$$P_{64-\mathrm{QAM}} = \sum_{i=1}^{28} \omega_i I(a_i, b_i, \overline{\gamma}, r, \rho), \qquad (19)$$

where $\overline{\gamma}$ is the average SNR per symbol and coefficients ω_i, a_i, b_i are listed in [12] and I is the integral representation: $I(z) = \frac{1}{\pi}\int_{-(\pi/2)}^{(\pi/2)} e^{-z \cdot \sin\phi} d\phi$. The BER performance of the VC system receiver over the Rayleigh fading channel again matches that of the non-VC receiver. It means by using a 3.84MHz ADC at the VC receiver saves almost 7/8 of the ADC power consumption and the computational complexity reduces from 11264 to 1024 operations without significant BER performance reduction. The VC system receiver can achieve higher energy saving performance and almost ideal SINR performance without significant BER degradation.

IV. CONCLUSION

In this paper, a practical Virtual Carrier system receiver that uses a narrowband analogue filter and a much lower sampling frequency ADC w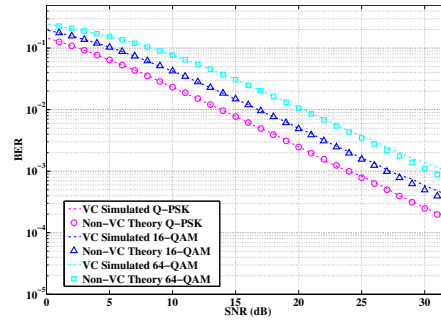as presented. In order to modify the existing LTE communication system to support a lower data rate transmission M2M system, the bandwidth efficiency and the energy saving performance should be considered. This paper shows that the VC system receiver can significantly improve the LTE downlink bandwidth efficiency and energy efficiency. At the same time, it provides a high SINR performance which means the BER degradation is negligible in the filter passband. Therefore, the VC system receiver could be a suitable solution to support the M2M system based on the LTE system.

REFERENCES

[1] M. F. L. Abdullah and A. Z. Yonis, "Performance of LTE Release 8 and Release 10 in wireless communications," in *CyberSec. Conf.*, 2012, pp. 236–241.

[2] Y. Chen and W. Wang, "Machine-to-Machine communication in LTE-A," in *Vehicular Technology Conference Fall (VTC Fall)*, 2010, pp. 1–4.

[3] R. Lu, X. Li, X. Liang, X. Shen, and X. Lin, "GRS: The green, reliability, and security of emerging machine to machine communications," *IEEE Commun. Mag.*, vol. 49, no. 4, pp. 28–35, 2011.

[4] Y. Zhang, R. Yu, S. Xie, W. Yao, Y. Xiao, and M. Guizani, "Home M2M networks: Architectures, standards, and QoS improvement," *IEEE Commun. Mag.*, vol. 49, no. 4, pp. 44–52, April 2011.

[5] M. Beale, "Future challenges in efficiently supporting M2M in the LTE standards," in *WCNC Workshops*, 2012, pp. 186–190.

[6] *3GPP TR 36.888, Study on Provision of Low-Cost Machine-Type Communications (MTC) User Equipments (UEs) Based on LTE.*

[7] E. Au, C. Wang, S. Sfar, R. Murch, W.-H. Mow, V. Lau, R. Cheng, and K. Letaief, "Error probability for MIMO zero-forcing receiver with adaptive power allocation in the presence of imperfect channel state information," *IEEE Trans. Wireless Commun.*, vol. 6, no. 4, pp. 1523–1529, April 2007.

[8] T. Sundstrom, B. Murmann, and C. Svensson, "Power dissipation bounds for high-speed nyquist analog-to-digital converters," *IEEE Trans. Circuits Syst. I, Reg. Papers*, vol. 56, no. 3, pp. 509–518, March 2009.

[9] K. Parhi and M. Ayinala, "Low-complexity welch power spectral density computation," *IEEE Trans. Circuits Syst. I, Reg. Papers*, vol. 61, no. 1, pp. 172–182, Jan 2014.

[10] J. Thompson and A. Smokvarski, "Bit Error Ratio performance of a receiver diversity scheme with channel estimation," *IET Communications*, vol. 1, no. 1, pp. 92–100, February 2007.

[11] F. Adachi, "BER analysis of 2PSK, 4PSK, and 16QAM with decision feedback channel estimation in frequency-selective slow rayleigh fading," *IEEE Trans. Veh. Technol.*, vol. 48, no. 5, pp. 1563–1572, Sep 1999.

[12] X. Tang, M.-S. Alouini, and A. Goldsmith, "Effect of channel estimation error on M-QAM BER performance in rayleigh fading," *IEEE Trans. Commun.*, vol. 47, no. 12, pp. 1856–1864, Dec 1999.

Waveform Performance For Asynchronous Wireless 5G Uplink Communications

Shendi Wang [†], Jean Armstrong [§] and John S. Thompson [†]

[†] *Institute for Digital Communications, The University of Edinburgh, EH9 3JL, Edinburgh, UK*
[§] *Department of Electrical and Computer Systems Engineering, Monash University, Monash, Australia*
Email: {Shendi.Wang, John.Thompson}@ed.ac.uk, Jean.Armstrong@monash.edu

Abstract—Machine type communications (MTC) could play a significant role in fifth generation (5G) wireless communications systems. In terms of reducing the side-lobes of orthogonal frequency-division multiplexing (OFDM) to support large numbers of asynchronous MTC devices, several waveform designs could be used. This paper provides closed form signal-to-interference-plus-noise ratio (SINR) and capacity results for this asynchronous scenario. We compare three candidate multi-carrier waveforms, which are OFDM, universal filtered multi-carrier (UFMC) and polynomial cancellation coded (PCC-OFDM). Our results indicate that both PCC and UFMC can provide better frequency roll-off than OFDM. PCC is more easier to implement and performs strongly against inter carrier interference (ICI) with cost of losing spectral efficiency and a higher peak-to-average power ratio (PAPR). UFMC is more robust to very dispersive multipath channels but with cost of increasing computational complexity.**

I. Introduction

Bigger, faster and higher are the main aims of the fifth generation (5G) of wireless communications systems. A previous study [1] highlighted one of the fundamental functions for 5G system will be support for the internet of things (IoT). Iot is synonymous with machine type communications (MTC) and exponential growth in MTC traffic is expected in the near future. One of the major challenges for future MTC is the scalability problem with massive machine to machine (M2M) communications over the air interface. The current 4G wireless network is based on the orthogonal frequency-division multiplexing (OFDM) [2] waveform. In order to protect its orthogonality, LTE uses synchronisation signals to avoid time offsets [3]. For MTC communications, M2M devices will not use synchronous signal transmission. They often send only a few bytes, which makes the overhead for synchronisation is too high. Instead in 5G systems, MTC traffic would be removed from standard uplink traffic with drastically reduced signalling overhead. By doing this, relaxing the synchronism requirements can significantly improve operational capabilities, bandwidth efficiency and even battery lifetime for low data rate M2M devices.

The 5GNOW project [1] has defined a new intermediate frame structure to support both high and low synchronisation requirements, which is called the unified frame layout. This aims to handle the very heterogeneous services and devices communicating over a 5G wireless access frame structure. In order to deal with the inter symbol interference (ISI) and inter carrier interference (ICI) effects, which are caused by

time and frequency offsets, several techniques can be used to reduce the OFDM side-lobes, e.g. filter bank multicarrier (FBMC) [4], which uses prototype filters in each sub-carrier with rectangular impulse responses. Due to the very narrow sub-carrier filters needed in FBMC, the filter length could be very long. Therefore, 5GNOW studies an alternative version, universal filtered multi-carrier (UFMC) [1], which groups a number of sub-carriers into a sub-band, and passes the signal though a finite impulse response (FIR) filter. In terms of reducing the OFDM side-lobes, polynomial cancellation coded orthogonal frequency-division multiplexing (PCC-OFDM) [5] is another possible solution. A previous study [6] has shown that the peak-to-average power ratio (PAPR) for PCC-OFDM is much higher than OFDM, and showed that the symmetric cancellation coding (SCC) can reduce the PAPR compared with PCC-OFDM. However, the bit error ratio (BER) performance over a multipath fading channel of SCC [6] is significantly poorer than PCC, especially when the carrier frequency offset (CFO) is large. Secondly, SCC does not improve the frequency roll-off in order to reduce the time offset effects unlike PCC.

Previous studies did several comparisons between UFMC and FBMC [1], however, there are no results comparing the time offset performance between PCC-OFDM, UFMC and OFDM. Our main contributions are as follows:

- Provide closed form results to compute the theoretical value of the signal-to-interference-plus-noise ratio (SINR) and capacity for time-offset transmission, which is perfectly match with Monte Carlo simulations.
- Provide a much detailed comparison between PCC-OFDM and UFMC, including different filter designs, power spectral density (PSD), SINR, upper band capacity, BER, computational complexity and PAPR.

This paper is organised as follows: Section II introduces the basic structure of UFMC and PCC-OFDM. Section III provides a time-offset model and ICI analysis. Section IV will compare PSD and side-lobe levels between OFDM, UFMC and PCC-OFDM. The simulation results will be presented in Section V and Section VI concludes the paper.

II. Uplink Waveform

This section will briefly introduce the three waveform types for system performance comparison.

223

A. OFDM

The baseband OFDM signal after constellation modulation and inverse fast Fourier transform (IFFT) operation includes a cyclic prefix (CP) to guard against ISI and ICI. Assume that message bits are to be transmitted over N sub-carriers and X_n denotes the modulation symbol to be transmitted in the frequency domain. The baseband time domain signal for an OFDM symbol can be expressed as:

$$x_v = \frac{1}{\sqrt{N}} \sum_{n=0}^{N-1} X_n \cdot e^{j2\pi nv/N} (v = 0, 1, ..., N-1), \quad (1)$$

where X is the fast Fourier transform (FFT) of x and v is the discrete time variable. Then the received signal over the multipath channel h (each channel tap l_H follows the quasi-static Rayleigh distribution) and additive white Gaussian noise (AWGN) g_v can be defined as:

$$y_v = x_v \otimes h + g_v, \quad (2)$$

where $\otimes$ denotes the convolution operation and a power spectral density $N_0/2$ is assumed for the noise samples g_v. After removing the CP in the receiver, the received signal for sub-carrier n at the output of FFT in the frequency domain can be expressed as:

$$Y_n = X_n \cdot H_n + G_n, \quad (3)$$

where H_n is the FFT of h and G_n is the FFT of the noise sequence g_v in the frequency domain.

B. UFMC

The block diagram of UFMC is shown in Fig. 1. Unlike OFDM, the principle of UFMC is grouping a number of sub-carriers into a sub-band (each sub-band transmitted for each user), which is passed to an N-point IFFT for conversion into the time domain. The time domain signal for one user d_v can be expressed as:

$$d_v = \frac{1}{\sqrt{N}} \sum_{k=0}^{N-1} D_k \cdot e^{j2\pi kv/N}, \quad (4)$$

where D_k is the symbol on the kth sub-carrier, and K is the total number of sub-carriers within one user. Then each user will be convolved with a rectangular narrow windowed filter with impulse response of b with length of L_F. At the output of the filter, the time domain signal s_v can be expressed as:

$$s_v = d_v \otimes b. \quad (5)$$

The received signal over a Rayleigh multipath channel with AWGN noise can be expressed as:

$$y_v = s_v \otimes h + g_v. \quad (6)$$

Note that each sub-band filter is designed as a band pass FIR filter, whose centre frequency matches with each sub-band's centre frequency. The received signal will be passed though a $2N$-point FFT to convert the time domain signal into the frequency domain. Then, we retain only even sub-carriers [7] which correspond to a data carrier.
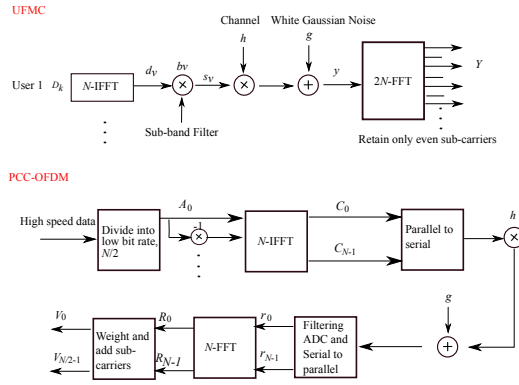

Fig. 1.   Block Diagram of UFMC and PCC-OFDM

C. PCC-OFDM

PCC is a coding technique for OFDM in which the data to be transmitted is mapped onto weighted groups of sub-carriers. Reference [5] has shown PCC-OFDM to be much less sensitive than OFDM to frequency offset and Doppler spread. The block diagram of a PCC-OFDM system is shown in Fig. 1, the baseband signal $A_0...A_{N/2-1}$ will pass through a PCC-OFDM modulator. In this case, pairs of sub-carriers have a relative weighting of +1, -1, and the input IFFT signal is organised as $A_0, -A_0..., A_{N/2-1}, -A_{N/2-1}$. After the N-point IFFT, the time domain samples c_v can be expressed as:

$$c_v = \frac{1}{\sqrt{N}} \sum_{n=0}^{N-1} A_n \cdot e^{j2\pi nv/N}. \quad (7)$$

The received signal over the Rayleigh multipath fading channel is then expressed as:

$$r_v = c_v \otimes h + g_v. \quad (8)$$

At the receiver, the data is recovered from the FFT outputs $R_0...R_N$. The mapping of data onto pairs of sub-carriers indicate that the ICI caused by one sub-carrier is substantially cancelled by the ICI caused by the other sub-carrier in the pair. Therefore, in the receiver, pairs of sub-carriers are combined by applying the weighting and then summing:

$$V_n = \frac{R_{2n} - R_{2n+1}}{2} (n = 0, 1, 2, ..., N/2 - 1). \quad (9)$$

One of the disadvantages of PCC-OFDM is the spectral efficiency is approximately half of that for OFDM as each data symbol is mapped to two carriers. For MTC communications, many M2M devices require only low data rate transmission. Therefore, in terms of reducing ICI effects, PCC-OFDM is another option for supporting M2M in 5G networks.

III. INTERFERENCE ANALYSIS

This section will introduce a time-offset transmission model and analyse its ICI to compute SINR and Shannon capacity.

A. System Model for Time offset

As mentioned above, the future 5G system for MTC communications should allow to transmit with relaxed synchronisation conditions regarding time misalignments. Therefore, we assume the received M2M signal is asynchronous and is suffered by time-offsets. The system model for time offset is shown in Fig. 2. Previous UFMC papers are often based on long OFDM symbol transmission, where the FFT size is chosen as 1024 [1]. In this paper, we pay attention to the performance of a short OFDM symbol which is affected by a significant time offset due to asynchronous transmission of different M2M users. Here we assume the uplink bandwidth is 1.25MHz and the sub-carrier spacing in 15 kHz, where the FFT size is 128 and supports up to 7 users. Each user's transmission occupies 14 sub-carriers in the frequency domain, and the users are spaced by 2 blank sub-carriers. In this paper, the number of transmitting users is set to 3 or 5. The scalar τ is the relative delay between adjacent users.
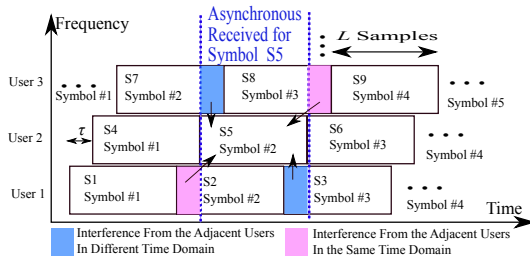

Fig. 2.   Time Offset Model

B. ICI Analysis

This paper will consider every second symbol for each user, in this case, the interference of symbols S_2, S_5, and S_8 will be computed as shown in Fig. 2. The symbol index number S is the same with the Fig. 2. Here we define L as the length of transmitted symbol in samples. Thus, for OFDM and PCC-OFDM, $L = N + L_{CP}$, where L_{CP} is the length of CP in samples. In order to provide a fair comparison, we choose the length of OFDM, PCC-OFDM and UFMC in samples to be the same. Thus, for UFMC, $L = N + L_F - 1 = N + L_{CP}$.

The interference ICI for each user is caused by the sidelobe attenuation on the adjacent users when the received signals are asynchronous. Thus, the interference of S_5 is dominated by the tail of τ samples from S_7 and the first of τ samples from S_3. The remaining samples of S_2 and S_8 are relatively orthogonal. In this case, the ICI also includes the miss orthogonality term from S_2 and S_8. Then, we can write the interference terms i_{term5} for S_5 as:

$$i_{term5} = \sum_{v=0}^{\tau-1} x_v(S_3) + \sum_{v=L-\tau}^{L-1} x_v(S_7) \qquad (10)$$
$$+ \sum_{v=0}^{\tau-1} x_v(S_2) + \sum_{v=L-\tau}^{L-1} x_v(S_8),$$

Similarly, the interference terms for symbol S_2 can be expressed as:

$$i_{term2} = \sum_{v=L-\tau}^{L-1} x_v(S_4) + \sum_{v=L-2\tau}^{L-1} x_v(S_7) \qquad (11)$$
$$+ \sum_{v=L-\tau}^{L-1} x_v(S_5) + \sum_{v=L-2\tau}^{L-1} x_v(S_8).$$

and for symbol S_8 can be expressed as:

$$i_{term8} = \sum_{v=0}^{2\tau-1} x_v(S_3) + \sum_{v=0}^{\tau-1} x_v(S_6) \qquad (12)$$
$$+ \sum_{v=0}^{2\tau-1} x_v(S_2) + \sum_{v=0}^{\tau-1} x_v(S_5).$$

Therefore, the interference term on the kth sub-carrier can be rewritten using the Fourier transform as:

$$I_{term2}(k) = \sum_{k=0}^{N-1} \sum_{v=L-\tau}^{L-1} (x_v(S_4) + x_v(S_5))e^{-j2\pi nk/N}$$
$$+ \sum_{k=0}^{N-1} \sum_{v=L-2\tau}^{L-1} (x_v(S_7) + x_v(S_8))e^{-j2\pi nk/N}, \qquad (13)$$

$$I_{term5}(k) = \sum_{k=0}^{N-1} \sum_{v=0}^{\tau-1} (x_v(S_3) + x_v(S_2))e^{-j2\pi nk/N}$$
$$+ \sum_{k=0}^{N-1} \sum_{v=L-\tau}^{L-1} (x_v(S_7) + x_v(S_8))e^{-j2\pi nk/N}, \qquad (14)$$

$$I_{term8}(k) = \sum_{k=0}^{N-1} \sum_{v=0}^{2\tau-1} (x_v(S_3) + x_v(S_2))e^{-j2\pi nk/N}$$
$$+ \sum_{k=0}^{N-1} \sum_{v=0}^{\tau-1} (x_v(S_6) + x_v(S_5))e^{-j2\pi nk/N}. \qquad (15)$$

Note that, when 2τ is longer than N, the interference term is mainly due to adjacent symbols (e.g. the interference of S_2 is mainly caused by S_4 and S_5). Then we can compute the SINR ρ for the time-offset model as:

$$\rho(k) = \frac{E\left[X(k)^2\right]}{\sigma^2 + E[|I_{term}(k)|^2]}, \qquad (16)$$

where $E[\cdot]$ denotes statistical expectation. Now, we can compute an estimate of the capacity $C_{Cap}(k)$ for sub-carrier k basic on our SINR equations as:

$$C_{Cap}(k) = \log 2(1 + \rho(k)), \qquad (17)$$

note that the upper bound capacity of PCC-OFDM should be half of C_{Cap} due to its half of spectral efficiency.

IV. OFDM SIDE-LOBE BEHAVIOUR: PSD

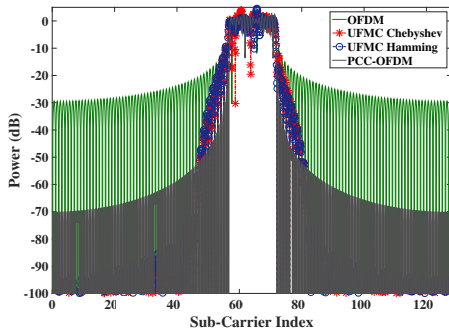This section will focus on comparing the side-lobe behaviour for the three waveforms: OFDM, UFMC and PCC-OFDM.

225

Fig. 3. Side-Lobe Behavior of OFDM, UFMC Chebyshev $f_{\mathrm{cf}} = 0.18$, A_{SL}=64dB, UFMC Hamming $f_{\mathrm{cf}} = 0.18$, and PCC-OFDM, $N = 128$

A. PSD: OFDM, UFMC, PCC-OFDM

Previous studies of UFMC focus on the Dolph-Chebyshev filter. However, the Hamming window is another most well-known approaches to reduce the side-lobe structure [8]. In order to compare their spectral behaviour, we set the normalised cut-off frequency to $f_{\mathrm{cf}} = 0.18$ and the side-lobe attenuation A_{SL} set to 40dB. The spectral behaviour of OFDM, UFMC (with Chebyshev and Hamming) and PCC-OFDM waveforms is shown in Fig. 3. Both UFMC and PCC-OFDM can reduce the side-lobe level significantly compared with OFDM and there is no significant differences between the Chebyshev and Hamming windows. Moreover, PCC-OFDM provides a better ICI protection due to its very rapid side-lobe roll-off.

B. Filters Design For UFMC

In order to achieve a low side-lobe attenuation without significant attenuation of the carrier in the pass-band, we consider several filter designs. The ratio γ between the number of sub-carriers per user N_{Sub} and the total number of available sub-carriers N can be defined as:

$$\gamma = \frac{N_{\mathrm{Sub}}}{N} = \frac{14}{128} = 0.1094. \qquad (18)$$

The normalised cut-off frequency should bigger than γ. Thus, we can consider three normalised cut-off frequencies for the UFMC filter as $f_{\mathrm{cf1}} = 0.15, f_{\mathrm{cf2}} = 0.18$ and $f_{\mathrm{cf3}} = 0.2$. The length of the filter L_{F} is set as 32 samples and A_{SL} is chosen as 40dB and 64dB. The filters' frequency responses are shown in Fig. 4, with increasing f_{cf}, the side-lobe level will be reduced. Meanwhile, the stop-band will move further away from the pass-band. In terms of achieving lower side-lobes and narrow pass-band, the filter with $f_{\mathrm{cf2}} = 0.18$ and A_{SL}= 40dB presents the best compromise design.

V. Simulation Results

In terms of the fair comparison, we assume L_{F} is set to 32 samples and L_{CP} is set to 31 samples to ensure they have a same transmission length in sample. The transmitted signal power for OFDM, UFMC and PCC-OFDM are the same. For
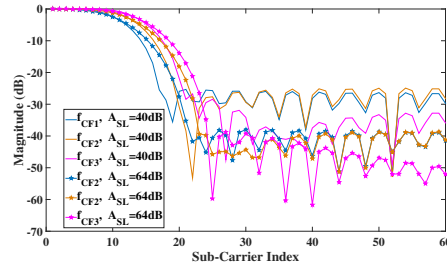

Fig. 4. Filter Frequency Responses, Chebyshev, L_{F}=32

the OFDM and UFMC systems, BPSK and QPSK will be used. Because the spectral efficiency of PCC-OFDM is half of the OFDM system, the corresponding constellation schemes for PCC-OFDM are chosen as QPSK or 16-QAM. The total number of MTC users is set to 3 or 5. As in Sec IV. B, the sub-carrier ratio $\gamma = 0.1094$, the normalised cut-off frequencies f_{cf} is set to 0.18 and the side-lobe attenuation A_{SL} is set to 40dB in the next simulations.

A. SINR and Upper Band Capacity

The SINR performance over the AWGN channel with a signal to noise ratio (SNR) of 30dB is shown in Fig. 5, and we assume τ is 50 samples time offset which is much longer than L_{CP} or L_{F}. The theoretical values are computed from equation (16), which perfectly match with the simulations. Compared with OFDM and UFMC, PCC-OFDM presents the best performance. The nearby sub-carriers of both OFDM and UFMC are significantly affected by ICI. UFMC can perform slightly better than OFDM (about 3.5dB higher SINR), but it still has a poorer SINR than PCC-OFDM.

The capacity performance with AWGN of 30dB is shown in Fig. 6 and the theoretical values C_{Cap} as described in equation (17) provide accurate closed-form results. The capacity of both OFDM and UFMC will be reduced when τ is longer than L_{CP} or L_{F}, compared with OFDM, UFMC improves the capacity about 1bit/sec/Hz when τ is larger than L_{F}. The PCC system provides the worst performance because of its reduced spectral efficiency even it can achieve the highest SINR performance.

B. BER Performance of OFDM, UFMC and PCC-OFDM

The BER performance for the AWGN channel is shown in Fig. 7. The results are plotted for $E_{\mathrm{b}}/N_{\mathrm{o}}$ and every multiple access scheme has the same transmitted signal power. Again L_{CP} is set to 31 samples, L_{F} is set to 32 samples, and τ is 70 samples. The Hamming filter with f_{cf} of 0.18 is used for UFMC. The results are similar with the SINR curves, for low data rate requirements, QPSK PCC-OFDM presents the best performance in terms of BER. When the BER is 10^{-3}, PCC-OFDM saves about 0.7dB $E_{\mathrm{b}}/N_{\mathrm{o}}$ compared with UFMC and is about 1.5dB better than OFDM. However, it will present the poorest $E_{\mathrm{b}}/N_{\mathrm{o}}$ efficiency when increasing the data rate via the use of 16-QAM modulation as compared to QPSK for OFDM and UFMC.
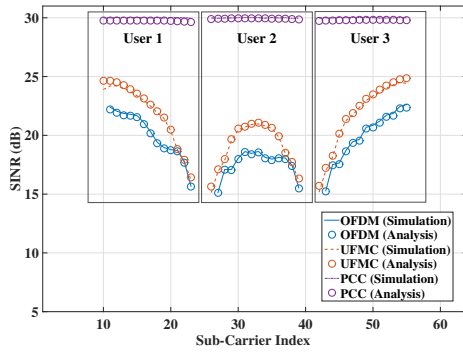
226

Fig. 5. SINR Performance with AWGN (SNR=30dB), UFMC(Chebyshev Filter,f_{cf}=0.18, A_{SL}=40dB), τ=50, L_{CP}=31, L_F=32, Spectral Efficiency = 2 bit/s/Hz

Fig. 6. Capacity Performance with AWGN (SNR=30dB), L_{CP}=31, L_F=32, Spectral Efficiency = 2 bit/s/Hz

Fig. 7. BER: AWGN, $\tau = 70$, Hamming f_{cf}=0.18, L_{CP}=31, L_F=32, The Total Number of Interfering User = 3, Spectral Efficiency = 1 or 2 bit/s/Hz
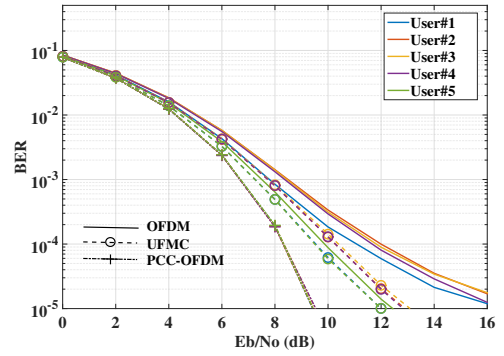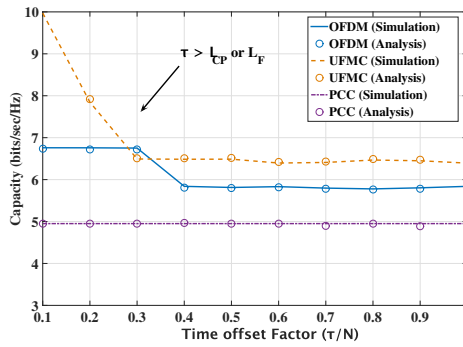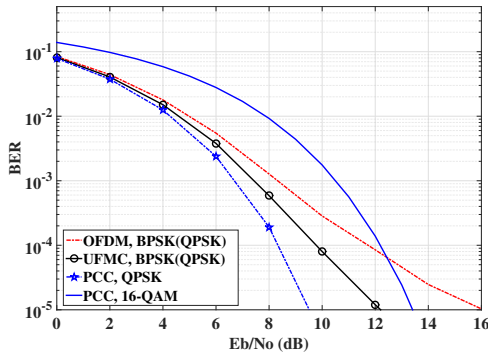

Fig. 8. BER: AWGN, $\tau = 70$, Hamming f_{cf}=0.18, L_{CP}=31, L_F=32, The Total Number of Interfering User = 5, Spectral Efficiency = 2 bit/s/Hz

In order to study each user's performance with large time offsets, we increase the number of interfering users to 5 as shown in Fig. 8. For UFMC and OFDM, the ICI of User No.1 and User No.5 is slightly less than User No.3. This closely matches with our SINR results, where the sub-carriers allocated at the middle of the frequency band will be significantly interfered by adjacent users. As the number of interfering users increases, the ICI will also be increased. However, for PCC-OFDM, there is no significant BER degradation when increasing the number of interfering users.

The BER performance for $\tau = 10$ samples over the Rayleigh multipath channel is shown in Fig. 9, where L_{CP} is 47 samples and L_F is 48 samples. The channel tap lengths are set to 10 and 70 samples and the modulation scheme for OFDM and UFMC is BPSK while for PCC-OFDM it is QPSK. The Hamming filter is used for the UFMC system with f_{cf} normalised to 0.18. When the number of channel taps is smaller than L_F and L_{CP}, both UFMC and PCC-OFDM can present better BER performance than OFDM. When the number of channel taps is 70 (much longer than L_{CP}), UFMC presents the best performance in terms of BER.

The BER performance for $\tau = 70$ samples over the Rayleigh multipath channel is shown in Fig. 10. It clearly shows that when the number of taps is smaller than L_{CP} or L_F, PCC-OFDM presents the best performance in terms of BER. When the number of taps is longer than L_{CP}, PCC-OFDM is no longer robust to the ISI effect. UFMC presents a slightly better BER performance when the number of channel taps is 70. Compared with UFMC, PCC-OFDM is more sensitive to the multipath channel effects.

C. Computational Complexity and PAPR

The computational complexity performance is shown in Table I. It clearly shows that the transmitter IFFT computational complexity of UFMC (for transmission the main cost is the filter convolution operations and for the receiver it is the $2N$ point FFT) is significantly higher than OFDM and PCC-OFDM (4096 operations more than OFDM and PCC-OFDM).
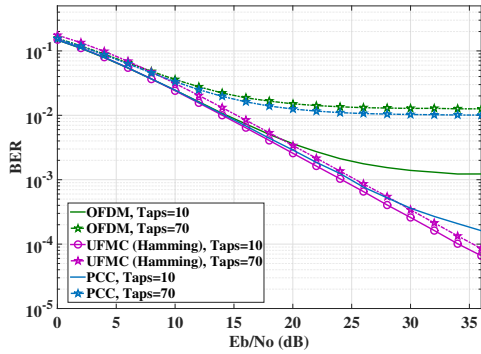
Fig. 9. BER: Rayleigh Multipath Channel Length= 10, 70, $\tau = 10$, Hamming f_{cf}=0.18, L_{CP}=47, L_{F}=48, Spectral Efficiency = 2 bit/s/Hz
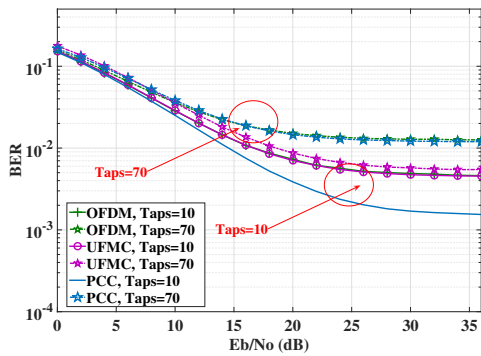
Fig. 10. BER: Rayleigh Multipath Channel Length= 10, 70, $\tau = 70$, Hamming f_{cf}=0.18, L_{CP}=47, L_{F}=48, Spectral Efficiency = 2 bit/s/Hz

When the filter length is increased, the IFFT computational complexity will be increased significantly.

The PAPR performance is shown in Fig. 11. Both UFMC and PCC-OFDM increase the PAPR compared with OFDM. The PAPR of PCC-OFDM is about 2.1 dB higher than OFDM and 1.7dB higher than UFMC at a complementary cumulative distribution function (CCDF) value of 10^{-2}. Thus, for PCC-OFDM, the sidelobe reduction comes at the cost of a slightly higher PAPR. This will require a higher power amplifier for the same signal coverage, assuming that the PAPR leads an increased amplifier back-off.

VI. CONCLUSION

In conclusion, this paper provides a detailed comparison between OFDM, UFMC and PCC. We highlight our key findings as: both UFMC and PCC-OFDM can provide better frequency roll-off than OFDM in terms of supporting low data rate asynchronous 5G M2M communications. PCC is easier to implement and can strongly against ICI with the

TABLE I
COMPUTATIONAL COMPLEXITY COMPARISONS

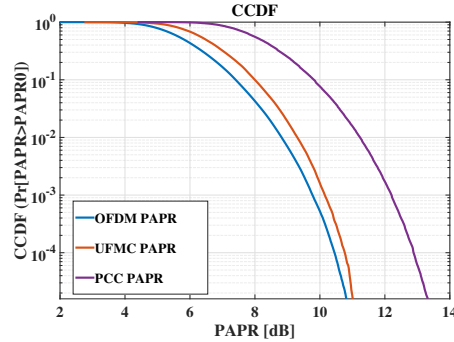| System: N=128	Transmitter (Ops)	Receiver (Ops)
OFDM	448	448
PCC-OFDM	448	448
UFMC, $L_{\text{F}} = 32$	4544	1024
UFMC, $L_{\text{F}} = 48$	6592	1024

Fig. 11. The PAPR of OFDM, UFMC and PCC, $N = 128$, Hamming f_{cf}=0.18, L_{F}=32

cost of halving spectral efficiency and higher PAPR. In the AWGN channel with a BER of 10^{-3} and a time offset of 70 samples, the $E_{\text{b}}/N_{\text{o}}$ of PCC-OFDM is about 0.7dB better than UFMC and 1.5dB better than OFDM. Compared with PCC, UFMC can slightly improve the performance in very dispersive multipath channel scenarios. However, it will significantly increase the computational complexity due to the transmit filter banks and the $2N$ point FFT that is required at the receiver. Thus, we can conclude that PCC can be used when channel conditions are good and the data requirement is low. UFMC can be used more widely in supporting 5G M2M communications.

REFERENCES

[1] G. Wunder *et al*, "5GNOW: non-orthogonal, asynchronous waveforms for future mobile applications," *IEEE Commun. Mag.*, vol. 52, no. 2, pp. 97–105, February 2014.

[2] S. Wang and J. Thompson, "Signal processing implementation of virtual carrier for supporting M2M systems based on LTE," in *IEEE VTC Spring*, May 2015, pp. 1–5.

[3] Z. Shen *et al*, "Overview of 3GPP LTE-Advanced carrier aggregation for 4G wireless communications," *IEEE Commun. Mag.*, vol. 50, no. 2, pp. 122–130, February 2012.

[4] B. Farhang-Boroujeny, "OFDM versus filter bank multicarrier," *IEEE Signal Process. Mag.*, vol. 28, no. 3, pp. 92–112, May 2011.

[5] J. Armstrong, "Analysis of new and existing methods of reducing intercarrier interference due to carrier frequency offset in OFDM," *IEEE Trans. Commun.*, vol. 47, no. 3, pp. 365–369, Mar 1999.

[6] T. Hashimoto *et al*, "ICI mitigation schemes for uncoded OFDM over channels with Doppler spreads and frequency offsets part II: Asymptotic analysis," in *Journal of Communications*, Sep 2012, pp. 686–700.

[7] X. Wang *et al*, "Universal filtered multi-carrier with leakage-based filter optimization," in *European Wireless Conference, Proceedings of European Wireless*, May 2014, pp. 1–5.

[8] F. Harris, "On the use of windows for harmonic analysis with the discrete Fourier transform," *Proc. IEEE*, vol. 66, no. 1, pp. 51–83, Jan 1978.

228

Bibliography

[1] C. Han, T. Harrold, S. Armour, I. Krikidis, S. Videv, P. M. Grant, H. Haas, J. S. Thompson, I. Ku, C.-X. Wang, T. A. Le, M. Nakhai, J. Zhang, and L. Hanzo, "Green radio: radio techniques to enable energy-efficient wireless networks," *IEEE Commun. Mag.*, vol. 49, no. 6, pp. 46–54, 2011.

[2] J. Tang, D. K. C. So, E. Alsusa, and K. A. Hamdi, "Resource efficiency: A new paradigm on energy efficiency and spectral efficiency tradeoff," *IEEE Trans. Wireless Commun.*, vol. 13, pp. 4656–4669, Aug 2014.

[3] G. Wu, S. Talwar, K. Johnsson, N. Himayat, and K. D. Johnson, "M2M: From mobile to embedded internet," *IEEE Commun. Mag.*, vol. 49, pp. 36–43, April 2011.

[4] H. S. Dhillon, H. C. Huang, H. Viswanathan, and R. A. Valenzuela, "Power-efficient system design for cellular-based machine-to-machine communications," *IEEE Trans. Wireless Commun.*, vol. 12, pp. 5740–5753, November 2013.

[5] Y. C. Pang, G. Y. Lin, and H. Y. Wei, "Context-aware dynamic resource allocation for cellular M2M communications," *IEEE Internet of Things Journal*, vol. 3, pp. 318–326, June 2016.

[6] A. Ali, W. Hamouda, and M. Uysal, "Next generation M2M cellular networks: challenges and practical considerations," *IEEE Commun. Mag.*, vol. 53, pp. 18–24, September 2015.

[7] S. Severi, F. Sottile, G. Abreu, C. Pastrone, M. Spirito, and F. Berens, "M2M technologies: Enablers for a pervasive Internet of Things," in *Networks and Communications (EuCNC), 2014 European Conference on*, pp. 1–5, June 2014.

[8] *3GPP Technical Report 36.888, Study on Provision of Low-Cost Machine-Type Communications (MTC) User Equipments (UEs) Based on LTE*, URL: http://www.3gpp.org/dynareport/36888.htm.

[9] D. Astely, E. Dahlman, G. Fodor, S. Parkvall, and J. Sachs, "LTE release 12 and beyond [accepted from open call]," *IEEE Commun. Mag.*, vol. 51, pp. 154–160, July 2013.

[10] M. Wang, W. Yang, J. Zou, B. Ren, M. Hua, J. Zhang, and X. You, "Cellular machine-type comm unications: physical challenges and solutions," *IEEE Wireless Communications*, vol. 23, pp. 126–135, April 2016.

[11] I. L. J. da Silva, A. L. F. de Almeida, F. R. P. Cavalcanti, R. Baldemair, and S. Fala-hati, "Improved data-aided channel estimation in LTE PUCCH using a tensor modeling approach," in *2010 IEEE International Conference on Communications (ICC)*, pp. 1–5, May 2010.

[12] L. Dai, B. Wang, Y. Yuan, S. Han, C. l. I, and Z. Wang, "Non-orthogonal multiple access for 5G: solutions, challenges, opportunities, and future research trends," *IEEE Commun. Mag.*, vol. 53, pp. 74–81, September 2015.

[13] G. Wunder *et al*, "5GNOW: Challenging the LTE design paradigms of orthogonality and synchronicity," in *Vehicular Technology Conference (VTC Spring), 2013 IEEE 77th*, pp. 1–5, June 2013.

[14] M. F. L. Abdullah and A. Z. Yonis, "Performance of LTE Release 8 and Release 10 in wireless communications," in *CyberSec. Conf.*, pp. 236–241, 2012.

[15] K. Doppler, M. Rinne, C. Wijting, C. B. Ribeiro, and K. Hugl, "Device-to-device communication as an underlay to LTE-Advanced networks," *IEEE Commun. Mag.*, vol. 47, pp. 42–49, Dec 2009.

[16] C. Gessner, A. Roessler, and M. Kottkamp, "UMTS long term evolution LTE technology introduction," 2012.

[17] R. Lu, X. Li, X. Liang, X. Shen, and X. Lin, "GRS: The green, reliability, and security of emerging machine to machine communications," *IEEE Commun. Mag.*, vol. 49, no. 4, pp. 28–35, 2011.

[18] A. Laya, L. Alonso, and J. Alonso-Zarate, "Is the random access channel of lte and lte-a suitable for m2m communications? a survey of alternatives," *IEEE Communications Surveys Tutorials*, vol. 16, pp. 4–16, First 2014.

[19] V. Gazis, "A survey of standards for machine to machine (M2M) and the internet of things (IoT)," *IEEE Communications Surveys Tutorials*, vol. PP, no. 99, pp. 1–1, 2016.

[20] K. Chang, A. Soong, M. Tseng, and Z. Xiang, "Global wireless machine-to-machine standardization," *IEEE Internet Computing*, vol. 15, pp. 64–69, March 2011.

[21] T. Taleb and A. Kunz, "Machine type communications in 3GPP networks: potential, challenges, and solutions," *IEEE Commun. Mag.*, vol. 50, pp. 178–184, March 2012.

[22] ETSI-TS, "102 690 v1.1.1, machine-to-machine communications (M2M); functional architecture," Octr 2011.

[23] L. Karim, A. Anpalagan, N. Nasser, J. N. Almhana, and I. Woungang, "An energy efficient, fault tolerant and secure clustering scheme for m2m communication networks," in *2013 IEEE Globecom Workshops (GC Wkshps)*, pp. 677–682, Dec 2013.

[24] J. G. Andrews, S. Buzzi, W. Choi, S. V. Hanly, A. Lozano, A. C. K. Soong, and J. C. Zhang, "What will 5G be?," *IEEE J. Sel. Areas Commun.*, vol. 32, pp. 1065–1082, June 2014.

[25] Y. Zhang, R. Yu, S. Xie, W. Yao, Y. Xiao, and M. Guizani, "Home M2M networks: Architectures, standards, and QoS improvement," *IEEE Commun. Mag.*, vol. 49, pp. 44–52, April 2011.

[26] F. Schaich, T. Wild, and Y. Chen, "Waveform contenders for 5G - suitability for short packet and low latency transmissions," in *IEEE Vehicular Technology Conference (VTC Spring)*, pp. 1–5, May 2014.

[27] A. Bartoli, J. Hernandez-Serrano, M. Soriano, M. Dohler, A. Kountouris, and D. Barthel, "Secure lossless aggregation over fading and shadowing channels for smart grid M2M networks," *IEEE Transactions on Smart Grid*, vol. 2, pp. 844–864, Dec 2011.

[28] K. Zheng, F. Hu, W. Wang, W. Xiang, and M. Dohler, "Radio resource allocation in LTE-Advanced cellular networks with M2M communications," *IEEE Commun. Mag.*, vol. 50, pp. 184–192, July 2012.

[29] J. Tang, D. K. C. So, E. Alsusa, K. A. Hamdi, and A. Shojaeifard, "Resource allocation for energy efficiency optimization in heterogeneous networks," *IEEE J. Sel. Areas Commun.*, vol. 33, pp. 2104–2117, Oct 2015.

[30] T. M. Schmidl and D. C. Cox, "Robust frequency and timing synchronization for OFDM," *IEEE Trans. Commun.*, vol. 45, pp. 1613–1621, Dec 1997.

[31] I. Glover and P. M. Grant, *Digital Communications*. Pearson Education, 2010.

[32] S. H. Muller and J. B. Huber, "OFDM with reduced peak-to-average power ratio by optimum combination of partial transmit sequences," *Electronics Letters*, vol. 33, pp. 368–369, Feb 1997.

[33] S. H. Han and J. H. Lee, "An overview of peak-to-average power ratio reduction techniques for multicarrier transmission," *IEEE Wireless Communications*, vol. 12, pp. 56–65, April 2005.

[34] M. Rumney, "3GPP LTE: Introducing single-carrier FDMA," *Agilent Technologies White Paper*, 2008.

[35] S. Srikanth, P. A. M. Pandian, and X. Fernando, "Orthogonal frequency division multiple access in WiMAX and LTE: a comparison," *IEEE Commun. Mag.*, vol. 50, pp. 153–161, September 2012.

[36] M. Sternad, T. Svensson, T. Ottosson, A. Ahlen, A. Svensson, and A. Brunstrom, "Towards systems beyond 3g based on adaptive ofdma transmission," *Proc. IEEE*, vol. 95, pp. 2432–2455, Dec 2007.

[37] D. Astely, E. Dahlman, A. Furuskr, Y. Jading, M. Lindstrm, and S. Parkvall, "LTE: the evolution of mobile broadband," *IEEE Commun. Mag.*, vol. 47, pp. 44–51, April 2009.

[38] J. Silverman, V. Vickers, and J. Sampson, "Statistical estimates of the n -bit Gray codes by restricted random generation of permutations of 1 to 2^n," *IEEE Trans. Inf. Theory*, vol. 29, pp. 894–901, Nov 1983.

[39] L. Grover, "Weighted code approach to generate Gray code," *IEEE Potentials*, vol. 34, pp. 39–40, May 2015.

[40] B. Sklar, "Rayleigh fading channels in mobile digital communication systems. I. characterization," *IEEE Commun. Mag.*, vol. 35, pp. 136–146, Sep 1997.

[41] E. Au, C. Wang, S. Sfar, R. Murch, W.-H. Mow, V. Lau, R. Cheng, and K. Letaief, "Error probability for MIMO zero-forcing receiver with adaptive power allocation in the presence of imperfect channel state information," *IEEE Trans. Wireless Commun.*, vol. 6, pp. 1523–1529, April 2007.

[42] I. Otung, *Communication engineering principles*. Palgrave Macmillan, 2001.

[43] G. Stphane, Le, *EEE8003: Advanced Modulation and Coding Techniques.* Newcastle University, School of Electrical, Electronic and Computer Engineering, 2010.

[44] J. S. Thompson and A. Smokvarski, "Bit Error Ratio performance of a receiver diversity scheme with channel estimation," *IET Communications*, vol. 1, pp. 92–100, February 2007.

[45] F. Adachi, "BER analysis of 2PSK, 4PSK, and 16QAM with decision feedback channel estimation in frequency-selective slow Rayleigh fading," *IEEE Trans. Veh. Technol.*, vol. 48, pp. 1563–1572, Sep 1999.

[46] B. H. Walke, S. Mangold, and L. Berlemann, *IEEE 802 wireless systems: protocols, multi-hop mesh/relaying, performance and spectrum coexistence.* John Wiley & Sons, 2007.

[47] G. J. Miao and M. A. Clements, *Digital signal processing and statistical classification.* Artech House, 2002.

[48] Y. Fan and J. S. Thompson, "MIMO configurations for relay channels: Theory and practice," *IEEE Trans. Wireless Commun.*, vol. 6, pp. 1774–1786, May 2007.

[49] B. Mulgrew, P. M. Grant, and J. S. Thompson, *Digital Signal Processing: Concepts and Applications.* Palgrave Macmillan, 2002.

[50] J. Jan and I. of Electrical Engineers, *Digital Signal Filtering, Analysis and Restoration.* IEE telecommunications series, Institution of Electrical Engineers, 2000.

[51] R. Losada and V. Pellisier, "Designing IIR filters with a given 3-dB point," *IEEE Signal Process. Mag.*, vol. 22, pp. 95–98, July 2005.

[52] A. D. S. Jayalath and C. Tellambura, "Reducing the out-of-band radiation of OFDM using an extended guard interval," in *IEEE Vehicular Technology Conference (VTC 2001 Fall 54th)*, vol. 2, pp. 829–833 vol.2, 2001.

[53] B. Farhang-Boroujeny, "OFDM versus filter bank multicarrier," *IEEE Signal Process. Mag.*, vol. 28, pp. 92–112, May 2011.

[54] J. Armstrong, T. Gill, and C. Tellambura, "Performance of PCC-OFDM with overlapping symbol periods in a multipath channel," in *IEEE, Global Telecommunications Conference*, vol. 1, pp. 87–91 vol.1, 2000.

[55] N. Michailow, M. Matthe, I. Gaspar, A. Caldevilla, L. Mendes, A. Festag, and G. Fettweis, "Generalized frequency division multiplexing for 5th generation cellular networks," *IEEE Trans. Commun.*, vol. 62, pp. 3045–3061, Sept 2014.

[56] D. Niyato, L. Xiao, and P. Wang, "Machine-to-machine communications for home energy management system in smart grid," *IEEE Commun. Mag.*, vol. 49, pp. 53–59, April 2011.

[57] P. Osti, P. Lassila, S. Aalto, A. Larmo, and T. Tirronen, "Analysis of PDCCH performance for M2M traffic in LTE," *IEEE Trans. Veh. Technol.*, vol. 63, pp. 4357–4371, Nov 2014.

[58] J. Kim, J. Lee, J. Kim, and J. Yun, "M2M service platforms: Survey, issues, and enabling technologies," *IEEE Commun. Surveys Tuts.*, vol. 16, pp. 61–76, First 2014.

[59] F. Pauls, S. Krone, W. Nitzold, G. Fettweis, and C. Flores, "Evaluation of efficient modes of operation of GSM/GPRS modules for M2M communications," in *IEEE Vehicular Technology Conference (VTC Fall) 78th*, pp. 1–6, Sept 2013.

[60] A. Gotsis, A. Lioumpas, and A. Alexiou, "M2M scheduling over LTE: Challenges and new perspectives," *IEEE Veh. Technol. Mag.*, vol. 7, pp. 34–39, Sept 2012.

[61] S.-E. Elayoubi, O. Ben Haddada, and B. Fourestie, "Performance evaluation of frequency planning schemes in OFDMA-based networks," *IEEE Trans. Wireless Commun.*, vol. 7, pp. 1623–1633, May 2008.

[62] F.-S. Chu, K.-C. Chen, and G. Fettweis, "Green resource allocation to minimize receiving energy in OFDMA cellular systems," *IEEE Commun. Lett.*, vol. 16, pp. 372–374, March 2012.

[63] A. Laya, L. Alonso, P. Chatzimisios, and J. Alonso-Zarate, "Massive access in the random access channel of LTE for M2M communications: An energy perspective," in *2015 IEEE International Conference on Communication Workshop (ICCW)*, pp. 1452–1457, June 2015.

[64] J. Misic, V. Misic, and N. Khan, "Sharing it my way: Efficient M2M access in LTE/LTE-A networks," *IEEE Transactions on Vehicular Technology*, vol. PP, no. 99, pp. 1–1, 2016.

[65] R. Ratasuk, N. Mangalvedhe, A. Ghosh, and B. Vejlgaard, "Narrowband LTE-M system for M2M communication," in *2014 IEEE 80th Vehicular Technology Conference (VTC2014-Fall)*, pp. 1–5, Sept 2014.

[66] Y. Gao, Z. Qin, Z. Feng, Q. Zhang, O. Holland, and M. Dohler, "Scalable amp; reliable iot enabled by dynamic spectrum management for M2M in LTE-A," *IEEE Internet of Things Journal*, vol. PP, no. 99, pp. 1–1, 2016.

[67] J. W. Qiu and Y. C. Tseng, "M2M encountering: Collaborative localization via instant inter-particle filter data fusion," *IEEE Sensors Journal*, vol. 16, pp. 5715–5724, July 2016.

[68] M. A. Mehaseb, Y. Gadallah, A. Elhamy, and H. Elhennawy, "Classification of LTE uplink scheduling techniques: An M2M perspective," *IEEE Communications Surveys Tutorials*, vol. 18, pp. 1310–1335, Secondquarter 2016.

[69] X. Xiong, L. Hou, K. Zheng, W. Xiang, M. S. Hossain, and S. M. M. Rahman, "SMDP-based radio resource allocation scheme in software-defined internet of things networks," *IEEE Sensors Journal*, vol. PP, no. 99, pp. 1–1, 2016.

[70] H. Li, D. Seed, B. Flynn, C. Mladin, and R. D. Girolamo, "Enabling semantics in an M2M/IoT service delivery platform," in *2016 IEEE Tenth International Conference on Semantic Computing (ICSC)*, pp. 206–213, Feb 2016.

[71] M. Beale, "Future challenges in efficiently supporting M2M in the LTE standards," in *2012 IEEE Wireless Communications and Networking Conference Workshops (WC-NCW)*, , pp. 186–190, 2012.

[72] S. Wang and J. S. Thompson, "Signal processing implementation of Virtual Carrier for supporting M2M systems based on LTE," in *IEEE Vehicular Technology Conference (VTC Spring)*, pp. 1–5, May 2015.

[73] K. Pedersen, F. Frederiksen, C. Rosa, H. Nguyen, L. Garcia, and Y. Wang, "Carrier aggregation for LTE-Advanced: functionality and performance aspects," *IEEE Commun. Mag.*, vol. 49, pp. 89–95, June 2011.

[74] B. Widrow, I. Kollar, and M.-C. Liu, "Statistical theory of quantization," *IEEE Trans. Instrum. Meas.*, vol. 45, pp. 353–361, Apr 1996.

[75] "LTE resource grid," URL: http://dhagle.in/LTE.

[76] T. Sundstrom, B. Murmann, and C. Svensson, "Power dissipation bounds for high-speed Nyquist analog-to-digital converters," *IEEE Trans. Circuits Syst. I, Reg. Papers*, vol. 56, pp. 509–518, March 2009.

[77] K. Parhi and M. Ayinala, "Low-complexity Welch power spectral density computation," *IEEE Trans. Circuits Syst. I, Reg. Papers*, vol. 61, pp. 172–182, Jan 2014.

[78] W. Henkel, G. Taubock, P. Odling, P. Borjesson, and N. Petersson, "The cyclic prefix of OFDM/DMT - an analysis," in *International Zurich Seminar on Broadband Communications, Access, Transmission, Networking*, pp. 22–1–22–3, 2002.

[79] X. Tang, M.-S. Alouini, and A. Goldsmith, "Effect of channel estimation error on M-QAM BER performance in Rayleigh fading," *IEEE Trans. Commun.*, vol. 47, pp. 1856–1864, Dec 1999.

[80] G. Wunder *et al*, "5GNOW: non-orthogonal, asynchronous waveforms for future mobile applications," *IEEE Commun. Mag.*, vol. 52, pp. 97–105, February 2014.

[81] M. O. Pun, M. Morelli, and C. C. J. Kuo, "Maximum-likelihood synchronization and channel estimation for OFDMA uplink transmissions," *IEEE Trans. Commun.*, vol. 54, pp. 726–736, April 2006.

[82] E. Hossain and M. Hasan, "5G cellular: key enabling technologies and research challenges," *IEEE Instrum. Meas. Mag.*, vol. 18, pp. 11–21, June 2015.

[83] F. Schaich and T. Wild, "Waveform contenders for 5G, OFDM vs. FBMC vs. UFMC," in *International Symposium on communications, Control and Signal Processing (ISCCSP)*, pp. 457–460, May 2014.

[84] G. Wunder *et al*, "5GNOW: Challenging the LTE design paradigms of orthogonality and synchronicity," in *2013 IEEE Vehicular Technology Conference (VTC Spring)*, pp. 1–5, June 2013.

[85] G. Wunder *et al*, "5GNOW: Intermediate frame structure and transceiver concepts," in *IEEE Globecom Workshops*, pp. 565–570, Dec 2014.

[86] Y. Zhou, A. I. Karsilayan, and E. Serpedin, "Sensitivity of multiband ZP-OFDM ultra-wide-band and receivers to synchronization errors," *IEEE Transactions on Signal Processing*, vol. 55, pp. 729–734, Jan 2007.

[87] S. Venkatesan and R. A. Valenzuela, "OFDM for 5G: Cyclic prefix versus zero postfix, and filtering versus windowing," in *2016 IEEE International Conference on Communications (ICC)*, pp. 1–5, May 2016.

[88] *3GPP, TSG-RAN WG184b, R1-162199, Waveform Candidates*, URL: http://www.ee.iitm.ac.in/ giri/pdfs/EE5141/R1-162199-Waveform-Candidates.docx.

[89] J. Armstrong, "Analysis of new and existing methods of reducing intercarrier interference due to carrier frequency offset in OFDM," *IEEE Trans. Commun.*, vol. 47, pp. 365–369, Mar 1999.

[90] T. Hashimoto *et al*, "ICI mitigation schemes for uncoded OFDM over channels with Doppler spreads and frequency offsets part II: Asymptotic analysis," in *Journal of Communications*, pp. 686–700, Sep 2012.

[91] B. Muquet, Z. Wang, G. B. Giannakis, M. de Courville, and P. Duhamel, "Cyclic prefixing or zero padding for wireless multicarrier transmissions?," *IEEE Trans. Commun.*, vol. 50, pp. 2136–2148, Dec 2002.

[92] F. Schaich and T. Wild, "Relaxed synchronization support of universal filtered multi-carrier including autonomous timing advance," in *International Symposium on Wireless Communications Systems (ISWCS)*, pp. 203–208, Aug 2014.

[93] S. Holford and P. Agathoklis, "The use of model reduction techniques for designing IIR filters with linear phase in the passband," *IEEE Trans. Signal Process.*, vol. 44, pp. 2396–2404, Oct 1996.

[94] F. Harris, "On the use of windows for harmonic analysis with the discrete Fourier transform," *Proc. IEEE*, vol. 66, pp. 51–83, Jan 1978.

[95] K.-S. Tang, K.-F. Man, S. Kwong, and Z.-F. Liu, "Design and optimization of IIR filter structure using hierarchical genetic algorithms," *IEEE Trans. Ind. Electron.*, vol. 45, pp. 481–487, Jun 1998.

[96] S. Brandes, I. Cosovic, and M. Schnell, "Reduction of out-of-band radiation in OFDM systems by insertion of cancellation carriers," *IEEE Commun. Lett.*, vol. 10, pp. 420–422, June 2006.

[97] K. Manolakis, D. M. G. Estevez, V. Jungnickel, W. Xu, and C. Drewes, "A closed concept for synchronization and cell search in 3GPP LTE systems," in *IEEE Wireless Communications and Networking Conference*, pp. 1–6, April 2009.

[98] S. M. Kang, C. H. Kim, S. M. Jung, and S. K. Han, "Timing-offset-tolerant universal-filtered multicarrier passive optical network for asynchronous multiservices-over-fiber," *IEEE/OSA Journal of Optical Communications and Networking*, vol. 8, pp. 229–237, April 2016.

[99] J. B. Dore, R. Gerzaguet, and D. Ktenas, "5G cellular networks with relaxed synchronization: Waveform comparison and new results," in *IEEE 83rd Vehicular Technology Conference (VTC Spring)*, pp. 1–5, May 2016.

[100] S. A. Cheema, K. Naskovska, M. Attar, B. Zafar, and M. Haardt, "Performance comparison of space time block codes for different 5G air interface proposals," in *WSA 2016; 20th International ITG Workshop on Smart Antennas*, pp. 1–7, March 2016.

[101] A. Aminjavaheri, A. Farhang, A. RezazadehReyhani, and B. Farhang-Boroujeny, "Impact of timing and frequency offsets on multicarrier waveform candidates for 5G," in *IEEE Signal Processing and Signal Processing Education Workshop (SP/SPE)*, pp. 178–183, Aug 2015.

[102] X. Wang, T. Wild, and F. Schaich, "Filter optimization for carrier-frequency- and timing-offset in universal filtered multi-carrier systems," in *2015 IEEE 81st Vehicular Technology Conference (VTC Spring)*, pp. 1–6, May 2015.

[103] H. Wang, Z. Zhang, Y. Zhang, and C. Wang, "Universal filtered multi-carrier transmission with active interference cancellation," in *Wireless Communications Signal Processing (WCSP), 2015 International Conference on*, pp. 1–6, Oct 2015.

[104] M. J. Narasimha, "Modified overlap-add and overlap-save convolution algorithms for real signals," *IEEE Signal Process. Lett.*, vol. 13, pp. 669–671, Nov 2006.

[105] J. Armstrong, T. Gill, and C. Tellambura, "Performance of PCC-OFDM with overlapping symbol periods in a multipath channel," in *IEEE Global Telecommunications Conference (GLOBECOM)*, vol. 1, pp. 87–91 vol.1, 2000.

[106] K. K. Wojcicki and K. K. Paliwal, "Importance of the dynamic range of an analysis windowfunction for phase-only and magnitude-only reconstruction of speech," in *2007 IEEE International Conference on Acoustics, Speech and Signal Processing - ICASSP '07*, vol. 4, pp. IV–729–IV–732, April 2007.

[107] S. Wang and J. S. Thompson, "Performance analysis of VC receiver systems for M2M communications using orthogonal frequency-division multiple access," *IET Communications*, vol. 10, no. 16, pp. 2061–2070, 2016.

[108] F. Jabbarvaziri, M. Alizadeh, A. Mohammadi, and A. Abdipour, "Low-complexity method for primary synchronisation in the third generation partnership project long term evolution downlink system," *IET Communications*, vol. 10, no. 10, pp. 1229–1235, 2016.

[109] J. Peng, S. He, B. Wang, Z. Dai, and J. Pang, "Digital predistortion for power amplifier based on Sparse Bayesian learning," *IEEE Transactions on Circuits and Systems II: Express Briefs*, vol. 63, pp. 828–832, Sept 2016.

[110] O. Arouk, A. Ksentini, and T. Taleb, "Group paging-based energy saving for massive mtc accesses in lte and beyond networks," *IEEE J. Sel. Areas Commun.*, vol. 34, pp. 1086–1102, May 2016.